

Effect of Partial Pressure of Oxygen and Activity of Carbon on the Corrosion of High Temperature Alloys in s-CO₂ Environments

By

Jacob Thomas Mahaffey

A dissertation submitted in partial fulfillment of
the requirements for the degree of

Doctor of Philosophy
(Nuclear Engineering and Engineering Physics)

at the

UNIVERSITY OF WISCONSIN-MADISON

2017

Date of final oral examination: November 8th, 2017

The dissertation is approved by the following members of the Final Oral Committee:

Dr. Mark Anderson, Research Professor, NEEP
Dr. Kumar Sridharan, Research Professor, NEEP
Dr. Adrien Couet, Assistant Professor, NEEP
Dr. Todd Allen, Research Professor, NEEP
Dr. Dane Morgan, Research Professor, MS&E

© Copyright by Jacob Thomas Mahaffey, 2017
All Rights Reserved

Executive Summary

Over the course of the past couple decades, increased concern has grown on the topics of climate change and energy consumption, focusing primarily on carbon emissions. With modernization of countries like India and China, there are no signs of slowing of global carbon emissions and energy usage. In order to combat this, new more efficient power conversion cycles must be utilized. The s-CO₂ Brayton cycle promises increased efficiency and smaller component sizes. These cycles will push the limits of current high temperature materials, and must be studied before implementation is made possible.

A large collection of high temperature CO₂ corrosion research has been reported over the last thirty years. While many of the studies in the past have focused on corrosion in research grade (RG) (99.999%) and industrial grade (IG) (99.5%) CO₂, very few have focused on studying the specific effects that impurities can have on the corrosion rates and mechanisms. The work described in this document will lay the foundation for advancement of s-CO₂ corrosion studies.

A testing facility has been constructed and was designed as an open flow s-CO₂ loop with a CO₂ residence time of 2 hours. This facility is capable of heating up to 750°C at pressures up to 20 MPa. Instrumentation for measuring oxygen and carbon monoxide were added to make measurements both before and after sample exposure, for the duration of testing.

Testing of both model and commercial alloys was conducted for temperatures ranging from 450-750°C at 20MPa for 1,000 hours. The effect of the partial pressure of oxygen (pO₂) was studied by adding 100ppm of O₂ to RG CO₂ during testing. The activity of carbon (a_C) was studied by adding 1%CO to RG CO₂. Each environment greatly altered the mechanisms and rates of oxidation and carburization on each material exposed to the environment.

Acknowledgments

Financial support for this project was provided by NREL Subcontract No. AXL-3-23308-01, under DOE Prime Contract No. DE-AC36-08GO28308 to Alliance for Sustainable Energy, LLC, Management and Operating Contractor for the National Renewable Energy Laboratory and Cooperative Agreement DE-NE0000677 from the U.S. Department of Energy, Idaho Operations and from the Department of Energy Nuclear Energy University Program (NEUP) Grant No. DE-NE0000677, and "Advancement of Supercritical Carbon dioxide Technology through round robin testing and fundamental modeling" DE-0001129 project 15-8495.

At this point, I would like to thank Dr. Mark Anderson for all of the guidance and knowledge passed down throughout my time at Wisconsin. I would also like to thank Dr. Kumar Sridharan and Dr. Adrien Couet for their willingness to challenge, and guide the scope of this research, as well as Paul Brooks for all of the technical help since the very beginning of this project. Additionally, I would like to thank Dr. Todd Allen, Dr. Dane Morgan for their assistance in providing additional pathways for my learning and understanding of this work.

I also thank all of the graduate students that have been apart of the s-CO₂ materials research group who have helped contribute to the success of this group, as well as helping and challenging me each day.

Finally, I would like to thank my family for their continued support throughout the entire process. Brenda for the support and understanding even during the late nights. Last, but not least, I thank all of my friends that have brought me to this chapter in my life.

Table of Contents

Executive Summary	i
Acknowledgements	ii
Table of Contents	iii
List of Tables	vi
List of Figures	vii
1 Introduction	1
1.1 Motivation for Studying s-CO ₂ Corrosion	1
1.2 s-CO ₂ Brayton Cycle Background	2
2 Literature Review/Background into Corrosion in s-CO₂ Environments	5
2.1 High Temperature Corrosion	5
2.1.1 Oxidation Thermodynamics	6
2.1.2 Reaction Kinetics	10
Pilling-Bedworth (PB) Ratio	12
2.1.3 Thermal Expansion Mismatch	13
2.1.4 Ion Depletion and Void Formation	15
2.1.5 Carburization	16
2.1.6 Phase Removal	18
2.2 Importance of Impurities on Corrosion	19
2.3 Alloys in consideration	20
2.3.1 Ferritic Steels	21
2.3.2 Austenitic Steels	22
2.3.3 Nickel Chromium Superalloys	22
2.4 Oxidation in s-CO ₂ Environments - Background	23
2.5 Carburization in s-CO ₂ Environments - Background	26
2.6 Effect of Impurities in s-CO ₂ Environments - Background	29
2.6.1 Oxygen Impurities in CO ₂ - Background	31
2.6.2 Carbon Monoxide Impurities in CO ₂ - Background	33
2.7 Modeling Efforts for s-CO ₂ Corrosion	34
2.7.1 Coupling of Oxidizing and Carburizing Environments	34
2.7.2 Chromia Growth and Defect Structure	36
2.8 High Temperature Steam and Supercritical Water Corrosion	40

3	Experimental Facility	42
3.1	Testing Procedure	42
3.2	Materials Characterization/Analysis	43
3.3	Facility Overview	44
3.4	Flow Rate Modifications	47
3.5	Gas Analysis and Purity of CO ₂ from Vendor (Airgas)	48
3.5.1	Mass Spectrometry	49
3.5.2	Impurities Modifications	51
3.5.3	Oxygen Determination	52
3.5.4	Oxygen Impurities Mixing	53
3.5.5	Gas Chromatography	55
3.6	Facility Accuracy and Repeatability - Round Robin Testing	57
4	Effects of pO₂ and a_C on Corrosion in CO₂ Environments	65
4.1	Altering pO ₂ Changes the Stability of Different Oxides	65
4.2	Altering a _C Changes the Carburization of the Underlying Material	71
4.3	Saturation of CO ₂ with CO Causes Carbon Deposition During Cool-down	81
4.4	Altering pO ₂ and a _C to Control Defect Concentration Leading to the Production of a Stoichiometric Oxide	85
5	Connecting Corrosion Mechanisms From Model Alloys to Commercial Alloys	88
5.1	Corrosion of Ni20Cr in sCO ₂ Environments	88
5.2	Corrosion of Haynes 625 in sCO ₂ Environments	94
5.2.1	Haynes 625 Delta Phase Embrittlement	96
5.2.2	Corrosion of Haynes 625 in s-CO ₂ Environments	99
5.3	Summary - Connecting Corrosion Mechanisms From Model Alloys to Commercial Alloys	108
6	Industrial Compatibility of Materials in CO₂ Environments	109
6.1	Research Grade vs. Industrial Grade Testing	109
6.2	Corrosion Results for Select Alloys in s-CO ₂ Environments	112
6.2.1	Corrosion of Haynes 230 in s-CO ₂ Environments	112
6.2.2	Corrosion of Inconel 740H in s-CO ₂ Environments	119
6.2.3	Corrosion of Haynes 282 in s-CO ₂ Environments	124
6.3	Comparison of s-CO ₂ Corrosion to High Pressure Steam and Ultra Supercritical Steam	132
7	Conclusions for Corrosion in s-CO₂ Environments	136
8	Future Work	140
	References	142

Appendices	154
A Alloy Compositions	155
B Volatility Diagrams	156
C Time Dependant Mass Change Data in s-CO ₂ Environments	158
D Raman Spectral Summary	162
E Raman Standards	163
F XRD Standards	166
G Round-Robin Mass Change	171
H Round-Robin Parameters and Transients	174
I 1,000 Hour Mass/Thickness Measurements [mg/mm ²]	175
J Summary of Commercial Alloy Performance in s-CO ₂	177
K Certificates for Tested Alloys	178
L Certificates of Conformance	209

List of Tables

2.1	Metal oxide thicknesses grown at 800°C for 100 hours in $pO_2=1\text{atm}$ [13].	11
2.2	Parabolic rate constants and activation energies for typical oxides grown in air at elevated temperatures[17, 18, 19].	12
2.3	Thermal expansion coefficients for select oxides, base material, and alloys [22, 23, 24].	14
3.1	Testing environments and temperatures for experiments conducted at UW-Madison.	42
3.2	Complete list of materials exposed during sCO_2 testing conducted at UW-Madison.	43
3.3	Mass spectrometer peak locations for molecules of interest.	50
3.4	Bottle mixing information and oxygen concentration for bottles used in 100ppm oxygen doped testing.	54
3.5	Testing matrix for round robin project.	58
3.6	Round Robin oxide thickness results for CO_2 exposure at 550°C for 1500 hours.	60
4.1	Equilibrium constants for the decomposition of CO_2 at 750°C.	75
5.1	Composition of Haynes 625.	94
6.1	Mass change of samples exposed to RG and IG CO_2	110
6.2	Composition of Haynes 230.	113
6.3	Composition of Inconel 740H.	120
6.4	Composition of Haynes 282.	125
6.5	Operating conditions for various steam environments.	133
A.1	Composition of tested materials.	155

List of Figures

1.1	Global carbon emission based on country, and maximum plant efficiency for Rankine Cycle	2
1.2	Phase diagram of CO ₂ showing the critical point and supercritical region. .	3
1.3	Compressibility of CO ₂ and typical turbine sizes for Rankine and Brayton Cycles	3
1.4	Rankine and Brayton cycle efficiencies with TS diagram	4
2.1	Exothermic Gibbs Free Energy diagram.	7
2.2	Phase diagram of iron and oxygen with oxidation of pure iron	9
2.3	Chromium phase diagram and diffusion schematic.	10
2.4	Schematic showing depletion of oxidizing element in binary alloy.	16
2.5	Carburization of 12% Cr steel	17
2.6	Selective oxidation of Ni-23Al at 1200°C	19
2.7	Allowable stress for selected alloys.	21
2.8	Surface SEM for alloy 347 after 1,000 hours in RG CO ₂ at 650°C and 20MPa.	24
2.9	Cross Sectional SEM for alloys 316L and 347 after 1,000 hours in RG CO ₂ at 650°C and 20MPa.	25
2.10	Pressure effects on CO ₂ corrosion for alloy T92.	26
2.11	GDOES carbon profile for T92 exposed to CO ₂ at 550°C.	27
2.12	Carbon oxygen ratios for T92 exposed to CO ₂ at 550°C at varying pressures.	28
2.13	Carbon deposition in alloy 600 after exposure to CO ₂ at 600°C.	29
2.14	Weight change analysis for atmospheric CO ₂ impurities testing conducted at 700°C for 500 hours.	30
2.15	Weight change analysis for atmospheric CO ₂ impurities testing conducted at 750°C.	30
2.16	Weight change analysis for atmospheric CO ₂ impurities testing conducted at 800°C.	31
2.17	Volatility diagram proposed for the VHTR He with carbon impurities. . . .	35
2.18	Unit cell of chromia.	36
2.19	Brouwer diagram for chromia at different partial pressures of oxygen. . . .	39
3.1	Picture of the testing facilities at UW-Madison.	44
3.2	Temperature and pressure profile for dual autoclave system operating at 650 and 750°C and 20MPa.	45
3.3	AutoCAD schematic of testing facility	46
3.4	Typical heating and cooling rates for one autoclave at 750°C.	47
3.5	Gas certificates for research and industrial grade CO ₂ from Airgas	48
3.6	Gas analysis equipment.	49

3.7	Mass/Charge Spectra comparing research and industrial grade CO ₂ with oxygen doped CO ₂	50
3.8	Mass/Charge Spectrum of CO ₂ with injected water.	51
3.9	Oxygen+carbon monoxide bottle mixing schematic.	52
3.10	Oxygen concentration for 10ppm mixing setup.	54
3.11	Certification result for GC used in s-CO ₂ corrosion testing.	55
3.12	GC Spectra comparing research and industrial grade CO ₂	56
3.13	Concentration of CO for first 200 hours of 550°C RG test.	57
3.14	Round Robin mass change results for CO ₂ exposure at 550°C for 1500 hours.	59
3.15	Cross-sectional SEM micrographs for Round Robin samples exposed to CO ₂ at 550°C for 1500 hours.	60
3.16	Round Robin T92 etched to show carbides after CO ₂ exposure at 550°C, 20MPa, 1500 hours.	61
3.17	Round Robin mass change results for CO ₂ exposure at 700°C for 1500 hours.	62
3.18	Round Robin oxide thickness results for CO ₂ exposure at 700°C for 1500 hours.	63
3.19	Cross-sectional SEM micrographs for Round Robin samples exposed to CO ₂ at 700°C for 1500 hours.	63
4.1	Temperature and environmental dependence on oxidation of chromium and nickel.	66
4.2	Mass change of pure Ni in CO ₂ environments.	67
4.3	SEM micrographs of pure Ni exposed to RG and RG+1%CO.	67
4.4	XRD measurements of pure Ni in CO ₂ environments.	68
4.5	Raman measurements of pure Ni in CO ₂ environments.	68
4.6	SEM cross-sectional imaging for pure Ni exposed to CO ₂ at 750°C/20MPa for 1000 hours in 1%CO and RG environments.	69
4.7	SEM cross-sectional imaging of grain boundary attack of pure Ni exposed to RG CO ₂ at 750°C/20MPa for 1000 hours.	70
4.8	Volatility diagrams for Cr-C-O phases at 750°C at 1 atm.	72
4.9	Oxygen consumption during oxygen mixed s-CO ₂ testing (left). Volatility diagram for Cr-C-O phases at 750°C at 1 atm with oxygen doped environment (right).	74
4.10	Volatility diagrams for Cr-C-O phases at 750°C at 1 atm with estimated pO ₂ and a _C through the oxide.	76
4.11	Mass change of pure Cr in CO ₂ environments.	77
4.12	SEM micrographs of pure Cr exposed to RG and RG+1%CO.	77
4.13	SEM micrograph of pure Cr exposed to CO/CO ₂ mixture [64].	78
4.14	SEM imaging of pure Cr after polishing part of the oxide.	79
4.15	XRD measurements of pure Cr in CO ₂ environments.	80
4.16	Gibbs Free Energy of the Boudouard Reaction.	81
4.17	Equilibrium of CO ₂ constituents as a function of pO ₂ at 750 and 450°C	82

4.18	Summary of time dependent mass loss data for graphite exposed to s-CO ₂ at 650 and 750°C/20MPa.	83
4.19	Pictures of graphite samples exposed to several CO ₂ environments.	84
4.20	SIMS carbon profile for Haynes 625 exposed to CO ₂ for 1000 hours at 750°C in RG, RG with 1% CO, and RG with 100ppm O ₂	84
4.21	SEM cross-sectional imaging for oxides grown on Haynes 625 at 750°C/20MPa for 1,000 hours in s-CO ₂ environments.	86
5.1	Mass change of Ni-20Cr in CO ₂ environments.	89
5.2	SEM micrographs for binary alloy Ni-20Cr exposed to RG CO ₂ at 750°C for 1000 hours.	90
5.3	Surface EDS line scan for binary alloy Ni-20Cr exposed to RG CO ₂ at 750°C for 1000 hours.	90
5.4	Surface SEM micrographs for binary alloy Ni-20Cr exposed to RG-100ppm O ₂ at 750°C for 1000 hours.	91
5.5	Surface EDS line scan for binary alloy Ni-20Cr exposed to RG-100ppm O ₂ at 750°C for 1000 hours.	92
5.6	Cross-sectional EDS line scan for binary alloy Ni-20Cr exposed to RG and RG-100ppm O ₂ s-CO ₂ at 750°C for 1000 hours.	93
5.7	Haynes 625 Time-Temperature-Transformation Graph.	95
5.8	Characterization of as received Haynes 625.	96
5.9	Haynes 625 Delta Phase Precipitation at 600<T<900°C	97
5.10	Delta phase precipitation for Haynes 625 from 550-750°C.	98
5.11	Microhardness measurements for Haynes 625 post CO ₂ exposure	98
5.12	Mass change of Haynes 625 in various CO ₂ environments.	99
5.13	Cross-section SEM micrographs for alloy Haynes 625 exposed to various CO ₂ environments.	100
5.14	EDS line scan for Haynes 625 exposed to RG CO ₂ at 750°C for 1000 hours.	101
5.15	EDS line scan for Haynes 625 exposed to RG CO ₂ -100ppm O ₂ at 750°C for 1000 hours.	101
5.16	EDS line scan for Haynes 625 exposed to RG CO ₂ -1%CO at 750°C for 1000 hours.	102
5.17	Cross-section SEM micrographs for alloy Haynes 625 exposed to RG CO ₂ -1%CO at 750°C for 200 hours and 1000 hours.	103
5.18	SIMS carbon profile for Haynes 625 exposed to CO ₂ for 1000 hours at 750°C in RG, RG with 1% CO, and RG with 100ppm O ₂	104
5.19	Raman mapping of Haynes 625 exposed to CO ₂ environments at 750°C after 1000 hours.	105
5.20	EDS mapping of Cr and Mo for alloy Haynes 625 exposed to CO ₂ environments at 750°C for 1000 hours.	106
5.21	SEM imaging of oxide cracking on the surface of Haynes 625 exposed to 1%CO-CO ₂ environments at 750°C for 200 and 1000 hours.	107

6.1	Base characterization of Haynes 2230.	113
6.2	Mass change measurements for Haynes 230 samples exposed to CO ₂ environments 1000 hours.	114
6.3	SEM/EDS imaging of Haynes 230 samples exposed to s-CO ₂ environments.	115
6.4	Raman spectra for alloy Haynes 230.	117
6.5	XRD spectra for alloy Haynes 230 after exposure to RG CO ₂ , RG + 100ppm O ₂ , RG + 1%CO environments at 750°C/20MPa for 800 hours.	118
6.6	SEM/EDS imaging for Haynes 230 exposed to s-CO ₂ with added O ₂ and CO impurities.	119
6.7	Base characterization of Inconel 740H.	120
6.8	Mass change measurements of Inconel 740H exposed to s-CO ₂ at 750°C.	121
6.9	SEM/EDS imaging for Inconel 740H exposed to RG CO ₂ at 750°C/20MPa for 1000 hours.	122
6.10	Surface SEM imaging for Inconel 740H exposed to RG + 100ppm O ₂ at 750°C/20MPa for 1000 hours.	123
6.11	Cross-sectional SEM imaging for Inconel 740H exposed to RG + 100ppm O ₂ at 750°C/20MPa for 1000 hours.	124
6.12	Mass change measurements for Haynes 282 after exposure to sCO ₂ environments.	125
6.13	Surface SEM/EDS of Haynes 282 after exposure to sCO ₂	126
6.14	Cross-sectional SEM/EDS of Haynes 282 after exposure to sCO ₂ environments.	127
6.15	Gamma-Prime denudization of Haynes 282	129
6.16	Depth of gamma prime denudization for different sCO ₂ environments.	130
6.17	Vickers hardness measurements for Haynes 282 exposed to sCO ₂ environments.	131
6.18	Steam corrosion results at 670°C for 293 hours at 1 bar and 267 bar.	133
6.19	Parabolic rate constants for s-CO ₂ and steam environments.	134
6.20	Overlay of s-CO ₂ corrosion with steam corrosion	134
B.1	550°C volatility diagrams for CO doped cases	156
B.2	550°volatility diagrams for O ₂ doped cases	156
B.3	750°C volatility diagrams for CO doped cases	157
B.4	750°C volatility diagrams for O ₂ doped cases	157
C.1	Mass change results for alloy T92.	158
C.2	Mass change results for alloy 316L.	158
C.3	Mass change results for alloy 310S.	159
C.4	Mass change results for alloys 347 and 800H.	159
C.5	Mass change results for alloys 617 and 718.	159
C.6	Mass change results for alloys H230 and H625.	160
C.7	Mass change results for alloys H282 and 740H.	160
C.8	Mass change results for pure Ni and Cr.	160
C.9	Mass change results for alloys Ni-20Cr and SiC.	161

D.1	Raman Spectra for RG CO ₂	162
D.2	Raman Spectra for IG CO ₂	162
E.1	Raman standard spectrum for Cr ₂ O ₃	163
E.2	Raman standard spectrum for Fe ₂ O ₃	164
E.3	Raman standard spectrum for Fe ₃ O ₄	164
E.4	Raman standard spectrum for FeCr ₂ O ₄	165
E.5	Raman standard spectrum for NiO.	165
F.1	XRD standard spectrum for Cr ₂ O ₃	166
F.2	XRD standard spectrum for Fe ₂ O ₃	167
F.3	XRD standard spectrum for Fe ₃ O ₄	167
F.4	XRD standard spectrum for FeCr ₂ O ₄	168
F.5	XRD standard spectrum for NiO.	168
F.6	XRD standard spectrum for Cr ₂ 3C ₆	169
F.7	XRD standard spectrum for Cr ₇ C ₃	169
F.8	XRD standard spectrum for Cr ₃ C ₂	170
G.1	Round Robin mass change results alloy T91 exposed to s-CO ₂ at 550°C, 20MPa for 1500 hours.	171
G.2	Round Robin mass change results alloy 316 exposed to s-CO ₂ at 550°C, 20MPa for 1500 hours.	171
G.3	Round Robin mass change results alloy 625 exposed to s-CO ₂ at 550°C, 20MPa for 1500 hours.	172
G.4	Round Robin mass change results alloy 120 exposed to s-CO ₂ at 550°C, 20MPa for 1500 hours.	172
G.5	Round Robin mass change results alloy 740 exposed to s-CO ₂ at 550°C, 20MPa for 1500 hours.	173
H.1	Round Robin testing information for UW.	174
I.1	1,000 hour mass change measurements for s-CO ₂ environments.	175
I.2	1,000 hour thickness measurements for s-CO ₂ environments.	176
J.1	Table of commercial alloy compatibility in s-CO ₂	177
K.1	Certificate for Alloy 310S.	178
K.2	Certificate for Alloy 316L.	182
K.3	Certificate for Alloy 347H.	183
K.4	Certificate for Alloy H625.	184
K.5	Certificate for Alloy H718.	188
K.6	Certificate for Alloy 740H.	191
K.7	Certificate for Alloy 800H.	193
K.8	Certificate for Alloy AFA-OC6,7,10.	195

K.9	Certificate for Alloy T92.	196
K.10	Certificate for Alloy T122.	197
K.11	Certificate for Alloy 617.	198
K.12	Certificate for Alloy Fe-12Cr.	199
K.13	Certificate for Alloy H230.	200
K.14	Certificate for Alloy pure Fe.	203
K.15	Certificate for Alloy pure Ni.	204
K.16	Certificate for Alloy GR22.	206
K.17	Certificate for pure Cr.	208
L.1	Certificate of conformance for example Omega pressure transducer.	209
L.2	Certificate of conformance for Sartorius high precision scale.	211
L.3	Certificate of conformance for Varian 450 Gas Chromatograph.	213
L.4	Certificate of conformance for SSI Supercritical-24 pump.	214
L.5	Manual for calibration of Alpha-Omega Series 3000 Trace Oxygen Analyzer.	215
L.6	Calibration for Platinum Resistance Temperature Detector.	218

Chapter 1

Introduction to s-CO₂ Corrosion

1.1 Motivation for Studying s-CO₂ Corrosion

Over the course of the past few decades, increased concern has grown on the topics of climate change and energy consumption, focusing primarily on carbon emissions. Many estimates show that the global energy usage could increase by 69% by 2040 [1]. While some of the developed countries of the world have shown slight decrease in carbon emission, the push for modernization and increased standard of living in much of the developing world (India, China, and Africa) has set in place a large rise in energy demand, observed in Figure 1.1. This rise in demand is coupled with a staggering increase in carbon emission as regulations on pollutants are not as strenuous in many countries. The recent world-wide pledge of limiting the global temperature increase to 2°C will only be possible if many different pathways are utilized. One major contributor, which maintains a positive economic impact, is increasing the efficiencies of current power production [2]. Conventional steam Rankine cycles have been pushed to their efficiency limits (Figure 1.1), and in order to obtain the jump in efficiency that is required to make the biggest difference, other cycles in power conversion must be explored [3]. This recent push has fueled both research and implementation of the Supercritical Carbon Dioxide (s-CO₂) Brayton cycle technology.

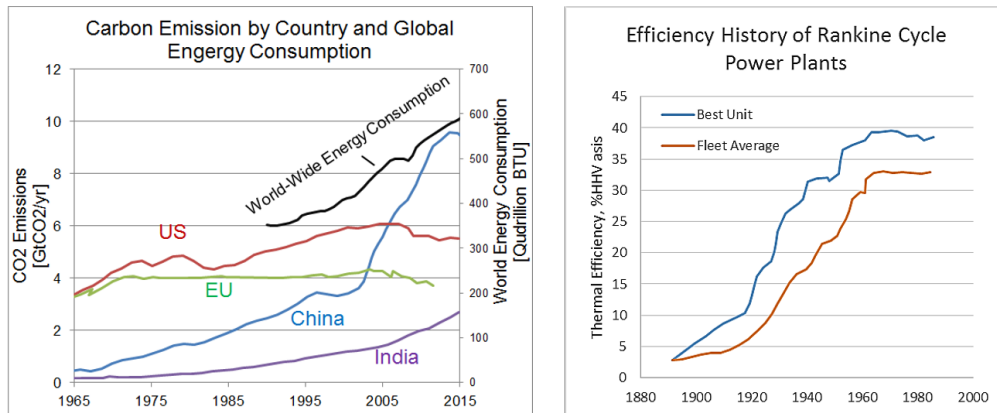


Figure 1.1: Global carbon emission based on country (Left) [4],[5], and maximum plant efficiency for Rankine Cycle (Right) [1].

1.2 s-CO₂ Brayton Cycle Background

The s-CO₂ Brayton Cycle utilizes carbon dioxide (CO₂) as the working fluid for power conversion. A supercritical fluid is described simply as a phase that contains properties of both liquid and gas. The dual nature of the properties of supercritical fluids is why they are so beneficial for efficiency gains in power plants. Once a fluid reaches the critical point, only decreasing either the pressure or temperature can convert it back to a gas or a liquid. Supercritical fluids take the shape of the container and are compressible much like a gas, but the density is substantially higher than the gas phase, and is much more similar to that of a liquid [6]. The phase diagram for CO₂ is given in Figure 1.2. The temperature and pressure region for the supercritical phase is also labeled.

The critical point is reached when CO₂ is heated to temperatures at or greater than 31°C, at a pressure exceeding 7.4MPa. This is considerably lower than water's critical point of 374°C and 21.8MPa [6]. The density of supercritical fluids changes very rapidly with temperature unlike gases and liquids. These rapid density changes near the critical point directly correlate to higher cycle efficiencies. The density as a function of temperature for several isobars for s-CO₂ is shown in Figure 1.3. The compressibility (volume changes with pressure) of s-CO₂

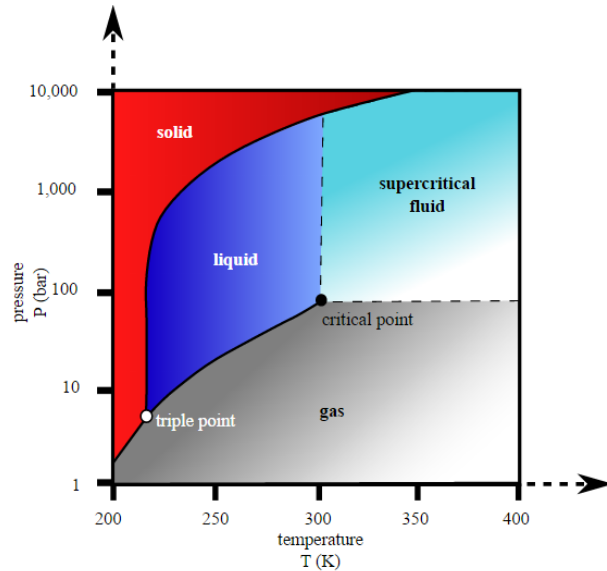


Figure 1.2: Phase diagram of CO_2 showing supercritical region [7].

also leads to significantly smaller turbine sizes which reduces initial investment costs. A comparison of the different turbine sizes is shown in Figure 1.3 as well [8].

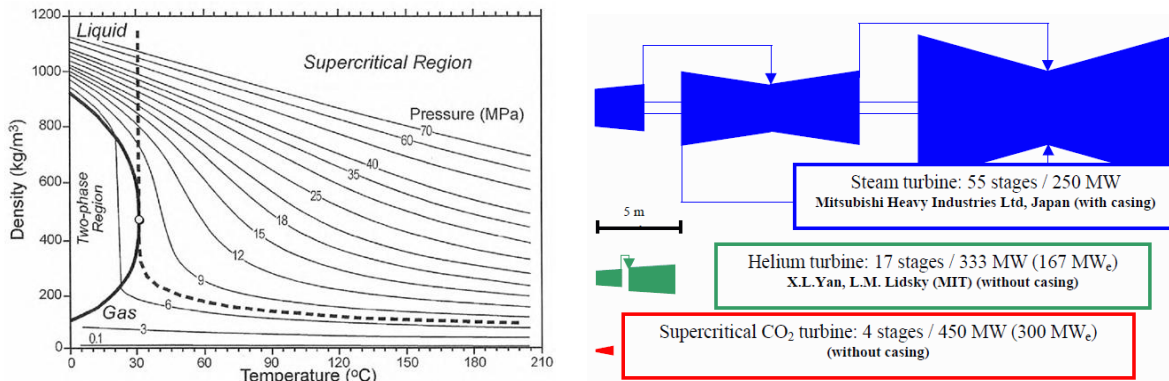


Figure 1.3: Density as a function of temperature for CO_2 in the supercritical phase (Left) [9], Turbine size comparison between Steam Rankine and s- CO_2 Brayton Cycle (Right) [8].

A large amount of research has been completed to accurately predict the efficiency of the s- CO_2 Brayton Cycle using these fluid properties. The efficiency of both Rankine and Brayton cycles are shown in Figure 1.4. [10]. Both s- CO_2 and helium Brayton Cycles are

plotted. Also given in Figure 1.4 is a TS diagram for a modeled configuration operating at 650°C [10].

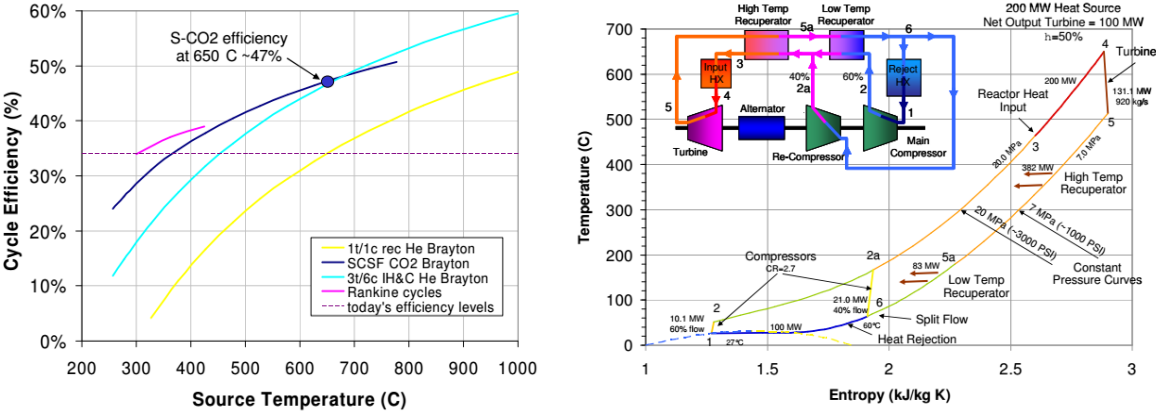


Figure 1.4: Cycle efficiencies for different temperature regimes (Left), TS diagram for split flow s-CO₂ Brayton Cycle (Right) [10].

It is observed that at lower source temperatures (<450°C), the traditional steam cycle is more efficient. Once temperatures exceed 450°C, the s-CO₂ cycle dominates in cycle efficiency. This is a very important aspect of these new cycles because it shows that very high temperatures and pressures are needed to achieve better efficiencies compared to the steam Rankine Cycle. The high temperature (450-750°C) and high pressure associated with the CO₂ Brayton cycle (~20MPa) make it an ideal candidate for nuclear applications, as current Boiling Water Reactors (BWR) and Pressurized Water Reactors (PWRs) operate at similar conditions. In fact, the use of CO₂ has been implemented in the past as coolant for MAGNOX reactors in Europe since 1956 [11]. These reactors were operated at much lower temperatures (typically <400°C). The real utility in use of CO₂ is pushing higher temperatures and pressures, which in return has a direct impact on the materials that can be used. Not only does the mechanical strength fail significantly for most alloys at these temperatures, but the corrosive behavior of CO₂ in the conditions must be considered [8, 10, 12].

Chapter 2

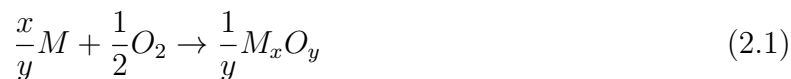
Literature Review/Background

Many texts have been produced on high temperature corrosion. The drive for this research stems from a range of applications from high temperature oxidation of power conversion cycles to combustion processes. An extensive background on literature pertaining to general high temperature corrosion will be provided in this section. A vast majority of the information presented in this chapter will be a combination from the texts: “High Temperature Oxidation and Corrosion of Metals” and “ASM Specialty Handbook, Heat Resistant Materials” which covers a large portion of the basics of corrosion specifically in high temperature environments [13, 14].

2.1 High Temperature Corrosion

High temperature oxidation can refer to many corrosion pathways that occur at “elevated temperatures.” The term “high temperature” or “elevated temperature” will be used in this report as anything exceeding 400°C. While many techniques have been developed for analyzing corrosion, they can be condensed in to two major categories, thermodynamic modeling, and experimental kinetic data. An introduction and discussion of these two categories will be completed in the following sections. The research conducted for this document focuses only on material exposure in CO₂, which only donates either oxygen, or carbon to react with the metal constituents. Therefore, oxidation and carburization will be the primary reaction pathways despite the importance of sulfidation, nitridation, or hydriding on general corrosion. Since the focus is on high temperature environments, emphasis will be placed on materials that have been proven in other extreme conditions, more specifically, alloys which produce a protective chromia layer.

In the most general case of oxidation, oxygen reacts with elemental metal to form an oxide. This is shown in Equation 2.1.



Despite the simplicity of the above equation, many other processes must occur for this to happen. A more detailed explanation for the oxidation process from [13] is as follows:

- Mass transport of oxidizing agent to scale-gas interface
- Diffusion of oxygen into the scale
- Diffusion of metal from alloy to alloy-scale interface
- Incorporation of metal into scale
- Diffusion of metal or oxygen through scale

These steps show that while Equation 2.1 might be thermodynamically favorable, many other steps must occur for the reaction to proceed. In fact, these other steps can greatly effect the kinetics and thermodynamics of the system specifically the oxidation/carburization processes.

2.1.1 Oxidation Thermodynamics

Thermodynamics of oxidation are used to predict the possibility of reaction, reaction selection, and potentially mechanisms of each reaction. Thermodynamics are based on the elements and compounds and do not reflect the rates in which the reactions occur. In oxidation, typically these equations will be dependent on the partial pressure of oxygen/activity of oxidant, and the Gibbs Free Energy of the reaction of interest. Each of these factors can

be calculated from known quantities. Partial pressure of oxygen (pO_2) or activity of carbon (a_C) can be calculated from the initial environmental chemical equilibrium. An estimate of these values can be calculated at the metal-oxide (M-O) interface as the phase equilibrium between chromium and chromia (Cr_2O_3). The exact pO_2 and a_C through the oxide becomes much more difficult to calculate, but must lie between the two boundary conditions. The Gibbs Free Energy for reactions can be typically found or calculated from literature. To illustrate the difference between thermodynamics and kinetics, an example Gibbs Free Energy diagram has been plotted in Figure 2.1.

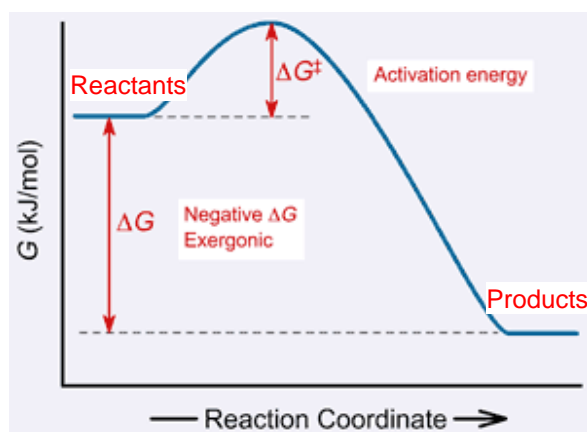


Figure 2.1: Gibbs Free Energy diagram for an exothermic reaction [15].

Figure 2.1 gives an example of an exothermic reaction, meaning that energy is produced during the forward reaction while converting reactants to products. Exothermic reactions have a negative ΔG , and are favorable for the forward reaction (spontaneous). The ΔG plotted above is calculated using the enthalpy, temperature and entropy of each of the compounds in the reaction. The values for enthalpy and entropy are stored in tables, and can be looked up for all reactions as a function of temperature. Ellingham diagrams use ΔG values to calculate equilibrium conditions for oxidation reactions as a function of temperature and pO_2 , which can be a good tool in determining which reactions occur. An Ellingham

Diagram is not given in this section because more focused calculations specifically for this research were completed and listed in Chapter 4 and Appendix B.

Thermodynamic data is typically used to predict reaction products and phases resulting from multicomponent systems. Treatment of phases and components can be predicted using the phase rule shown in Equation 2.2. This rule uses the composition and the number of phases present to predict the degrees of freedom in the system. This is incredibly powerful when considering pure metals, binary or ternary alloys exposed to isobaric, and isothermal conditions. If pure iron is exposed to oxygen at constant temperature and pressure, the phase rule in Equation 2.2 must hold true (the +2 goes to 0 due to isothermal and isobaric conditions) with composition ($C=2$). This shows that the number of phases present dictates the degrees of freedom in the stoichiometry of the oxide. If two phases are present in the phase diagram, a stoichiometric oxide is formed, if only one phase is present, a univariant composition occurs. The phase diagram as well as a cross-sectional image of iron oxide is given in Figure 2.2. This univariant composition causes concentration gradients throughout the oxide, which drives diffusion of ions, and further grows the scale. The two phase regions do not have this gradient, and therefore does not promote diffusion, and inhibits growth in the two phase region. This can be observed by the sharp interfaces between the oxide layers.

$$F = C - P + 2 \quad (2.2)$$

A phase diagram for Cr-O-C system at 900°C is plotted in Figure 2.3 as well as the diffusion schematic of a similar system. The oxide is shown to be more stable than the carbides, and only in very low oxygen potentials can carbides form. It was therefore believed that carbides could only form in CO/CO_2 systems or other mixed environments due to the very low pO_2 . The carbides are usually deposited in the base material where the partial pressure of oxygen is at its lowest. Since this figure is given at 900°C, calculations were done

to produce volatility diagrams using the conditions that will be tested for this research, and can be found in Chapter 4, and Appendix B.

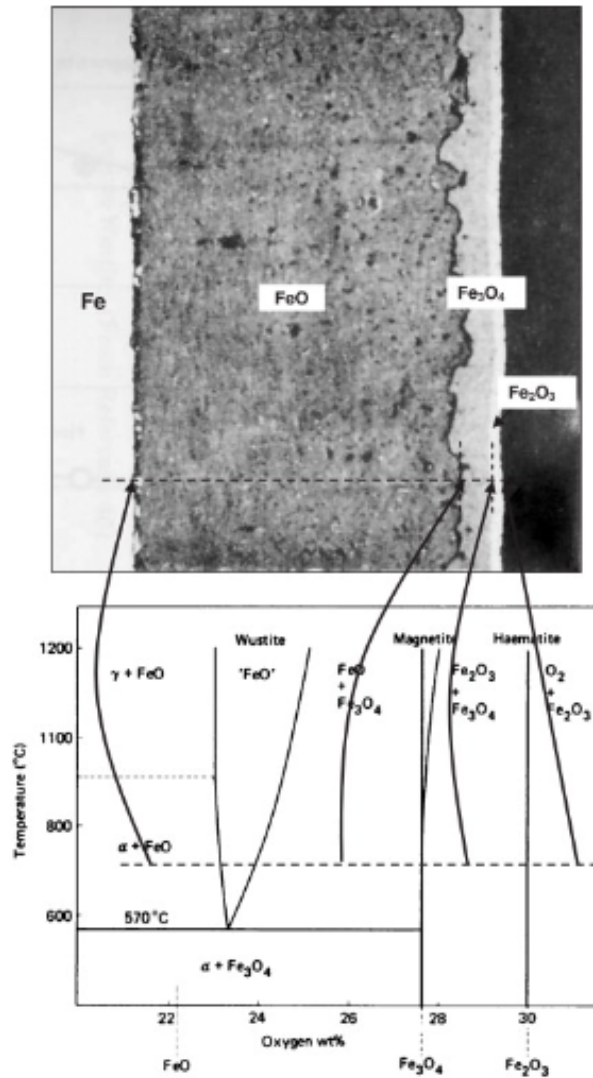


Figure 2.2: Oxide layer grown on pure iron with phase diagram showing application of the phase rule [13].

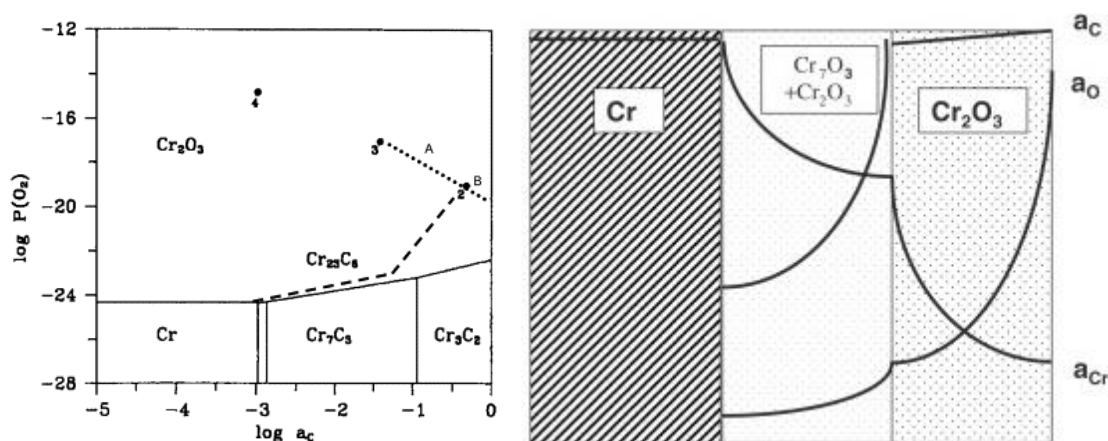


Figure 2.3: Chromium-oxygen-carbon volatility diagram at 900°C (Left). Schematic of oxygen and carbon activity throughout the scale and base material (Right) [13].

2.1.2 Reaction Kinetics

Kinetics dictate how fast the reaction occurs, and are just as important to corrosion as thermodynamics. An example of this is presented in Table 2.1, which shows the relative speeds of oxidation for several pure metals. This data shows that iron is much more susceptible to attack, and grows an oxide hundreds of times thicker than chromium when exposed to the conditions presented in Table 2.1. This type of analysis is near impossible to determine without experimental work. This is because the rate of the reaction is controlled by the activation energy, which was given in Figure 2.1 above as ΔG^\ddagger . Unfortunately, the amount of energy needed for the reaction to occur (ΔG^\ddagger) cannot be easily calculated using basic principles. Some computational models such as DFT modeling can attempt to predict ΔG^\ddagger , but usually multicomponent systems such as oxidation of commercial alloys is nearly impossible to calculate, and experimental work must be done to obtain accurate information on the reaction rate. Fortunately, a significant amount of work has been completed on oxidation of pure alloys, binary alloys, and commercial alloys in many environments which can be applied/compared to s-CO₂ systems.

Table 2.1: Metal oxide thicknesses grown at 800°C for 100 hours in pO₂=1atm [13].

Metal	Scale thickness (mm)
Fe	1.1
Ni	0.01
Cr	0.003
Al*	0.001

*Measured on Ni-50Al

Reaction kinetics are closely related to the diffusion of ions or oxygen through the scale as long as gaseous transport to the material is not limiting. A good model for ion and oxygen transport throughout the scale is given by Wagner's Theory of Oxidation. One of the core assumptions of this model is that either the oxygen or ion transport through the scale is the limiting kinetic step in the oxidation process [16]. This means that after the initial surface is oxidized, the rate of reaction is controlled by diffusion of either ions through the oxide to the oxide-gas interface, or oxygen diffusion to the metal-oxide interface. In either case, the governing differential equations are commonly solved to the parabolic form for oxide thickness (X) as a function of time (t) and rate constant (k_p) given in Equation 2.3.

$$X^2 = 2k_p t \quad [cm^2/s] \quad (2.3)$$

Many oxides grow based on parabolic kinetics in idealized situations, including iron, chromium, and aluminum. Equation 2.3 shows that the reaction slows down as the square root of time. This is because the oxide thickness is increasing, and therefore increases the diffusion path length which slows the limiting step in the process. The only unknown from the above equation is k_p which is the parabolic rate constant. This constant can be predicted using diffusion models, but typically mass transport through oxides are magnitudes higher than the predicted values due to defects in the crystalline lattice. This is another reason why experimental data is almost always used to calculate reaction rates.

Experimental data takes a large amount of time to acquire, and therefore, it is usually valuable to take existing data, and extrapolate out to longer times (Equation 2.3) or different temperatures. Temperature extrapolation for oxide growth uses the Arrhenius Equation 2.4. Table 2.2 gives data for the other constants in Equation 2.4 for pure iron, nickel, and chromium oxides.

$$k_p = k_o \exp\left(\frac{-Q}{RT}\right) \quad (2.4)$$

Table 2.2: Parabolic rate constants and activation energies for typical oxides grown in air at elevated temperatures [17, 18, 19].

	$K_{p,1273K}$ [cm^2/s]	Q [kg/mol]	$K_{p,1023K}$ [cm^2/s]
Fe:	2E-08	164	3.8E-10
Ni:	1.4E-12	120	8.7E-14
Cr:	1.3E-13	243	4.6E-16

Since chromium is the primary added alloying element for corrosion resistance at the temperatures that this research focuses on ($< 1000^\circ C$) it is important to compare the parabolic rate constants from the literature to the results of these experiments. Using Equation 2.4, $k_{p,750^\circ C} = 4.6 \times 10^{-16} cm^2/s$. The constants in Table 2.2 were found in pure oxygen at $1000^\circ C$, so some variation in rate constant is expected when comparing to CO_2 corrosion.

It is also important to mention that the partial pressure of oxygen (pO_2) also has a large effect on the corrosion kinetics. While the exact magnitude for each alloy is difficult to determine due to reasons mentioned previously, a very large difference in corrosion rates is typically observed when the pO_2 is altered.

Pilling-Bedworth (PB) Ratio

One way to determine if an oxide forms a protective scale is to calculate the Pilling-Bedworth (PB) Ratio [20]. This ratio compares the amount of metal lost to the oxide gained shown

in Equation 2.5. The volumes correspond to the oxide thickness (X) and metal loss(X^M). Each of these values is calculated using Equations 2.6, and 2.7 from the weight change (ΔW), area of flat sample (A), the molecular weights of the metal and oxide (MW), The density of the oxide and metal ($\rho_{ox,M}$), and the stoichiometric components of the oxide (x,y) given in Equation 2.1.

$$R_{PB} = \frac{V_{oxide}}{V_{Metal}} \quad (2.5)$$

$$MetalLoss : X^M = \frac{A * W_M * x}{16\rho_M y} * \frac{\Delta W}{A} \quad (2.6)$$

$$OxideThickness : X = \frac{MW_{ox}}{16\rho_{ox} y} * \frac{\Delta W}{A} \quad (2.7)$$

Typical values for the PB ratios for FeO , Fe_2O_3 , Fe_3O_4 , NiO , Al_2O_3 and Cr_2O_3 are given by 1.69, 2.14, 2.10, 1.68, 1.29, and 2.00 respectively [21]. Usually, PB ratios over two means that the oxide will chip off, and is not protective (Fe_3O_4, Fe_2O_3). PB ratios under 1 usually means that the oxide is too thin, implying volatility, or cracking occurred, and is not protective. Finally a PB ratio between one and two indicates a protective scale (NiO , Al_2O_3 , Cr_2O_3).

2.1.3 Thermal Expansion Mismatch

Thermodynamics and kinetics produce a good explanation for why and how the oxide is formed, and are directly related to how corrosion effects the underlying material. One of the concerns during oxidation is metal loss, and the resulting detrimental effects on the mechanical properties of the material. Metal loss occurs as the material is oxidized, and can be rapidly increased if oxide exfoliation (spallation) occurs due to the removal of the

protective oxide layer. Exfoliation of the oxide usually occurs due to stress build up between the base material and scale interface. This stress can be caused by growth of the oxide, oxide growth on curved surfaces, environmental stresses (flow), and temperature transients (due to differences in thermal expansion coefficients). The last example is the most important for the current research as typically thin oxide scales are grown on flat surfaces, and in quasi-static conditions, but are subject to temperature changes during testing intervals.

Since the oxide is grown at high temperatures, cooling the system will cause the oxide and metal to contract at different rates and magnitudes, this is given by the thermal expansion coefficients for each constituent, and can be very different for some oxides compared to the base alloy. Typically, values for the metal alloy are larger than that of the oxide, which compresses the oxide as the system cools. Table 2.3 gives the thermal expansion coefficients for common alloys and typical oxides.

Table 2.3: Thermal expansion coefficients for select oxides, base material, and alloys [22, 23, 24].

Material	$10^6\alpha$ (K^{-1})	T ($^{\circ}C$)
Fe	15.3	0–900
FeO	15	400–800
FeO	12.2	100–1,000
Fe ₂ O ₃	14.9	20–900
Ni	17.6	0–1,000
NiO	17.1	20–1,000
Cr	9.5	0–1,000
Cr ₂ O ₃	7.3	100–1,000
Cr ₂ O ₃	8.5	400–800
Alloy 800	16.2–19.2	20–1,000

It can be observed that the mismatch between chromia and nickel is less than the difference between chromia and alloy 800H, which could be one reason why exfoliation of oxide is more readily observed on austenitic steels (such as 800H) over nickel based alloys. If the

oxide stays adherent on the surface, other stress relief mechanisms can occur. The stresses can cause creep and plastic deformation of the base material underneath the oxide, which deforms the grain structure, and shape of the material. This is also detrimental to application purposes.

2.1.4 Ion Depletion and Void Formation

Diffusion of the oxidizing elements plays a very important role in scale formation. There are many different situations which can arise as the oxidizing elements diffuse towards the surface, and eventually bonds to oxygen to form the scale. For example, alloys with very dilute amounts of chromium will form less stable oxides if the chromium in the base material is not able to replace the amount being oxidized. This situation also relies on excess oxygen near the surface to react with chromium. The diffusion of chromium is primarily substitutional with the nickel matrix, or vacancy diffusion. This means that as the chromium is used, it is expected to see a depletion of chromium near the metal-oxide interface, and an increase in nickel concentration. This is sketched in Figure 2.4. It is important to note that if diffusion through the matrix is fast compared to the oxidation rate, no depletion is observed.

Ion depletion can be studied by looking at the ratio of the oxidation rate to the diffusion coefficient of the particular oxidant (k_c/D). The value of k_c/D is considerably larger for Ni-Cr alloys compared to Fe-Cr alloys meaning that the depletion should be higher for nickel alloys. Ni-Al has the lowest, and usually no depletion is observed for these alloys. The enrichment of nickel and depletion of chromium is also subject to increases in vacancy concentration as the scale is formed. If enough vacancies coalesce, voids can form directly beneath the oxide-metal interface. This is a very general explanation of the Kirkendall Effect, and has been observed in many oxidation studies. Voids near the oxide metal interface have been observed to increase spallation rates of the oxide. In other cases, voids have been theorized

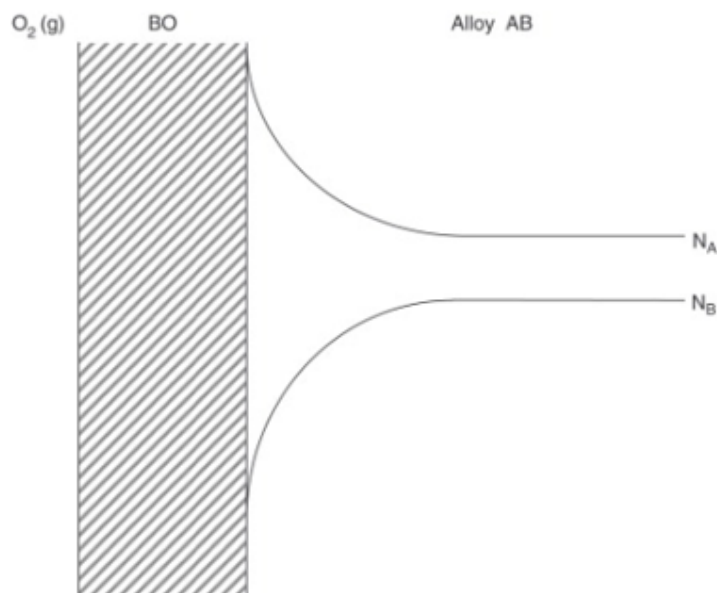


Figure 2.4: Concentration profile of binary alloy showing depletion of oxidizing element near scale surface [13].

to create micro-environments through diffusion of the gaseous elements which leads to either internal oxidation, or carburization beneath the oxide [25, 26]. This typically occurs near grain boundaries where diffusion is fastest.

2.1.5 Carburization

A majority of the discussion thus far has been about oxidation of alloys. CO_2 can also donate carbon during the corrosion process. It was discussed previously that carbides were not thermodynamically favorable in the pure CO_2 mixed environment (Appendix B), but many reports and studies have shown otherwise [26, 27]. The evidence of carburization indicates that the partial pressure of oxygen must drop several orders of magnitude throughout the oxide which is predicted by Wagner's Theory. The resulting carbon activity must also reach a high enough point before carbides will form. It has been theorized that micro environments beneath the scale cause complete reduction of CO_2 to leave high carbon activity zones

specifically along grain boundaries and other high diffusion pathways [26]. This has been studied in great detail for 9-12%Cr alloys. An example is given in Figure 2.5 where 200 microns of the base material has been carburized.

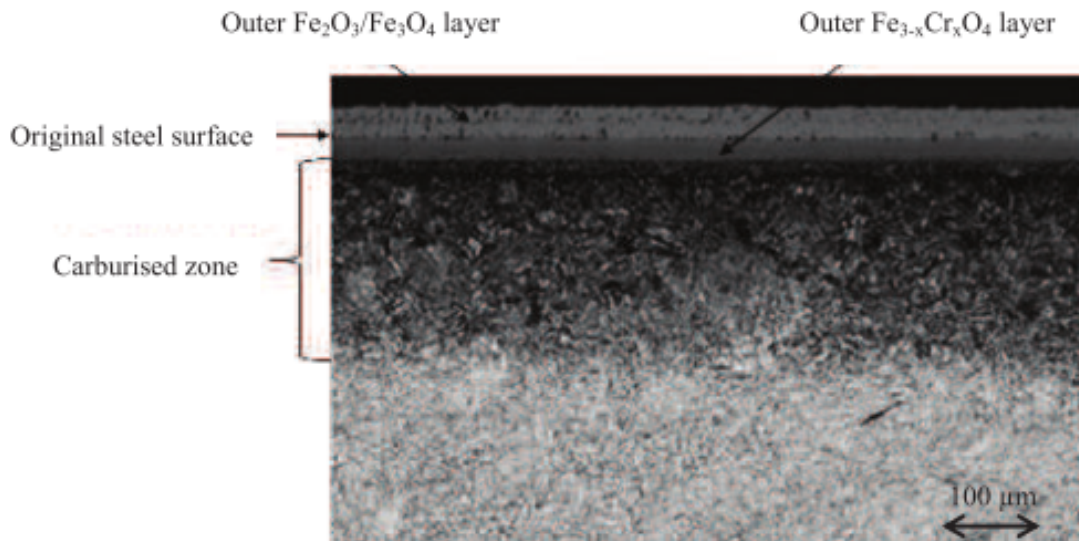


Figure 2.5: Carburization zone of 12% Cr steel exposed to CO_2 at 550°C for 5000 hours at 200 bar [26].

Very little carburization has been observed for nickel based superalloys exposed to pure CO_2 . This is most likely due to slower reaction rates, and the mechanistic differences in oxide formation. Carburization is very concerning in Fe-Cr alloys as the effected region has been shown to be up to 10 times larger than the oxide that is produced. Carbides have been known to increase the strength, but greatly decrease the ductility in the alloy. This can lead to brittle fracture and more oxide exfoliation, resulting in increased material loss.

In extreme cases when the carbon activity exceeds 1, metal dusting can occur which completely destroys the underlying material. In iron based alloys, metal dusting is usually caused by the metastable Fe_3C carbide formation, whereas nickel alloys are due to graphitization. This is a current concern in blast furnaces which operate between $450\text{-}750^\circ\text{C}$ in high CO/CO_2 environments [28].

2.1.6 Phase Removal

While oxidation is easily observed at the surface of the alloy, several effects occur below the oxide due to the corrosion process. If the oxygen potential is high enough in the base material, internal oxidation can occur. This is usually enhanced along grain boundaries due to faster diffusion. For example this has been observed in H230 for both air and oxygen doped CO₂ conditions [25, 29].

The formation of the oxide also depletes the base alloy of oxidizing elements such as chromium, aluminum and nickel. This can be very detrimental to the mechanical properties. The highest strength nickel based superalloys derive their strength from the precipitation of the gamma prime (a Ni₃Al phase). If the aluminum used for the gamma prime phase is removed during the formation of the oxide, then the strengthening mechanism of the alloy is compromised. This is observed in Figure 2.6. The etched alloy shows 50-70 microns of gamma prime phase removal due to selective oxidation of aluminum. This will be an important consideration when testing oxygen rich CO₂ environments.

If the oxygen potential is high enough at the scale interface, carbides can also be removed through decarburization forming CO. This is one form of internal oxidation, and is once again usually enhanced along grain boundaries. Catastrophic decarburization has been observed in the past for boiler tube walls which resulted in rupture of the tube [13]. The removal of carbides can greatly reduce the strength of alloys which leads to failure. For this reason, it has been theorized that purely oxidizing or carburizing environments are more detrimental than environments consisting of both such as corrosion in CO₂ [30]. Decarburization will be studied in environments containing the highest oxygen partial pressures.

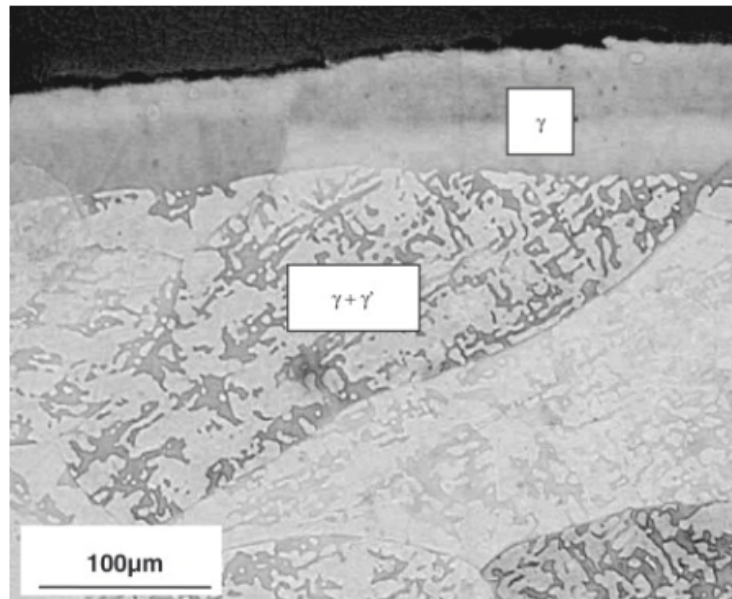


Figure 2.6: Removal of gamma prime phase in Ni-23Al caused by selective oxidation of aluminum at 1200°C [13].

2.2 Importance of Impurities on Corrosion

It has been widely accepted that impurities in the oxidizing gas or liquid can dramatically effect the corrosion rates of materials. One such example has been observed in steam oxidation, which can cause up to ten times the corrosion rate of dry air [31, 32]. On the other hand, great success has been achieved in carbon steel production by monitoring the excess air in combustion processes. If the excess air is not monitored, up to 2% of the base material could be oxidized, whereas the lower partial pressure of oxygen (no excess air) environment greatly reduces the corrosion rate. Nuclear systems have also had to account for impurities, specifically in the coolant chemistry, which can cause very high oxidation rates on fuel cladding [33].

2.3 Alloys in consideration

While corrosion is the main focus of this research, many other factors such as mechanical properties (strength, toughness, weldability, etc) and cost play just as big of a role in alloy selection. Figure 2.7 displays the allowable stress given for a range of materials [34]. It can be observed that ferritic and austenitic steels cannot be used at temperatures exceeding 650°C due to their low strength at these temperatures. Since the current motivation/necessity is for materials that can withstand temperatures above 700°C (to reach higher plant efficiencies), nickel based superalloys will be the prime focus of this research (Haynes 625, Haynes 230, Inconel 740H, and Haynes 282). Each of these alloys was selected due to compositional differences, and compatibility in current facilities. Several other commercial alloys (Ferritic, Austenitic, Nickel Based Superalloys) and model alloys (Ni, Cr, Ni-20Cr) have been tested as well. Compositions for each alloy are listed in Appendix A, and certificates in Appendix K.

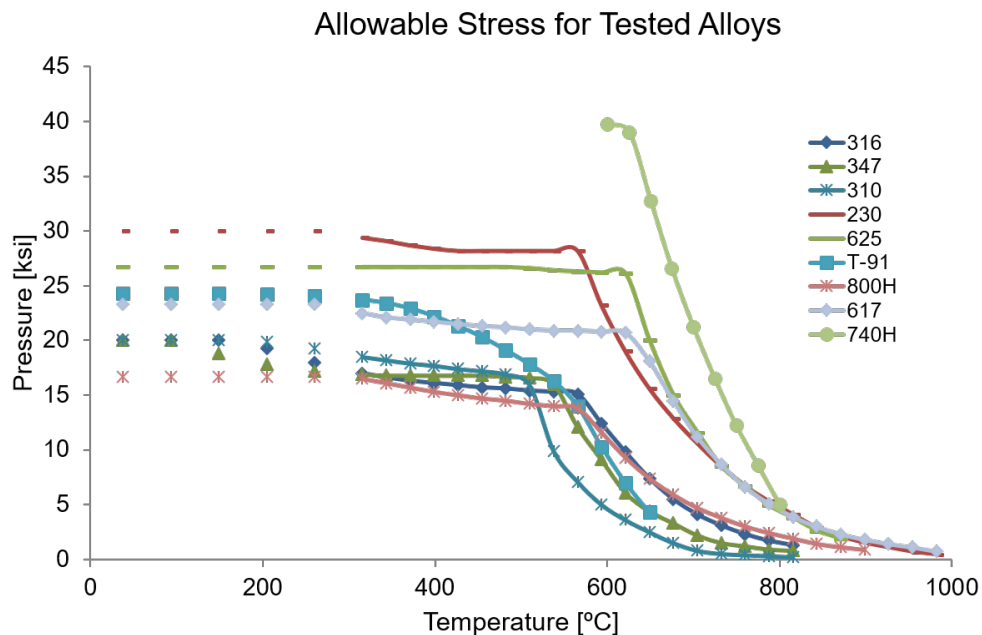


Figure 2.7: Temperature dependence on allowable stress for selected alloys. Found in Process Piping [34].

2.3.1 Ferritic Steels

Ferritic steels are characterized by the ferrite structure. Ferrite refers to body centered cubic (BCC) iron with limited solid solution carbon. The small amount of carbon dissolved into the matrix is used for strengthening the alloy. Ferritic alloys are known for their relatively good oxidation resistance due to higher concentrations of chromium than carbon steels (typically forming iron oxide outer layers, with a protective inner chromium iron rich spinel). They are not particularly good in terms of mechanical strength at high temperatures, and can not be used at temperatures exceeding around 600°C at elevated pressure. These alloys are also susceptible to sigma phase embrittlement, which occurs at temperatures above 550°C [35]. This causes the BCC lattice to collapse and form a tetragonal crystalline structure, which increases the hardness and subsequently decreases the toughness which can cause brittle failure of these alloys. Ferritic steels are typically used as furnace materials, thermocouple

protection tubes, and other high temperature, low stress environments where corrosion would otherwise be catastrophic for carbon steels, due to low production costs.

2.3.2 Austenitic Steels

Austenitic alloys are characterized by the face centered cubic (FCC) gamma iron phase. This phase is relatively soft, and ductile, but can dissolve much more alloying elements than ferrite. This allows for precipitation and solid solution hardening, and very high concentrations of chromium for oxidation resistance. Alloy 310S for instance, contains up to 25% chromium, and has been known in many environments to form a thin protective chromia layer. These alloys are used in a wide variety of applications, but just like the ferritic alloys provide low strength at temperatures over 600°C.

2.3.3 Nickel Chromium Superalloys

The first nickel based superalloys were created in the early 1900's in the form of nickel chromium resistance heating elements. Since then, many changes to these alloys has propelled them to be some of the most desirable selections for high temperature, high stress, and corrosive environments. Figure 2.7 shows the higher strength at temperatures up to about 750-800°C when compared to the ferritic and austenitic steels discussed previously. Nickel superalloys typically derive their strength from either solid solution strengtheners (W, Mo) or aluminum additions which precipitate the gamma prime (Ni_3Al, Ti) phase throughout the gamma nickel matrix. Examples of solid solution strengthened nickel based alloys are Haynes 230 and Haynes 625 which have large quantities of tungsten (precipitates in to tungsten carbides), and molybdenum respectively. Haynes 282 and Inconel 740H are examples of Gamma prime strengthened superalloys, but also have solid solution strengthening elements as well. Another subsection of nickel based superalloys, consists of iron rich version

of the alloys. These alloys are typically better for compatibility (weldability) with iron rich stainless steels. Alloy 718 is a good example of a hybrid iron-rich superalloy.

2.4 Oxidation in s-CO₂ Environments - Background

Previous work performed by UW-Madison focused on corrosion behavior of several ferritic-martensitic steels (T91 and HCM12A), austenitic stainless steels (316L, 310S, AL-6XN and 800H), as well as nickel-based alloys (Haynes 230 and Alloy 625) in s-CO₂ environment up to 650°C and 20MPa [36, 37, 38, 39]. In these studies, ferritic steels were shown to exhibit the highest corrosion rates with a relatively thick oxide scale (thin outer hematite (Fe_2O_3), followed by a magnetite (Fe_3O_4), and inner iron chromium spinel layer ($FeCr_2O_4$)). 316L stainless steel demonstrated slightly better corrosion resistance than the ferritic steels, developing a similar oxide structure. The other austenitic steels studied contained considerably more chromium (>20wt%), and exhibited better oxidation resistance due to the predominant growth of a chromium rich oxide layer. Nickel-based alloys demonstrated the best oxidation resistance and similarly developed a chromium-rich oxide layer. These results are also supported by studies conducted by other researchers in which Ni-base superalloys were shown to exhibit excellent corrosion resistance in very pure CO₂ at temperatures up to 750°C and pressures ranging from atmospheric to 20MPa [37, 40, 41, 42, 43, 44, 45, 46].

One of the most extensive studies on corrosion of alloys in high temperature/pressure CO₂ was generated from the research conducted under the MAGNOX reactor program in the U.K [27]. This program dealt primarily with ferritic and austenitic steels, therefore, testing temperatures rarely exceeded 600°C at elevated pressure. In order to operate the s-CO₂ cycle at higher temperatures, Ni-based alloys must be used due to their high temperature strength. However, there is a lack of information on higher temperature performance of Ni-based alloys in s-CO₂ environment.

Another recent study was conducted at UW-Madison on several austenitic alloys. These alloys are considered much better when it comes to oxidation resistance compared to ferritic alloys due to the higher concentration of chromium. The increased concentration generally leads to a more uniform and protective chromia (Cr_2O_3) layer. SEM of the surface of alloy 347 in s-CO₂ at 650°C and 20MPa after exposure is given in Figure 2.8.

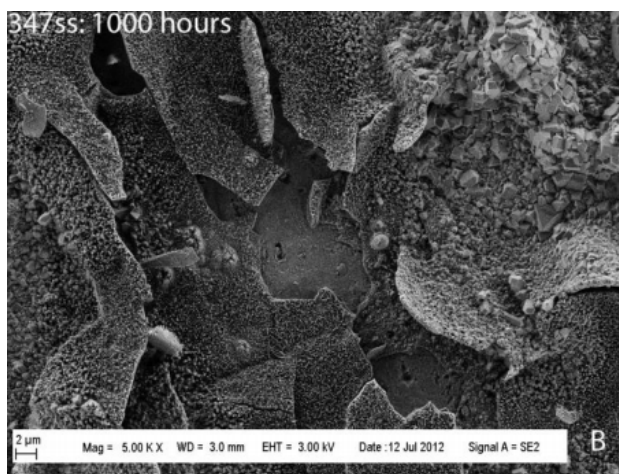


Figure 2.8: Surface SEM for alloy 347 after 1,000 hours in RG CO₂ at 650°C and 20MPa[47].

The surface SEM clearly shows evidence of spallation of the oxide. Exfoliation of the oxide is very disastrous for industrial applications, and could lead to failure of the turbo-machinery, or loss of mechanical strength. In order to study the oxide in more detail, SEM and EDS analysis of the cross section of the oxide was completed. This is shown in Figure 2.9 along with alloy 316L for comparison.

The EDS analysis shows that alloy 347 produced a dual layer oxide composed of an iron rich outer layer, and an inner iron chromium spinel. The oxide thickness for alloy 347 was thinner than the oxide on alloy 316L. It is theorized that 347 produced a more chromium rich spinel which decreased iron and oxygen diffusion through the oxide. This is supported by the chromium concentration in Figure 2.9 as well.

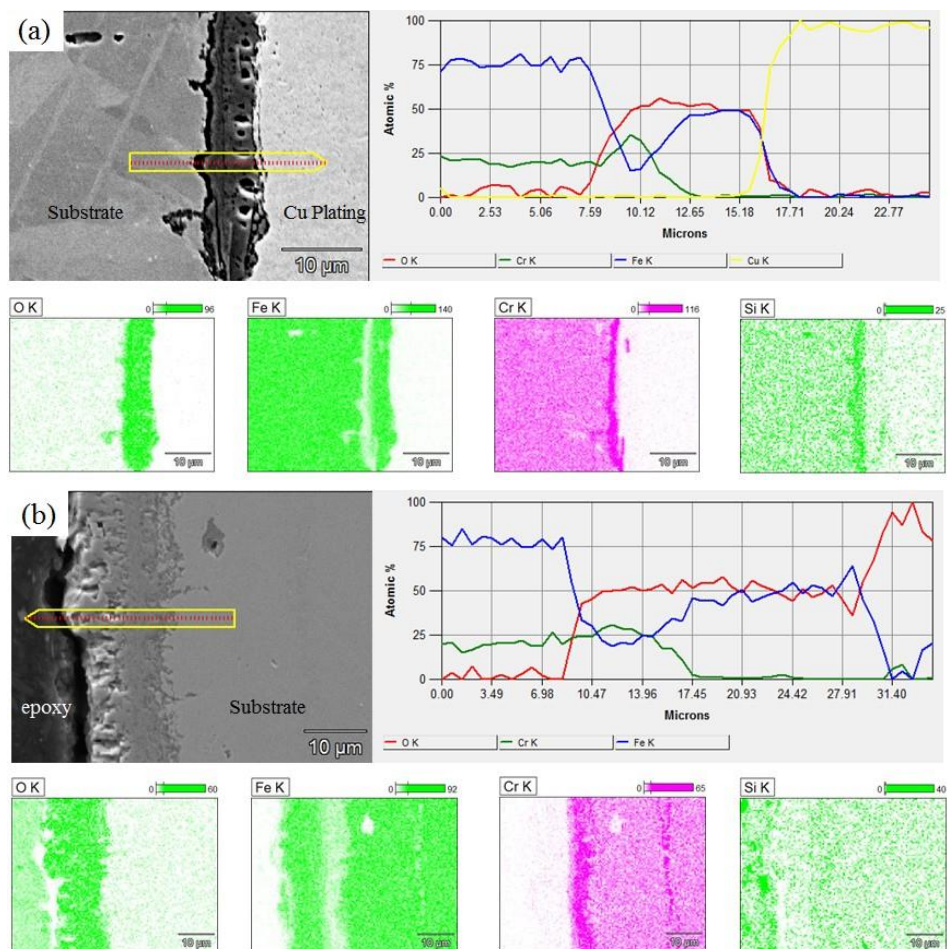


Figure 2.9: Cross Sectional SEM for alloys 347(a) and 316L(b) after 1,000 hours in RG CO₂ at 650°C and 20MPa[47].

2.5 Carburization in s-CO₂ Environments - Background

Some of the most recent work conducted on s-CO₂ corrosion has been focused on ferritic alloy T92 [26]. In this work, the effects of pressure on both oxidation and carburization were studied. This is particularly relevant as it has been highly debated what the exact effects of pressure is on CO₂ corrosion. If pressure does not play a major role on corrosion, it would be unnecessary to conduct testing at pressure, which would result in much easier experimental conditions. SEM cross sections of the oxide layers grown in CO₂ at 550°C at 1 and 250 bar are given in Figure 2.10.

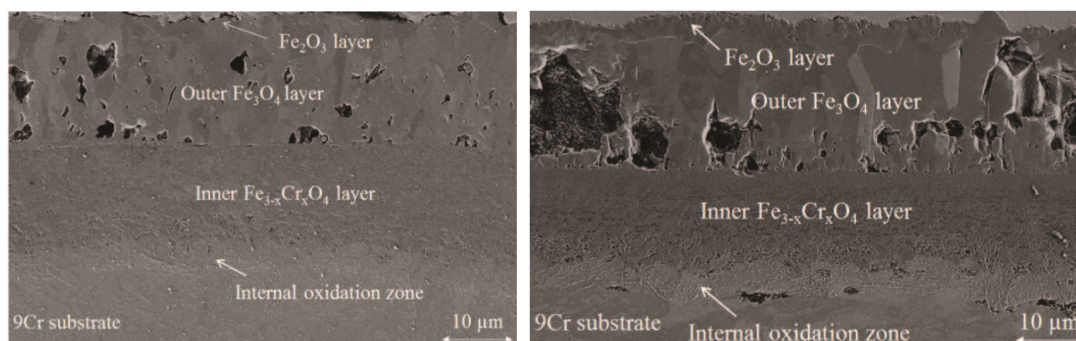


Figure 2.10: Corrosion of alloy T92 at 550°C for 350 hours in 1 bar (left) and 250 bar (right)[26].

A triple oxide layer composed of an outer hematite, magnetite, and inner iron-chromium spinel layer was observed. The ratios of these layers were expected to be different due to differences in the partial pressure of oxygen. The hematite thickness was slightly thicker, and the magnetite layer was more porous in the pressurized test conditions. Another purpose of this study was to examine the effects of pressure on the carburization rates. It was theorized that the increased pressure would lead to increased carburization of the base material. Using glow discharge optical emission spectroscopy (GDOES) the carbon concentration through the oxide and base material was measured. The carbon spectrum is given in Figure 2.11.

The GDOES spectrum for T92 shows a large increase in carbon in the base material

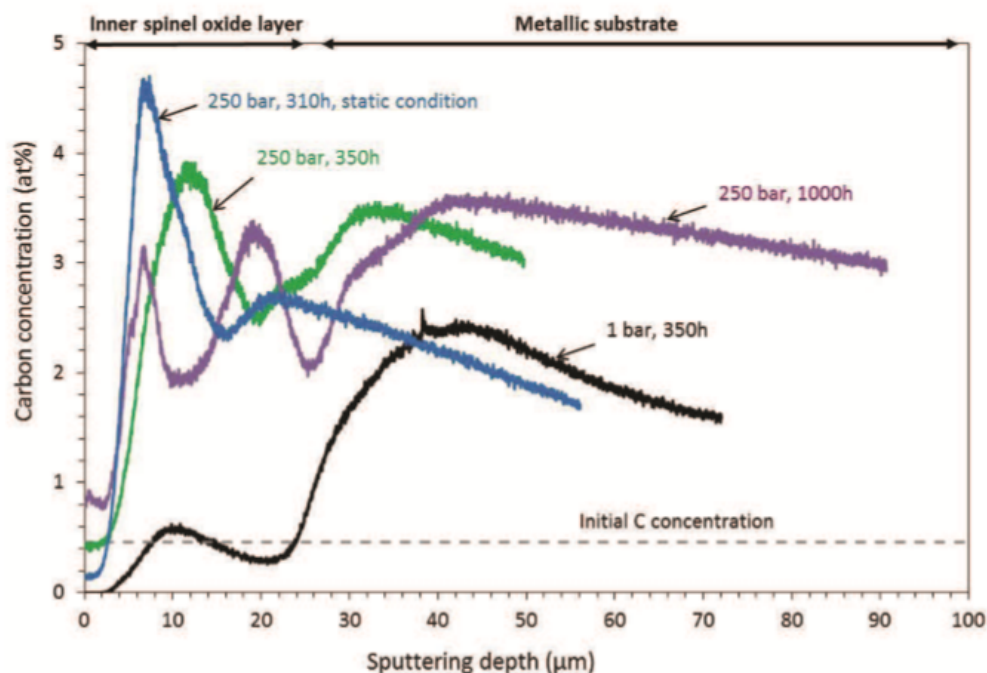


Figure 2.11: GDOES carbon profile for T92 exposed to CO_2 at 550°C in different conditions.[26].

compared to the original amount expected for T92. The increased concentration of carbon proves that carburization occurred due to exposure to CO_2 . The depth and intensity of the carburization was found to be much larger in the high pressure conditions. Using the intensity of the carbon profile, the ratio of carbon to oxygen uptake on the mass gain was plotted as a function of time for each pressure in Figure 2.12.

It was observed that the pressure has little effect on the oxide thickness (Figures 2.10 and 2.12), but had a large effect on the ratio of carbon to oxygen uptake. This result shows that increasing the pressure of environment greatly increases the carbon activity and uptake. Also interesting, is that the ratio of carbon to oxygen uptake was much higher in static conditions. This is most likely due to the build up of carbon monoxide in the static conditions, which increases the environmental carbon activity even higher.

The mechanisms involved in the corrosion of ferritic alloys are very different than those

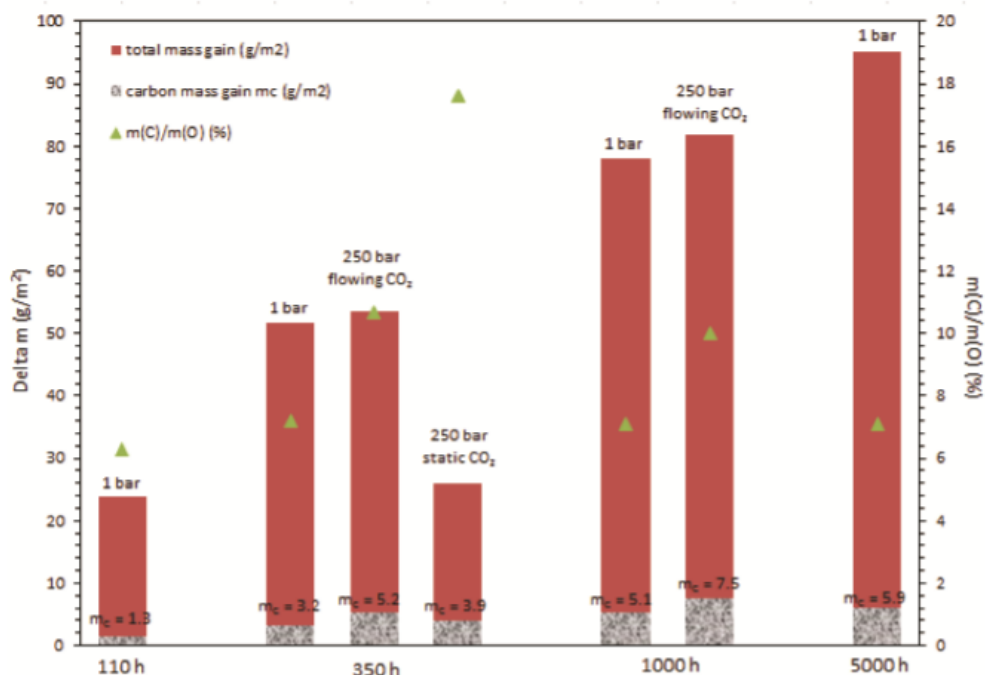


Figure 2.12: Carbon oxygen ratios for T92.[26].

expected for nickel based superalloys. Not only is the reaction rate much lower in nickel chromium alloys, but the matrix material of nickel is much different than the iron matrix in ferritic alloys. Unfortunately not many studies have been produced on carburization in CO₂ on nickel chromium alloys. One study has shown carbon at the metal oxide interface, as well as throughout the oxide. This is given in Figure 2.13.

Figure 2.13 shows carbon primarily at the interface of the oxide base material. The magnitude of this carbon deposition is very low in comparison to the depth and magnitude shown for the T91 samples previously. This is most likely due to the coupling of carburization rates and oxidation rates. A thermodynamic model for the coupling of the two will be presented later in Chapter 4.

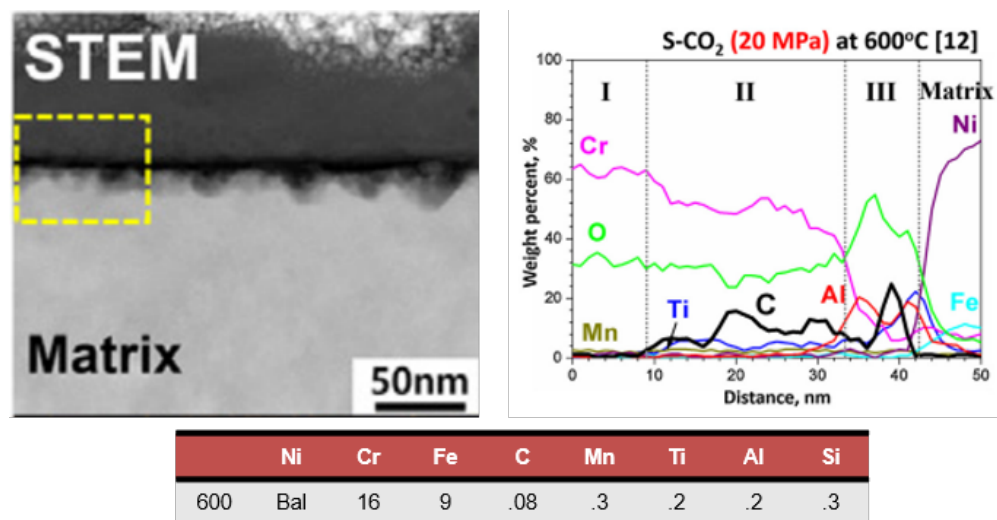


Figure 2.13: STEM and EDS measurements for alloy 600 exposed to s-CO₂ at 600°C, 20MPa, for 1000 hours [48].

2.6 Effect of Impurities in s-CO₂ Environments - Background

As with most other corrosive environments, trace impurities in the CO₂ gas can be expected to effect the corrosion behavior. Most of the aforementioned studies used either research grade (99.999% pure) or industrial grade CO₂ (99.95% pure). The supplier certified value for oxygen concentration was <50ppm in industrial grade CO₂ compared to research grade which is <1 ppm. However, very few studies have systematically examined the effects of trace oxygen and carbon monoxide concentrations on corrosion at relevant temperatures and pressures in s-CO₂ environments.

One study conducted by Pint tested impurities in CO₂ on atmospheric conditions [49]. Sample were exposed to CO₂ at 1 bar was and 700, 750, and 800°C with .15% O₂ and 10% water additions for 500 hours. The weight change summary for each conditions are listed in Figures 2.14-2.16.

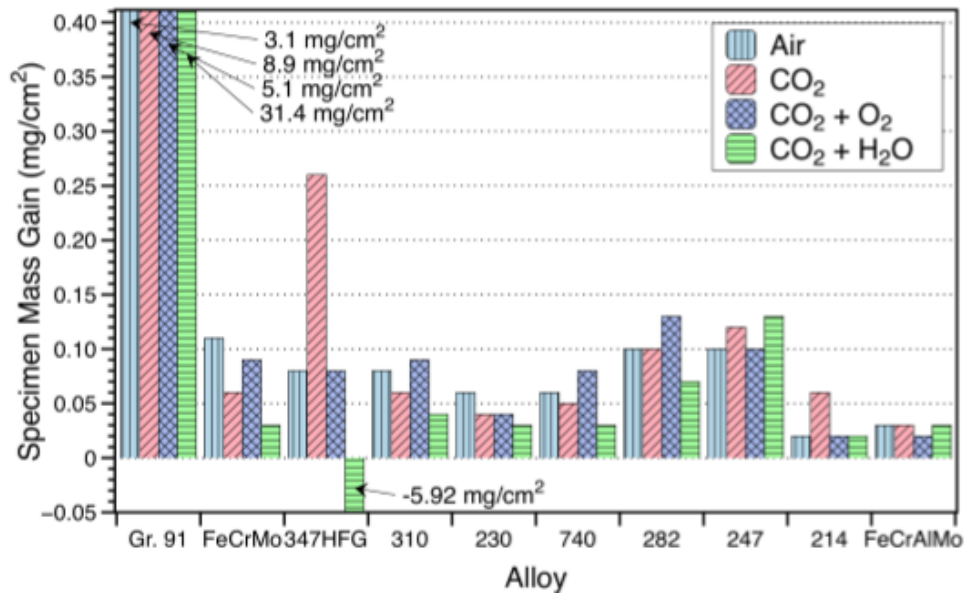


Figure 2.14: Weight change analysis for atmospheric CO₂ impurities testing conducted at 700°C for 500 hours [49].

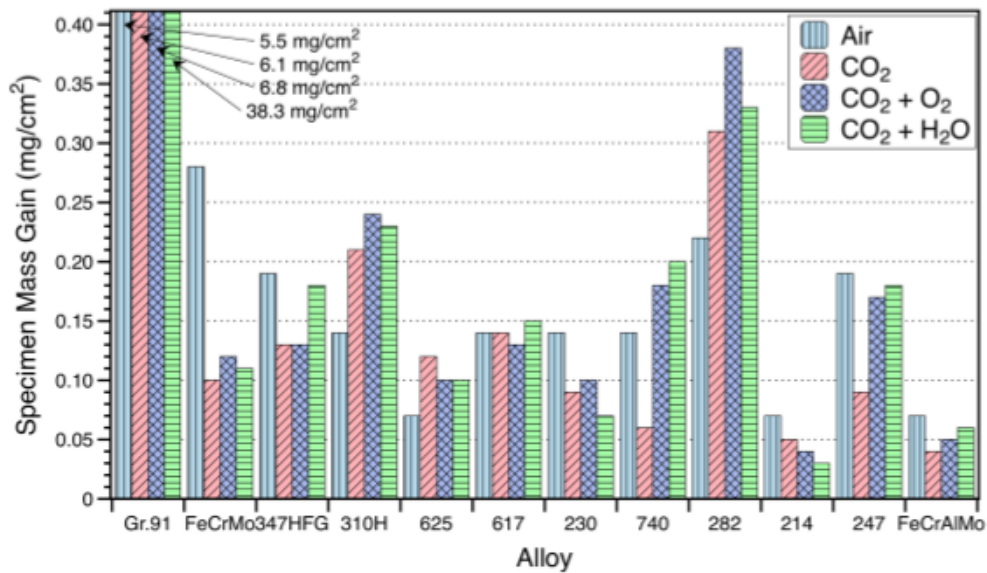


Figure 2.15: Weight change analysis for atmospheric CO₂ impurities testing conducted at 750°C for 500 hours [49].

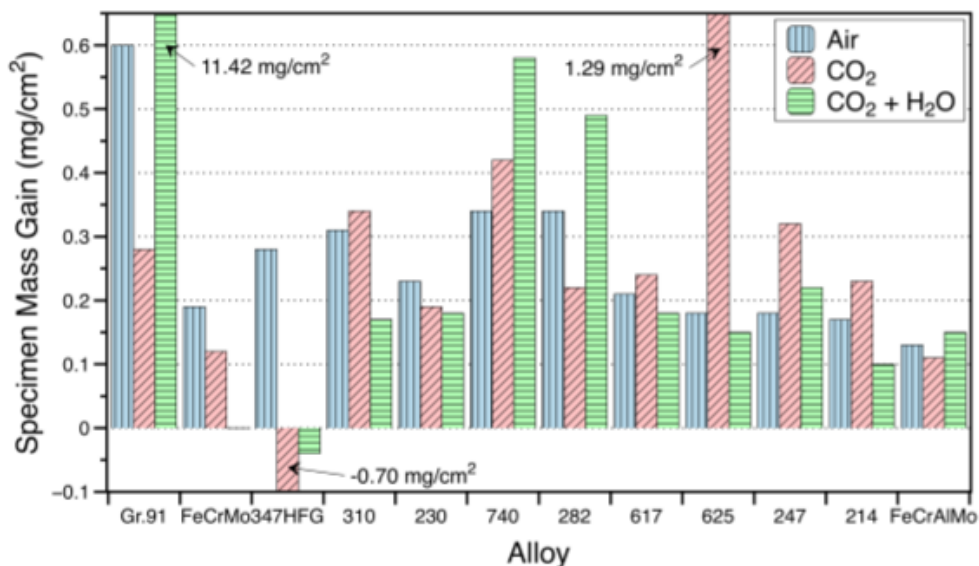


Figure 2.16: Weight change analysis for atmospheric CO₂ impurities testing conducted at 750°C for 500 hours [49].

The testing conducted by Pint gives good insight on the effects of impurities, but was completed at atmospheric pressure. Another area of improvement with this paper was the lack of SEM, EDS, and XRD characterization of the samples. Without compositional and bonding analysis very little information on the exact effects of these impurities can be obtained.

2.6.1 Oxygen Impurities in CO₂- Background

Adding oxygen to CO₂ provides an interesting change in the environmental chemistry, and therefore the corrosion mechanism. Oxygen will be present in CO₂ either through leaks in the system, or from the initial gas concentration received from the supplier (Figure 3.5) If the partial pressure of oxygen is low enough in the pure CO₂ environments, it could be concluded that the rate limiting step is actually the transport of oxygen to the metal. In contrast, saturating the CO₂ with excess oxygen, the system should behave more like dry air

or pure oxygen corrosion where Wagner's Theory holds true. If this is the case, it could be expected that the diffusion of chromium or oxygen through the scale would be rate limiting.

Previous work by Meier [50] has examined the corrosion of Fe-Cr alloys exposed to a 50% CO₂- Ar gas mixed with 1-3% oxygen additions in the temperature range of 550-650°C. It was concluded that addition of oxygen up to 1% had very little effect on the oxidation rate compared to a non-oxygen mixed environment. Once the oxygen concentration was increased to 3%, a reduction in weight change was observed. It was theorized that the increased oxygen potential greatly reduced the carbide formation, and therefore increased chromium diffusion to the surface producing a more protective oxide.

Another more recent study by Bouhieda [51] investigated the effects of added oxygen impurities (1-10ppm) in CO₂ on initial stage oxidation of T92 (Fe-Cr rich) steel at 550°C using oxygen-18 as a tracer element. This study concluded that free oxygen oxidized the metal surface before the CO₂ which provided resistance to further corrosion. This would indicate that oxygen, not CO₂, is the most reactive species. Bouhieda also concluded that low oxygen impurity levels (1ppm) produced a more uniform chromia layer compared to the higher oxygen impurity level (10ppm) environment which produced a higher iron-rich oxide due to kinetically limiting the oxidation process. While these studies have shown the importance of initial stage oxidation and the significant effect of oxygen on corrosion, the mechanisms associated with oxidation of Fe-based alloys is very different from what is observed for nickel-based alloys containing substantial amounts of chromium [49]. It is therefore the goal of this research to better understand the effects that oxygen impurities have in s-CO₂ corrosion.

2.6.2 Carbon Monoxide Impurities in CO₂- Background

The ratio of CO to CO₂ is also very important to the corrosion process. It will be shown in Section 3.5.5 that carbon monoxide is produced as a product of corrosion in pure CO₂. The build up in carbon monoxide greatly effects the thermodynamic equilibrium. As CO increases, the pO₂ decreases rapidly, and is accompanied by an increase in the carbon activity in the system. It has been discussed above that decreasing the partial pressure of oxygen can sometimes have very beneficial effects on the corrosion rate. This could decrease the possibility for Fe or Ni rich oxides to form, and create a more uniform and protective Cr₂O₃ layer.

The addition of CO to the CO₂ stream would also increase the carbon activity, which increases the potential for carburization. While carburization might not be particularly detrimental to the alloy, it has been observed that the carburized zone could effect more material than the oxidation process does (as observed for ferritic alloys). If the carbon activity increases enough, the potential for metal dusting from formation of metastable carbides or graphitization can occur. This has been observed in blast furnaces where the CO concentration is very high, and therefore needs to be studied in detail in CO₂ environments before implementation of these materials. It has been generally accepted that pure CO₂ will oxidize the material surface, and potentially decarburize the sample, whereas CO has been observed to generally carburize the material [13, 28, 52]. Some inconsistencies in this observation have been explained by the formation of subsurface micro-environments that can be filled with a trapped atmosphere which increases the carbon activity significantly [26]. This balance between oxidation, carburization, and decarburization will be explored by the research conducted for this project.

2.7 Modeling Efforts for s-CO₂ Corrosion

2.7.1 Coupling of Oxidizing and Carburizing Environments

A large effort has been completed in order to model CO₂ corrosion, and more generally, environments that cause both oxidation and carburization. Initially, it is very surprising to observe carburization in an environment that is considered readily oxidizing such as CO₂, but by making assumptions about the oxide interactions with the environment, carbon deposition becomes reasonable. The most prevalent studies in CO₂ corrosion currently support the Available Space Model, which was proposed back during studies on the MAGNOX reactors [27], and more recently extended by Rouillard and Young [26, 53]. This model was proposed for iron-chromium alloys which produce a duplex oxide, and while the nickel-chromium alloys behave different, many similarities arise between the two. One important distinction is that the corrosion rate for nickel chromium alloys is significantly lower, and therefore, the boundary conditions in this study will be solved based on thermodynamics, and not kinetic data (as done for the available space model).

The approach being used incorporates the model proposed for the VHTR He corrosion mechanisms set forth by Quadackers [30, 54]. In this model, the partial pressure of oxygen is related to the activity of carbon by thermodynamic equilibrium equations. Then phase boundaries are divided up in the stability diagram, which can be observed in Figure 2.17, into multiple regions (counterclockwise from bottom left: inert, oxidizing, oxidizing and carburizing, carburizing and oxidizing, and carburizing).

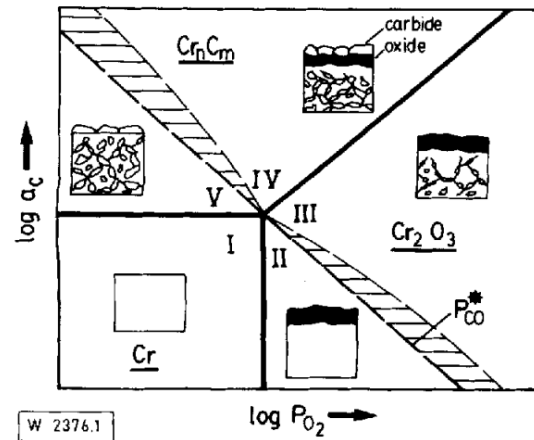


Figure 2.17: Volatility diagram proposed for the VHTR He with carbon impurities [30].

In order to correlate this model to the CO₂ environment, a few assumptions must be made during subsequent calculations:

- Activity coefficients of all species are all equal to 1
- Chromium depletion is neglected (concentration equal to 1)
- Chromium is the only reactive species with oxygen and carbon
- pO_2 at oxide-environment interface is fixed using the environmental testing conditions
- pO_2 at metal-oxide interface is constant, and based on phase equilibrium of Cr and Cr_2O_3

The final model for CO₂ environments will be presented with supporting data in Chapter 4.

2.7.2 Chromia Growth and Defect Structure

In order to understand the growth mechanisms of chromia, or for that matter any ceramic, it is usually a good idea to consider the primary point defect. Point defects control many of the processes associated with ceramics such as diffusion, oxidation, reduction, electrical conductivity, and others [55]. Chromia forms as the corundum structure which is a hexagonal close packed lattice of oxygen atoms with two thirds of the octahedral sites being occupied by chromium. This can be observed for the side view of the unit crystal in Figure 2.18 below. It is important to mention that Al should be switched with Cr (both produce corundum lattice).

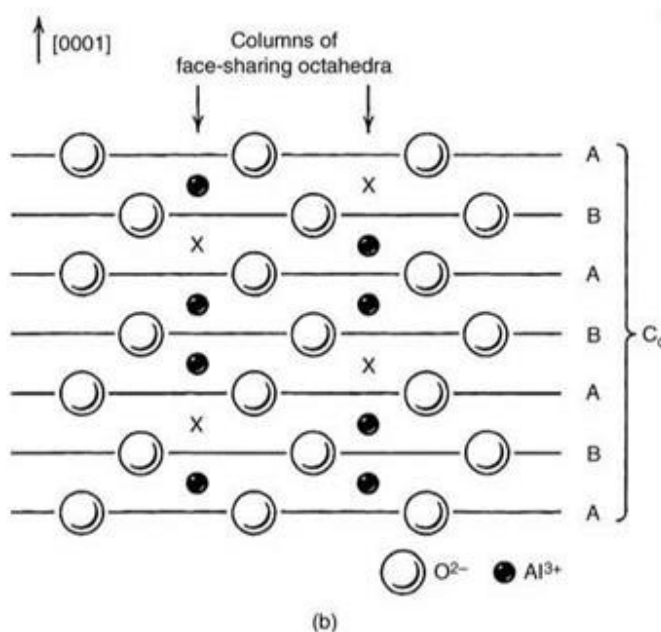


Figure 2.18: Corundum unit cell of stoichiometric chromia [55].

This structure is highly stable with the cations spaced furthest from each other. The structure is important as it can give insight into which point defects have the lowest energy of formation. The point defects are heavily dependent on temperature and partial pressure of oxygen (pO_2). The dependency on pO_2 is one of the main focuses of this research, and

therefore the impact on the defect structure of chromia formation will be relevant.

Before studying chromia growth on commercial alloys which contain many elements, first the theoretical explanation for pure chromium in varying oxygen environments will be presented. This model is based on solid state diffusion of chromium and oxygen through the chromia lattice which is very different than gaseous diffusion model discussed in the previous section, and therefore it will be important to distinguish the two. Fortunately, many studies have been completed on the topic of chromia growth in pure oxygen environments. One of the most extensive and complete theories has been completed by Lutu [56]. In this, the defect structure of chromia was altered by varying the environmental pO_2 by use of the Rhines pack method [57]. The Rhines pack method uses a buffer mixture of oxidized and non-oxidized material in a vacuum furnace to precisely control the pO_2 using the chemical equilibrium condition of the metal and oxide. In this particular study, Ni/NiO mixture was used to obtain pO_2 values of 10^{-12} , 10^{-13} , 10^{-14} at temperatures of 800, 850, and 900°C respectively.

Oxides grown on pure Cr were analyzed using photoelectrochemical measurements as well as TEM-ASTAR (for grain orientation) to determine the primary defect and morphology of the oxide respectively. It was shown that chromium always produced a duplex oxide consisting of an inner n-type equiaxed oxide with outer columnar growth consisting of: n-type semi-conduction (anionic) at low pO_2 , insulating at middle pO_2 , and p-type (cationic) at high pO_2 . The semi-conduction of the external scale was dependent on the pO_2 with the internal scale the same for all conditions (anionic). This indicates that the internal growth of chromia should be controlled by the oxygen vacancy point defect. The external scales would then be controlled by different point defects. For example the external n-type chromia growth would have chromium interstitials as the major point defect (the orientation of the external scale dictates outward growth, and the n-type semi-conduction from PEC measurements could only be produced by chromium interstitials). The major point defect in the external p-type growth (in high pO_2) would correspond to chromium vacancies. Finally,

the insulating oxide (medium pO_2) would consist of either oxygen and chromium vacancies, or chromium vacancies and interstitials (two defects are listed as it is assumed they are in equilibrium). The later of the defect structures for the insulating oxide has been refuted as the existence of by chromium interstitials and vacancies in the same lattice would intuitively seem impossible. In other words, the main defect in the external scale was either determined by the Cation-Frankel (n-type) or Schottky (p-type) defect structure.

In order to model these results, the construction of the Brouwer Diagram for chromia was calculated. As discussed above, the major point defect at the M-O interface would consist primarily of oxygen vacancies due to the low pO_2 associated with the phase equilibrium between chromium and chromia. The external scales were found to have different semi-conduction types, and therefore, the major point defect is expected to change. A complete list of equations and calculations can be found in Latu's study [58]. In order to condense this, the electro-neutrality equations for n-chromia is given in Equation 2.8 and p-type given in 2.9.

$$3[Cr_i^{\bullet\bullet}] + 2[V_O^{\bullet\bullet}] + [h\cdot] = [e'] \quad (2.8)$$

$$3[V_{Cr}^{\prime\prime}] + [e'] = 2[V_O^{\bullet\bullet}] + [h\cdot] \quad (2.9)$$

Equilibrium constants for defect formation were calculated using Factsage 7.0 and used to plot the Brouwer Diagram for all three pO_2 conditions in Figure 2.19. The ultimate goal of this study was to try to minimize the total defect concentration found in the oxide. This can theoretically be accomplished by producing chromia at a pO_2 that would produce equal amounts of chromium and oxygen vacancies (the primary defects in high temperature corrosion). If the two defect concentrations are equal, a stoichiometric oxide should be produced, meaning the exact chemistry of chromia would be Cr_2O_3 . Minimization of the

total defect concentration should result in a reduction in the corrosion rate as the defect concentration controls diffusion through the oxide.

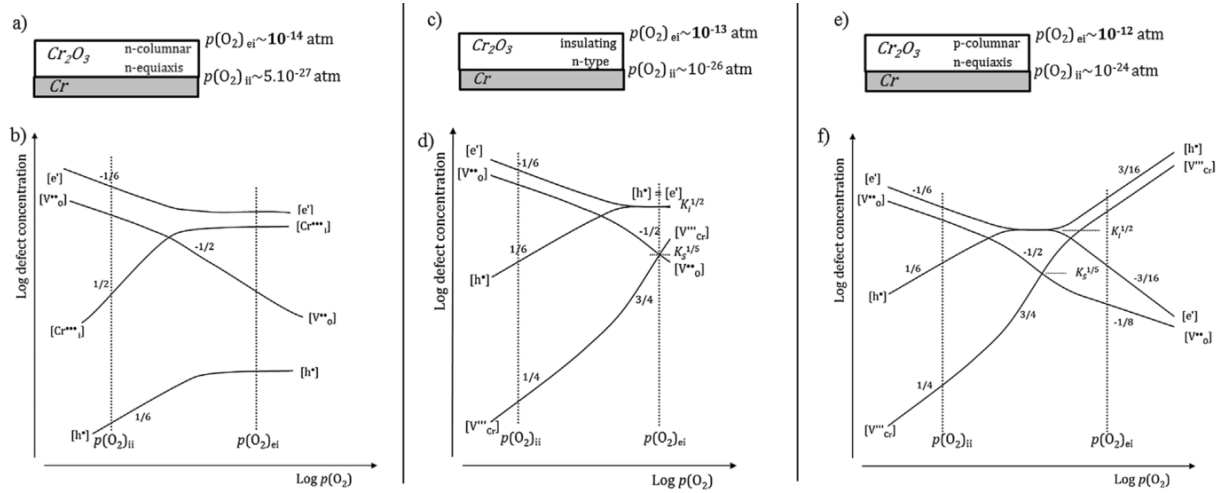


Figure 2.19: Brouwer diagram for chromia formation for low atmospheric $p\text{O}_2$ (Left) Medium $p\text{O}_2$ (Middle), and high $p\text{O}_2$ (Right) [56].

This model explains the growth of pure chromium in the presence of highly controlled buffered oxygen systems. The varying CO_2 environments in the research in this document are held at semi-steady state by saturating the environment with either O_2 or CO and continuously refreshing the system. This means that the $p\text{O}_2$ in the oxygen doped case is very high ($p\text{O}_2 \sim 10^{-4}$) and the $p\text{O}_2$ in the CO environment is very low ($p\text{O}_2 \sim 10^{-16}$) indicating that the chromia growth in the high $p\text{O}_2$ and low $p\text{O}_2$ cases in the CO_2 study should behave similar to the Latu study. The system becomes infinitely more complex when commercial alloys, which contain multiple elements, are used since the addition of intrinsic and extrinsic point defect for each species must be considered.

An example of deviation from the above model due to commercial alloy composition can be observed in the study presented by Ledoux in which n-type chromia growth was grown on the surface of alloy HR120 despite being exposed to relatively high $p\text{O}_2$ [59]. In this paper, it was concluded that the root cause was the formation of a thin Cr-Mn spinel layer on the

surface of the oxide. This oxide then acted as a diffusion barrier for oxygen and therefore strongly reduced the pO_2 to levels that produce n-type semi-conduction.

In CO_2 environments, it would be expected that both the formation of other oxides as well as carbon deposition would greatly effect the semi-conduction type that is expected from the model presented above. In fact, the pO_2 in the oxygen rich CO_2 environments contains a much higher pO_2 than the paper discussing HR120. This is contrasted by the CO rich CO_2 environment in which Cr/Al are the only oxides expected to form. In this case, external chromia growth would be expected to grow as the n-type semi-conduction for all alloys as the oxidation kinetics for non-chromium elements (Al for example) are much lower than chromium and not expected to form on the surface. In CO rich conditions, it is expected that carbon will be deposited as well, which would also effect the growth mechanisms.

In reality, the stoichiometric growth of an oxide is not only based on the pO_2 , but also the chromium concentration. In the study listed previously, the stoichiometric oxide was grown on pure chromium. This is quite different from what is expected during the oxidation of commercial alloys. In both cases, Cr is expected to be limited to the surface by diffusion, a process that cannot be observed in pure Cr. The depletion of Cr in commercial alloys has been studied extensively, and is expected to occur in testing done in this work. Therefore, it will be important to observe if the depletion of Cr at the M-O interface has a strong effect on the growth of a stoichiometric oxide.

2.8 High Temperature Steam and Supercritical Water Corrosion

One important comparison will be between s- CO_2 corrosion with high temperature steam and supercritical water (SCW). Since the Brayton Cycle could potentially replace the Rankine Cycle, it is important to be able to understand the differences in the mechanisms and rates of corrosion and the materials demands that will occur if s- CO_2 is used. Several studies

have been completed on SCW and high temperature steam and have been summarized in [60, 61]. One major difference is that the pH of supercritical water is much different than s-CO₂ at elevated temperature due to the presence of charge carrying species. This can lead to dissolution of reaction products in to the fluid. Another difference is the formation of volatile chromium hydroxides that are unable to form in s-CO₂ due to the lack of hydrogen. This is one major benefit of s-CO₂ corrosion. The partial pressure of oxygen has also been calculated to be higher in SCW and steam conditions compared to CO₂. This could lead to the favorability of several oxides that cannot be produced in CO₂. A summary of results in the two environments is given in Section 6.3.

Chapter 3

Experimental Facility

3.1 Testing Procedure

Stock material of each alloy were received from various vendors. The composition of each alloy is listed in Appendix A. Samples were laser cut or electrical discharge machined (EDM) to dimensions of 0.5 x 0.5 x 0.062 inches and a 1/8 inch diameter hole was drilled in the corner to suspend the samples from a supporting alumina rod in the autoclave. Each sample was polished to 800 grit using silicon carbide polishing paper. A final cleaning of ethanol and deionized water was conducted. Typically, six samples were used at the start for each testing condition with one sample being permanently removed from the set for additional analysis at each 200 hour interval. This procedure leaves at least two samples that are exposed to the full 1000 hours at the end of testing for each environment. Testing environments and temperatures can be found in Table 3.1. A summary of the materials tested in each of these conditions is given in Table 3.2.

Table 3.1: Testing environments and temperatures for experiments conducted at UW-Madison.

		Gas Purity			
Temperature		IG	RG	RG + 100ppm O ₂	RG + 1%CO
	450°C	x	x		
	550°C	x	x		
	650°C	x	x	x	
	700°C		x		
	750°C	x	x	x	x

Table 3.2: Complete list of materials exposed during sCO₂ testing conducted at UW-Madison.

		450C		550C		650C				700C	750C				
		IG	RG	IG	RG	IG	RG	10ppm O ₂	100ppm O ₂	RG	IG	RG	10ppm O ₂	100ppm O ₂	1%CO
Ferritic	T92	x	x		x*		x**								
	T122	x	x				x**								
Austenitic	347	x	x	x	x	x	x	x	x		x	x	x	x	
	316L	x		x	x*		x**			x*					x
	310S		x	x	x	x	x**	x	x		x	x	x	x	
	709						x					x			
	800H	x				x	x**	x	x						
High Temp Superalloys	718		x	x	x	x	x	x	x		x	x	x	x	
	H625		x	x	x*	x	x**	x	x	x*	x	x	x	x	x
	H230		x	x	x	x	x**	x	x		x	x	x	x	x
	617		x	x	x	x	x	x	x		x	x	x	x	
	740H					x	x	x	x	x*	x	x	x	x	
	H282					x	x	x	x		x	x	x	x	x
	HR120				x*					x*					
	Pure Fe		x												
Model Alloys	Fe12Cr		x												
	Pure Ni														x
	Pure Cr														x
	Ni20Cr							x	x		x	x	x	x	
	SiC					x		x	x		x	x	x	x	
	AFA OC6,7,10	x	x												
Other Materials	PM2000						x**								
	PE16						x**								
	Al-6XN						x**								

RG: 99.999%, IG: 99.5%, Impurities: RG + Quantity Listed

*Exposed out to 1500 hours **Exposed out to 3000 hours

3.2 Materials Characterization/Analysis

Tests were performed for a total of 1000 hours with samples being removed from the autoclave every 200 hours to obtain time dependent trends. Mass change (per unit area) due to corrosion was determined by making mass measurements before and after exposure to each CO₂ environment at each time interval using a high precision Sartorius scale with an accuracy of $\pm 2\mu g$. Surface area calculations are completed by using a micrometer that is accurate to .002mm. Three length and width measurements are taken along the edges, and five thickness measurements across different locations on the surface are used to calculate the entire surface area of the sample. Samples were examined using scanning electron microscopy (SEM) in conjunction with energy dispersive spectroscopy (EDS) for both surface and cross-sectional

oxide imaging. Raman spectroscopy and X-ray diffraction (XRD) were used for analyzing oxide stoichiometry and phase identification. Additional sample specific analysis will be discussed in the sections in which they are presented.

3.3 Facility Overview

A high temperature, high pressure autoclave was constructed for exposing the samples to $s\text{-CO}_2$. The system is a modified version of the testing facility described in more detail in previous papers [36, 40]. Certificates for many of the devices used in this facility are given in Appendix L. The new facility consists of two autoclaves capable of simultaneous operation at independent temperatures, and is depicted in Figure 3.1. The autoclaves are designed to handle temperatures up to 750°C at 20MPa. The temperature can be regulated within $\pm 1^\circ\text{C}$ and the pressure within $\pm 0.017\text{MPa}$. A graph of the temperature and pressure profile at testing conditions is plotted in Figure 3.2.

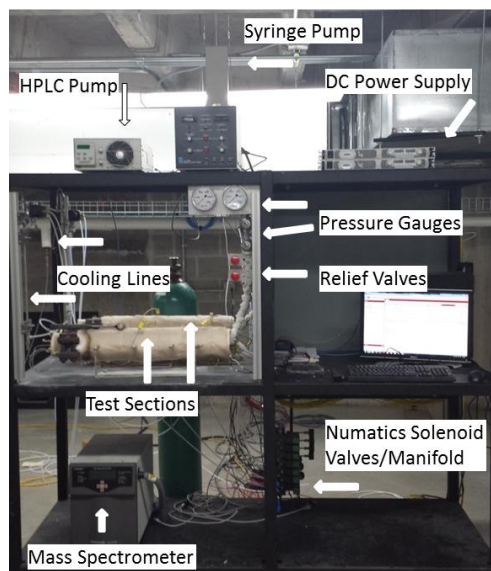


Figure 3.1: Overview picture of one of the testing facilities at UW-Madison used for $s\text{-CO}_2$ corrosion experiments.

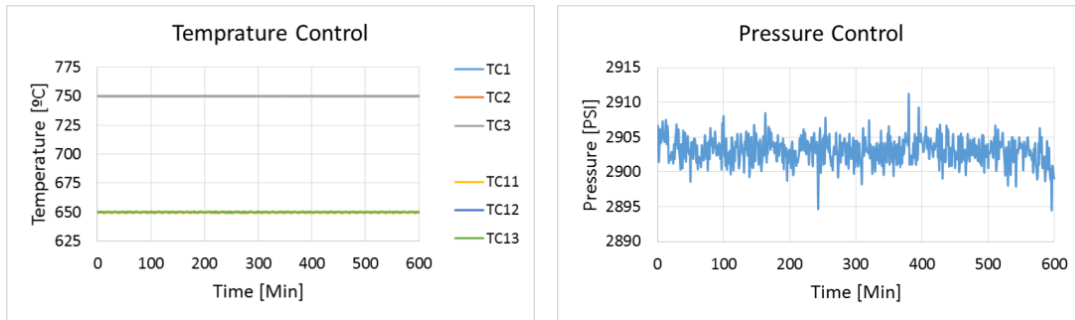


Figure 3.2: Temperature and pressure profile for dual autoclave system operating at 650 and 750°C and 20MPa (2900psi).

Each autoclave was designed to work independent of the other through a valve system that isolates the inlet lines of the autoclaves. Three thermocouples (calibrated using a certified platinum resistance temperature detector) located internally in both autoclaves along with three separate custom tape heaters are used to regulate the temperature. This is done using PID controls in Labview, and is able to produce a temperature profile with a variance of less than 2°C. Each autoclave also has an Omega pressure transducer to monitor the pressure for the duration of the testing. The AutoCAD drawing depicting pressure transducers, thermocouples, and valve locations is shown in Figure 3.3.

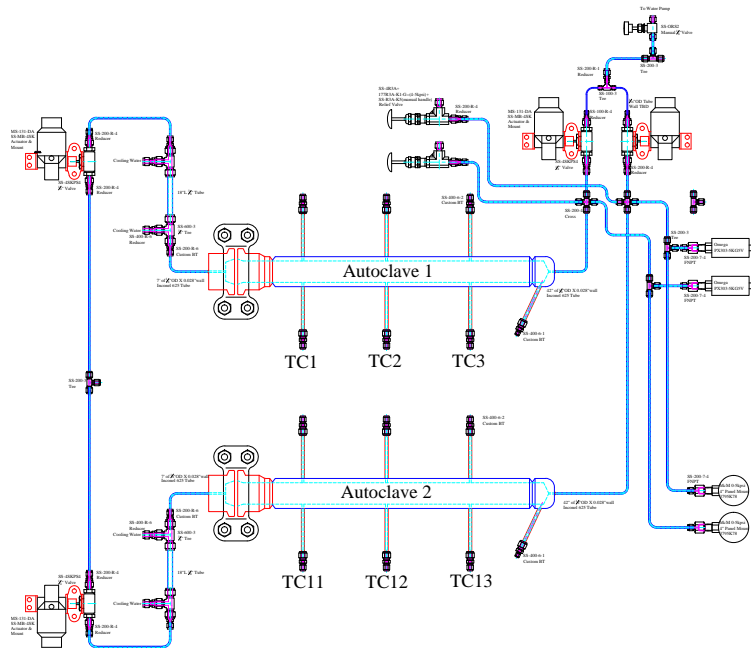


Figure 3.3: AutoCAD schematic of testing facility with locations of internal thermocouples (TCX).

One important consideration in corrosion testing is the stress that is experienced during heating and cooling. These stresses occur due to a mismatch in thermal expansion coefficients of the oxide and the base alloy, and can be very important due to the cyclic nature of this testing. While a slow heating and cooling rate would reduce the possibility of cracking from stress, additional oxidation would occur during this time. In order to reduce both effects, a heating and cooling rate of less than 5% of the total testing time and slower than $5^{\circ}\text{C}/\text{min}$ was set. Typical heating and cooling rates of the autoclaves have been plotted in Figure 3.4.

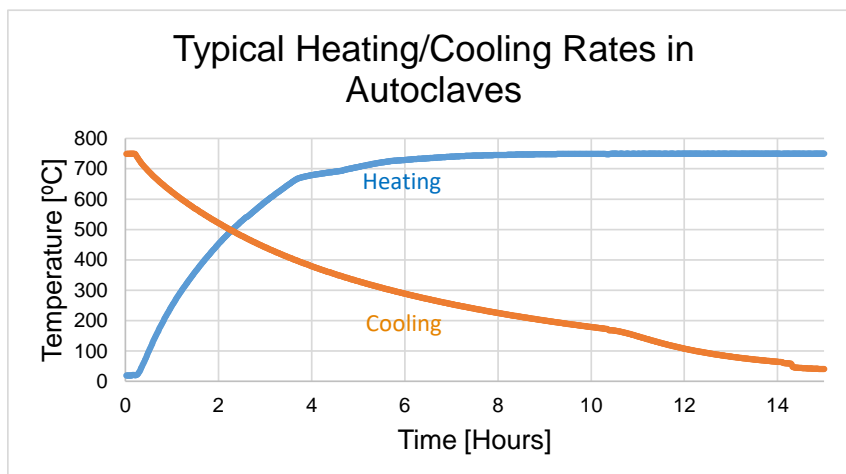


Figure 3.4: Typical heating and cooling rates for one autoclave initially at 750°C.

3.4 Flow Rate Modifications

One major flaw of the system described previously[36] was the lack of control on the flow rate of CO₂. The previous design used a high pressure regulator and a metering valve to regulate the flow of CO₂ through the autoclave. While this design allowed for slow enough flow through the system for operation, the flow rate and pressure drop across the regulator caused freezing of the CO₂ which led to irregular flow rates. In order to get better results, a constant flow is desired in order to refresh the system with a continuous supply of CO₂. A uniform flow rate is also very important when exposing samples to impurities, as the reaction rate with the samples should not be rate limited by the flow of CO₂. In order to create a constant flow rate, CO₂ freezing must not occur. This concern was addressed by increasing the length in which the pressure drop occurs in the system by using 6 feet of capillary tubing (25 μ m ID) to create the frictional force required to pressurize the system to 20MPa. The capillary line is also heated using NiCr wire to maintain a temperature around 70°C. The length of capillary was calculated and tested to produce a flow rate of around .06kg/hr of CO₂ per autoclave. This flow rate was chosen to produce a residence time of CO₂ in the

autoclaves of roughly two hours. The residence time was determined as an optimal balance between pumping capability, reducing flow effects on corrosion, and keeping the CO₂ in the autoclaves as fresh as possible.

3.5 Gas Analysis and Purity of CO₂ from Vendor (Airgas)

Impurities mixed testing was compared to research grade (RG) and industrial grade (IG) corrosion tests. The impurity concentration limits of RG CO₂ are much lower than IG CO₂, but the cost is about 20 times higher which is probably not feasible for industrial application. The purity limits of RG and IG CO₂ are listed in Figure 3.5.

CERTIFICATE OF ANALYSIS		CERTIFICATE OF CONFORMANCE	
CARBON DIOXIDE - RESEARCH		Carbon Dioxide, Industrial Grade	
Part Number:	CD R200	Reference Number:	
Cylinder Analyzed:	117987	Cylinder Volume:	
Laboratory:	ASG - Riverton - NJ	Cylinder Pressure:	
Analysis Date:	Feb 27, 2012	Valve Outlet:	
Lot #:	82-124305199-1		
ANALYTICAL RESULTS		<u>Customer:</u>	
Component	Requested Purity	Bostik Inc.	
CO2Research	99.999%	Milwaukee, WI.	
AR + O2 + CO	<1 PPM	For reference Only - "Signature ON FILE"	
TOTAL HYDROCARBONS	<1 PPM	Test	Purity Limits
Moisture	<3 PPM	Moisture	32 ppm
Nitrogen	<5 PPM	Total Hydrocarbons	50 ppm
		Oxygen	50 ppm
		Non-Volatile Residue ppm (Wt/Wt)	10 ppm
		Assay	99.5%

Figure 3.5: Certificates and purity limits for research(left) and industrial grade(right) CO₂ from Airgas.

In order to study and understand the effects that impurities such as oxygen and carbon monoxide have on corrosion in s-CO₂, it was important to obtain accurate measurements of each constituent as a function of time. The composition of the gas was measured for the duration of testing at both the inlet and exit using an Alpha Omega 3000 series trace oxygen analyzer (± 1 ppm O₂), a ThermoStar Pfeiffer mass spectrometer (Hydrocarbons/others: >50ppm), and a Varian 450 gas chromatograph (CO/CH₄: >50ppb). These instruments

are shown in Figure 3.6. Both RG and IG carbon dioxide bottles were tested using all three analysis techniques to characterize oxygen, carbon monoxide, water vapor, and hydrocarbon concentrations. The results of this initial testing are given in following sections.

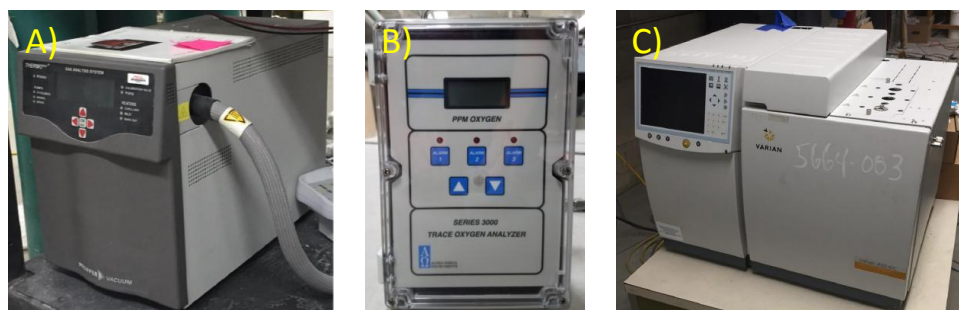


Figure 3.6: Instrumentation used to measure the chemical composition of CO_2 .
A: Thermostar Mass Spectrometer for hydrocarbons ($>\text{C}1$) and water concentration,
B: Alpha Omega 3000 Series Trace O_2 analyzer for oxygen content, C: Varian 450 Gas Chromatography used to measure CO .

3.5.1 Mass Spectrometry

Mass spectrometry was used to primarily determine the concentration of water vapor as well as hydrocarbons ($>\text{C}1$). This technique is limited by the ability to analyze molecules that have similar mass to charge ratios. More specifically determining oxygen and carbon monoxide concentrations in CO_2 . The mass spectrometer breaks apart and ionizes the molecules into all of the possible constituents. For example, a sample of carbon dioxide will end up with mass/charge peaks for carbon dioxide, carbon monoxide, diatomic oxygen, monatomic oxygen, as well as carbon. The resulting elements and molecules become ionized (single or double), which results in more peaks for CO_2 . Since carbon monoxide and diatomic oxygen are identified by the mass spectrometer from the bulk gas, determining these concentrations with accuracy better than roughly 100ppm is nearly impossible. A summary of peak locations for species of interest are summarized in Table 3.3.

Table 3.3: Mass spectrometer peak locations for molecules of interest.

	CO₂	CO	O₂	H₂O
Mass Number	44,28,16,12,45, 22,46,13,29	28,12,29,16, 14,30	32,16,34,33	18,17,16,20, 19

Relative intensity of the mass/charge peaks gives information on the concentration of each component. Intensity vs the mass charge ratio for RG, IG, and 100ppm oxygen doped CO₂ (measured originally through other means) is plotted in Figure 3.7.

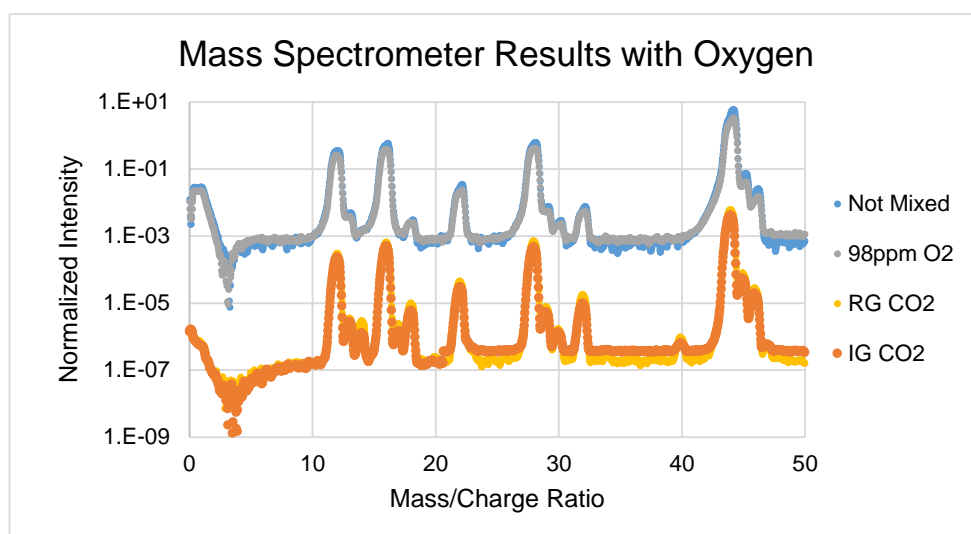
**Figure 3.7:** Mass Spectra comparing research and industrial grade CO₂ with oxygen doped CO₂.

Figure 3.7 shows no discernible difference between RG, IG, or oxygen enriched CO₂. This result was not surprising due to the previous discussion. The main purpose of using mass spectroscopy was to determine water and large hydrocarbon concentrations. In order to calibrate the system, a stainless steel line was heated as water was slowly injected at a known rate to flowing CO₂. The result of this water testing is graphed as function of time in Figure 3.8.

The water concentration is directly related to the intensity of mass number 18 (plotted in red). Injection of water began at around 200 minutes after the system was completely

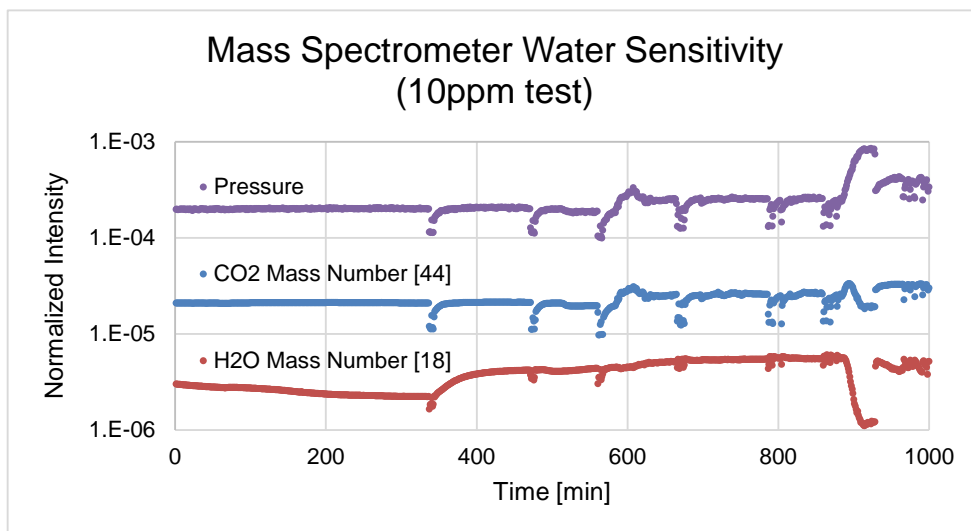


Figure 3.8: Mass/Charge Spectrum showing increased water concentration at 350 min after injection into CO₂ stream.

flushed with CO₂. It can be observed that the water concentration started increasing after 350 minutes (very close to the two hour residence time of the system). Using the increase from the base line, the mass spectrometer was calibrated for water concentration. Since the sampling line contains flowing CO₂, pressure deviations were expected. Pressure differences change peak intensities, and therefore the pressure measurements were plotted in Figure 3.8 as well. The deviations in the ratios for CO₂ to water closely match the spikes in pressure.

3.5.2 Impurities Modifications

In order to conduct impurities tests, a procedure for mixing oxygen and carbon monoxide impurities at low concentrations in CO₂ was constructed. Each CO₂ bottle was connected to the desired impurity bottle, a separate sealable volume (minicyl), and a vacuum pump. The goal was to completely evacuate the atmosphere in the lines, then inject the CO₂ bottles with the desired impurity based on molar concentrations by measuring the pressure drop from a known volume (minicyl) of impurity. Measurements of oxygen and carbon monoxide

concentrations were taken for each bottle before testing using techniques described in the following section. A graphical representation of the mixing setup is shown in Figure 3.9.

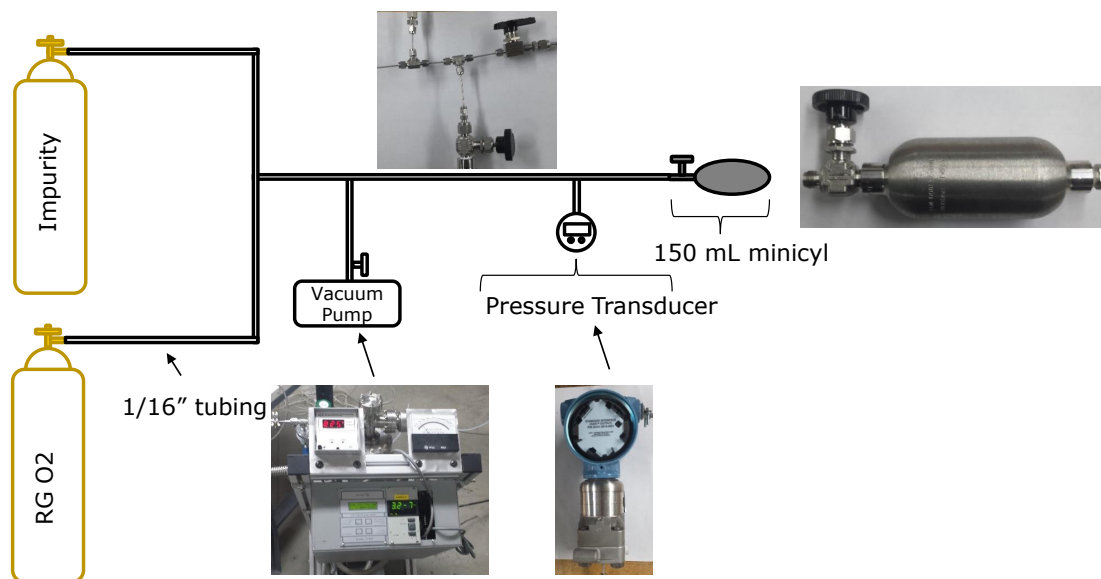


Figure 3.9: Schematic of procedure used to mix gaseous oxygen and carbon monoxide in to liquid CO₂.

3.5.3 Oxygen Determination

Oxygen concentration was measured continuously using an Alpha Omega 3000 series Trace Oxygen Analyzer. This instrument uses an electrochemical cell that has been designed to withstand CO₂ environments by utilizing a proprietary electrolyte instead of the standard potassium hydroxide cell. The instrument has an accuracy of ± 1 ppm. While it was theorized that no oxygen would be detected after exposure (from RG CO₂) to the samples due to reaction with the metal, initial oxygen concentration could be very important. The amount of oxygen present in the system should control reaction rates, and maybe thermodynamic capability to react with some elements. This was discussed in more detail previously in Section 2. The oxygen sensor is also very important in impurities testing where the initial

and final concentrations can be measured, which shows total reaction rate of the system.

Preliminary measurements of the oxygen concentration were completed to compare RG and IG CO₂ from the supplier. This measurement was conducted in order to test the purity limits set by the supplier. RG CO₂ showed no measurable amount of oxygen in 10 different bottles, which matched the certification. IG CO₂ showed a very wide range of measured oxygen concentration from no measurable amount up to 80ppm (well above the certified value). It was informed by the supplier that the limits are nearly arbitrary for the IG CO₂. While many of the IG bottles did not contain a measurable amount of oxygen, some seem to be spiked very high, which could be a concern for testing and implementation in industrial applications.

3.5.4 Oxygen Impurities Mixing

Ensuring precise and accurate concentration of impurities is necessary to study the effects on corrosion. The system described in Figure 3.1 was used to mix RG CO₂ with oxygen. A total of 10 bottles were doped with 100 ppm oxygen to prove this method, and measurements showed an average concentration of 114 ± 9 ppm. A summary of the bottle concentrations is listed in Table 3.4. It was found that the solubility of oxygen in liquid CO₂ was less than the solubility in the vapor phase, therefore, as the pressure in the feed bottles dropped (due to use of CO₂ during testing), so did the concentration of O₂ in inlet line of the autoclaves. For this reason, bottles were replaced when the oxygen concentration reached about 85ppm and thus the exposure of the samples averaged close to 100ppm of O₂.

In order to obtain oxygen concentrations down to 10 ppm, a separate testing facility was used to inject a small volume of high oxygen concentration (~ 400 ppm oxygen) CO₂ with a bulk stream of RG CO₂. This was accomplished by using a Siemens Coriolis mass flow meter to measure the mass flow rate of the bulk RG stream, and injecting small quantities of

Table 3.4: Bottle mixing information and oxygen concentration for bottles used in 100ppm oxygen doped testing.

Bottle #	Gas Weight [kg]	Goal Concentration [ppm]	Delta P [psi]	Calculated O ₂ Concentration [ppm]	Measured O ₂ Concentration [ppm]
K32463		120	171	121	106
AGAC91156	27.4	120	167	121	98
A000104	27.2	135	191	138	116
LK414987	27.3	140	194	142	125
TWH560762	28.0	140	212	150	129
dl33610	27.5	130	175	125	107
TW07339645	27.2	135	194	141	121
2154153Y	27.2	135	188	136	117
1749112Y	27.2	135	184	133	114
Average					115
St dev					9

mixed CO₂ using a Bronkhorst mini-coriflow mass flow controller. The oxygen concentration after mixing was measured using the Alpha Omega oxygen sensor at the inlet line, and a feedback system was used to toggle the oxygen levels to within a max range of ± 2 ppm of the set concentration for the duration of the testing. Figure 3.10 shows a 15 hour test that was conducted to prove this method.

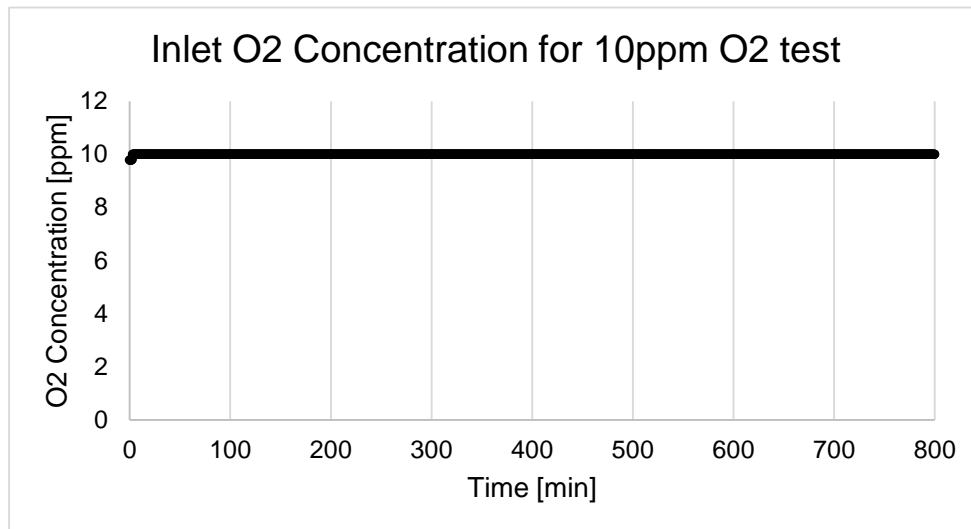


Figure 3.10: Oxygen concentration using feedback mixing system for 10ppm oxygen mixed testing.

3.5.5 Gas Chromatography

Gas chromatography was used to measure carbon monoxide concentrations down to a lower limit of detection of 50ppb. This process works by first using a molecular sieve to remove any molecules larger than carbon monoxide. Then the resulting gas flows through a heated capillary line which separates the molecules by their size. A methanizer is then used to convert carbon monoxide into methane. The effluent then combines with a given flow of feed gas which is burned. The resulting flame temp gives the concentration of carbon monoxide and methane in terms of intensity. The retention time for carbon monoxide in this specific piece of equipment is around 5.2 min, and methane is around 4.5 min. The company certified test result is given in Figure 3.11.

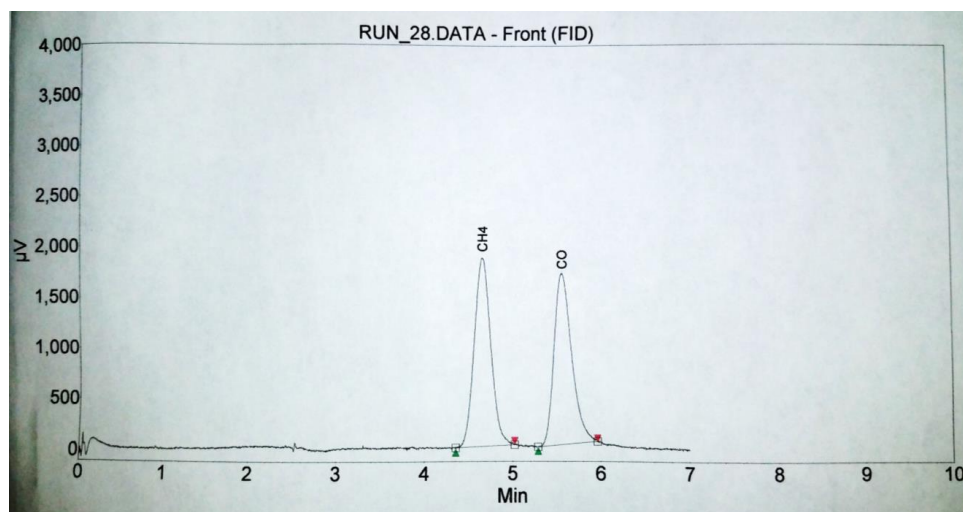


Figure 3.11: Certification result for GC used in s-CO₂ corrosion testing.

Carbon monoxide is an interesting impurity to track since it is one possible product of corrosion. If oxygen is consumed, it is expected that a build up of carbon monoxide will form. The carbon monoxide can either be further reduced, or react with itself to form carbon and CO₂ (this reaction is discussed in a later Chapter 4). It is unknown if the previous reaction rate is fast enough to remove the carbon monoxide, or if a build up is observed. The build

up of carbon monoxide during testing as well as the differences in the initial concentration of carbon monoxide in RG and IG are therefore very important. A plot comparing the spectral results of RG and IG CO₂ is shown in Figure 3.12.

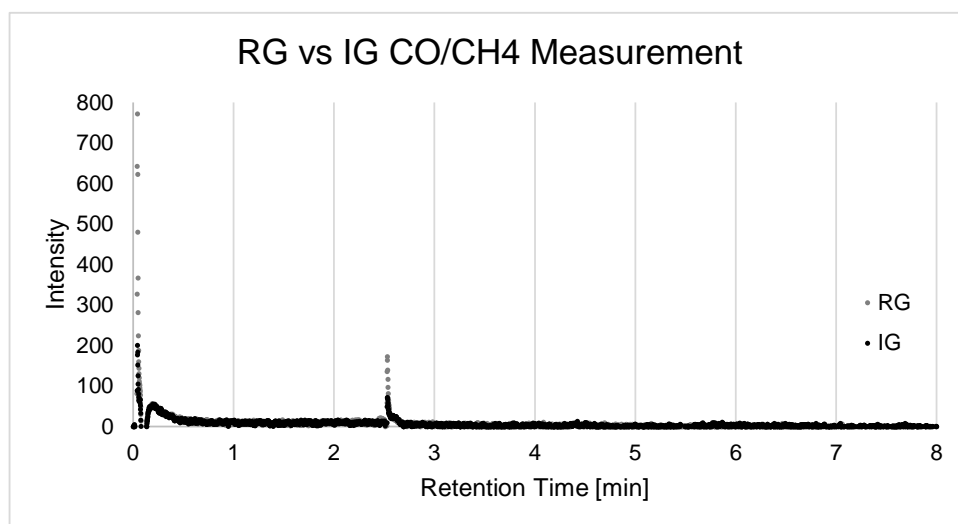


Figure 3.12: GC Spectra comparing research and industrial grade CO₂.

No observable difference in initial carbon monoxide was determined between the RG and IG CO₂. The concentration of carbon monoxide was measured during a RG CO₂ test at 550°C after exposure to samples, and is plotted in Figure 3.13. The purpose of this measurement was to understand the kinetics and mechanisms involved during corrosion. Since the CO₂ oxidized many different alloys with different compositions, the exact carbon monoxide concentration does not give a specific rate constant for individual alloy oxidation processes. Instead, the concentration gives a total rate constant of the system.

Figure 3.13 clearly shows an initial maximum concentration of carbon monoxide production followed by a decay curve. This was expected as the system as a whole should produce a protective oxide based on the alloys that were exposed, which reduces the reaction rate with time. This graph is important as it shows that carbon monoxide is produced and stays in the CO₂ on the time scales relevant to this testing. If the CO₂ was not refreshed, as would be the

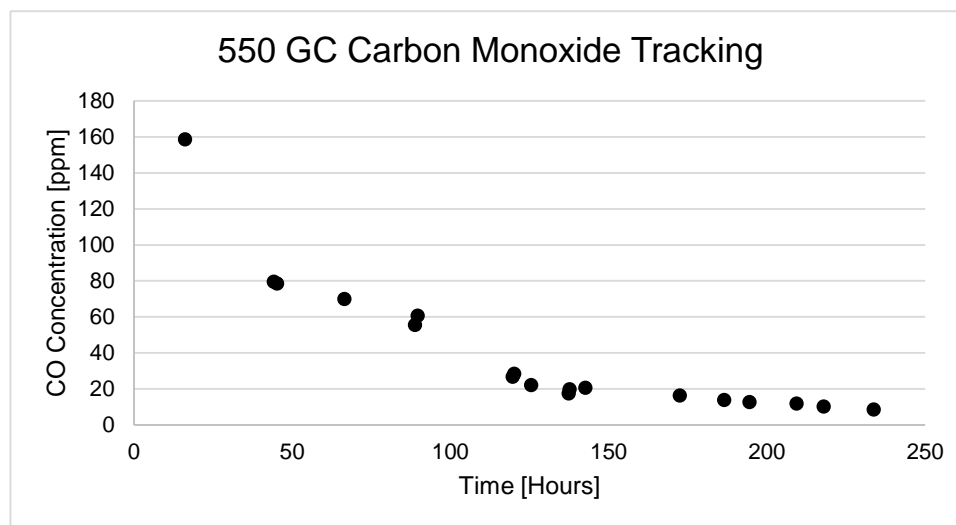


Figure 3.13: Concentration of CO for first 200 hours of 550°C RG test.

case in a closed loop cycle, carbon monoxide would slowly build up, as the corrosion process continues. In fact, by knowing the mass flow rate and applying an integration method to Figure 3.13, it was calculated that the carbon monoxide in this system would reach about 1% after 200 hours. For this reason, one of the major testing cycles was conducted using 1%CO. A total of five bottles were mixed for corrosion testing with an average CO concentration of $.78 \pm .15\%$.

3.6 Facility Accuracy and Repeatability - Round Robin Testing

One important area of this research was to prove that the systems at UW are comparable to other testing facilities, and that the results obtained from these systems are accurate. It was also important to come up with a consistent analysis procedure that can be reproduced for comparison with any future testing. In order to accomplish this, a multinational collaboration has begun to compare the results of 7 of the leading institutions in s-CO₂ corrosion. This testing was conducted on 5 alloys that were prepared by the same supplier,

and then exposed to CO₂ at each facility. The testing facilities were located at the following institutions: University of Wisconsin-Madison, Oregon State University, Oakridge National Laboratory, National Energy Technology Laboratory, Carleton University, Korea Advanced Institute of Science and Technology, and Commonwealth Scientific and Industrial Research Organization. The testing matrix for this collaboration is listed in Table 3.5.

Table 3.5: Testing matrix for round robin project.

Alloy	Test Temperatures	Samples per Lab
740H	700°C only	6
625	550°C and 700°C	12
316	550°C and 700°C	12
HR 120	550°C and 700°C	12
Grade 91	550°C only	6

Each of the locations listed previously has provided information from each testing cycle including temperature and pressure ramp rates/transients, system flow rate, as well as the cleaning procedure for each test. These are hypothesized to be the most important factors during CO₂ corrosion. The ramp rate and cool-down rate could effect initial oxide formation, as well as the stresses related to thermal expansion differences between the oxide and base material. Any transient temperature or pressure shifts are also noted as they could also cause differences in the corrosion process. The flow rate is extremely important as well due to the build up of carbon monoxide discussed previously in Figure 3.13. This would indicate that the differences in flow rate would ultimately subject samples to environmental differences in pO₂ and a_C which will result in different corrosion mechanisms (will be discussed in great detail in subsequent sections). The final note worthy condition is the cleaning procedure that the autoclaves undergo before loading the samples. It is theorized that any left over water could greatly enhance the corrosion rates of the samples. All of the testing conditions,

parameters, and transients for the UW testing are given in Appendix H.

Since the testing is still being completed by many labs, a final comparison between all of the labs has not been conducted. Data for UW is finished, and has been compared to initial data from other facilities. The initial data has shown decent repeatability between several labs and UW. The mass change data for the round robin samples from the UW testing is given in Figure 3.14, and a comparison of mass change from each of the labs can be found in Appendix G.

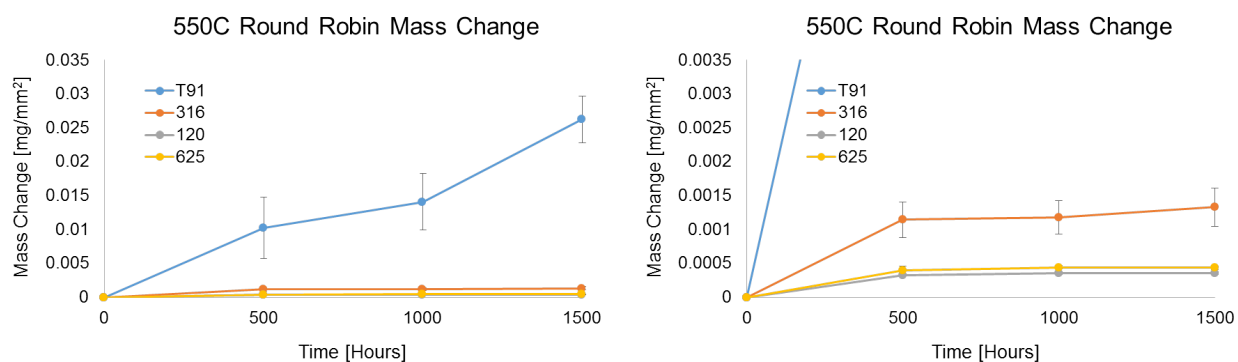


Figure 3.14: Mass change results for the Round Robin alloys at 550°C, 20MPa, for 1500 hours.

Mass change measurements obtained in this testing showed good similarity to testing previously done at UW. The mass results follow expectations with the ferritic alloy gaining the most, followed by the austenitic steel, and finally the nickel-based superalloys performing the best. Since it is theorized that mass change is effected by both oxidation and carburization of the substrate, oxide thickness measurements are also necessary to show that samples are mechanistically corroded in a similar way. A summary of the thickness measurements at UW is given in Table 3.6.

Thickness measurements were obtained by comparing several cross-sectional SEM images, and selecting an average image to take at least 15 measurements. If the oxide contained nodules or had thick and thin regions, both were measured independently and listed separately

Table 3.6: Oxide thickness results for the Round Robin alloys at 550°C, 20MPa, for 1500 hours.

Sample	Thickness [microns]		Min [Microns]	Max [Microns]	St Dev [microns]
	Continuous	Nodules	Continuous	Continuous	Continuous
T91	39.7				.7
316	.5	6.1	.28	.77	.1
120	3.15		2.4	3.7	.5
625	.21		.16	.32	.0

in the table. In order to compare SEM imaging between facilities, a standard magnification of 1.5kx was selected. While most samples produced oxides much too thin for this magnification to resolve, it was selected and has been presented for the 550°C and 700°C testing in Figures 3.15 and 3.19 respectively.

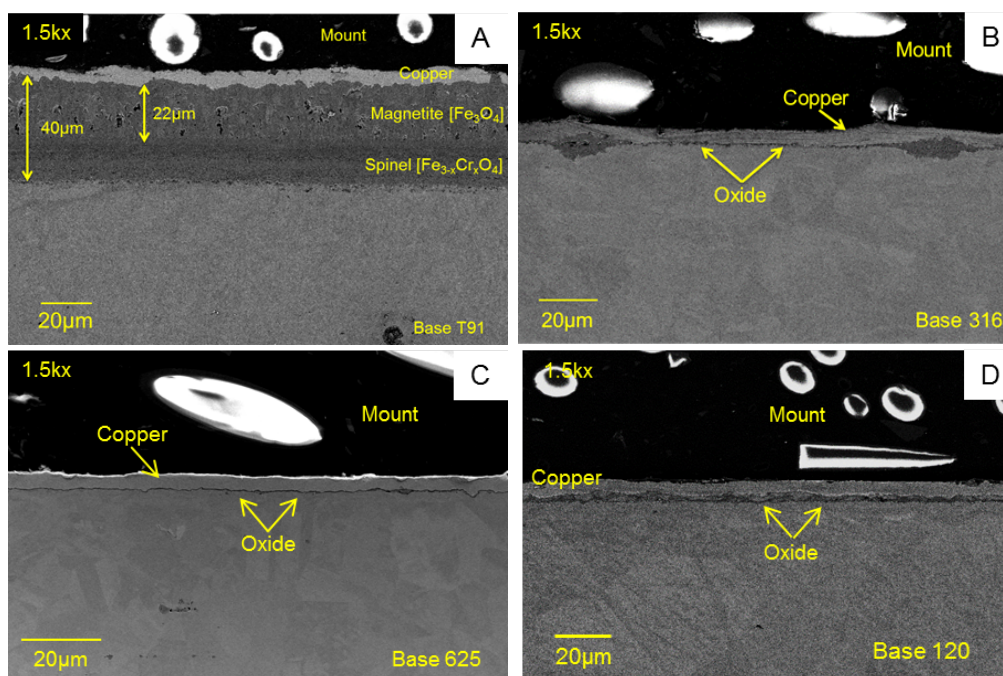


Figure 3.15: Cross-sectional SEM micrographs for Round Robin samples T92(A), 316L(B), 625(C), 120(D) exposed to CO₂ at 550°C for 1500 hours.

In order to understand the coupling of oxidation and carburization, the ferritic sample T92 was etched to selectively attack the carbides. This was done using a 5% nitric acid-ethanol mixture for 30 seconds. The ferritic alloy was selected since it showed the thickest oxide and highest mass change, indicating the most carburization as well. Imaging was performed before and after etching the sample, and is given in Figure 3.16.

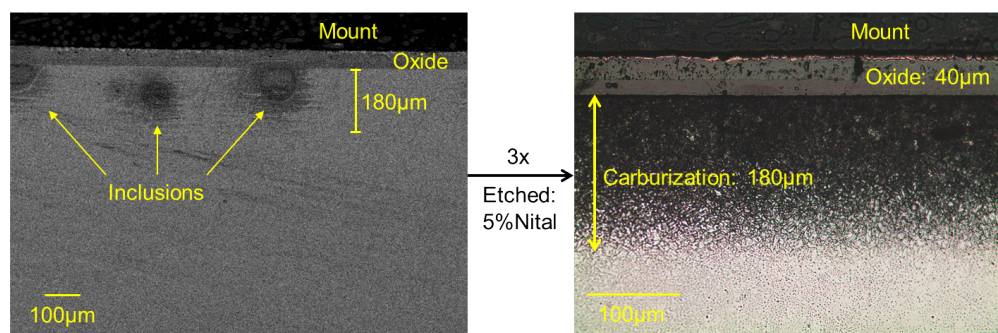


Figure 3.16: Round Robin T92 etched to show carbides after CO₂ exposure at 550°C, 20MPa, 1500 hours.

The carburization depth for the T92 samples appears to penetrate roughly 180 microns below the metal oxide interface. This is roughly four and a half times thicker than the oxide growth which indicates that more of the material is effected than just the oxidized surface. Carburization is strongly coupled to the oxidation rate, which means that far less carbon deposition is expected in nickel-chromium alloys. Carburization has been linked to increased hardness, decreased ductility which leads to mechanical failure, and break away corrosion [27].

Large spherical inclusions can also be observed in Figure 3.16. These inclusions are randomly dispersed below the oxide, and some extend into the spinel region. This would indicate that some of the inclusions were formed before the oxide existed in that region and simply grew through these regions. The inclusions also only existed in the carburized region as observed through the etching which would suggest that these inclusions were caused by carburization. The carbon content in these regions appears to be very high, and caused

significant phase precipitation. This precipitation is similar to metal dusting which occurs when the activity of carbon is much higher than can be supported by the matrix and causes rapid destruction of the material upon cool-down. If this is indeed initiation of metal dusting, the implications are very severe as this material could not be used due to the potential of failure in these conditions.

Only 316L and the nickel based superalloys were exposed to 700°C as the temperatures are well above the mechanical strength of T92 (as well as the corrosion resistance). The mass change results at 700°C are given in Figure 3.17.

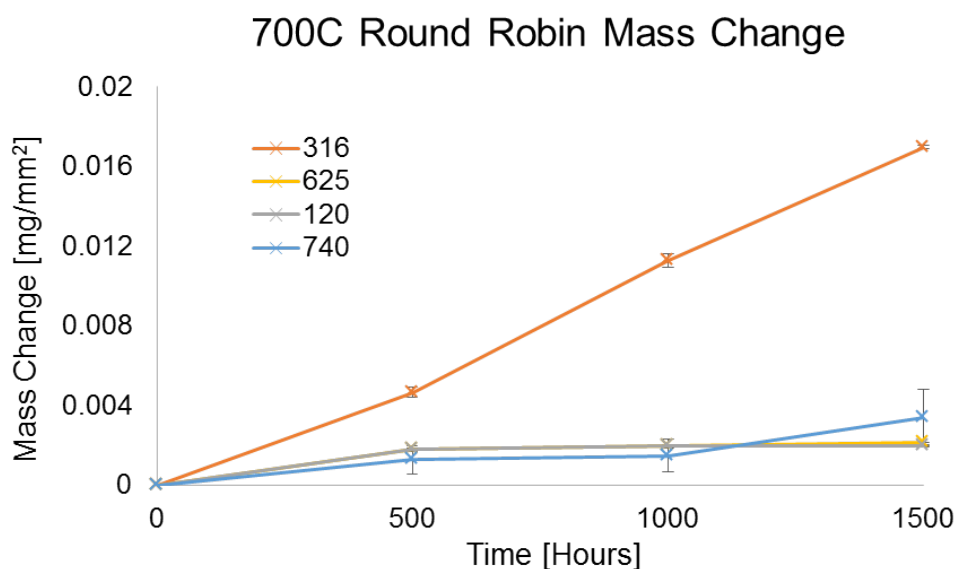


Figure 3.17: Mass change results for the Round Robin alloys at 700°C, 20MPa, for 1500 hours.

The mass change of the nickel-chromium alloys still appear protective, and minimal relative to alloy 316L. 316L showed near linear kinetics, which is an indication of poor corrosion resistance at this temperature. Additional evidence for this can be observed in the SEM micrographs for 316L which showed large nodule formation, as well as cracking at the interface of the external and internal growing oxides. This result would be a good comparison

to other facilities once they have conducted SEM in order to see if mechanistically similar results occur.

Sample	Thickness [microns]		Min [Microns]	Max [Microns]	St Dev [microns]
	Continuous	Nodules	Continuous	Continuous	Continuous
316	2.9	36	2.2	3.8	.4
120	1.3	3.1	.70	2.3	.5
625	1.3		1.0	1.6	.1
740	1.0		.57	1.5	.3

Figure 3.18: Oxide thickness results for the Round Robin alloys at 700°C, 20MPa, for 1500 hours.

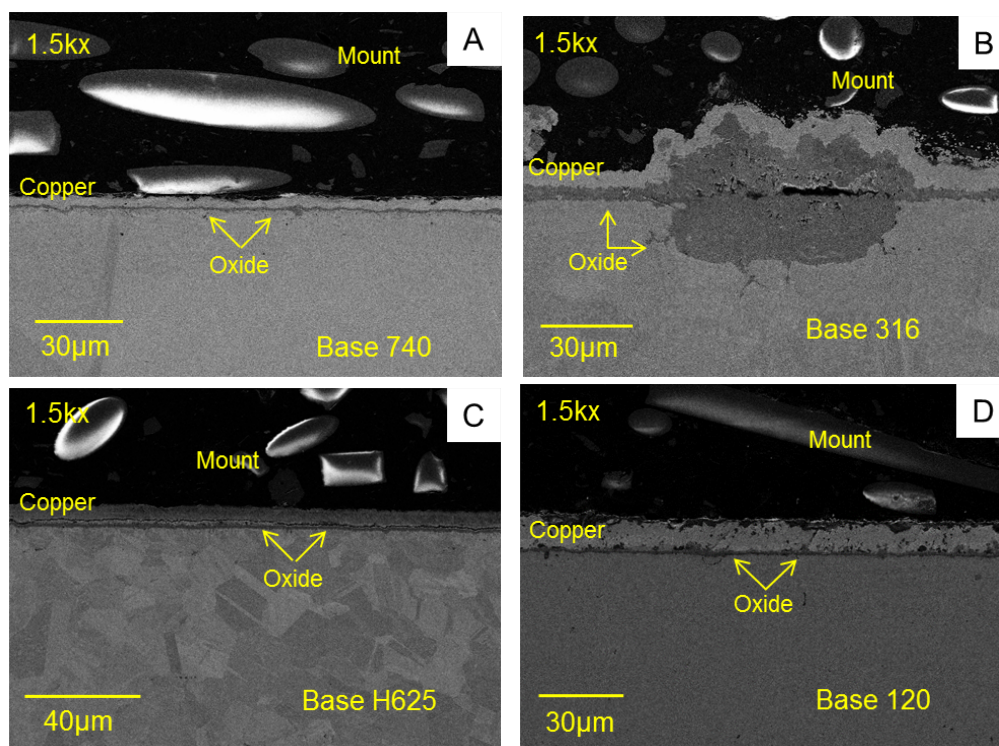


Figure 3.19: Cross-sectional SEM micrographs for Round Robin samples 740H(A), 316L(B), 625(C), 120(D) exposed to CO₂ at 700°C for 1500 hours.

At this point, the other groups have not produced any SEM micrographs for comparison. Since the mass change measurements are so similar for all but one group, it is reasonable to conclude that the UW system is capable of repeatable tests. A few pressure transients of a couple hours occurred during testing of the samples, but no appreciable differences in the samples were observed which indicates that these transients don't have a large effect on the corrosion mechanisms as they only last for a small percent of the total testing. Since one lab produced data that was 3-10 times higher, it would be interesting to determine the source of deviation. Since temperature and pressure transients don't seem to have enough of an effect on the overall corrosion to produce the differences observed by Oakridge, it would be useful to study the differences in flow rate and the cleaning procedure to see if any impurities were left in the autoclave before the start of their testing cycles.

Chapter 4

Effects of pO_2 and a_C on Corrosion in CO_2

Environments

Corrosion in sCO_2 environments is complex due to the coupling of pO_2 and a_C . As one component is changed, the other is altered in the opposite direction. In order to study effects of pO_2 and a_C , three different tests were performed: Research grade CO_2 (base-line), Research grade $CO_2 - 100\text{ppm } O_2$ (high pO_2), and Research grade $CO_2 - 1\%CO$ (high a_C). Each of these tests was conducted in order to prove different theoretical predictions:

- Altering pO_2 changes the stability of different oxides (specifically Ni-NiO).
- Coupling of pO_2 and a_C throughout the oxide leads to carburizing environments at the M-O interface.
- Saturation of CO_2 with CO (high environmental a_C) causes carbon deposition during cool-down.
- Controlling pO_2 and a_C can be used to alter defect concentration leading to the production of a stoichiometric oxide.

4.1 Altering pO_2 Changes the Stability of Different Oxides

Since pure CO_2 has a significantly lower partial pressure of oxygen than air, the oxidation reactions for several metals were studied to determine if some oxides were not thermodynamically possible in CO_2 . The main focus of this study is on high temperature application, therefore nickel-chromium superalloys are of highest interest. The partial pressure of oxygen needed to oxidize these metals (Ni and Cr) has been plotted as a function of temperature in

Figure 4.1. The partial pressure of oxygen produced from pure CO_2 dissociation as well as 1% CO-CO_2 mixture is also plotted in order to determine which oxides were thermodynamically allowed. The $p\text{O}_2$ for $\text{RG} + 100\text{ppm O}_2$ was not included as it was much higher than even the RG conditions.

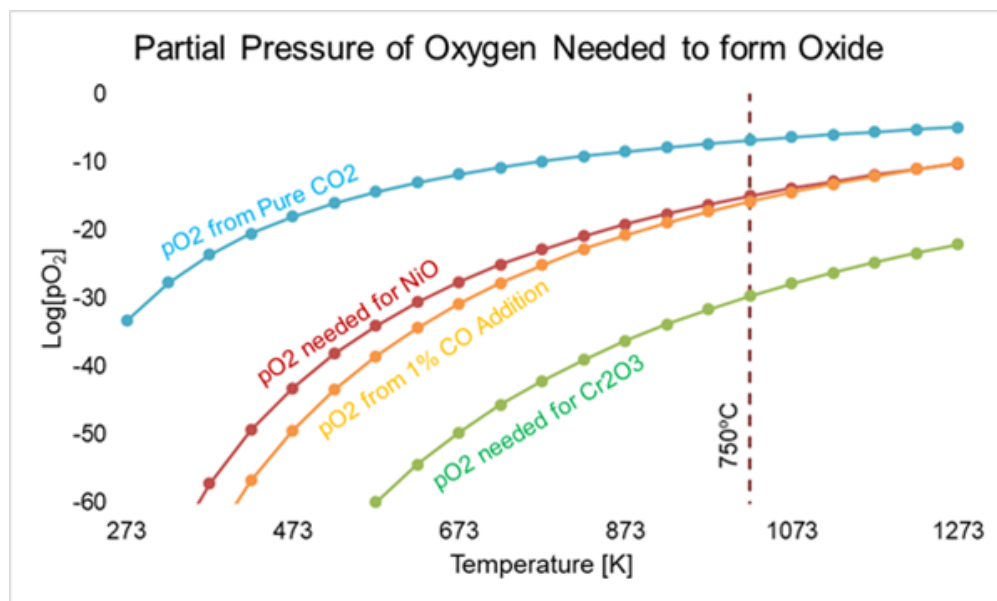


Figure 4.1: Temperature and environmental dependence on oxidation of chromium and nickel.

The data presented in Figure 4.1 shows that oxides of chromium and nickel will form at the partial pressure of oxygen produced from the dissociation of pure CO_2 ($\sim 10^{-9}$ at 750°C). When 1% carbon monoxide is added, the formation of nickel oxide can only form at very high temperatures. It is important to point out that these calculations are only valid for 100% pure CO_2 and metal atoms with no restrictions, and an infinite amount of time. In order to prove this theory, testing was conducted on pure Ni samples in pure CO_2 (RG) and 1% CO mixed CO_2 at 750°C , 20MPa, for 1000 hours. The mass change measurements for the pure Ni samples is given in Figure 4.2.

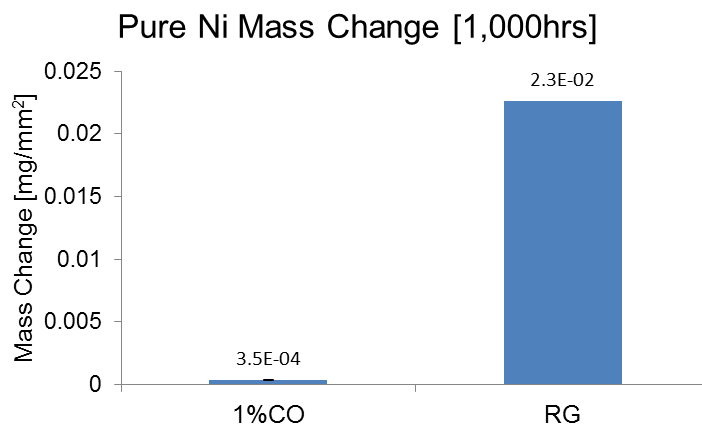


Figure 4.2: Mass change measurements of pure Ni exposed to RG and RG + 1%CO at 750°C for 1000 hours.

Mass change measurements show almost two orders of magnitude higher mass gain for pure Ni exposed to RG CO₂, and almost no mass gain on samples exposed to RG-1%CO environments. This would indicate that the Ni was rendered inert in the more reducing CO-CO₂ environment. In order to more closely observe this effect, SEM was conducted on the surface of each sample, and is given in Figure 4.3. A layer of Ni rich oxide was observed on the surface of the RG sample, whereas only small islands of Si and Mn rich oxides were found on the surface of the samples exposed to 1%CO-CO₂.

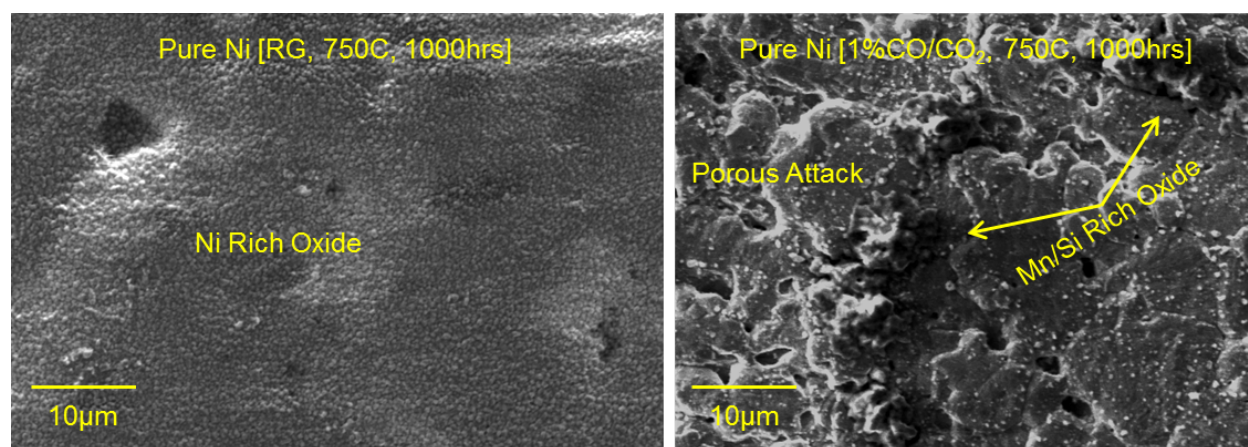


Figure 4.3: SEM micrographs of pure Ni exposed to RG (*left*) and RG+1%CO (*right*).

Interestingly, the sample exposed to the CO rich environment showed a large amount of porosity and removal of the Ni on the surface of the sample. This is theorized to be due to the formation of volatile nickel carbonyls which are created at intermediate temperatures during heating and cooling of the system. XRD and Raman spectroscopy was performed on these samples in order to further prove the stability of NiO in RG CO₂ conditions, and is presented in Figure 4.4 and 4.5.

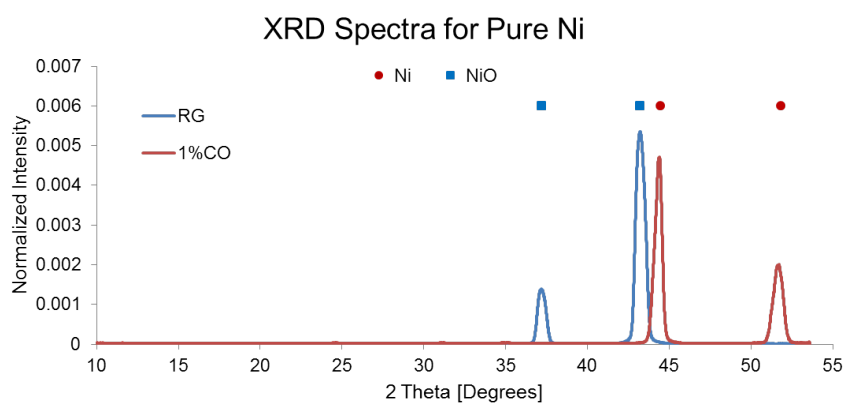


Figure 4.4: XRD measurements of pure Ni exposed to RG and RG + 1%CO at 750°C for 1000 hours.

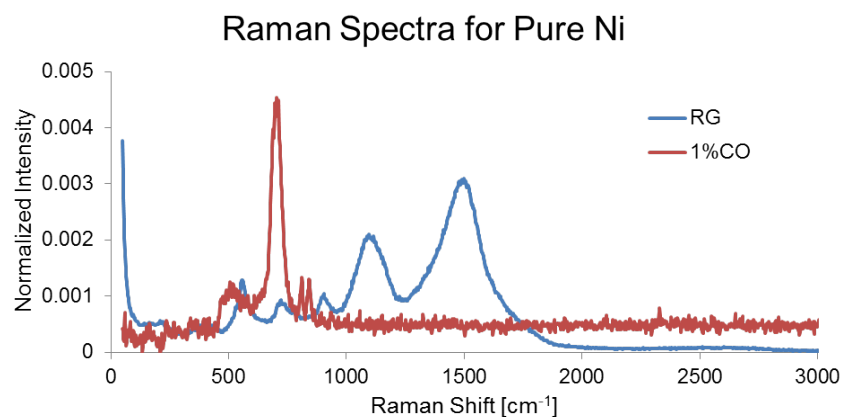


Figure 4.5: Raman measurements of pure Ni exposed to RG and RG + 1%CO at 750°C for 1000 hours.

Both XRD and Raman support the formation of NiO on the surface of the sample exposed to RG CO₂ and the lack of NiO on the surface of the sample exposed to the 1%CO mix. While no oxides were detected in the XRD spectrum for the 1%CO sample, Raman spectroscopy revealed the presence of manganese rich oxide, which is supported by EDS measurements which also showed Mn and Si enrichment. Trace amounts of both Si and Mn were found in the bare Ni cert, and have oxides with a much lower thermodynamic stability than Ni. SEM cross-sectional images are given in Figure 4.6.

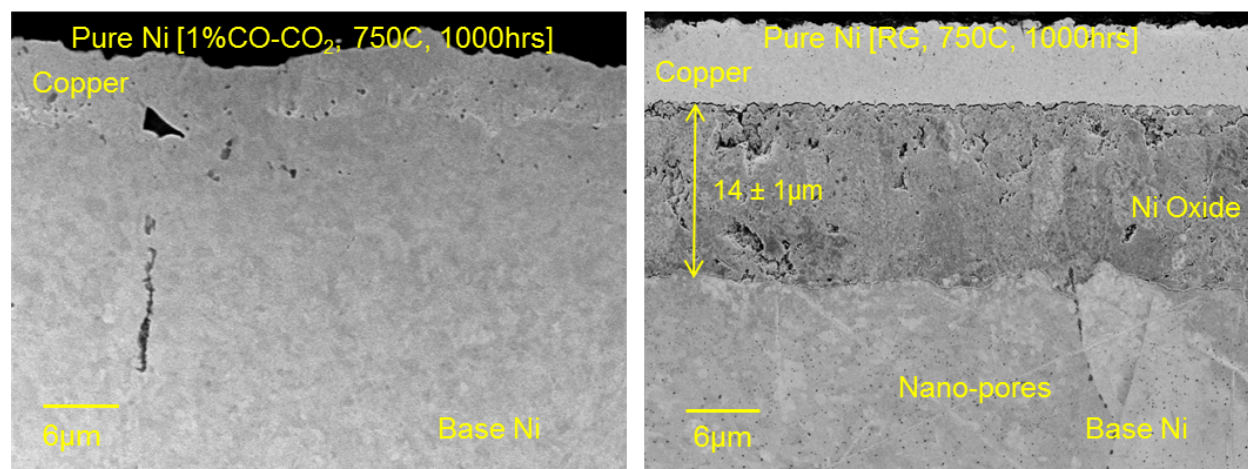


Figure 4.6: SEM cross-sectional imaging for pure Ni exposed to CO₂ at 750°C/20MPa for 1000 hours in 1%CO (left) and RG (right) environments.

Cross Sectional SEM images confirm the lack of oxide on Ni exposed to the CO rich environment, and the presence of a thick oxide on the sample exposed to RG CO₂ (14µm). Both samples experienced porous attack near the surface of the sample. The pores are attributed to nickel carbonyl formation at lower temperatures which is highly volatile. The sample exposed to RG CO₂ also exhibited enhanced grain boundary attack near the surface with depletion of nickel along grain boundaries up to 100µm. Both nickel depletion and depth of porosity can be more easily observed in Figure 4.7. Similar attack of the Ni sample exposed to 1%CO occurred, but with the lack of oxide formation on the surface. It is

important to note that the original surface of the nickel samples was polished to 800 grit, and that the large surface roughness is likely due to the removal of nickel.

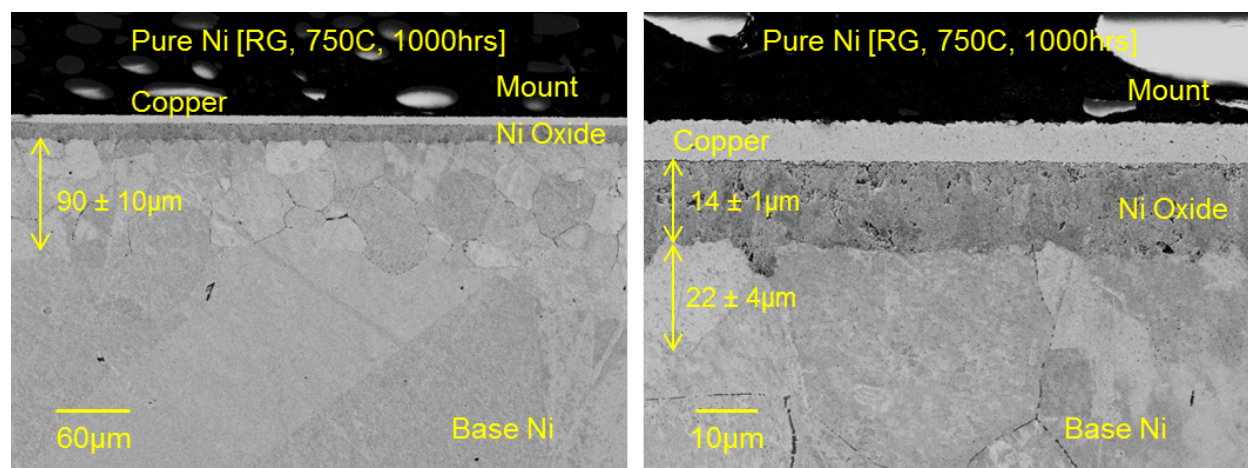


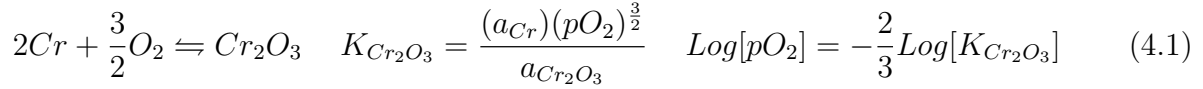
Figure 4.7: SEM cross-sectional imaging of grain boundary attack of pure Ni exposed to RG CO₂ at 750°C/20MPa for 1000 hours at 200x (left) and 1000x (right).

Ni depletion corresponds to enrichment of Mn and Si which were found as scattered oxides on the surface of the sample exposed to 1%CO-CO₂. The depleted grain boundaries also correspond to increased porosity which is due to the increased diffusion pathways in these regions. The corrosion of nickel appears to be very detrimental in RG CO₂ conditions, and should be avoided.

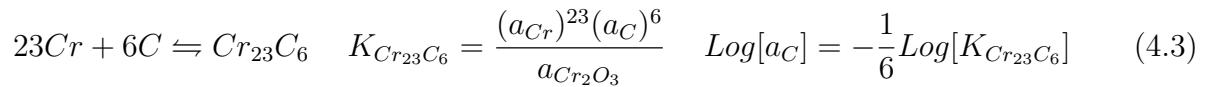
The fact that Ni can be readily rendered non-reactive is a very important, and could be used to mitigate corrosion on commercial alloys in these environments. It should be mentioned that while the pO₂ can be lowered easily to inhibit NiO formation, the corresponding increase in a_C could lead to increased carbon deposition as well as carburization which will be discussed in the following sections.

4.2 Altering a_C Changes the Carburization of the Underlying Material

In order to adapt the model laid out for the VHTR plotted previously in Figure 2.17 to CO_2 , the first step was to re-create the Cr-O-C stability diagram. This is done by using the chemical equations shown in Equations 4.1-4.4 (Equilibrium constants were found using HSC software [62]). From the chemical balance, the equilibrium equations can be found and are listed next to each chemical equation. At this point, it is usually of interest to study where two phases are in equilibrium with each other with respect to the reactive species (pO_2 and a_C). This is done for Equation 4.1 by setting a_C and $a_{Cr_2O_3}$ equal to each other, leaving just pO_2 in the equation. Finally, the equilibrium equation is related to the Gibbs Free Energy shown in Equation 4.2, and solved for the relevant pO_2 and a_C values. The same method is used for each carbide species ($Cr_{23}C_6$ shown in Equation 4.3). A more complicated system is the equilibrium between the oxide and carbide. The chemical and equilibrium equations for Cr_2O_3 and $Cr_{23}C_6$ are listed in Equation 4.4. Now the contribution of oxide and carbide activities are set to each other. This leaves a relationship between the pO_2 and a_C which indicates that oxide to carbide equilibrium is determined by both oxygen and carbon potential. These equations produce the volatility diagram given in Figure 4.8.



$$K_{Cr_2O_3} = Ae^{\frac{-\Delta G}{RT}} \quad \frac{(a_{Cr})(pO_2)^{\frac{3}{2}}}{a_{Cr_2O_3}} = Ae^{\frac{-\Delta G}{RT}} \quad (4.2)$$



$$K_{O \rightarrow C} = 6\text{Log}[a_C] - 17.25\text{Log}[pO_2]$$

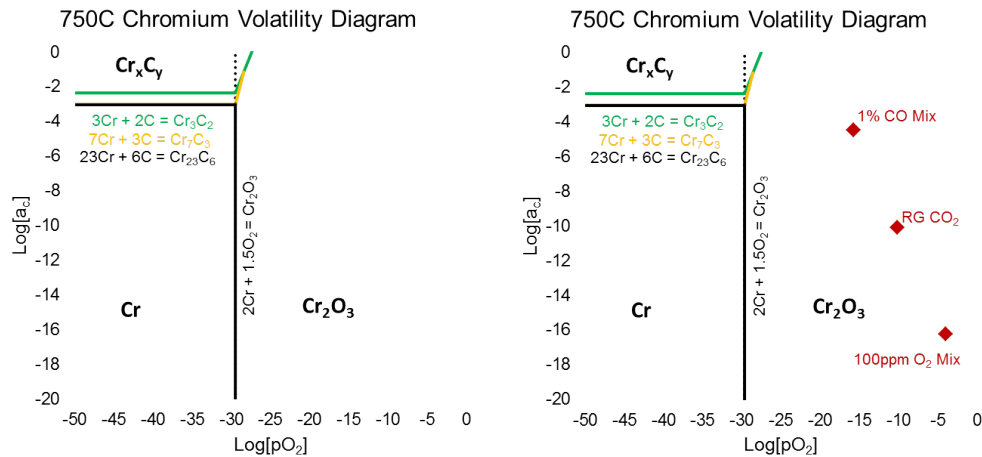
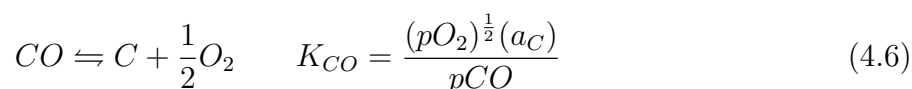
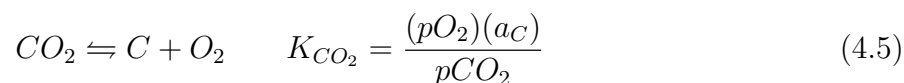


Figure 4.8: Volatility diagram for Cr-C-O phases at 750°C at 1 atm (Left). Volatility diagram with environmental conditions for RG CO₂, RG + 100ppm O₂, and RG + 1%CO mixed CO₂ (Right).

The volatility diagram in Figure 4.8 represents which phases should exist given a partial pressure of oxygen and activity of carbon. This can be expanded explicitly to the CO₂ environments in this study by implementing the gaseous equilibrium given by Equations 4.5 and 4.6. The environmental conditions of interest are research grade CO₂ (considered 100% pure), 100ppm oxygen mixed RG CO₂, and 1% CO mixed RG CO₂. The pO_2 and a_C values for the environmental dissociation are plotted in red on the volatility diagram in the right graph of Figure 4.8.



The testing environment sets the boundary condition for the oxide-environment interface. A more important boundary condition is the one between the metal and oxide. This boundary condition controls the corrosion process, and will determine whether oxidation or carburization occurs (or both). The partial pressure of oxygen should be roughly equal to the phase equilibrium pO_2 calculated between Cr and Cr_2O_3 since both are present at the interface. This pO_2 value is different from the environmental condition, therefore, the a_C must also change in order to maintain the chemical equilibrium. In order to calculate the new a_C , the most reactive species must be considered. For example, in the 100ppm oxygen doped testing, only oxygen was consumed during oxidation (given in Figure 4.9).

The oxygen consumption graph in Figure 4.9 represents measurements before s-CO₂ has been heated (green), as well as after the s-CO₂ exits the autoclaves after exposure to samples (blue and red). Using the flow rate of s-CO₂, the total reaction rate for each system could be calculated. Unfortunately, this doesn't provide much useful information as the sample composition, surface area, and the autoclave will effect these measurements. Regardless,

the trends observed show that samples at 750°C consumed more oxygen which indicates faster reaction rates. Since the oxygen concentration follows a similar pattern expected for mass change of the samples, and eventually reaches a near-steady-state, it can be assumed that oxygen is consumed preferentially in these environments. Therefore, it is assumed that only the pO_2 changes throughout the oxide, while the a_C stays close to the same value (concentration of CO_2 stays roughly the same). Figure 4.9 shows the change in pO_2 leading to the equilibrium state between chromium and chromia for the oxygen mixed testing.

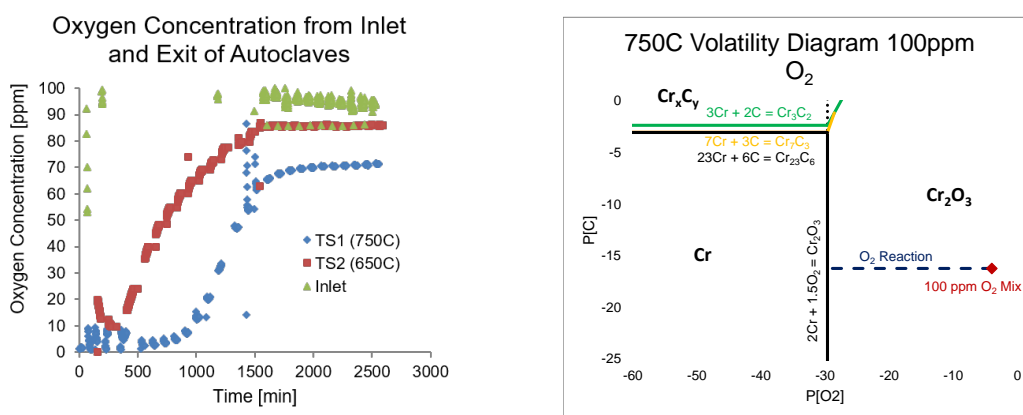
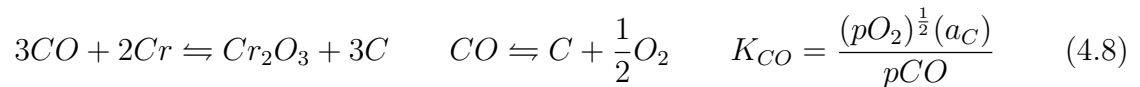
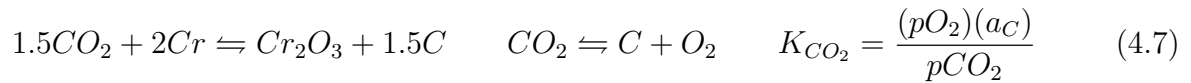


Figure 4.9: Oxygen consumption during oxygen mixed s- CO_2 testing (left). Volatility diagram for Cr-C-O phases at 750°C at 1 atm with oxygen doped environment.

The more complicated environments to model are RG CO_2 and 1%CO mixed environments, in which the a_C is directly coupled to the pO_2 . In these environments, the oxidation reaction either occurs due to reduction of CO_2 or CO. In either case, oxygen is consumed to form the oxide, resulting in a higher a_C . This is given by the chemical Equations 4.7 and 4.8. Since it is unknown which species is most reactive with the metal, it is useful to consider both reactions in order to create a range of possible carbon activities as a function of partial pressure of oxygen. In order to calculate this, a relationship must be drawn between CO_2 , CO, O_2 , and C. This relationship ends up being the chemical equilibrium equations given by 4.6 and 4.5 since it ultimately depends on mass balance of CO_2 in the system. The

mass balance for carbon is used to solve the resulting system of equations, and is given by Equation 4.9. Equilibrium constants were calculated empirically from Equation 4.10 with parameters given by [63]. A summary of the equilibrium constants for the decomposition is given in Table 4.1. Using these values for CO₂ equilibrium gives a range of values for the activity of carbon as the partial pressure of oxygen drops through the scale to the value at the oxide interface. This is represented by the dashed blue lines plotted in Figure 4.10.



$$N_{total_C} = 1 = N_{CO_2} + N_{CO} + N_C \quad (4.9)$$

$$\ln[K_i] = a_i/T + b_i + c_i * T + d_i * T^2 \quad (4.10)$$

Table 4.1: Equilibrium constants for the decomposition of CO₂ at 750°C.

	CO ₂ = CO + .5O ₂	2CO = CO ₂ + C	C + O ₂ = CO ₂
K	1.28E-10	3.71E-01	1.65E+20

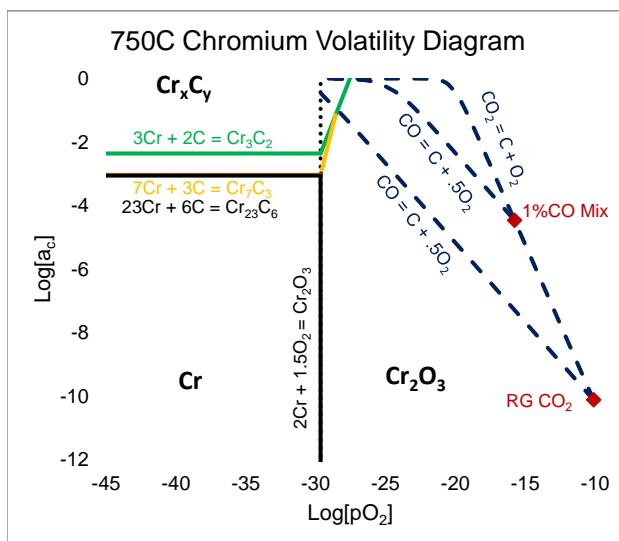


Figure 4.10: Volatility diagram with lines representing mass balance of pO_2 and a_C through the oxide for RG and RG + 1%CO environments.

Figure 4.10 shows that by treating the oxide as a diffusion barrier, the coupling of pO_2 and a_C results in carburizing environments near the M-O interface. This means that the system should actually reach an equilibrium between chromium oxide and chromium carbide instead of pure chromium and the oxide. This would indicate that corrosion of pure Cr in CO_2 should form a duplex layer with the oxide at the environment interface, a carbide layer between the oxide and base metal, and finally chromium. Carbides would only be measurable for an equilibrium condition which can easily be reached kinetically. The gap between environmental condition to the Cr_2O_3 - Cr_xC_y phase equilibrium should be proportional to the potential gap and therefore dictate kinetics. This would mean that the more carburizing environment (1%CO) should produce more carbides than the RG environment. In order to test this theory as well as the validity of the dual corrosion layer theory, pure Cr samples were exposed to RG CO_2 and RG + 1%CO at 750°C and 20MPa for a total of 1,000 hours. The mass change of these two tests are given in Figure 4.11.

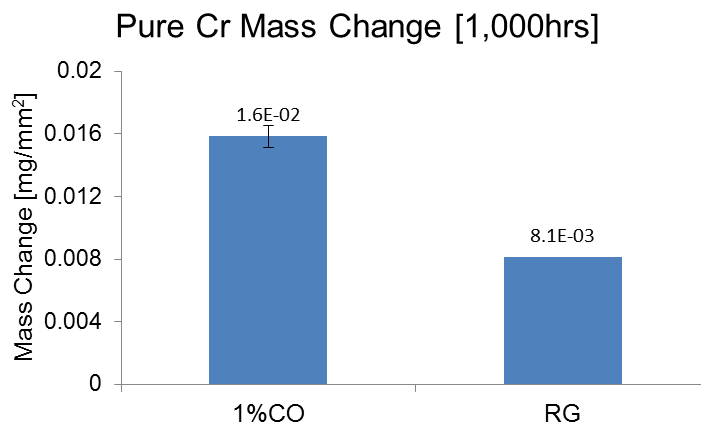


Figure 4.11: Mass change measurements of pure Cr exposed to RG and RG + 1%CO at 750°C for 1000 hours.

Initial mass change shows that the samples exposed to 1%CO gained about twice as much mass as the samples exposed to RG CO₂. In order to determine if the additional mass was a result of increased carbon deposition, samples were mounted and imaged using SEM which is given in Figure 4.12.

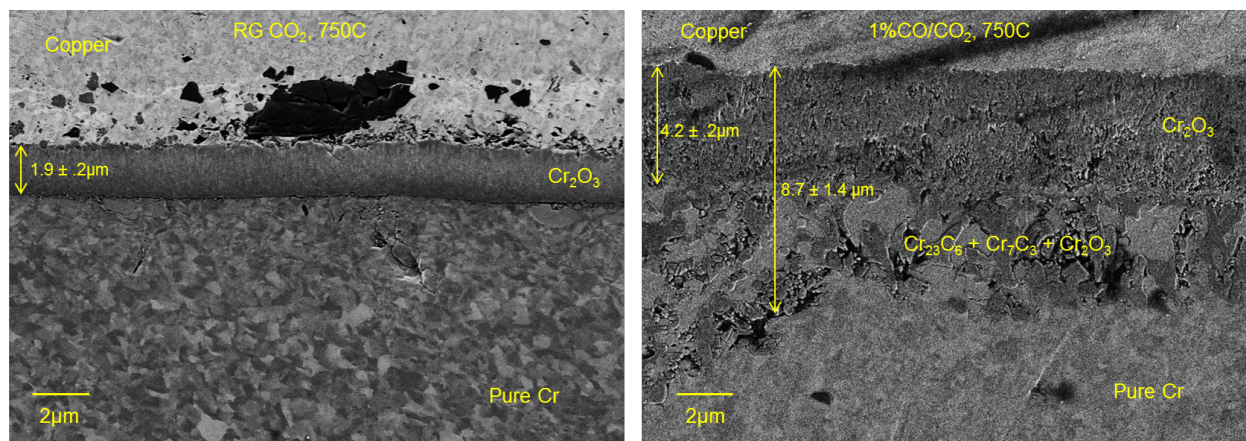


Figure 4.12: SEM micrographs of pure Cr exposed to RG (*left*) and RG+1%CO (*right*).

The SEM micrographs in Figure 4.12 show that the average oxide thickness in the CO mixed environment is roughly twice the thickness of the sample exposed to RG CO₂. The oxide in the RG condition shows a very compact, uniform layer with very little porosity.

This is contrasted by the highly porous oxide of the pure Cr exposed to the CO mixed environment. Also important, is the internal attack found on the sample exposed to CO mixed CO₂. Since a pure Cr sample was used, stratified layers would indicate the presence of a separate phase which would alter diffusion in that region. This would only be possible if carbides were present. The carbide layer beneath the oxide (predicted in the model above) was also observed by Zheng and Young on an atmospheric CO/CO₂ test completed at 900°C after XRD and Electron Probe Micro-Analyzer (EPMA) analysis of the internal layer [64]. SEM micrographs from their work is presented in Figure 4.13.

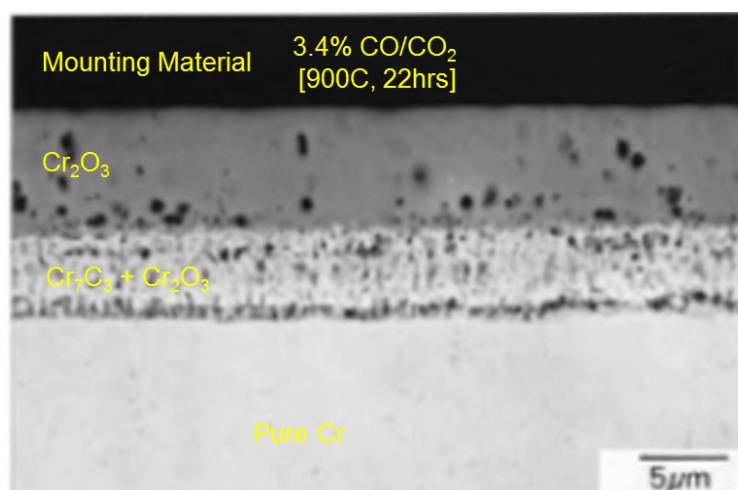


Figure 4.13: SEM micrograph of pure Cr exposed to 3.4% CO/CO₂ at 900°C for 22 hours [64].

The internal oxidized and carburized layer found in [64] appears very similar to the dual layer found in this study. In order to determine chemical and bonding information of the internal layer of the pure Cr sample, the oxide was carefully polished off to reveal three regions (Base Cr, Carbide+Oxide, Oxide) as seen in Figure 4.14. SEM images for each of the layers is also given in Figure 4.14.

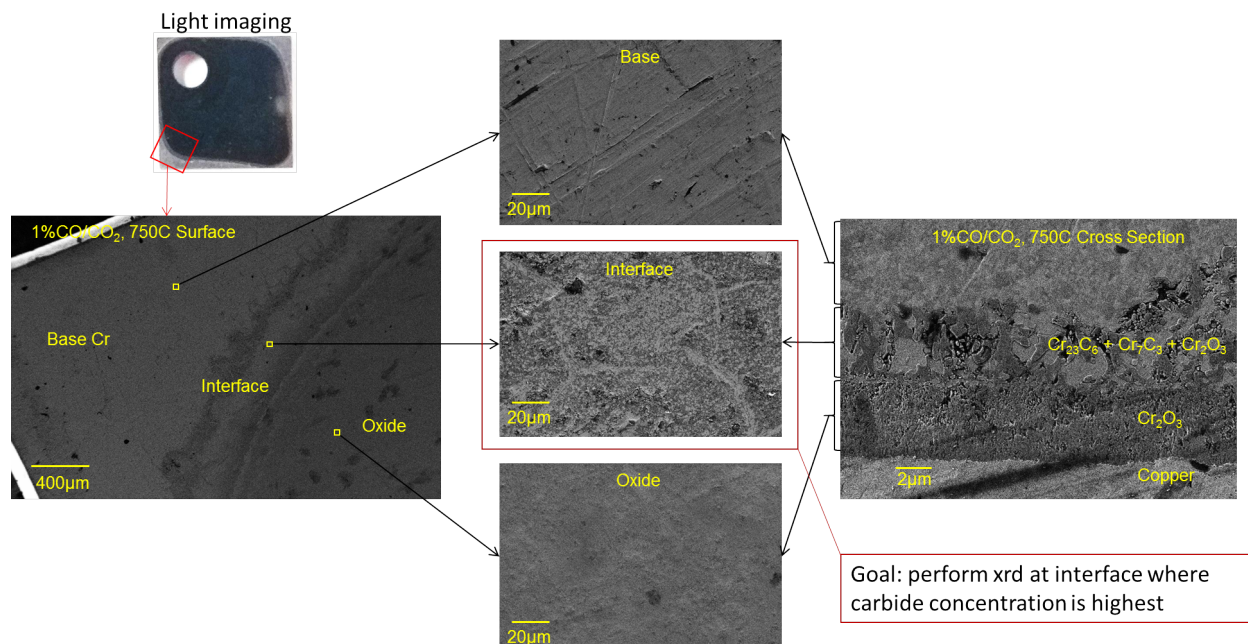


Figure 4.14: Pure Cr post polishing after being exposed to RG + 1%CO at 750°C for 1000 hours.

SEM imaging proves that the intermediate layer between the oxide and base Cr on the surface is indeed the internally stratified region. This is given by the dispersed oxide islands (dark regions) in the matrix of pure Cr (light regions) found in the middle image in Figure 4.14. XRD was conducted on the unpolished and polished (interface region) sample to observe the differences in the oxide vs the internally oxidized layer given in Figure 4.15.

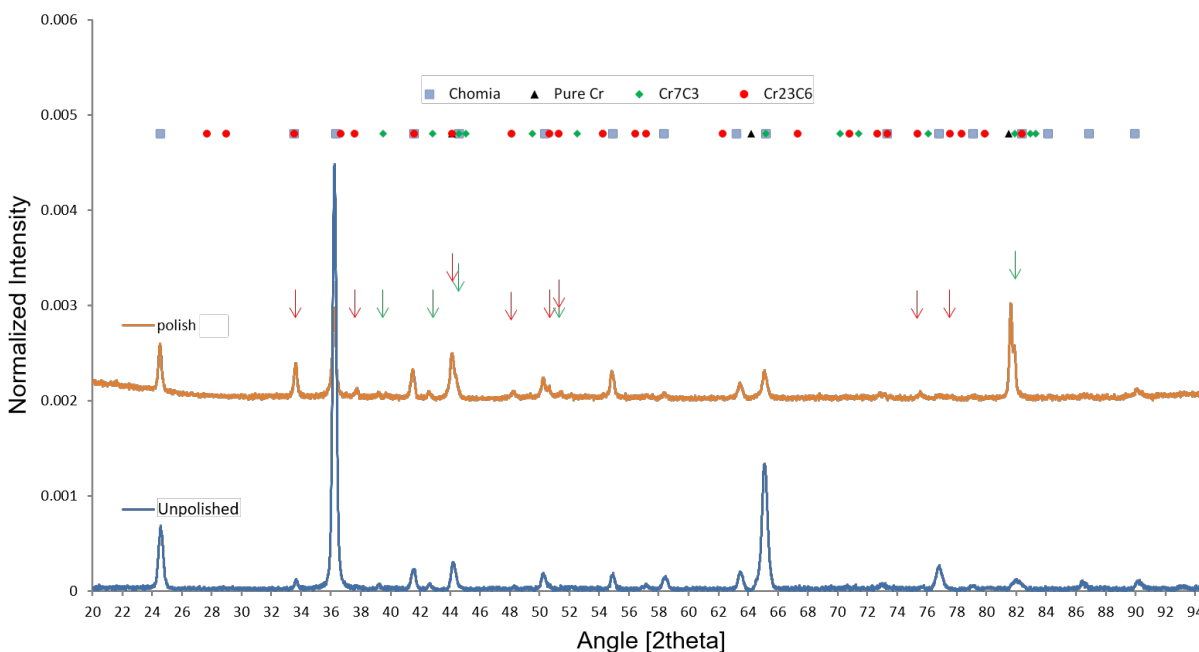


Figure 4.15: XRD measurements of pure Cr before and after polishing after exposure to RG + 1%CO at 750°C for 1000 hours.

XRD results clearly show the evidence of chromium rich carbides (Cr_7C_3 , Cr_{23}C_6) in the polished region, and not on the unpolished sample. The presence of inter-facial carbides was predicted by the modeling above which stated that the oxide acting as a diffusion barrier would create a_C values high enough to reach an equilibrium between the oxide and carbide phases of chromium. It is important to note that the pure Cr samples exposed to RG CO_2 did not show any internal attack. It is possible that carburization was much higher in 1%CO- CO_2 because the equilibrium condition was easier to reach compared to RG conditions. This conclusion would indicate that carburization as seen in the 1%CO environment is not as kinetically favorable in the RG environment. Kinetically limited carburization will be supported later when studying corrosion of Haynes 625.

4.3 Saturation of CO₂ with CO Causes Carbon Deposition During Cool-down

Carbon deposition discussed previously was in the form of chromium carbides, and expected to form at the interface between the metal and oxide. Another carbon deposition mechanism that will be studied is through the Boudouard Reaction given by Equation 4.11. The reverse reaction utilizes carbon monoxide to deposit carbon at low temperatures $T < 700^\circ\text{C}$, and is common in blast furnace chemistry during alloy fabrication. The Gibbs Free Energy for the Boudouard Reaction is given as a function of temperature in Figure 4.16.

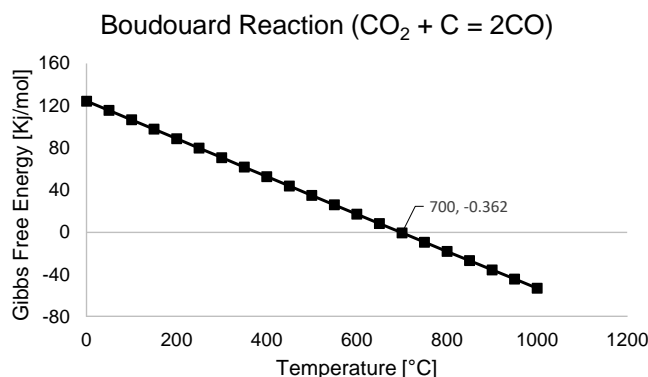


Figure 4.16: Gibbs Free Energy of Formation for the Boudouard Reaction.

The carbon precipitated through the Boudouard Reaction is different from the carbide production discussed earlier which is bonded to chromium and was found only beneath the oxide. The carbon found due to the Boudouard Reaction should precipitate as pure carbon and would be expected to deposit uniformly given a constant temperature as the carbon monoxide reacts with itself. The Gibbs Free Energy of the Boudouard Reaction shows that carbon deposition is only possible at temperatures below 700°C . Above which, carbon

removal would be expected by the forward reaction through reaction with CO_2 . Since the impurities testing in this work was only done at 750°C , pure carbon would only be deposited during ramp and cool-down of the system, and carbon removal would occur at operating temperatures.

Another way of thinking about this is by considering the CO_2 environment as a solution with C dissolved as CO. At 750°C , the 1%CO condition would be considered saturated with the maximum (or more) amount of CO. As the temperature cools, carbon monoxide must react to precipitate carbon because the CO_2 cannot hold as much CO as in the high temperature. This is perhaps more easily observed by looking at the chemical equilibrium of CO_2 , CO, and C as a function of $p\text{O}_2$ for two temperatures. Figure 4.17 gives the shift in equilibrium from 750 to 450°C .

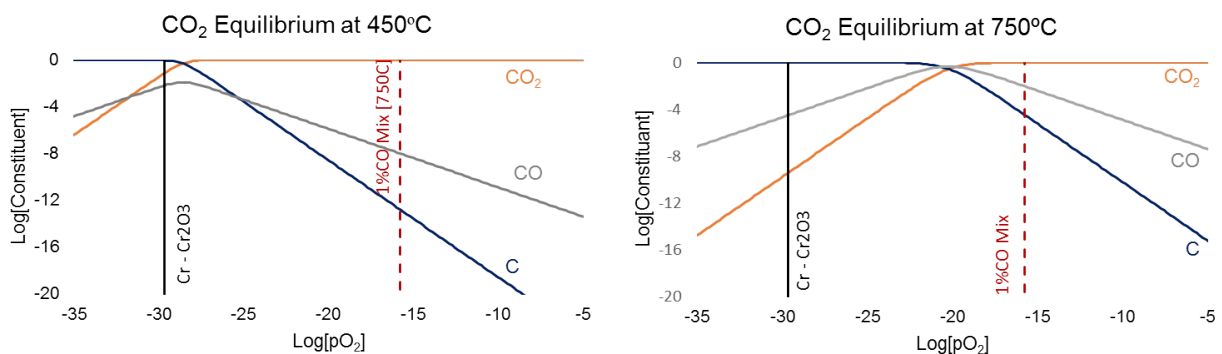


Figure 4.17: Equilibrium of CO_2 constituents as a function of $p\text{O}_2$ at 750 and 450°C .

Carbon deposition therefore requires the presence of carbon monoxide. While RG testing does produce some carbon monoxide during the corrosion process, these concentrations are very low (1-100ppm). At these levels, the deposition of carbon during temperature transients would not amount to easily measurable quantities. This mechanism of carbon deposition would only be observable in high CO environments such as the 1%CO testing.

Since the Boudouard Reaction could be responsible for deposition or removal of carbon

in the system, it was important to study the kinetics. The reverse reaction is very difficult to measure, so the forward reaction was studied using pure carbon in the presence of flowing CO_2 at 650 and 750°C. This was done to determine if the reaction rate for decarburization was relevant on the time scales of the testing completed in this work (1,000 hours). The mass loss at 200 and 400 hours was recorded, and is plotted in Figure 4.18. Since oxygen impurities were also being investigated, graphite samples were exposed to oxygen doped CO_2 , and are also included in Figure 4.18 to show carbon removal.

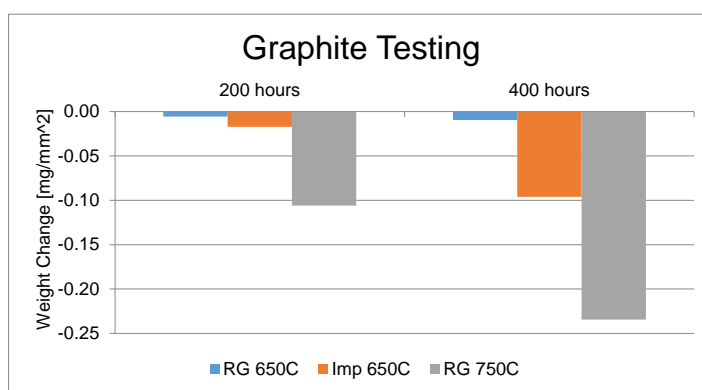


Figure 4.18: Mass loss of NGB18 graphite samples exposed to research grade, and 100ppm oxygen doped CO_2 at 650 and 750°C at 20Mpa.

Images of the graphite samples both before and after exposure are shown in Figure 4.19. These images show the increased attack and carbon removal at 750°C that was also observed by the mass change measurements. These results prove that the kinetics of the Boudouard Reaction occur in the above conditions at time scales relevant to the testing parameters.

Two mechanisms of carbon ingress from the environment have been discussed, one deposits carbon in the form of carbides (carburization) at the interface between the metal and oxide due to coupling of $p\text{O}_2$ and a_C through the oxide, and the other deposits carbon during temperature transients due to saturation of CO and the Boudouard Reaction. The second form of carbon deposition should cover the surfaces that the environment is subjected to.

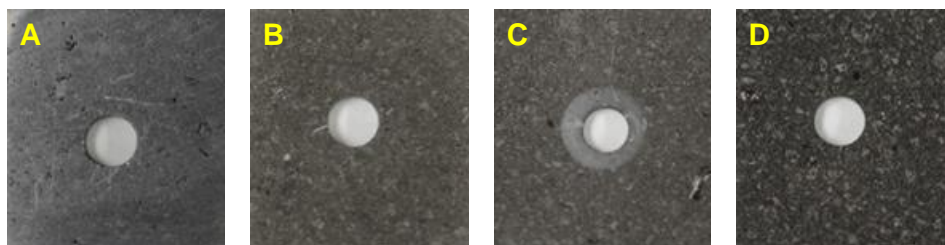


Figure 4.19: Graphite samples exposed to different CO_2 environments after 400 hours: Untested (A), 650°C RG (B), 650°C (C) 100ppm oxygen doped RG, 750°C RG (D).

In order to prove both mechanisms Secondary Ion Mass Spectroscopy (SIMS) analysis was completed on a $300\mu\text{m}^2$ area as a function of depth (sputtered using Cs^+ ions) through a Haynes 625 sample exposed to RG CO_2 , as well as 1%CO- CO_2 at 750°C, 20MPa for 1,000 hours. The carbon depth profile for the two conditions is given in Figure 4.20.

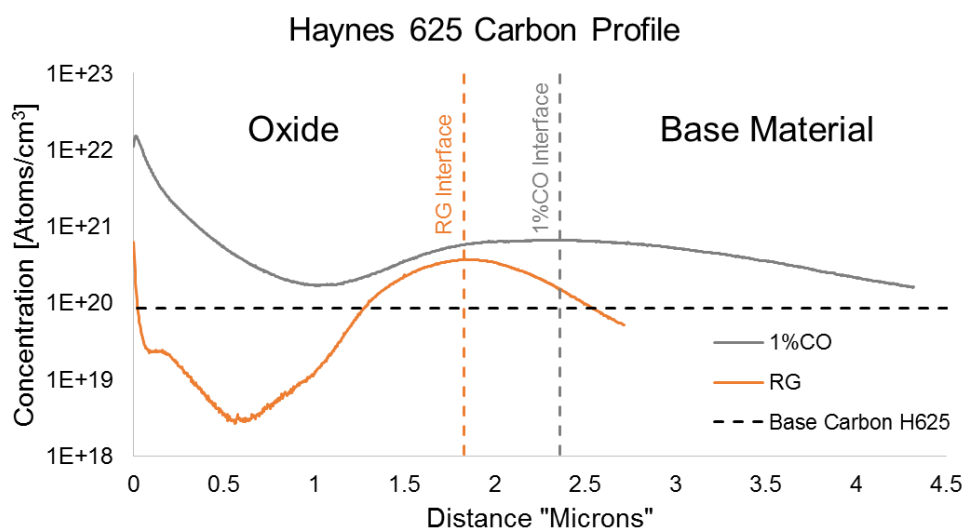


Figure 4.20: SIMS carbon profile for Haynes 625 exposed to CO_2 for 1000 hours at 750°C in RG and RG with 1% CO.

Figure 4.20 shows that both RG and CO mixed CO_2 conditions deposited carbon at the interface between the oxide and base material, and was about two times larger in the RG + 1%CO environment. This local maximum in the curve corresponds to the formation of

carbides. Carbon was also observed throughout the oxide in the 1%CO environment which is an indication of the precipitation of carbon through the Boudouard Reaction. Little to no carbon was observed in the oxide produced in the RG CO₂ environment and is most likely due to concentration limitation of CO during cool-down. The CO concentration in the RG environment (estimated to be by 1-100ppm) is much lower than the 1% CO condition which is forced to maintain a constant concentration of CO by the feed gas.

4.4 Altering pO_2 and a_C to Control Defect Concentration Leading to the Production of a Stoichiometric Oxide

It was previously discussed in Chapter 2.7.2 that the formation of a stoichiometric oxide could lead to a more protective and compact oxide with fewer voids. It has been theorized that non-stoichiometric oxides produce an increased number of voids due to vacancy annihilation or coalescence [58]. Void production is reduced in stoichiometric oxides due to the minimization of the total vacancy concentration. By using defect equilibrium equations discussed in Chapter 4.4 above, the pO_2 required to balance the chromium and oxygen vacancies (therefore minimizing) is given in Equation 4.12.

$$pO_2 = \frac{(k_i)^2(k_{red})^{4/15}}{(k_{ox})^{2/3}} \quad (4.12)$$

The equilibrium constants in Equation 4.12 vary considerably based on large predictive accuracy errors. These constants are further invalidated when deviation from pure Cr composition to commercial alloys is considered. It is therefore very unlikely that a pO_2 value could be accurately predicted from theory, and in order to produce a stoichiometric oxide with low void fraction, experimental data needed to be collected. This was attempted by using SEM to study the oxide morphology grown on pure Cr and Haynes 625 given in Figures

4.12 and 4.21 respectively. As it appears, RG conditions are relatively close to the stoichiometric conditions predicted by [56], [65], [66]. This could be the reason why lower porosity and more protective characteristics are observed in RG conditions and deviation from this environment is highly destructive. The void network can be observed in the mixed CO₂ conditions, but not in RG for chromia grown on alloy Haynes 625 in Figure 4.21. Similar results were found on pure chromium exposed to RG and 1%CO-CO₂ in Figure 4.12. The protective behavior in RG CO₂ is extremely useful as it indicates that pure CO₂ is quite possibly the best oxidizing environment at this temperature for corrosion of chromium rich alloys. Any addition of other gaseous species would only enhance the oxidation and produce less protective oxides.

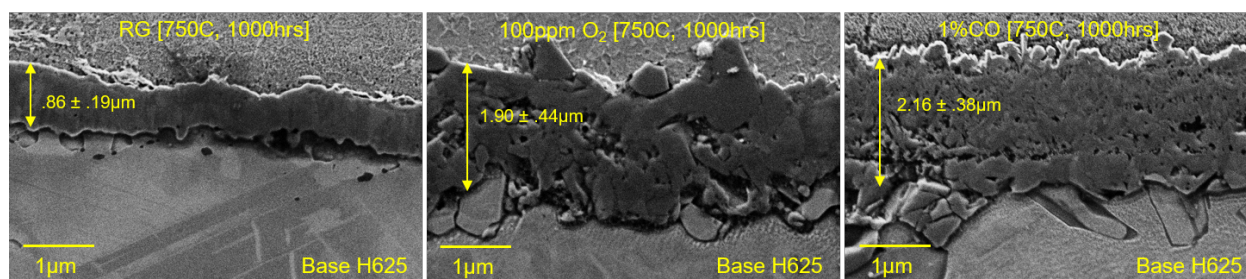


Figure 4.21: SEM cross-sectional imaging for oxides grown on Haynes 625 at 750°C/20MPa for 1,000 hours in RG, RG + 100ppm, and RG + 1%CO environments.

The growth of a compact oxide (possibly stoichiometric) on the surface of the Haynes 625 was very promising as it indicated that the depletion of Cr as well as the addition of other alloying and matrix elements had little effect on the growth of the oxide. In fact, it will be shown in subsequent sections that RG CO₂ is the best corrosion environment compared to CO₂ with added impurities for all commercial alloys tested. This would indicate the utility in monitoring and regulating gas composition to keep purity near RG conditions.

While the results in this document appear to indicate the growth of a stoichiometric oxide due to regulation of the pO₂, this process is likely a result of gaseous diffusion of CO₂ (dis-

cused in Section 4.2) instead of solid state diffusion of chromium and oxygen. It was shown in Sections 4.3 and 4.2 that carbon was found in both the oxide as well as between the M-O interface. Several studies have determined that solubility and diffusion of carbon through chromia is very low [67] and [68]. This would indicate that gaseous diffusion is involved during the corrosion process, and that the solid state diffusion model is not entirely accurate. While gaseous diffusion is accepted as the primary mode for transport through the oxide, the mechanisms for solid state diffusion still apply. It is theorized that gaseous diffusion through the oxide occurs through micro/nano-channels or other high diffusion pathways. In either case, the environmental pO_2 and the pO_2 which corresponds to the metal-oxide phase boundary are still set. This would indicate that the defect model would apply in localized regions throughout the oxide and mean that $RG\ CO_2$ is still likely to form a stoichiometric oxide layer, while the impurities mixed conditions would form an oxide with higher defect concentrations. The increase in defect concentration would lead to enhanced porosity, which would enhance gaseous diffusion, and other negative effects (carbon deposition). It is therefore useful to understand that while solid state diffusion might not explicitly influence the corrosion rate, it is a secondary effect, and appears to result in a significant effect on corrosion in $s\text{-}CO_2$.

Chapter 5

Connecting Corrosion Mechanisms From Model Alloys to Commercial Alloys

Now that several mechanisms of corrosion in CO_2 have been studied on pure Cr and Ni samples, it is important to relate to commercial alloys to understand the effect that trace elements have on corrosion. This has already been discussed slightly in the sections containing the SIMS profile and discussion of stoichiometric oxide production for Haynes 625. Additional discussion of Haynes 625 and a Ni-20Cr binary alloy will be discussed in this chapter.

5.1 Corrosion of Ni20Cr in sCO_2 Environments

Binary alloy Ni-20Cr was selected for testing due to the similar composition of most nickel chromium superalloys. This alloy was also of interest as it should combine the effects observed in the previous chapter of both pure nickel and chromium materials exposed to CO_2 . Testing was conducted at 750°C , 20MPa for a total of 1,000 hours in both RG and RG + 100ppm O_2 environments. The mass change measurements for these two conditions are given in Figure 5.1.

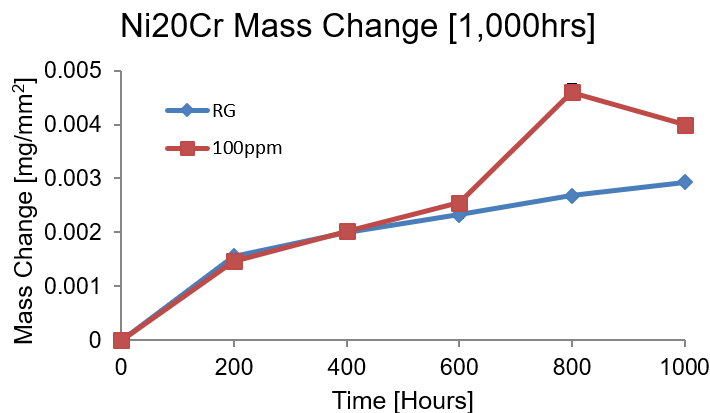


Figure 5.1: Mass change measurements of Ni-20Cr exposed to RG and RG-100ppm O₂ at 750°C for 1000 hours.

Initially, both samples appeared to gain a similar amount of mass through 600 hours. Then, a sudden spike in the samples exposed to oxygen rich CO₂ was observed at 800 hours followed by a sudden drop. The increased oxidation rates at 800 hours could be indicative of transition from chromium oxidation to nickel oxidation due to depletion of chromium at the M-O interface. Surface SEM and EDS line-scans have been conducted on these samples and is given in Figures 5.2 and 5.3 for RG and Figures 5.4 and 5.5 for oxygen rich testing.

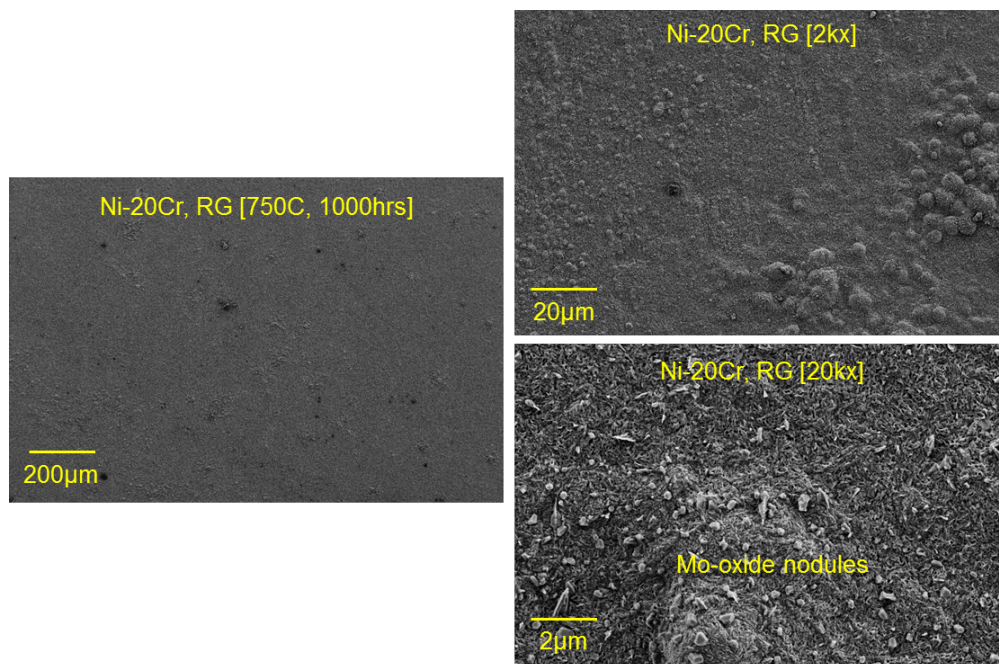


Figure 5.2: SEM micrographs for binary alloy Ni-20Cr exposed to RG CO₂ at 750°C for 1000 hours.

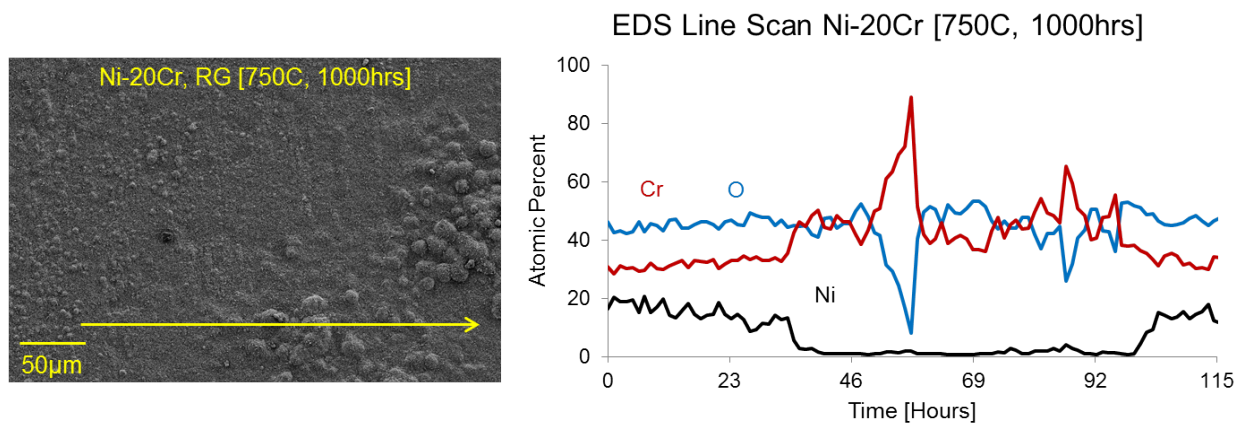


Figure 5.3: Surface EDS line scan for binary alloy Ni-20Cr exposed to RG CO₂ at 750°C for 1000 hours.

The oxide surface produced in RG CO₂ appears uniform with a few areas of ballooning or enhanced oxidation. EDS line scans reveal a thin chromium layer for the entire oxide (Ni signal is due to base material). Interestingly, at 20kx, small precipitation of Molybdenum rich oxide nodules were observed. These nodules are found on the surface of all samples exposed in the autoclave at temperatures above 700°C. This is due to the volatility of Mo-oxide which has been well studied and shown to occur rapidly at temperatures over 700°C [69]. Therefore, the small Mo rich nodules found on the surface would be caused by precipitation during cool-down which originated from either other samples or the autoclave, which contain high amounts of molybdenum.

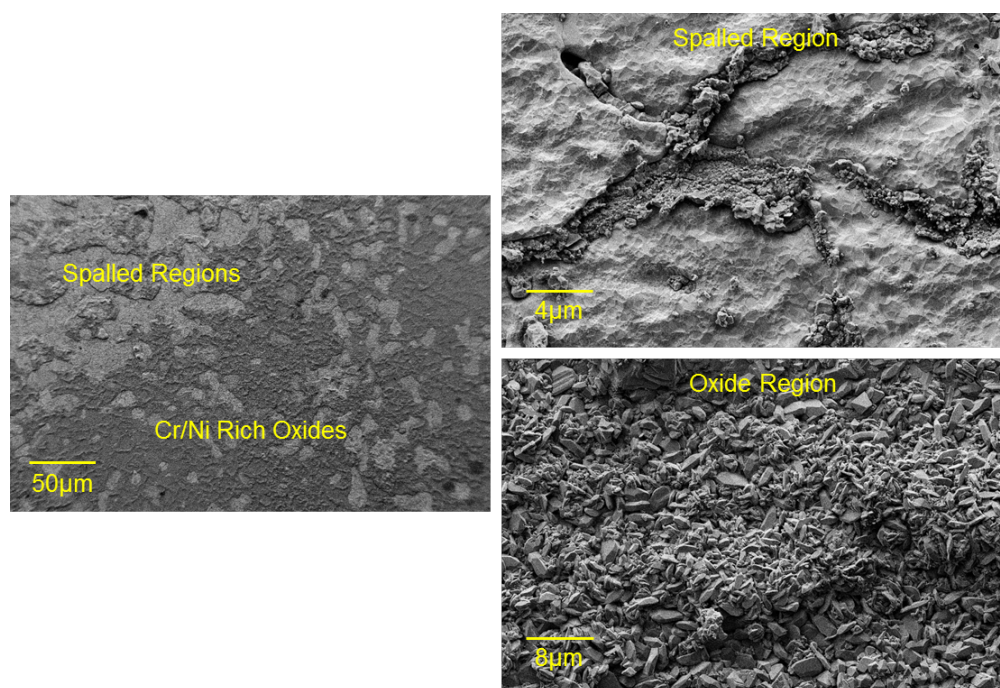


Figure 5.4: Surface SEM micrographs for binary alloy Ni-20Cr exposed to RG-100ppm O₂ at 750°C for 1000 hours.

Unlike the uniform surface found on the Ni-20Cr sample exposed to RG CO₂, the surface of the sample exposed to the oxygen rich environment contained large regions of spalled oxide, as well as ballooning on the surface. Closer examination of the spalled regions shows fracture

surfaces which are roughly the same size as the chromia grains with no subsequent oxidation. This would indicate exfoliation during the cool-down process when thermal stresses are largest.

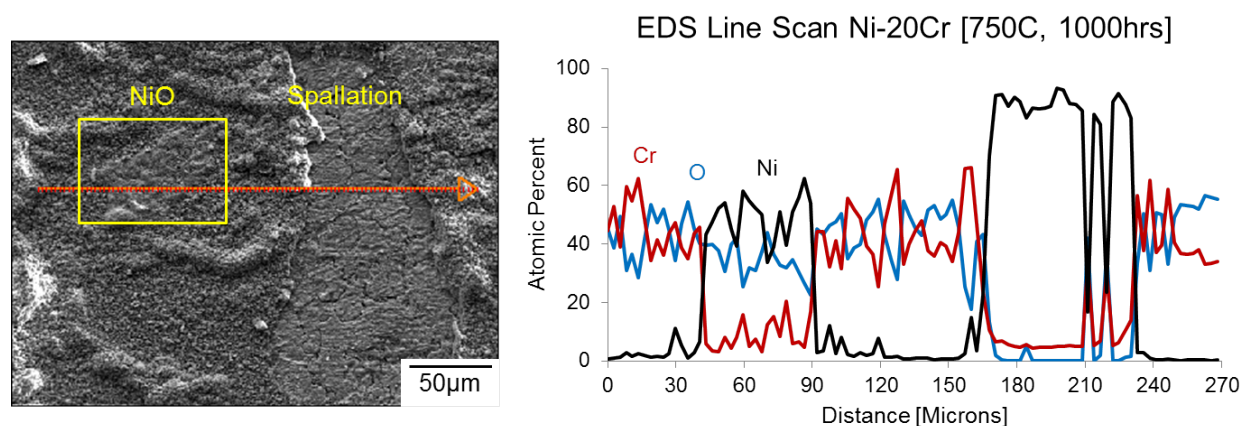


Figure 5.5: Surface EDS line scan for binary alloy Ni-20Cr exposed to RG-100ppm O₂ at 750°C for 1000 hours.

Figure 5.5 presents a line scan through the uniform oxide, an area of enhanced oxidation, as well as a spalled region. The uniform oxidation region contains pure chromia indicating protective oxide growth. The region of enhanced oxidation shows a strong signal for NiO which is likely due to the depletion of chromium and high pO₂ in this environment. Interestingly, the spalled region consists of almost pure Ni, which would indicate that the region below the oxide is almost completely devoid of chromium. If this is true, it would indicate that once Cr is completely consumed, Ni begins to oxidize which could then destabilize the adherence of the oxide and lead to exfoliation during cool-down of the system. Cross-sectional SEM and EDS is given in Figure 5.6 to further prove depletion of chromium in areas of nickel oxide formation.

The depletion of chromium is dictated by both the diffusion rate of chromium through the matrix, as well as the corrosion rate. This was discussed previously in Section 2.1.4. In this particular case, the reaction rate appears much faster than the diffusion rate of chromium,

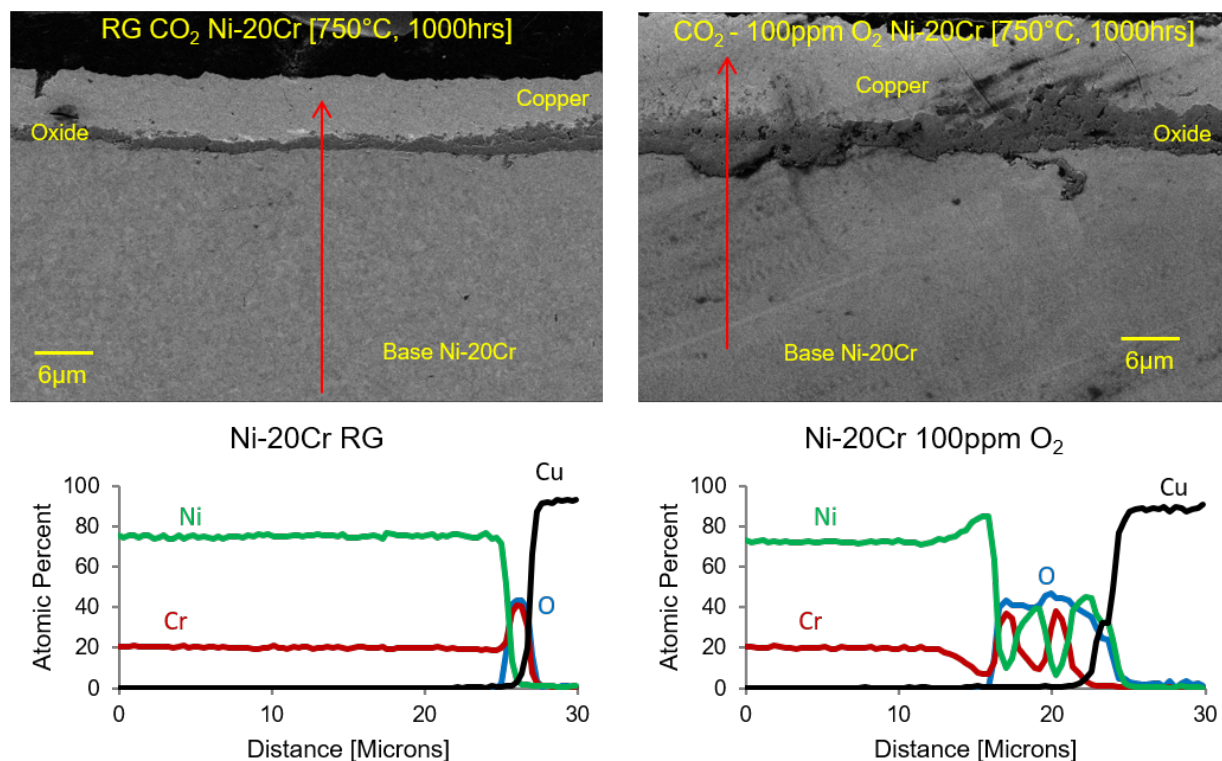


Figure 5.6: Cross-sectional EDS line scan for binary alloy Ni-20Cr exposed to RG and RG-100ppm O₂ s-CO₂ at 750°C for 1000 hours.

and therefore a large depletion of chromium is observed. If exfoliation of the oxide does not happen, it would be reasonable to assume that chromium would be able to re-saturate beneath the oxide as the diffusion length through the oxide would increase (corrosion rate decreases) with oxide thickness. This would indicate that nickel oxide formation could be a meta-stable behavior caused by saturation of oxygen in the system. In the RG system, no depletion is observed, which would indicate the reaction rate was never fast enough compared to the diffusion rate of chromium for depletion. It will therefore be necessary to see if minor alloying elements can decrease the corrosion rate, or increase the diffusion of chromium in commercial alloys to prevent the formation of nickel oxides.

Comparing the results of Ni-20Cr to pure Cr, pure Cr oxidized about three times faster in

RG conditions, which indicates that the nickel matrix does in fact slow the diffusion of Cr to the M-O interface and therefore inhibits the corrosion. This is also evident from the depletion of Cr in the spalled regions (depletion of Cr is not possible on pure Cr samples). If the pO_2 is high enough to oxidize Ni, the interface is more susceptible to attack and enhanced corrosion, which is seen in the 100ppm environment where a near breakaway condition appears to be reached before eventual scale exfoliation. The enhanced oxidation and spallation in the oxygen rich environments indicates that any added oxygen impurity could be detrimental to alloy compatibility in CO_2 environments.

5.2 Corrosion of Haynes 625 in sCO_2 Environments

Commercial alloy Haynes 625 was selected for additional study due to its low cost, availability, and high industrial interest. Before performing any corrosion studies, the as received material was analyzed in order to understand the composition, micro-structure, and phases present. The material was received in plate form from Haynes directly and was solution annealed at $1050^\circ C$ before being quenched to room temperature. The composition of this alloy is given in Table 5.1.

Table 5.1: Composition of as received Haynes 625.

	Si	P	Mn	C	Cr	Ni	Mo	Nb	Co	Fe	Al	Ti
Atom %	0.25	0.006	0.26	0.02	21.89	Bal	8.59	3.51	0.28	5	0.22	0.29

The nickel and chromium concentration of this alloy is similar to the Ni-20Cr alloy discussed previously with the exception of large quantities of Mo, Nb, and Fe. Haynes 625 (H625) utilizes niobium to form γ'' , and solid solution molybdenum for high temperature strength. This alloy has been shown to exhibit excellent corrosion resistance at temperatures up to $980^\circ C$, due to its relatively high Cr content. However, delta phase precipitation (a Ni_3Nb phase that precipitates as disk-shaped morphology) is known to form at temperatures

exceeding 600°C resulting in long term embrittlement. Long-term aging effects such as carbide formation (from bulk alloy carbon), γ'' , and delta phases precipitation can be found in the TTT diagram in Figure 5.7 [70].

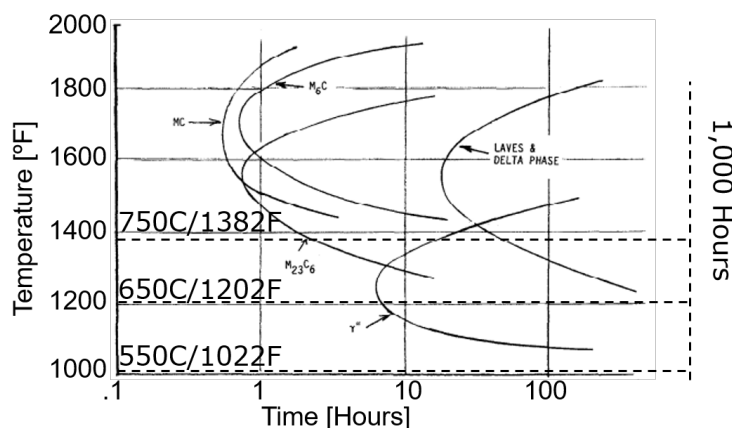


Figure 5.7: Time-Temperature-Transformation Plot for Haynes 625 [71]

In order to determine grain size, as well as which phases were present in the as received alloy, SEM, EDS, and etching techniques were used. Haynes 625 was etched using HCl-2% H_2O_2 by submergence for 10 second intervals until grain boundaries were visible under light microscopy. A summary of the grain structure as well as phase precipitation in the as received samples is given in Figure 5.8.

No delta phase was observed in the as received samples of H625 which is a result of the high annealing temperature which would dissolve any of this phase before being quickly quenched through the temperatures needed to form delta phase. Some titanium rich carbides were formed in the material during creation, and can be observed by the EDS mapping as well as the corresponding line-scan.

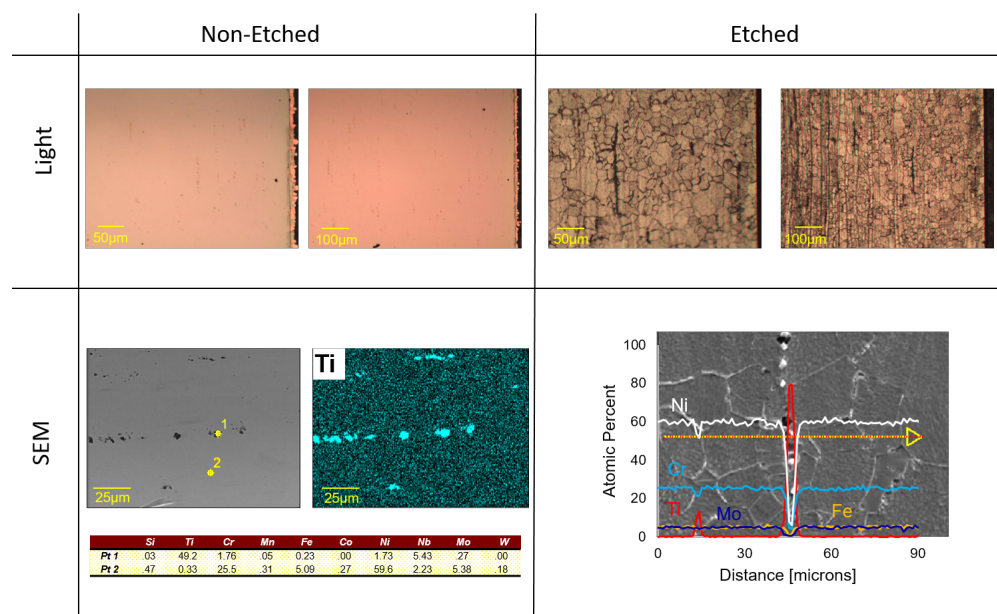


Figure 5.8: SEM,EDS, and light microscopy characterization of as received Haynes 625.

5.2.1 Haynes 625 Delta Phase Embrittlement

While this alloy is highly attractive to industry for use in high temperature power cycles, it should be noted that delta phase embrittlement has been identified as a major issue for long term use. Since this alloy is being considered for implementation, it is therefore necessary to characterize the effects of delta phase precipitation before studying the corrosion effects of CO₂. A few papers have been published on delta phase precipitation in H625 during long term aging processes. The temperature dependence on precipitation as well as the yield stress is plotted for Haynes 625 aged from 600-900°C for 500 hours is given in Figure 5.9 [72]. The second data set indicates an intermediate aging step at corresponding temperatures for 5 hours.

The maximum effect of delta phase precipitation appears to exist between aging temperatures of 700 and 750°C. The increase in yield stress of 50% would suggest an corresponding decrease in ductility, which can lead to brittle fracture mechanisms. Haynes 625 was tested

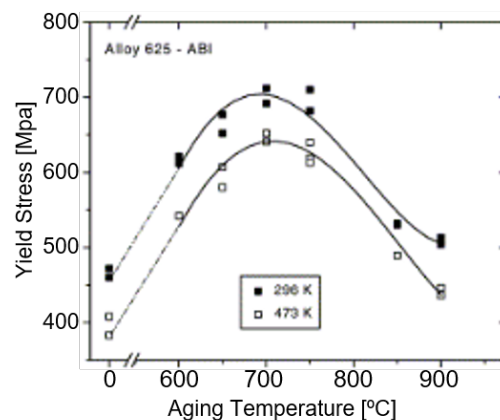
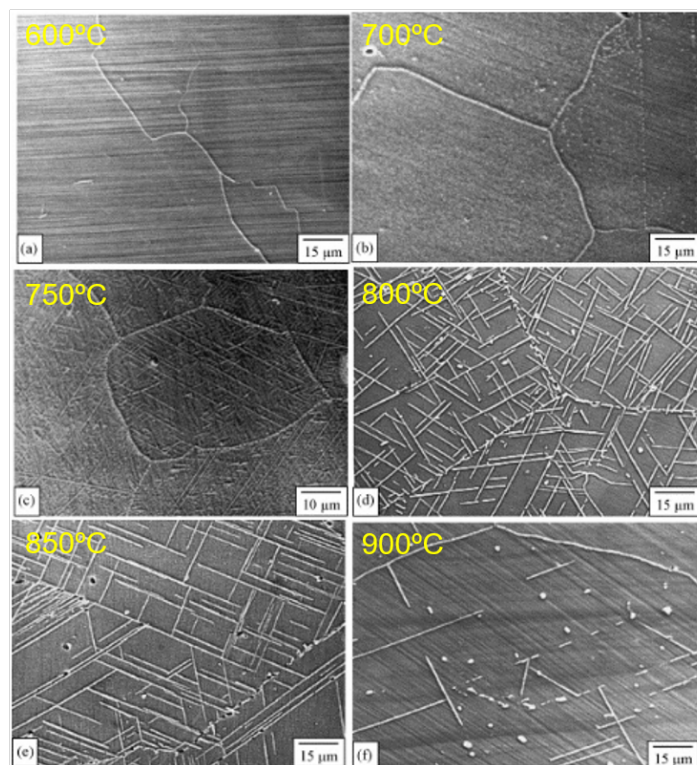


Figure 5.9: SEM images of delta phase precipitation in alloy Haynes 625 for various temperatures (Left). Yield stress for aging of alloy Haynes 625 for select temperatures (right) [72].

in this work at 550, 650, and 750°C, and has been etched to observe delta phase precipitation. SEM images showing delta phase precipitation due to heat treatment during CO₂ testing are given in Figure 5.10. Delta phase appears as elongated precipitates in the images.

The SEM images of delta phase have good agreement with literature, showing that the highest concentration of delta phase occurs at 750°C followed by 650°C, and no precipitation at 550°C. Since corrosion samples were used, no tensile testing could be conducted on the post exposure H625 samples. Instead, micro-hardness measurements were used. Micro-hardness measurements were taken as a function of depth from the oxide in order to determine if corrosion also caused any softening or hardening of the material. Each plotted data point represents 4 measurements taken at a plane parallel to the oxide, and are in accordance

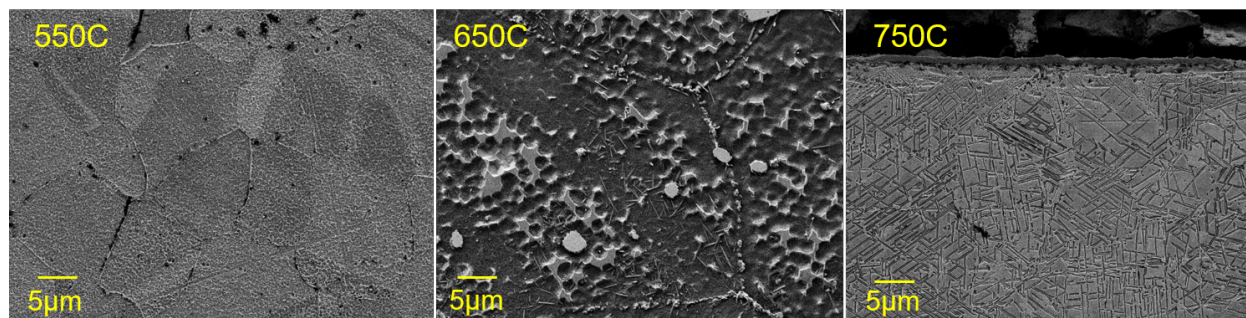


Figure 5.10: Delta phase precipitation on Haynes 625 exposed to CO_2 from 550-750C for 1,000 hours. Etched using $\text{HCl} - \text{H}_2\text{O}_2$.

with ASTM-E92 standards. Hardness profiles for each environment and temperature are plotted in Figure 5.11.

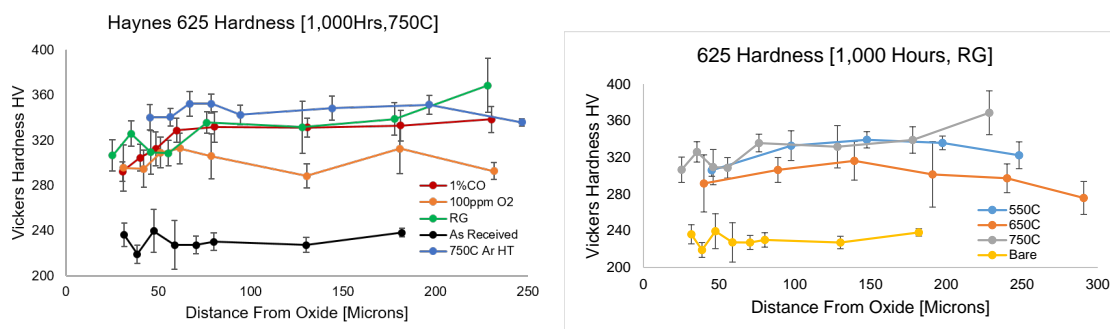


Figure 5.11: Hardness measurements as a function of depth from the oxide for alloy Haynes 625 exposed to different CO_2 environments (left) and temperature (right).

Hardness measurements indicate that corrosion had very little effect on material hardening, but was increased by similar amounts in every test from the as received material. By revisiting the TTT diagram for Haynes 625, it can be observed that carbide precipitation occurs at all of the temperatures listed, and most likely is the cause for the hardness increase. While delta phase appears to have no effect on the hardness of the alloy, it was shown in the literature to effect yield stress which isn't captured in the methodology used in this study. The SIMS profile for H625 was presented earlier to show carbon deposition mechanisms in

Figure 4.20. The increased carbide formation near the oxide is also not captured in the hardness profile due to the limited depth of carburization ($< 5\mu m$).

It is the opinion of this author that Haynes 625 should not be used at temperatures above 600°C as indicated by the manufacture due to precipitation of delta phase. Since this opinion is not shared with many industry members, it was decided to characterize the compatibility in s- CO_2 .

5.2.2 Corrosion of Haynes 625 in s- CO_2 Environments

Haynes 625 was tested in several s- CO_2 environments ranging from $450\text{-}750^{\circ}\text{C}/20\text{ MPa}$ for 1,000 hours in RG CO_2 and impurities mixed (100ppm O_2 , 1% CO) RG CO_2 at 750°C . The time dependent mass change results for all conditions are given in Figure 5.12. Error bars representing the standard deviation between mass change of the samples at each time interval have also been reported, but are very small relative to the total mass change experienced by the coupons.

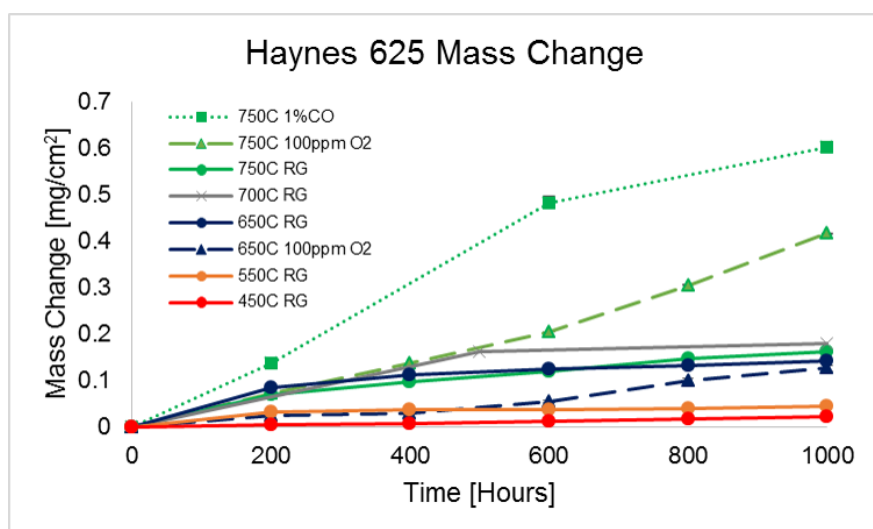


Figure 5.12: Mass change measurements of Haynes 625 exposed to CO_2 environments for 1000 hours.

Mass change results show that Haynes 625 experienced very little corrosion when exposed to RG CO₂. The mass change increased as a function of temperature, with the exception of 700 and 750°C in RG CO₂. This deviation from normality will be discussed later. The samples exposed to impurities mixed CO₂ showed the highest mass change with 1%CO gaining the most mass followed by 100ppm O₂ mixed CO₂. The oxygen rich environment appeared linear after an initial time, which has been theorized to be the initiation of nickel oxidation (discussed previously) due to depletion of chromium. SEM cross-sectional imaging for several of the conditions is given in Figure 5.13.

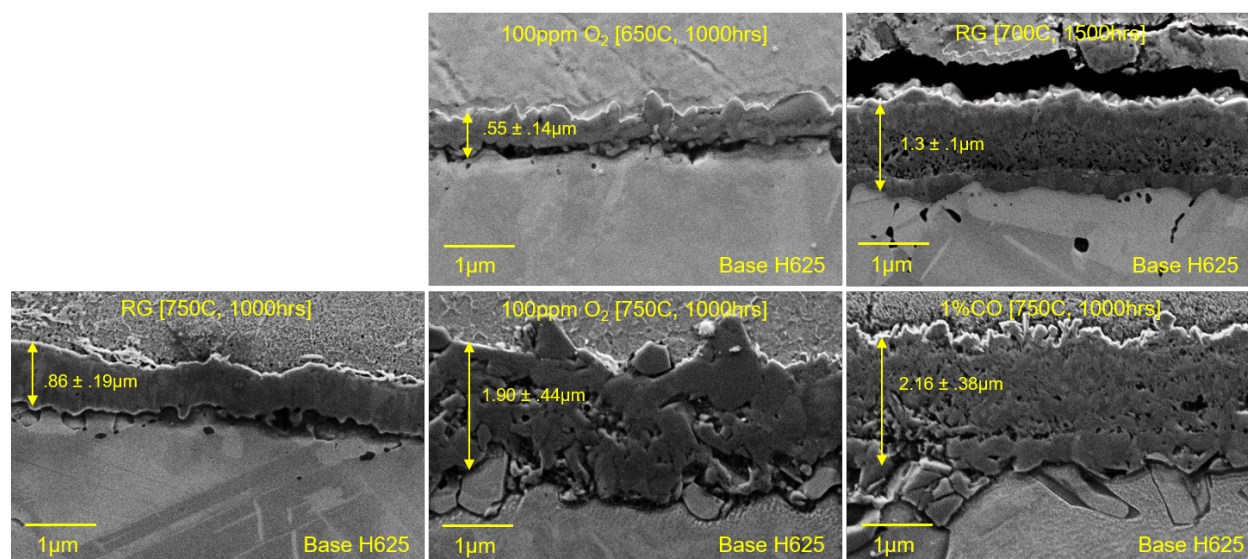


Figure 5.13: Cross-section SEM micrographs for alloy Haynes 625 exposed to various CO₂ environments.

Thickness measurements of the oxide given in the SEM images shows a good correlation to the mass change measurements presented previously. This would indicate that the majority of the mass gained by the sample is through the oxide and not through carbon deposition (either mechanism). The composition of each oxide was found using EDS line-scans for RG, RG + 100ppm O₂, and RG + 1%CO given in Figures 5.14, 5.15, and 5.16 respectively.

The oxide grown on Haynes 625 in RG CO₂ was found to be chromium rich with very

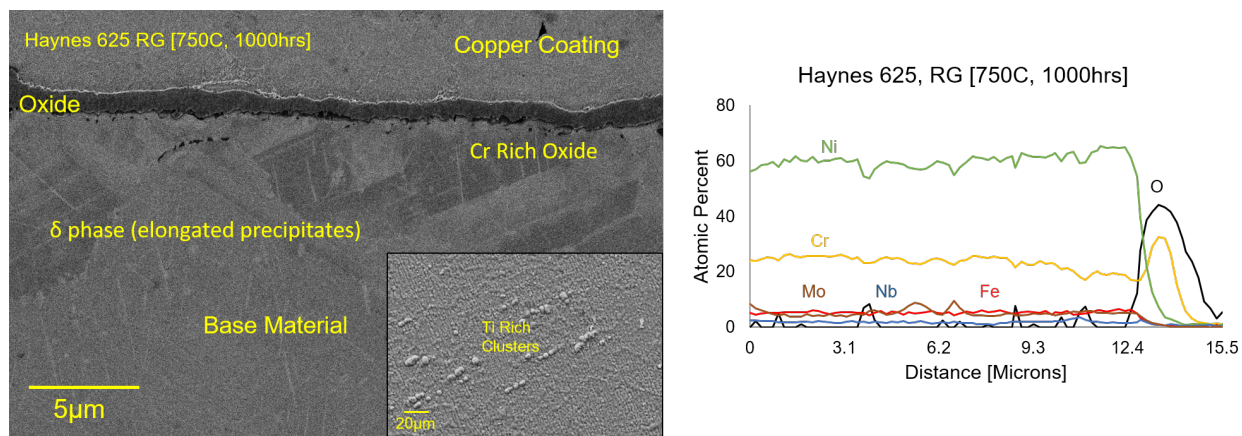


Figure 5.14: EDS line scan for Haynes 625 exposed to RG CO₂ at 750°C for 1000 hours.

little depletion of Cr below the scale. This oxide was thin, and exhibited a uniform grain growth. This is contrasted by the oxide grown in oxygen mixed CO₂ which experienced a very different morphology, and was composed of Cr, Mn, Ni, and Fe shown in Figure 5.15.

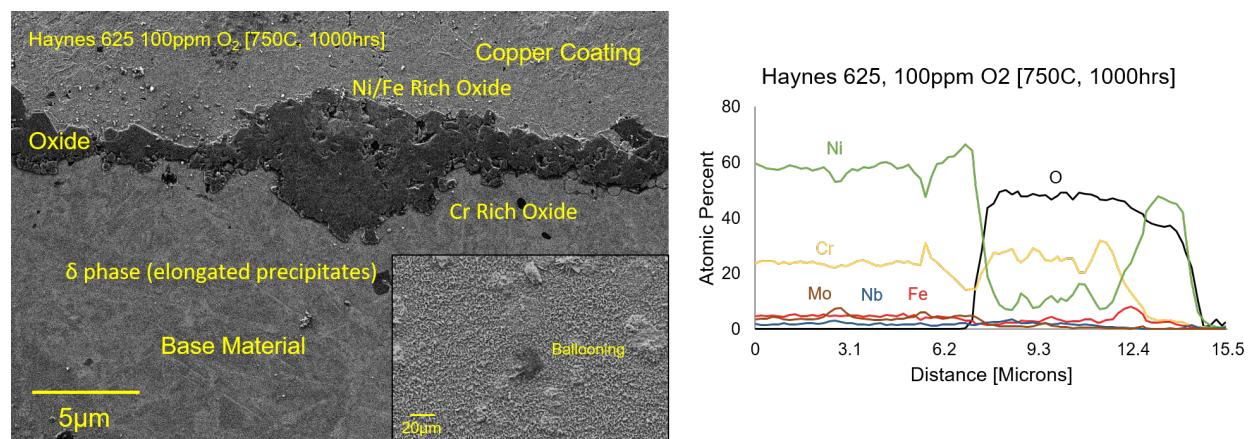


Figure 5.15: EDS line scan for Haynes 625 exposed to RG CO₂-100ppm O₂ at 750°C for 1000 hours.

The oxide grown in oxygen rich CO₂ contained large nodules all over the surface, which were determined to be areas of nickel oxidation as well as enhanced chromium oxidation (EDS line-scan). This was also observed in the oxidation of the Ni-20Cr binary alloy previously, and was concluded to lead to eventual exfoliation of the oxide in these regions. A large

chromium depleted region was also found below these nodules, as predicted earlier. Very little nickel oxide was found on the surface of sample exposed to RG CO₂, which is believed to be due to kinetic limitations which were not present in the oxygen rich environments. Large surface nodules were also observed on the surface of samples exposed to RG CO₂ with 1%CO, but the cross-sectional morphology is vastly different. An example is given in Figure 5.16.

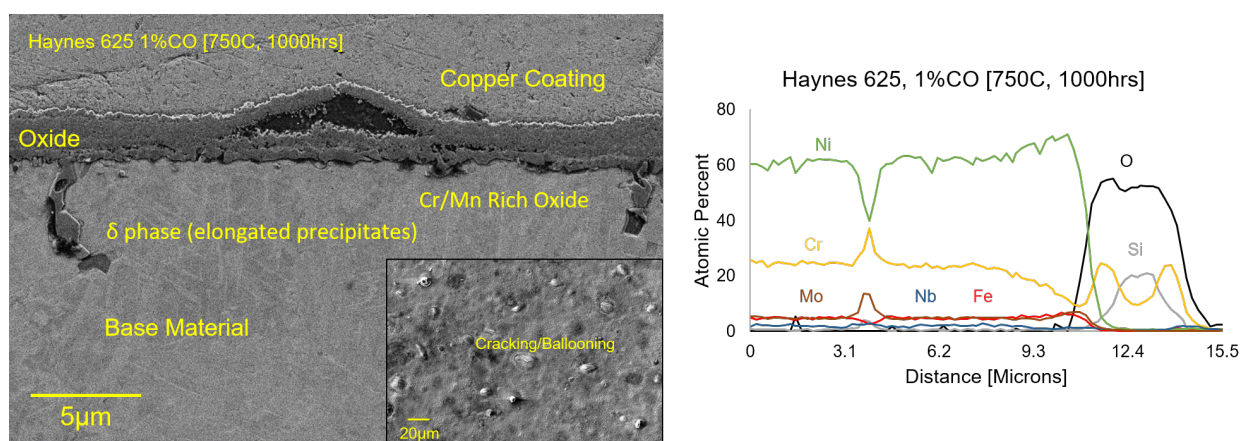


Figure 5.16: EDS line scan for Haynes 625 exposed to RG CO₂-1%CO at 750°C for 1000 hours.

It was observed that the nodules on the surface of samples exposed to CO rich CO₂ also exhibited cracking. The composition of oxide was found to be chromium rich (the silicon peak corresponds to polishing media left in the cracked regions). This oxide also contained high porosity and two distinct layers. The duplex oxide is more easily observed in Figure 5.17 which shows the oxide at 200 and 1000 hours.

The ratio of the thickness two layers observed in Figure 5.17 grows evenly as a function of time. The innermost layer appears to consist of an equiaxed region, and the outer oxide layer consists of smaller grains with a large amount of porosity. This mirrors the discussion of the growth of stoichiometric chromia in Chapter 4.4 and the oxide layers produced on pure chromium in RG and RG + 1%CO given in Figure 4.12 previously. This would indicate that

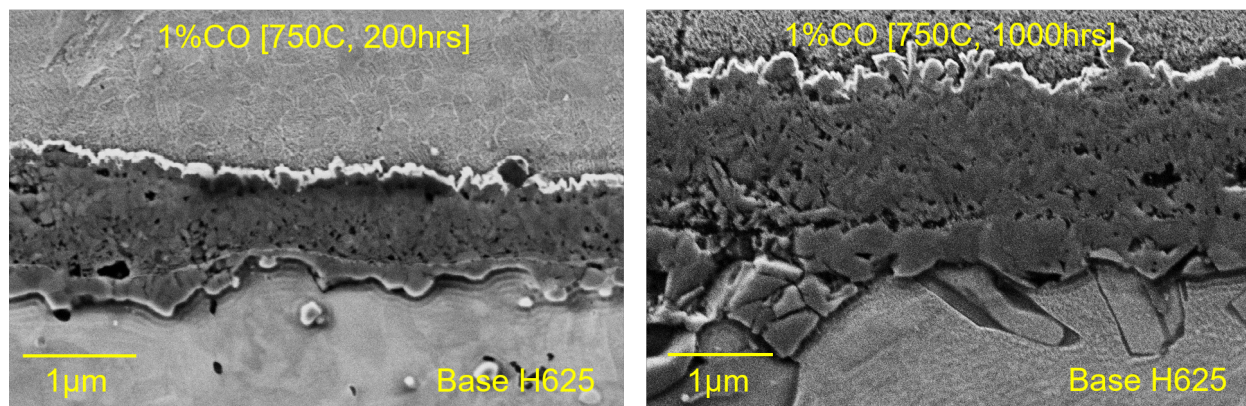


Figure 5.17: Cross-section SEM micrographs for alloy Haynes 625 exposed to RG CO₂-1%CO at 750°C for 200 hours (left) and 1000 hours (right)

the defect concentration in 1%CO mixed CO₂ at 750°C are probably far from equilibrium, and therefore, produced a voided region due to defect annihilation or coalescence. Interestingly, the Haynes 625 sample exposed to 700°C RG CO₂ also exhibited the duplex oxide morphology (Figure 5.13). This would indicate that the temperature, and therefore chromium mobility play an important role in the formation of a stoichiometric oxide. It can then be concluded that the pO₂ needed to form a stoichiometric oxide at 700°C is very different than that found in 750°C CO₂. Further studies on this phenomenon would need to be completed in order to fully characterize the pO₂ needed at each temperature and alloy for the formation of a stoichiometric oxide. The presence of porosity throughout either oxide is concerning as it has been theorized that voids or pores can lead to micro-environments which lead to carbon deposition [26].

Two carbon deposition mechanisms were discussed previously, one of which relied on high CO concentration during temperature transients which would cause precipitation of carbon due to CO₂ equilibrium changes. This effect should be enhanced if there is added volume and surface area throughout the oxide (porosity). The other carbon deposition mechanism was for carburization of the base material due to treating the oxide as a diffusion barrier.

The SIMS profile for carbon through the oxide and base material for RG, RG + 100ppm O₂, and RG + 1%CO is given in Figure 5.18. Unfortunately, it is believed that the sputtering profile for the oxide in RG + 100ppm O₂ was conducted through one of the nodules, and therefore the M-O interface was not sampled.

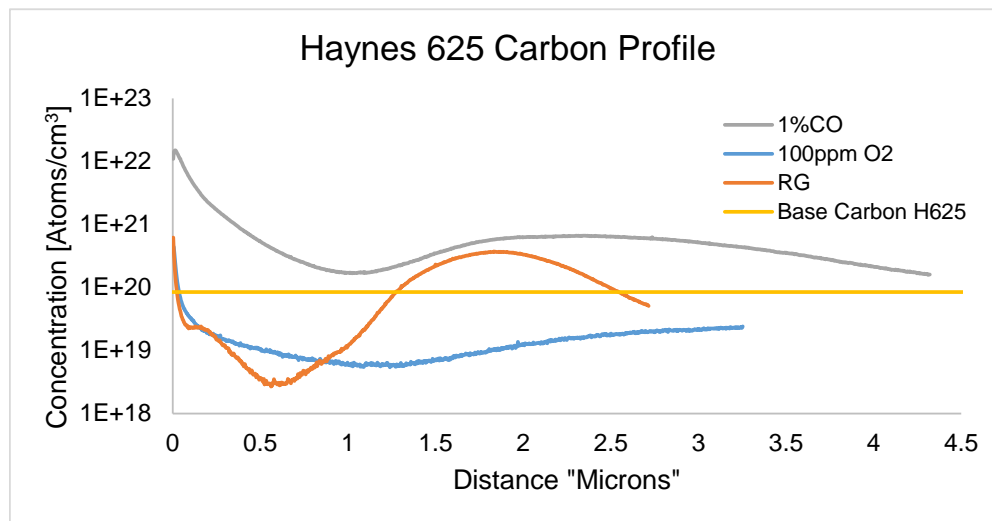


Figure 5.18: SIMS carbon profile for Haynes 625 exposed to CO₂ for 1000 hours at 750°C in RG, RG with 1% CO, and RG with 100ppm O₂.

The SIMS profile was discussed previously in regards to carbon deposition. Another way to observe carbon bonding is by using raman spectroscopy. This method can be used to map an entire region with high resolution using a correlative peak matching to carbon (1350, 1525cm⁻¹) and oxide (400-800cm⁻¹) bonding. The spectral results for oxides grown on Haynes 625 in RG + 100ppm O₂ and RG + 1%CO are given in Figure 5.19.

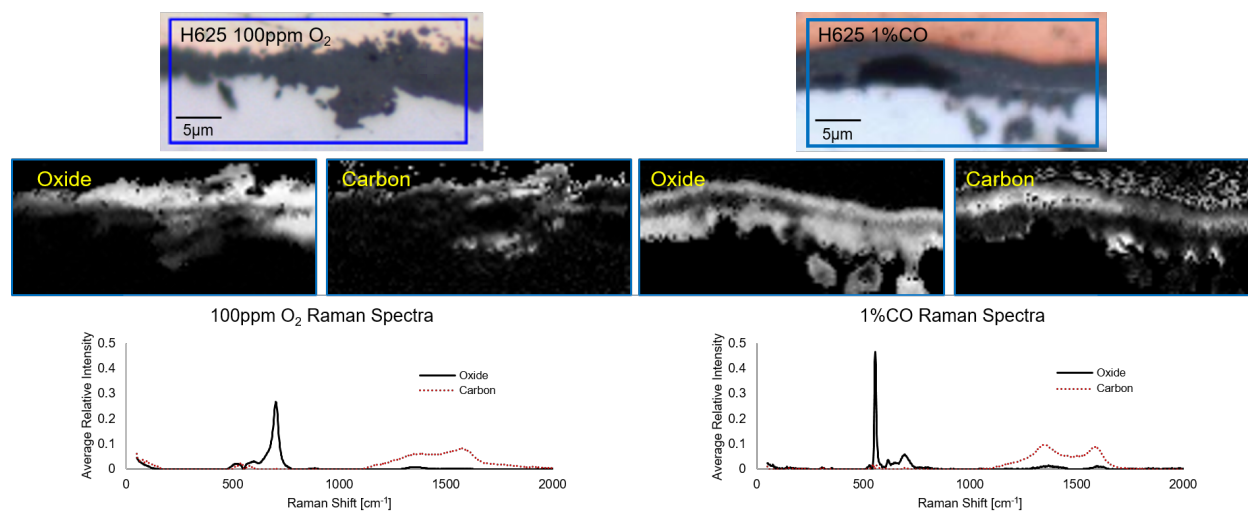


Figure 5.19: Raman mapping of Haynes 625 exposed to RG CO₂-100ppm O₂ (left) and RG-1%CO (right) at 750°C after 1000 hours.

The raman spectra show strong correlation (white regions) for carbon throughout the oxide found in the sample exposed to CO rich CO₂. The carbon regions in the oxygen rich environment are primarily found directly above and below the oxide, which was attributed to signal noise, and the mounting procedure. Raman mapping for the sample exposed to RG CO₂ found little correlation to carbon bonding, so it was not included. EDS mapping was also conducted on the cross-section of the oxides in each environment, and are given in Figure 5.20.

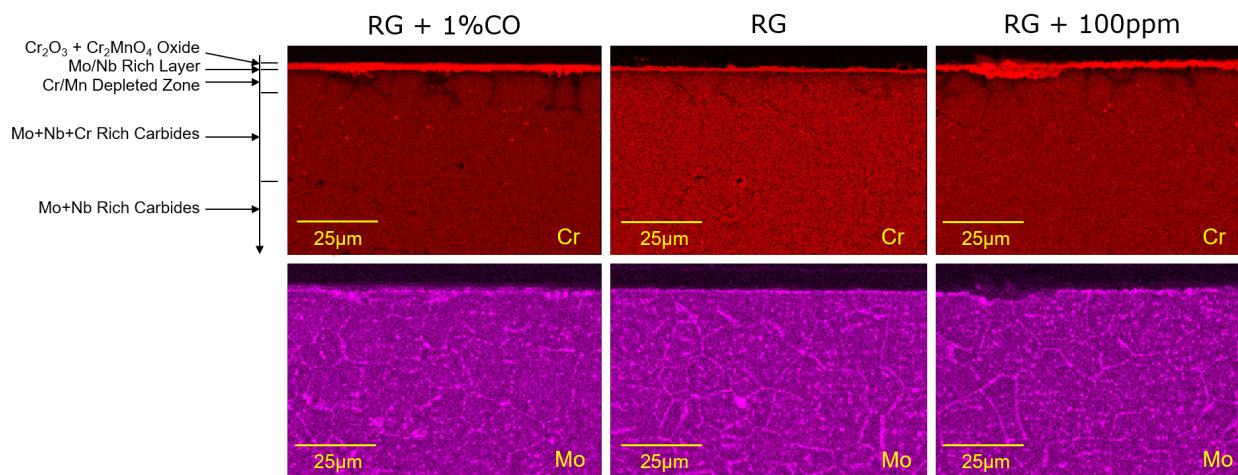


Figure 5.20: EDS mapping of Cr and Mo for alloy Haynes 625 exposed to CO_2 environments at 750°C for 1000 hours.

EDS mapping of the Haynes 625 samples shows a Cr depleted zone directly underneath the oxide, which corresponds to enrichment of molybdenum. This could indicate precipitation of a molybdenum rich intermetallic phase, or that the carburized region consists of carbides that are molybdenum rich. While molybdenum carbides are similar in Formation Energy, the depletion of chromium would cause an increase in favorability of the molybdenum carbide phase precipitation in this region. This would be one area of improvement on the thermodynamic model presented earlier as only chromium was considered for the phases. Once the chromium in Haynes 625 reaches bulk concentration below the oxide, chromium rich carbides occur. It is believed that these carbides are caused by heat treatment of the material, and not from the environment since increased carbon concentration was not observed past a maximum of roughly 5 microns below the oxide. This is further supported by the presence of chromium carbides in the oxygen rich environment which should not have experienced carburization between the M-O interface.

If the carbon deposited in 1%CO oxide occurs during cool-down, it is reasonable to assume that the same carbon would be liberated in the form of CO during steady state operation

(750°C). This was shown previously through the Boudouard Reaction. The formation of CO gas in the oxide would lead to volume expansion and the resulting stresses in the oxide which could enhance cracking. This is contrasted to the cracking which is typically a result of the compressive stress during cool-down due to differences in the thermal expansion coefficient of the metal and oxide. In order to test which cracking mechanism is most likely, surface SEM of the 200 hour sample was compared to the 600 hour sample (given in Figure 5.21).

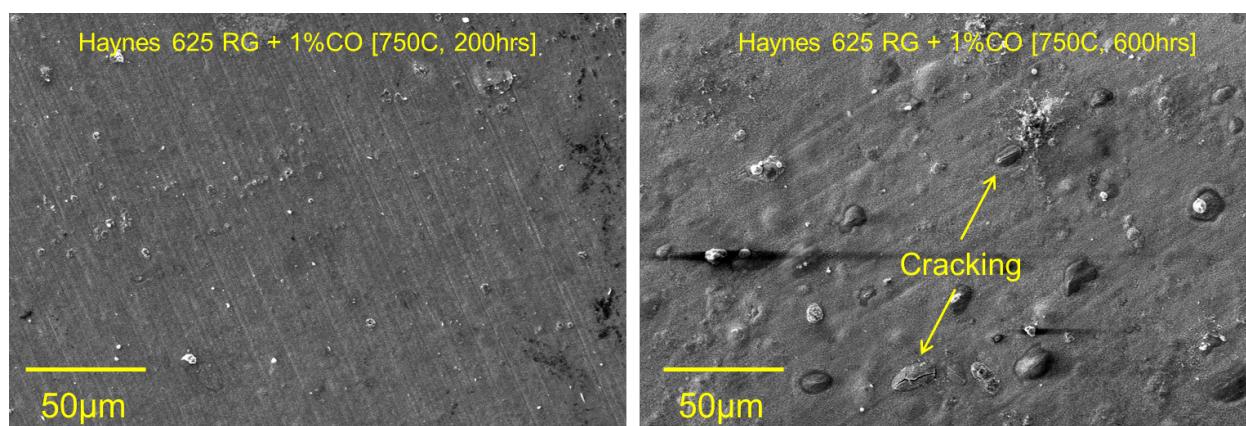


Figure 5.21: SEM imaging of oxide cracking on the surface of Haynes 625 exposed to 1%CO-CO₂ environments at 750°C for 200 (Left) and 1000 hours (Right).

The 200 hour sample would have experienced cool-down once, but never experienced carbon monoxide liberation during subsequent testing, and the oxide showed no evidence of cracking. The 600 hour sample would have one cycle of carbon liberation, and did experience oxide cracking. This could be refuted by the fact that the oxide is thicker at the longer time scale, but thicker chromium oxides have been observed on many samples without the presence of cracking similar to what is observed in the 1%CO conditions. Cracking of the oxide also increases bulk transport of the environmental CO₂ to the base material since the oxide is no longer acting as a diffusion barrier. This explains the enhanced thickness and mass change measurements found in the CO rich environment.

5.3 Summary - Connecting Corrosion Mechanisms From Model Alloys to Commercial Alloys

Conclusions for Model to Commercial Alloy Mechanisms:

- Chromium preferentially oxidizes to produce a protective oxide until depletion reaches a certain point in which nickel oxide will form. This leads to decreased adhesion of the scale, and enhanced corrosion.
- Ni-20Cr experienced a lower corrosion rate than pure Cr due to the Ni matrix slowing Cr diffusion, while Haynes 625 exhibited the lowest corrosion rate presumably due to minor alloying elements such as Mn stabilizing the oxide.
- Carbon deposition mechanisms are observed in Haynes 625.
- Oxide cracking observed after the 600 hours of exposure in 1%CO-CO₂ indicate carbon monoxide formation during ramp rates leading to expansive stress on the oxide.
- Carburization of base material is limited to the first few microns.
- RG CO₂ appears to produce most protective oxidizing environment at 750°C as NiO cannot form (due to kinetic limitations), and carbon is not deposited through the oxide due to saturation of CO during cool-down.

Chapter 6

Industrial Compatibility of Materials in CO₂

Environments

The motivation of this research was to be able to apply the knowledge learned to help design future s-CO₂ Brayton Cycle components. It is therefore important to conduct testing with industrial practicality in mind. For example, industry will not use highly pure CO₂ as the cost is too high. The goal of constructing any plant would be to minimize the cost of construction, and therefore it is also very likely that many different commercial alloys will be used. Because of this, testing was conducted using IG CO₂, and additional commercial alloys were exposed to each condition both of which are presented in this section as a summary of results.

6.1 Research Grade vs. Industrial Grade Testing

All of the aforementioned results have been conducted using highly pure research grade CO₂ mixed with impurities at high accuracy to ensure no other contaminants could effect the corrosion mechanisms being studied. Unfortunately, due to the cost difference between research and industrial grade gases, it would be highly unlikely that RG CO₂ would be used in the Brayton Cycle plants. Since application is one goal for this research, it was crucial to test industrial grade (IG) CO₂ to determine if any observable differences occur. IG testing was conducted at 550, 650, and 750°C at 20 MPa. RG testing was used as a baseline comparison.

In order to get an initial screening of the differences between RG and IG testing, mass change measurements for each test were compared. A summary of the longest exposure

time for IG and the corresponding mass change for RG is given in Table 6.1. In order to compare the two measurements, percent difference measurements were calculated as well as the absolute value of the difference.

Table 6.1: Comparison of mass change of commercial alloys exposed to RG and IG s-CO₂ for temperatures between 550-750°C at 20MPa for 600 or 1,000 hours.

	550C (600hrs)			650C			750C		
	IG	RG	% Diff	IG	RG	% Diff	IG	RG	% Diff
T92									
347	2.0E-04	1.3E-03	85	1.2E-03	3.5E-04	-229 (Excluded)			
316L	3.2E-04	1.1E-03	70						
310S	1.7E-04	4.4E-04	61	7.7E-04	2.2E-03	65	2.5E-03	1.9E-03	-34
800H				2.2E-03	1.3E-03	-69			
H718	2.6E-04	7.3E-04	65	8.8E-04	1.2E-03	29	2.7E-03	3.1E-03	15
H625	1.9E-04	3.9E-04	50	6.3E-04	1.4E-03	56	1.7E-03	1.6E-03	-3
H230	1.8E-04	4.5E-04	59	5.9E-04	5.2E-04	-13	1.5E-03	1.1E-03	-39
617	1.5E-04	4.1E-04	63	1.3E-03	2.0E-03	37	2.2E-03	2.8E-03	23
740H				8.6E-04	8.6E-04	0	2.5E-03	2.9E-03	14
H282				1.3E-03	1.5E-03	13	3.7E-03	4.8E-03	24
	Average % Difference:		65	Average % Difference:		15	Average % Difference:		0
	Absolute Value of Difference:		4.8E-04	Absolute Value of Difference:		5.9E-04	Absolute Value of Difference:		5.4E-04

The average percent difference for the testing environments decreases as the temperature increases. Since the total corrosion rate increases with temperature exponentially, the percent difference would be expected to lower only if systematic errors occur. Systematic errors in this testing corresponds to: Ramp and cool-down rates, impurities from cleaning, flow rates, and temperature/pressure excursions. These effects would be rather consistent on the corrosion rate for each test as they only effect the system during short time-scales or at transient conditions. A more accurate measure would then be the magnitude of the difference observed between the two conditions (given in Table 6.1). This value is nearly constant between all three temperatures which once again indicates that systematic errors in testing caused the differences in mass change between RG and IG environments. The lack of difference between RG and IG testing is further supported by SEM/EDS between the two conditions which showed no major differences in morphology or composition between the

samples.

While this might appear counter-intuitive based on the impurities results presented previously since IG CO₂ should contain higher levels of either oxygen or carbon monoxide, the certificate for IG is based on purity limits, not absolute values. This was further confirmed with the supplier which mentioned that IG bottles could range from RG purity to the purity limit. Once this was known, IG bottles were tested and found to have a very wide range of impurities, which was given previously in Section 3.5. Since the gas analysis techniques were unknown at the time of IG testing, specific bottle concentrations were not obtained. This would indicate that IG testing could have been nearly identical to the RG testing as it appears by the mass change. The highly variable range of IG CO₂ could be concerning for industry. Simple gas analysis tools such as an oxygen sensor and a GC setup with controlled gas injection, similar to what was used in this study, could be implemented to adjust these parameters during operation.

Conclusions for RG vs IG Testing:

- Analysis of IG gas showed wide range of purity ranging from RG levels to beyond limits set by supplier (>50ppm).
- Samples exposed to RG and IG CO₂ showed similar mass change, oxide morphology, and composition.
- The small differences in mass change are attributed to systematic differences in testing including but not limited to: Ramp-up and cool-down rates, impurities from cleaning, flow rates, and temperature/pressure excursions.

6.2 Corrosion Results for Select Alloys in s-CO₂ Environments

A large collection of data has been compiled at UW on commercial alloy compatibility in s-CO₂. This was completed to aide materials selection for construction of s-CO₂ Brayton Cycle facilities. Data was collected for alloys exposed to CO₂ at temperatures ranging from 450-750°C at 20MPa for up to 1,000 hours. A summary of tested alloys was given previously in Table 3.2. The 1,000 hour mass change data is given in Appendix I as well as estimated thickness ranges based on the growth of 100% dense, stoichiometric chromia growth. While this assumption is not realistic due to the formation of other oxides, voids, as well as spallation, the conversion from mass change to thickness was found to be around 30% accurate for all materials excluding samples that experienced oxide exfoliation. A summary of the actual oxide thickness (determined from SEM imaging) is given in Appendix I for select alloys and conditions.

Since a majority of the testing in this research was conducted at 750°C, much more data has been collected for nickel based superalloys. Using industrial input, four alloys were selected for additional study H625 (discussed above), Haynes 230, Haynes 282, and Inconel 740H. Each of these alloys has a unique composition that gives rise to different corrosion mechanisms in CO₂, and will be discussed in more detail in this section.

6.2.1 Corrosion of Haynes 230 in s-CO₂ Environments

Haynes 230 (H230) is a nickel based superalloy that utilizes tungsten (14%) and molybdenum (1%) for solid solution strengthening. The tungsten saturates the alloy and precipitates out as tungsten carbides during alloy fabrication. These tungsten carbide precipitates appear as lighter contrast “islands” in SEM micrographs, several of which will be presented later. Similar to Haynes 625 and different than many other nickel based superalloy, gamma prime is not utilized as a strengthening mechanism. This is due to the low aluminum concentration

found in this alloy. H230 is ASME pressure vessel code certified, which makes it attractive for industry implementation. Heat treatment of the alloy is conducted between 1150-1250°C and quenched to remove most deleterious phases [70]. The total composition of Haynes 230 is given in Table 6.2.

Table 6.2: Composition of as received Haynes 230.

	Si	P	Mn	C	Cr	Ni	Mo	W	Co	Fe	Al	Ti	La
Atomic Percent	0.31	0.005	0.52	0.1	22.08	Bal	1.23	14.17	0.21	1.02	0.37	<.01	0.012

Base characterization of H230 has been conducted through light and SEM imaging for both as received and etched samples to reveal the original micro-structure, and is given in Figure 6.1. The received samples of H230 were solution annealed, and therefore most of the precipitates were dissolved in the matrix outside of some tungsten carbides which can be observed in Figure 6.1.

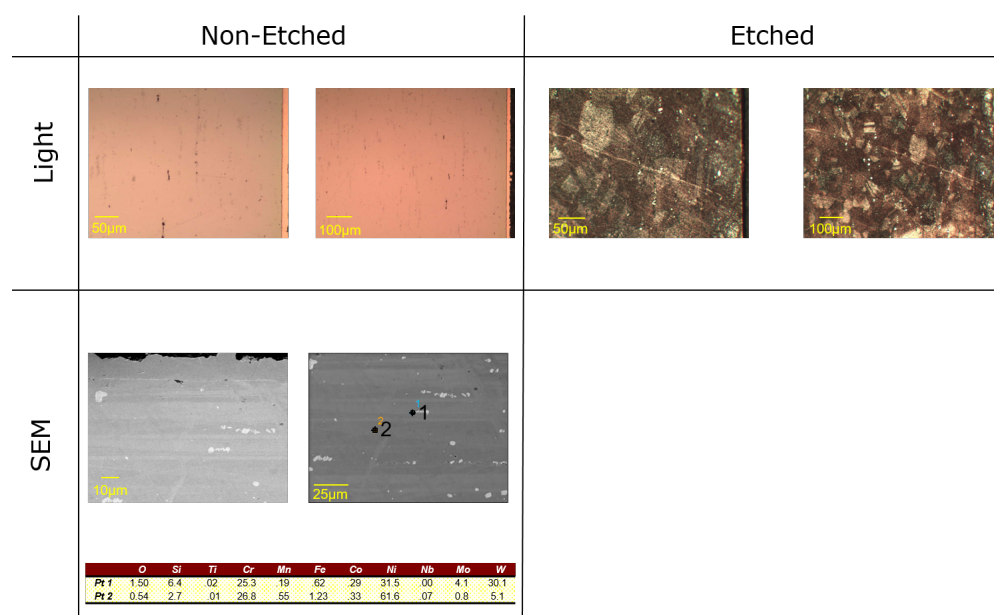


Figure 6.1: Base characterization of Haynes 230 Including light and SEM imaging for pre and post etched as received samples

Testing of Haynes 230 was conducted at temperatures ranging from 450-750°C at 20MPa for 1,000 hours in RG, RG + 100ppm O₂, and RG + 1%CO. Mass change for each condition is summarized in Figure 6.2.

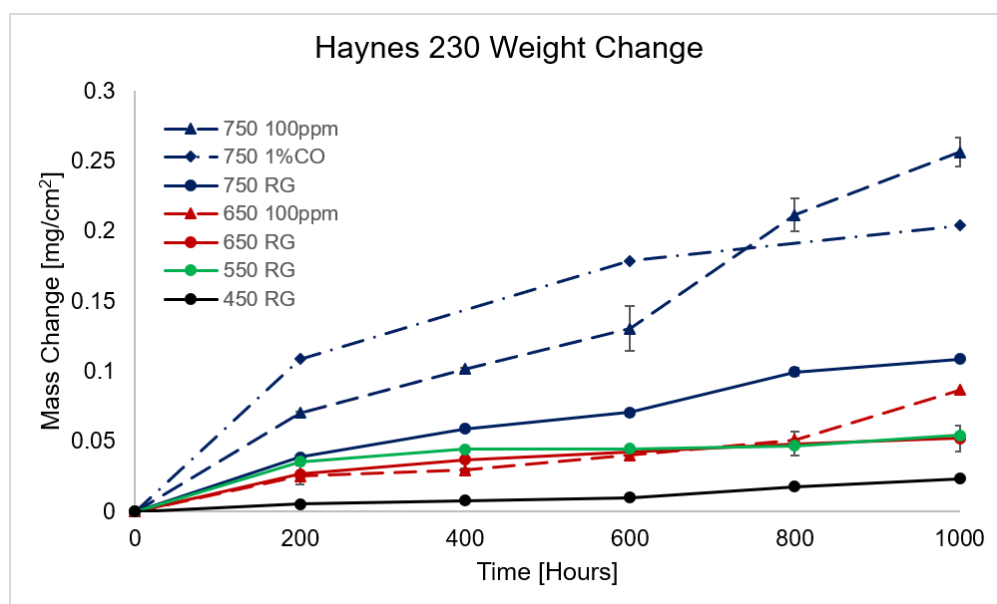


Figure 6.2: Mass change measurements for Haynes 230 samples exposed to CO₂ environments ranging from 450-750°C at 20MPa for 1000 hours.

Mass change of Haynes 230 indicated much better corrosion protection than all of the other tested alloys. The corrosion resistance even extends to impurities mixed testing which showed slightly enhanced corrosion, but not to the extent of all other alloys. In order to study the oxidation mechanics and understand why this alloy performed much better, surface and cross-sectional SEM was conducted, and is given in Figure 6.3.

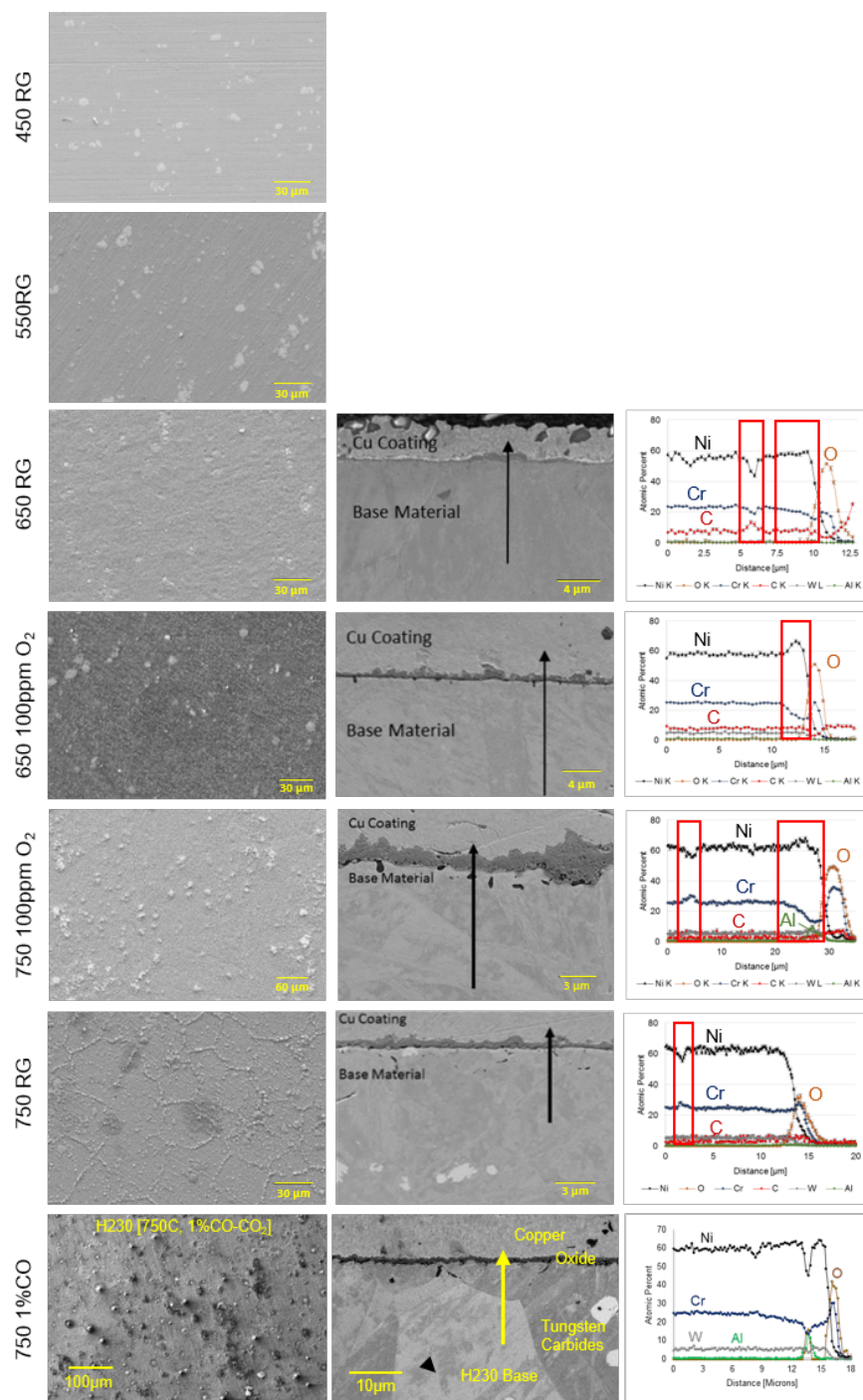


Figure 6.3: SEM/EDS imaging of Haynes 230 samples exposed to s-CO₂ ranging from 450-750°C/20MPa for 1,000 hours in RG, RG + 100ppm O₂, and RG + 1%CO.

Cross section images of 450 and 550°C were not listed since the oxide was very thin and discontinuous due to slow reaction rates at these temperatures. The slow reaction rates are observed in the surface SEM images which still show polishing lines, as well as tungsten carbide clusters which are a part of the base material (seen as lighter marks on the surface). Also interesting is the visible grain boundaries on the surface image of 750°C. EDS mapping has shown enrichment of chromium along these regions, and is a result of faster oxidation at grain boundaries.

The cross section images of Haynes 230 exposed to RG CO₂ shows a continuous coherent oxide, with the thickest oxide grown at 750°C. The oxide produced on Haynes 230 is much thinner than that observed on the Ni-20Cr binary alloy, indicating much slower diffusion rates due to minor alloying elements. Some internal corrosion effects are observed in the 750°C testing, which resulted in void formation. These voids are formed due to enhanced diffusion of chromium in these regions compared to the base material. Voided regions on this sample are characterized by depletion of Cr, which has been shown in other studies to lead to exfoliation of the oxide, and subsequent weakening of the material. In order to understand this void effect, as well as examine the composition of the oxide, EDS line scans were conducted on these samples. The line scans follow the arrows presented in the SEM images in Figure 6.3.

A few observation can be made from the composition of the oxides given for Haynes 230. First, the oxide is primarily composed of chromium and oxygen. The bonding structure was determined from XRD and raman analysis, and shows the presence of primarily (Cr_2O_3) which is given in Figures 6.5 and 6.4.

The raman spectra for IG CO₂ shows good agreement with the pure chromia reference spectrum. The Haynes 230 samples exposed to RG CO₂ contained a higher peak at roughly 700cm⁻¹, which matches the bonding peak for manganese with oxygen. This would indicate oxygen bonding to both chromium as well as manganese. The characteristic D and G carbon

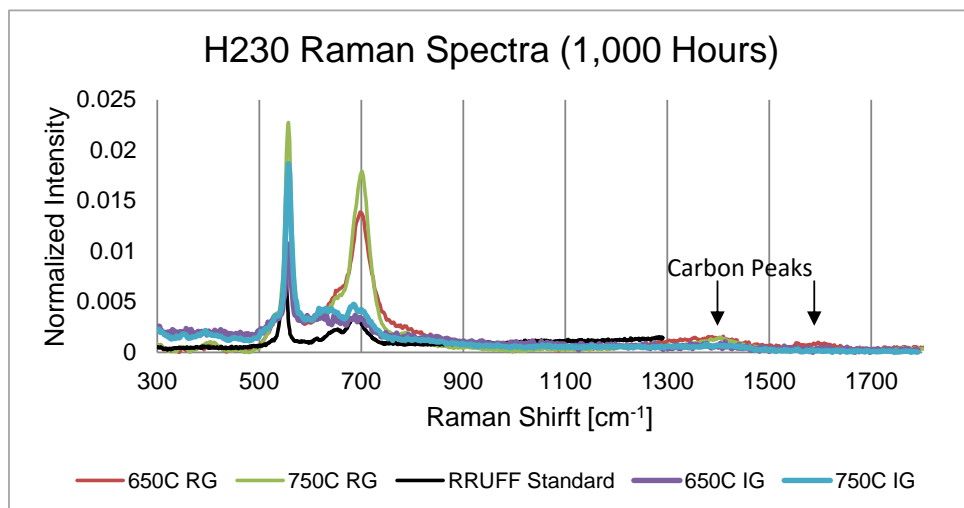


Figure 6.4: Raman spectra comparing exposure of alloy Haynes 230 to $s\text{-CO}_2$ at 650 and 750°C/20MPa for 1,000 hours in RG and IG purity.

bands are labeled in Figure 6.4 as well. These peaks show that some carbon-carbon bonding is found near the surface. This would indicate deposition of carbon during the exposure to CO_2 (cool-down). In order to check these observations for bonding structure, low incident angle XRD was used. A two degree incident angle was used due to the penetration depth of the x-rays through the thin oxide. The XRD spectrum for bare Haynes 230 is displayed alongside the 750°C exposed Haynes 230 sample in Figure 6.5.

The peaks in Figure 6.5 have been labeled for convenience for nickel gamma phase (base matrix), chromia, manganochromite, BCC Cr, Cr_7C_3 , and Cr_23C_6 . Strong base metal peaks are observed meaning that with a 2 degree incident angle, the x-rays still penetrate the oxide completely, therefore these peaks are ignored. The rest of the peaks correspond to the bonding structure of chromia and manganochromite, which supports both the raman spectral results, as well as the EDS compositional mapping.

A large depletion in chromium is also observed beneath the oxide from the EDS line scans in Figure 6.3. This gives a few insights into the mechanism of corrosion for this

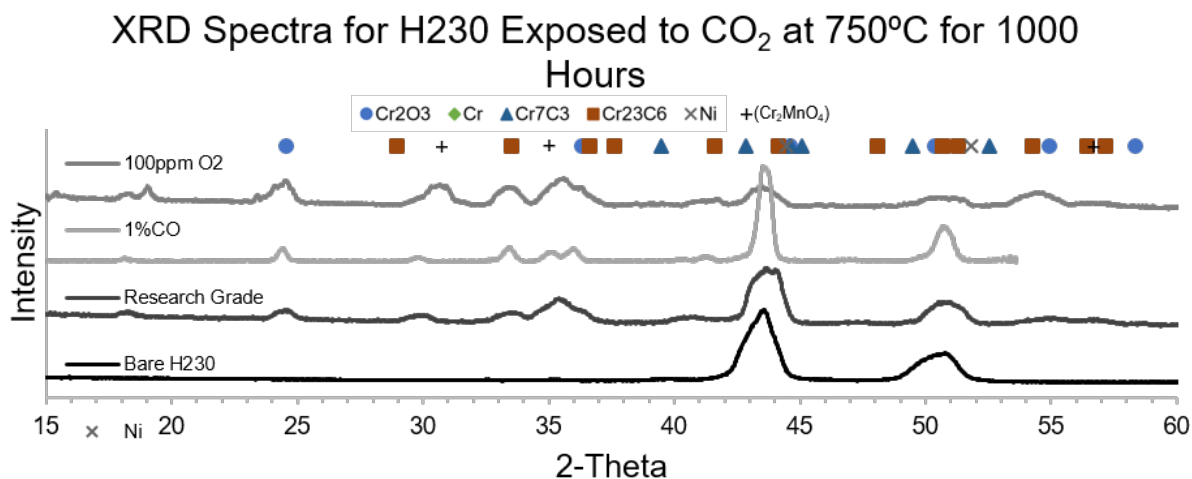


Figure 6.5: XRD spectra for alloy Haynes 230 after exposure to RG CO₂, RG + 100ppm O₂, RG + 1%CO environments at 750°C/20MPa for 800 hours as well as untested Haynes 230.

alloy. First, it shows that the diffusion of chromium in this region (directly beneath oxide) is faster than the base material. This could be caused by decreased grain size, increased grain boundary diffusion, increased dislocation or vacancy concentration, or potentially formation of different phases (chemical or physical). The depleted region also shows us that the steady state equilibrium may not have been reached in this case, and that the diffusion of chromium plays an important role in the kinetics of the oxide formation. If no depletion was observed, then it could be theorized that the partial pressure of oxygen dictates the oxide formation. This is observed in the line scans for 650°C exposure. The depletion zone also shows that the diffusion of chromium is slow enough compared to the oxidation rate to induce void formation.

Impurities results for H230 show similar corrosion mechanisms discussed previously with respect to Haynes 625. The oxide produced in the oxygen rich environment shows larger nodules that have some nickel rich oxidation (smaller number density compared to H625). The oxide produced in both impurities rich environments were found to be thicker than the

one produced in pure CO₂. The faster oxidation rate also increased the magnitude of the voided region and internal oxidation beneath the surface oxide. This is more easily observed in Figure 6.6.

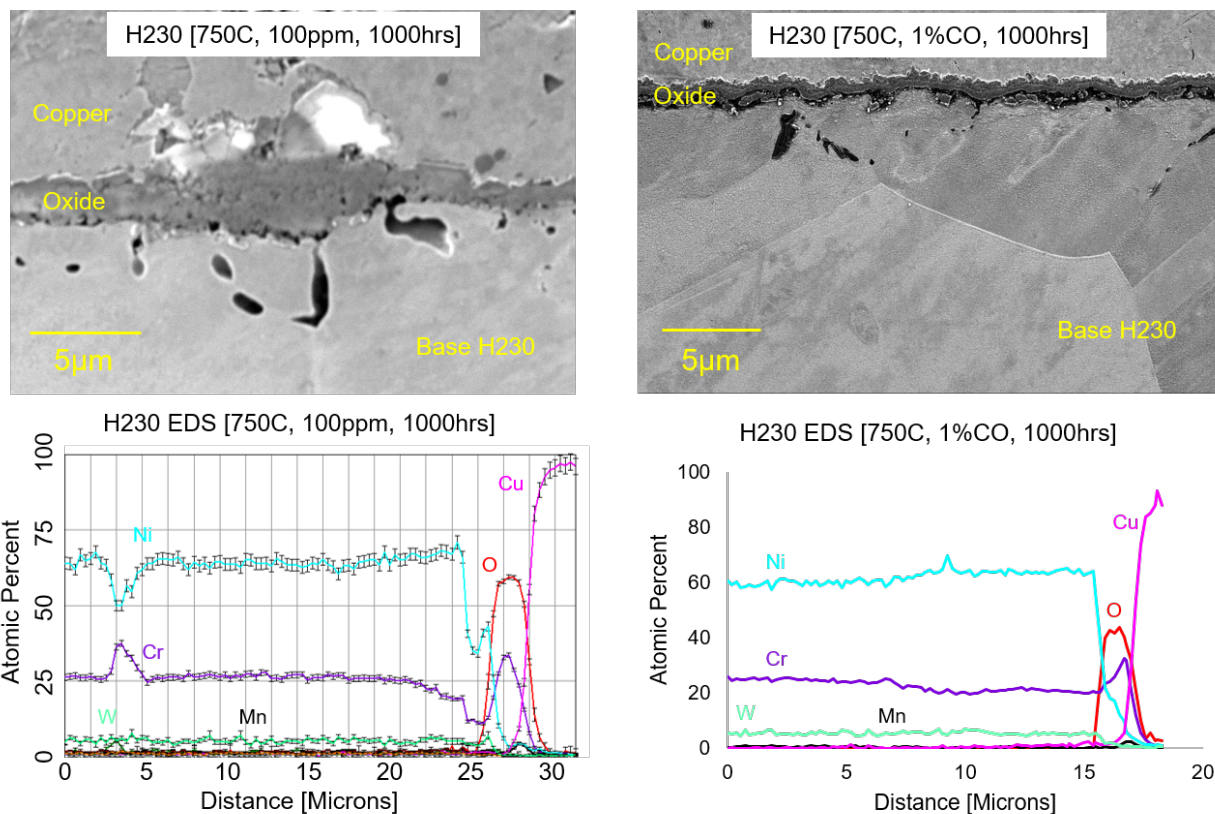


Figure 6.6: SEM/EDS imaging for Haynes 230 exposed to s-CO₂ at 750°C/20MPa for 1,000 hours in RG + 100ppm O₂ (Left) and RG + 1%CO (Right)

6.2.2 Corrosion of Inconel 740H in s-CO₂ Environments

Inconel 740H is currently of interest in the highest temperature sections of the s-CO₂ Brayton Cycle due to its very high strength at elevated temperatures. The high temperature strength comes from high levels of solid solution cobalt as well as gamma prime precipitation (a Ni₃Al phase). Gamma prime precipitates slowly at elevated temperature, which means that this alloy requires significant heat treatment as well as thermal aging before use [73]. 740H

is currently pressure vessel code certified, and therefore is one of the top choices for high temperature/high pressure components. A complete list of the composition of Inconel 740H can be found in Table 6.3.

Table 6.3: Composition of Inconel 740H.

	C	Mn	Fe	S	Si	Cu	Ni	Cr	Al	Ti	Co	Mo	Nb
Atomic Percent	0.023	0.245	0.1491	0.003	0.17	0.0015	50.04	24.57	1.33	1.33	20.09	0.35	1.46

Base characterization of 740H has been conducted through light and SEM imaging for both as received and etched samples to reveal the original micro-structure, and is given in Figure 6.7. The condition of the as received 740H was not aged, and therefore most of the precipitates were dissolved in the matrix outside of some titanium carbides which can be observed in Figure 6.7 as dark regions.

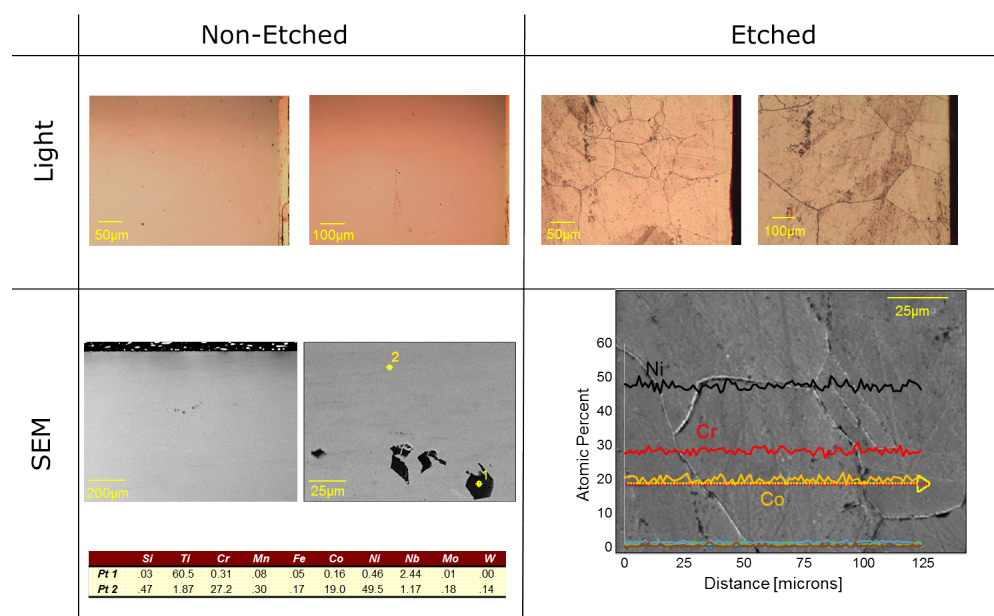


Figure 6.7: Base characterization of Inconel 740H Including light and SEM imaging for pre and post etched as received samples

The titanium precipitates in the SEM imaging appear to be the only non-homogeneous regions. These precipitates form preferentially along grain boundaries, which will be of interest later. 740H samples were exposed to s-CO₂ at 750°C/20MPa, for 1,000 hours in both RG and RG + 100ppm O₂. The mass change measurements are given for both conditions in Figure 6.8.

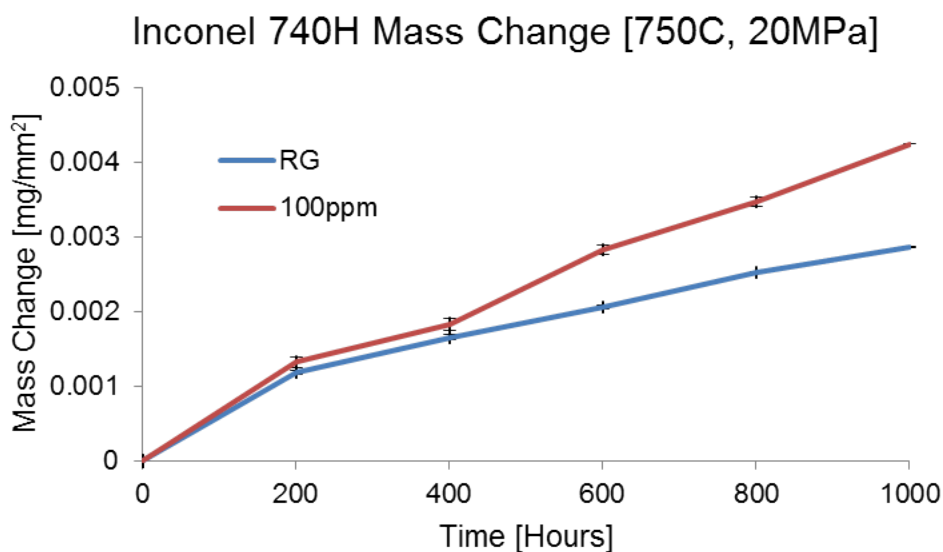


Figure 6.8: Mass change measurements of Inconel 740H exposed to RG and RG + 100ppm O₂ at 750°C/20MPa for 1000 hours.

Mass change measurements between the two conditions are similar with a slight deviation beginning at the 600 hour mark. This type of behavior is consistent with many of the nickel based superalloys tested in these conditions, and was related to the depletion of chromium, and subsequent oxidation of other elements such as nickel. This was caused by the increased pO₂ characteristic of the oxygen rich environment, which is limited in RG CO₂. SEM and EDS for the 740H sample exposed to RG CO₂ is given in Figure 6.9.

Cross-sectional SEM of 740H shows a thin protective chromium rich oxide with discontinuous internal oxidation of aluminum. The alumina (Al₂O₃) formation is due to the increased

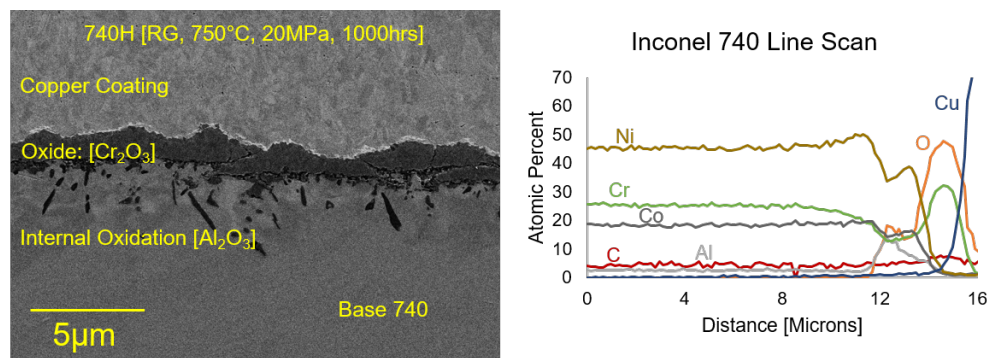


Figure 6.9: SEM/EDS imaging for Inconel 740H exposed to RG CO₂ at 750°C/20MPa for 1000 hours.

concentration of aluminum for gamma prime precipitation which wasn't present for the H230 or H625. The presence of alumina would indicate that the precipitation of gamma prime would be inhibited in these regions. The denudization of gamma prime will be discussed more in 6.2.3.

The Gibbs Free Energy of Formation for alumina is much lower than that of chromia. It is therefore reasonable to theorize that this could effect the formation of chromium carbides between the M-O interface by the mechanism discussed previously. This effect would behave similar to the difference between RG and 1%CO mixed environment in that there would exist a higher potential barrier, which would reduce the amount of carbides that would be present. In order to test this, additional analysis would need to be conducted on these samples such as GDMS, GDOES, SIMS, or another method for carbon detection.

Many different oxide morphologies were observed on the 740H samples exposed to RG + 100ppm O₂. Surface SEM of different oxidation mechanisms is given in Figure 6.10.

The morphology in the samples exposed to RG CO₂ experienced the “plate like” chromia growth observed in Figure 6.10. Whisker and step-like growth are common in high pO₂ conditions, and is theorized to be caused by very rapid metal diffusion along dislocation pathways. The more interesting surface features are the large nodules found in several places

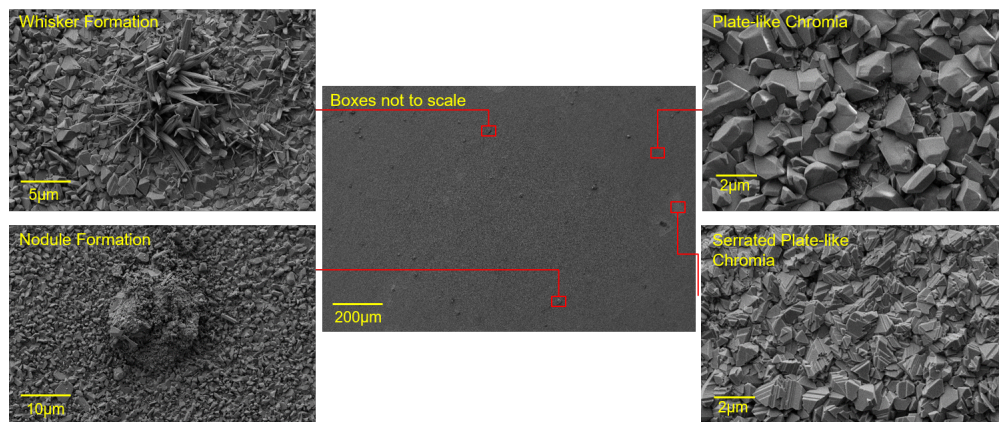


Figure 6.10: Surface SEM imaging for Inconel 740H exposed to RG + 100ppm O₂ at 750°C/20MPa for 1000 hours.

across the oxide (found in RG CO₂ environments as well). These nodules were typically greater than 10 microns in diameter. Cross-sectional SEM of one of these nodules is given in Figure 6.11.

While a majority of the surface oxidation of 740H was composed of chromia as observed by the right images in Figure 6.11, nodules were observed in several places which contained a large amount of titanium. These nodules were primarily found along grain boundaries. Since the composition of 740H has fairly low titanium, it is theorized that these nodules correspond to the titanium carbide clusters found on the surface of the as received samples. This would indicate that these precipitates oxidize leading to enhanced corrosion inward along grain boundaries, which could be a concern as increased attack along grain boundaries could lead to mechanical failure during use.

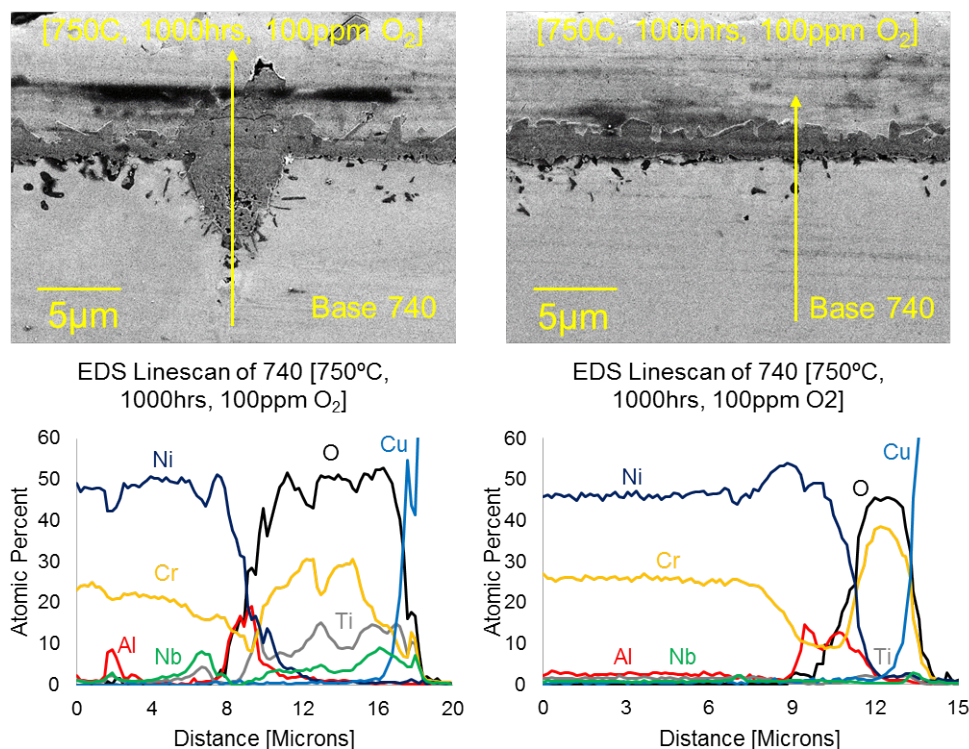


Figure 6.11: Cross-sectional SEM imaging for Inconel 740H exposed to RG + 100ppm O₂ at 750°C/20MPa for 1000 hours.

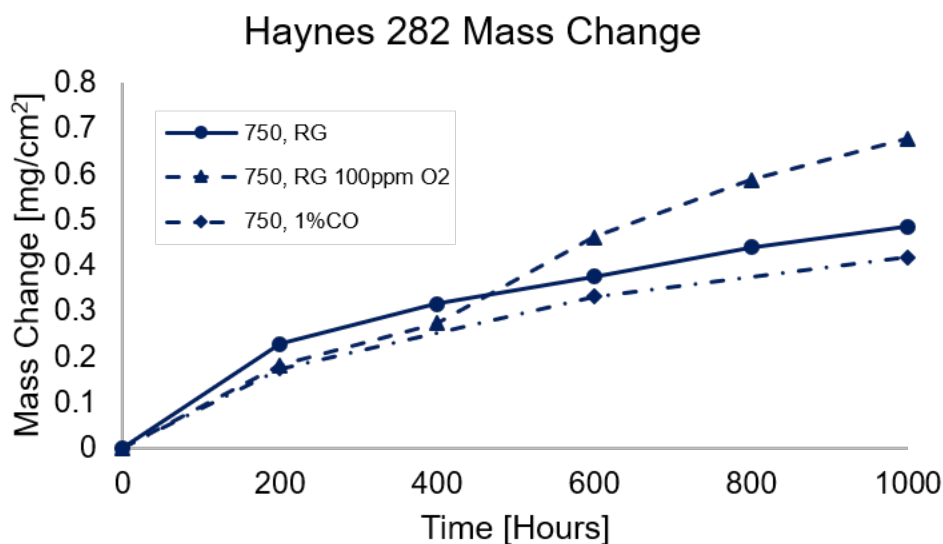
6.2.3 Corrosion of Haynes 282 in s-CO₂ Environments

Another alloy of considerable interest is Haynes 282 (H282). Very similar to Inconel 740H, this alloy is a nickel based superalloy that utilizes gamma prime precipitation for high temperature strength. This alloy also contains a large amount of molybdenum and cobalt for solid solution strengthening. H282 must be heat treated in a two stage aging process: 1010°C for 2 hours, air cool to 788°C for 8 hours, air cool [74]. This alloy is the only one mentioned in this work that is not pressure vessel certified, but the strength characteristics similar to Inconel 740H, and potentially the higher temperature compatibility (better creep rupture resistance) make this alloy highly attractive to industry[75]. The composition of H282 is given in Table 6.4.

Table 6.4: Composition of as received Haynes 282.

	Ni	Cr	Co	Mo	Ti	Al	Fe	Mn	Si	C	B
Haynes 282	57	20	10	8.5	2.1	1.5	1.5	.3	.15	.06	.005

Due to the high temperature compatibility of H282, samples were only exposed to s-CO₂ at 750°C/20MPa for 1,000 hours in RG, RG + 100ppm O₂, and RG + 1%CO. The mass change measurements for each test are given in Figure 6.12.

**Figure 6.12:** Mass change measurements for Haynes 282 after exposure to sCO₂ environments at 750°C, 20MPa for up to 1000 hours.

The mass gain measurements for H282 are very different than the trends observed for both Haynes 625 and Haynes 230. H282 experienced the greatest mass increase in the oxygen rich CO₂, and very similar trends for the RG and CO mixed environments. This could indicate superior resistance to carburization compared to the other alloys. In order to determine the reasoning, surface and cross-sectional SEM was conducted. These results are presented in Figures 6.13 and 6.14 respectively.

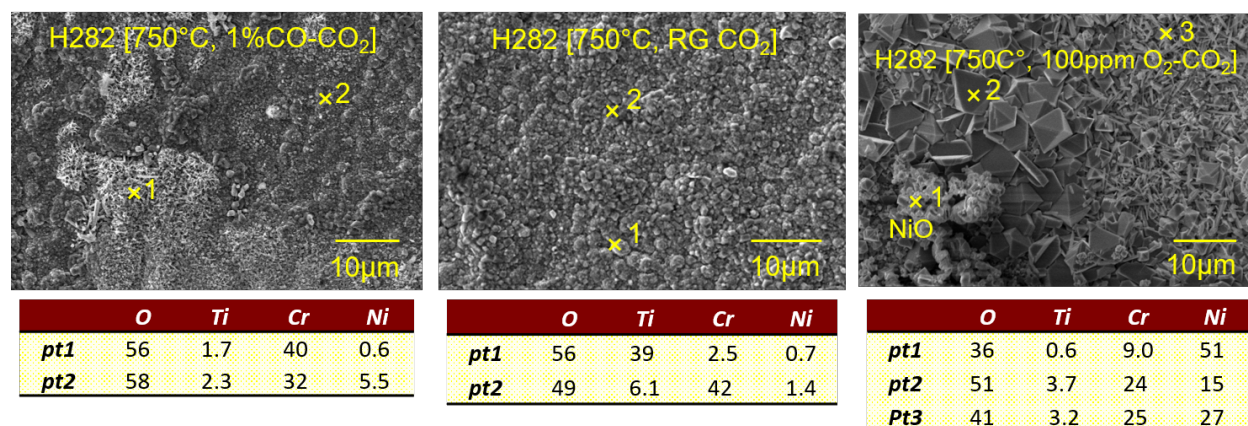


Figure 6.13: Surface SEM/EDS of Haynes 282 after exposure to sCO₂ environments at 750°C, 20MPa for up to 1000 hours.

Surface SEM shows the presence of NiO on the surface of the oxide exposed to the oxygen rich environment which has been observed for all other nickel based alloys. Interestingly, the surfaces of the RG and RG mixed with CO environments appeared very similar (Ti rich nodule is believed to be from Ti precipitate in as received sample similar to 740H). The only difference would be the appearance of smaller oxide grain size in the CO mixed environment. The surface chromia composition was found to be similar for each oxide.

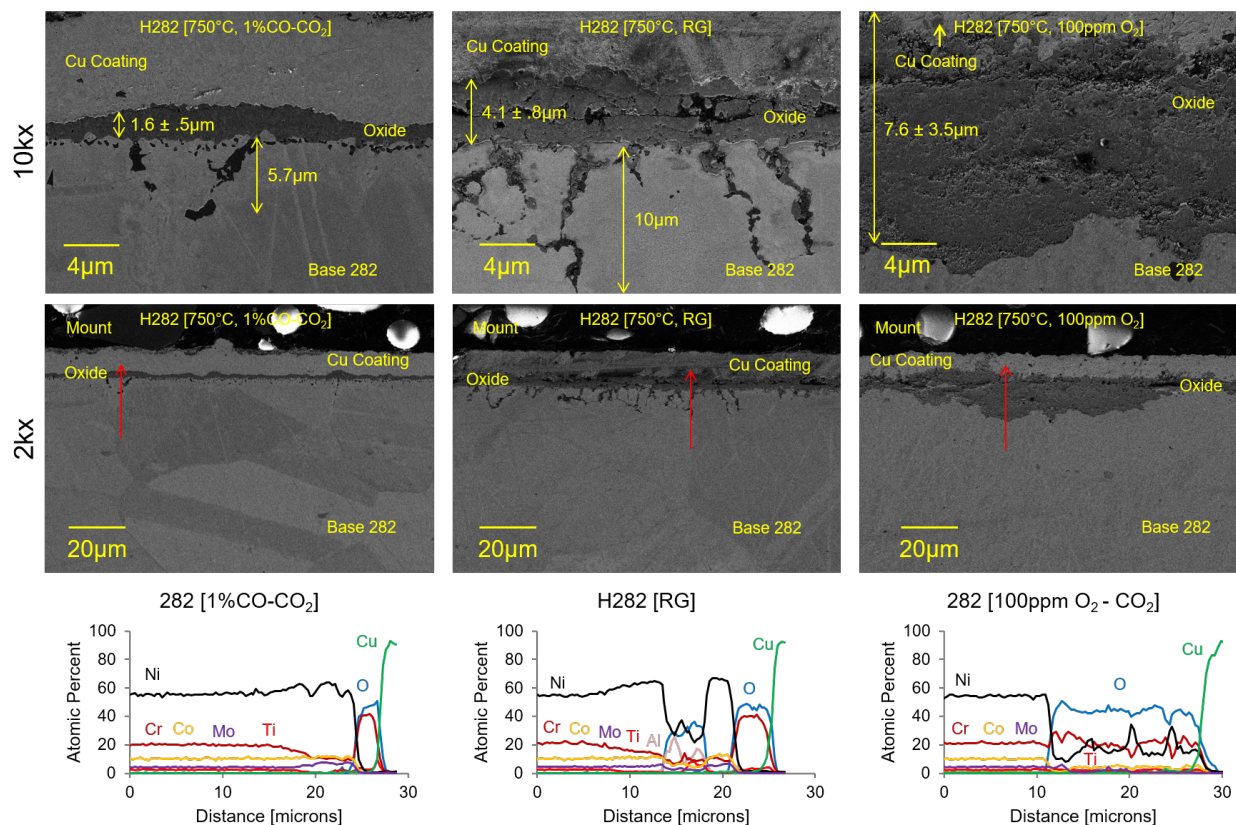


Figure 6.14: Cross-sectional SEM/EDS of Haynes 282 after exposure to $s\text{CO}_2$ environments at 750°C , 20MPa for up to 1000 hours.

Cross-sectional SEM reveals very different oxide characteristics between each of the environments. The RG CO_2 environment experienced enhanced internal oxidation when compared to the impurities mixed environments. This is perhaps shadowed by the internal growth of oxide in the oxygen mixed environment which shows an oxide thickness that is roughly as large as the external and internal oxidation of the RG case. Internal oxidation is much smaller in the 1%CO environment. This is most likely caused by the lower $p\text{O}_2$ and therefore, the potential for oxidation in the CO mixed environment is likely limited by the oxygen diffusion and not the chromium potential like the other two environments.

EDS line scans through the oxide show the presence of aluminum and chromium in the

internal attack observed in the RG CO₂ environment. The oxide in the oxygen rich environment consists of both Ni and Cr which confirms the surface EDS results. Since aluminum is primarily used for high temperature strength through the precipitation of gamma prime in this alloy, it is necessary to determine if the oxidation of aluminum effects the precipitation of this high temperature strengthening component.

Due to heat treatment of the material during fabrication, no gamma prime was observed in the as received material. After 1,000 hours at 750°C during s-CO₂ testing, precipitation and coarsening of this phase should reach roughly 100nm [76]. Gamma prime precipitates in circular or square precipitates uniformly through the nickel matrix. In order to observe gamma prime, the samples were etched using a solution of HCl-H₂O₂ for 10 second intervals until the phases were observable. An example of gamma prime precipitates post exposure as well as the denudization of gamma prime is given in Figure 6.15.

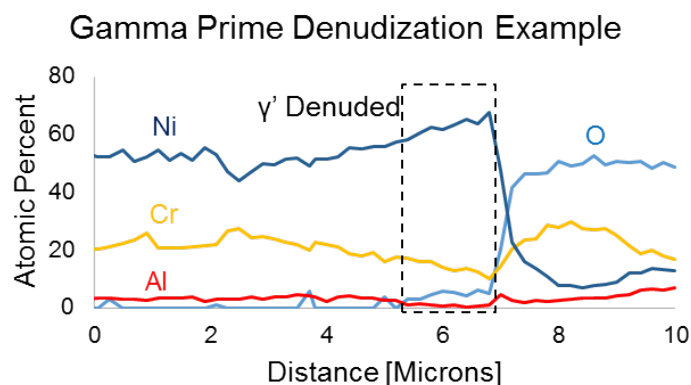
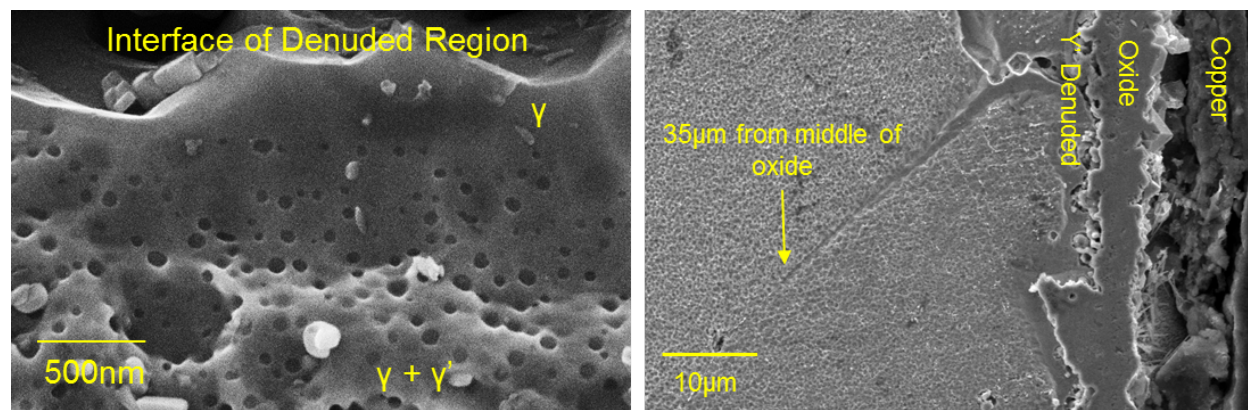


Figure 6.15: SEM/EDS of gamma-prime denudization due to selective oxidation of aluminum after exposure to RG + 100ppm O₂ at 750°C, 20MPa, for 1000 hours (Etched using HCl-H₂O₂).

The denuded region of gamma prime corresponds to an increase in nickel as well as a depletion of aluminum as observed in the EDS line-scan in Figure 6.16. The removal of gamma prime follows beneath the oxide and is enhanced along grain boundaries. Figure 6.15 shows grain boundary attack up to 35 microns beneath the surface. This effect penetrates deeper than the internal oxidation process which was found to be between 1-8 microns based on the environment. The removal of gamma prime could result in lower high temperature strength. Bulk denudization of gamma prime for each environment is given in Figure 6.16.

While gamma prime is primarily used for high temperature strength, carbides and other phases can effect the room temperature hardness of the bulk material. These phases can also

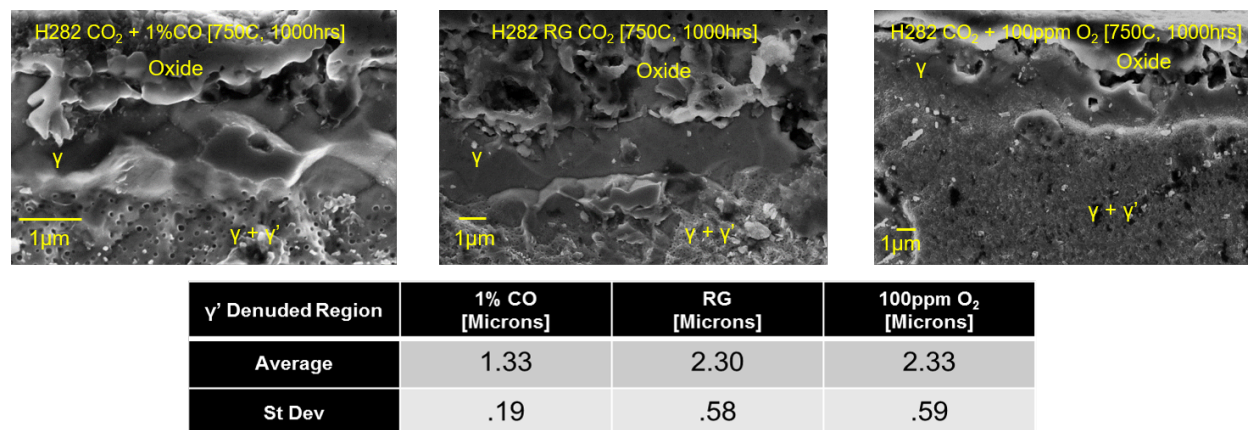


Figure 6.16: Comparison of gamma prime denudization for different sCO₂ environments at 750°C and 20MPa for 1000 hours.

be effected by the selective oxidation of elements near the surface of the alloy. In order to observe the macroscopic hardness changes, a grid of Vickers hardness indents in accordance with ASTM-E92 standards were conducted on samples exposed to s-CO₂ at 750°C/20MPa for 1,000 hours. A summary of the results as well as the hardness for the untreated sample is given in Figure 6.17.

The surface hardness decrease appears to be similar for each environment, which would indicate that despite the differences in oxide thickness, and internal attack of hardening phases, the hardness was unaffected. The bulk increase in hardness is most likely due to carbide precipitation during the heat treatment during s-CO₂ testing.

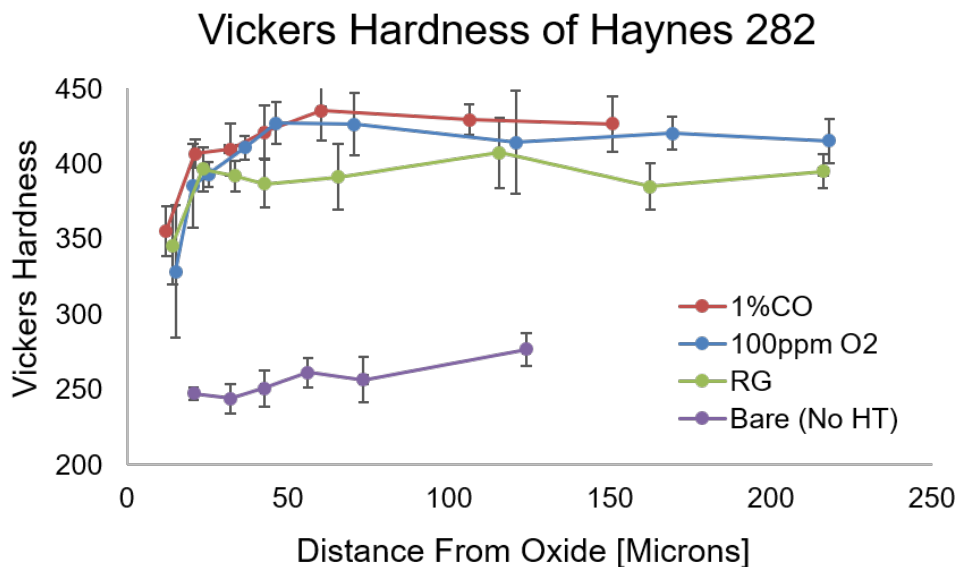


Figure 6.17: Vickers hardness as a function of depth from the oxide for Haynes 282 after exposure to sCO₂ environments at 750°C, 20MPa, for 1000 hours.

Conclusions for Industrial Alloy Testing:

- Haynes 625 experienced good corrosion resistance in RG CO₂ but performed much worse when exposed to impurity rich CO₂.
- Both carbon deposition mechanisms were observed in the Haynes 625 alloy exposed to 1%CO-CO₂.
- Haynes 625 exposed to RG CO₂ showed similarities to previous work on oxidation defect control which would indicate the formation of a nearly stoichiometric chromium oxide.
- The lack of Al and Ti in both Haynes 230 and Haynes 625 reduces internal oxidation depth and magnitude compared to the gamma prime strengthened alloys (could increase carburization).
- Haynes 230 exhibited the best corrosion resistance in all s-CO₂ environments.

- Inconel 740H was susceptible to internal oxidation of chromium and aluminum which was enhanced at grain boundaries due to oxidation of titanium carbide precipitates in the as received samples.
- Haynes 282 was susceptible to internal oxidation of chromium and aluminum.
- Haynes 282 exhibited excellent resistance to impurities testing compared to other alloys, specifically RG + 1%CO.
- Selective oxidation of aluminum along grain boundaries in Haynes 282 resulted in gamma prime denudization up to 35 microns beneath the oxide.
- A summary of these commercial alloys, as well as others that have been tested as a result of this work have been summarized in Appendix J.

6.3 Comparison of s-CO₂ Corrosion to High Pressure Steam and Ultra Supercritical Steam

One final comparison to the research conducted on the commercial alloys is between corrosion resistance in s-CO₂ and steam environments. Current power cycles use high temperature steam as the working fluid, and therefore a large amount of data has been collected on materials in these environments. It is also important to compare to higher efficiency cycles like supercritical, or ultra supercritical steam cycles to determine the compatibility of materials in both s-CO₂ and high pressure steam conditions. A summary of different steam cycles and parameters is given in Table 6.5.

In order to compare s-CO₂ corrosion to steam corrosion, the same type of alloy must be used. Since nickel base alloys are the most likely candidates due to high temperature strength and corrosion resistance, these alloys will be compared. A metric for comparing results equally must be used as most data does not occur with the same testing parameters

Table 6.5: Operating conditions for various steam environments [77].

Nomenclature	Conditions	Net Plant Efficiency (HHV)
Subcritical	2400 psi/1050F/1050F (165 bar/566C/566C)	35%
Supercritical (SC)	3600 psi/1050F/1075F (248 bar/566C/579C)	38%
Ultra-Supercritical (USC)	>3600psi/1100F/1150F (>248 bar/593C/621C)	>42%
Advanced Ultra-Supercritical (A-USC)	4000-5000 psi/1300-1400F (276-345 bar/704-760C)	>45%

such as exposure time, and temperature. Fortunately the parabolic rate constant, given in Equation 2.3, is commonly used. Mass change measurements as well as parabolic rate constants for two steam environments (1 bar and 267 bar) is given in Figure 6.18.

Alloy	Mass gain, mg/cm ²		K _p , g ² /cm ⁴ /s	
	1 bar	267 bar	1 bar	267 bar
H230	0.069	0.61±0.06	2.26 x 10 ⁻¹⁵	1.74 x 10 ⁻¹³
H263	0.072	0.45±0.08	2.49 x 10 ⁻¹⁵	9.73 x 10 ⁻¹⁴
H282	0.050	0.51±0.07	1.19 x 10 ⁻¹⁵	1.23 x 10 ⁻¹³
IN617	0.083	0.32±0.03	3.31 x 10 ⁻¹⁵	4.94 x 10 ⁻¹⁴
IN625	0.078	9.69±0.62	2.89 x 10 ⁻¹⁵	4.46 x 10 ⁻¹¹
IN740	0.046	0.43±0.11	1.02 x 10 ⁻¹⁵	8.90 x 10 ⁻¹⁴

Figure 6.18: Mass gain and parabolic rate constant for steam corrosion results at 670°C for 293 hours at 1 bar and 267 bar [78].

This steam testing was conducted at two different pressures, and resulted in very different corrosion rates. The effect of pressure in s-CO₂ corrosion was discussed previously, and was found to have little effect on the oxidation process (some effect on carburization). This is an important distinction between water and CO₂ because higher efficiency cycles depend on increased fluid pressure, which may not be as feasible from a corrosion standpoint in steam. A large amount of steam corrosion studies were analyzed previously by Halcomb and were aggregated in Figure 6.19. Parabolic rate constants for the s-CO₂ testing conducted at UW

have also been plotted in Figure 6.19. Each point in Figure 6.19 represent the parabolic rate constant for a nickel base alloy for a given condition. In order to better compare the data, an overlay of the two graphs has been created and given in Figure 6.20.

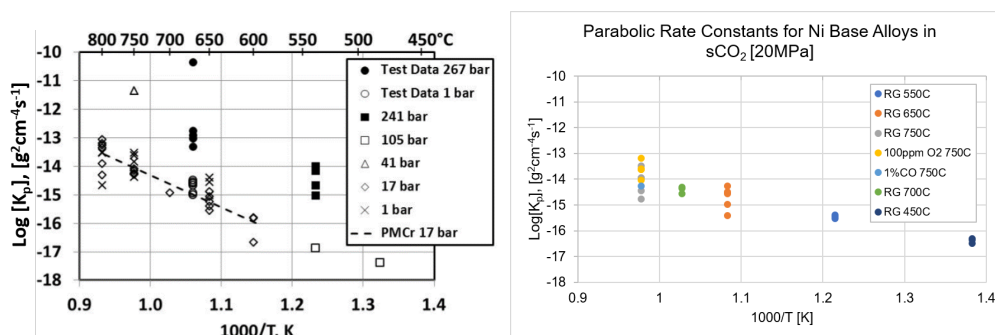


Figure 6.19: Parabolic rate constants for nickel base alloys exposed to s-CO₂ (UW-Madison) and steam environments [78],[79],[80],[81],[82],[83],[84].

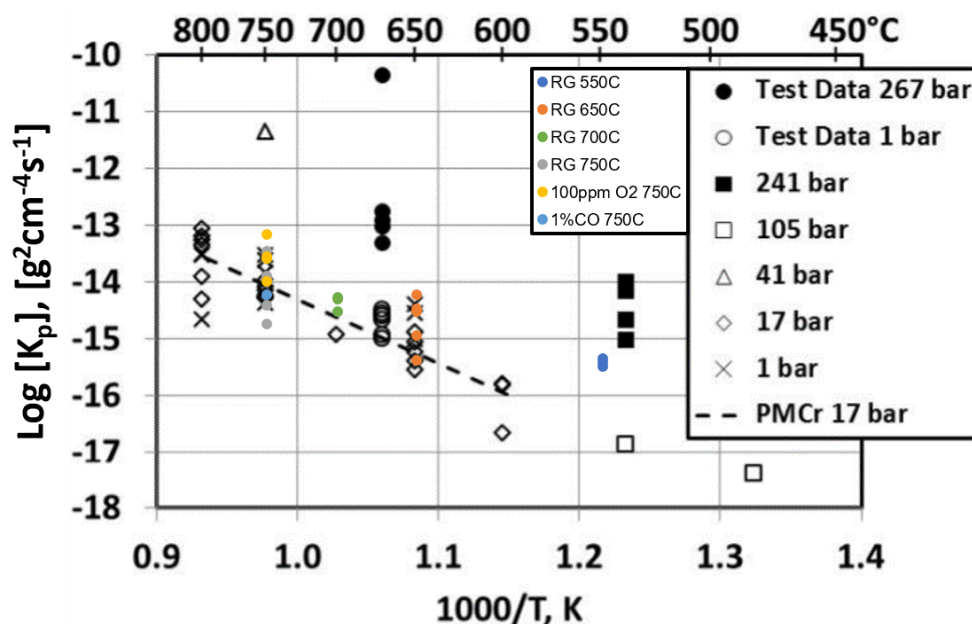


Figure 6.20: Comparison overlay of s-CO₂ and steam parabolic rate constants for high temperature corrosion.

The corrosion results found in s-CO₂ (200bar) show great agreement with samples exposed to atmospheric steam. The high pressure steam environments exhibited 1-3 orders of magnitude higher mass change when compared to s-CO₂ corrosion rates. This result shows that even the most corrosive CO₂ environments (impurities mixed) are much less corrosive than high pressure steam. The same nickel base alloys were used when comparing the parabolic constants, and it would appear that similar mechanisms were experienced between atmospheric steam and s-CO₂. High pressure steam produced much larger parabolic constants which would indicate very different mechanisms. In those studies, it was theorized that the increased pressure dramatically increased the pO₂ and therefore the solid state diffusion of chromium through the oxide. This explanation doesn't account for inward growing chromia which was the focus of a previous chapter in this work on s-CO₂ corrosion. The higher corrosion rate in high pressure steam isn't highly surprising as the pO₂ values are very different, and the presence of charge carriers (H⁺, OH⁻) in steam could lead to enhanced corrosion mechanisms.

Chapter 7

Conclusions for Corrosion in s-CO₂ Environments

Results have been compiled for thermodynamic modeling of s-CO₂ systems, as well as exposure testing in s-CO₂ at 450, 550, 650, 700, and 750°C at 20MPa for 1,000 hours in a variety of environments (IG, RG, RG + 10ppm O₂, RG + 100ppm O₂, and RG + 1%CO). Thermodynamic calculations show that oxidation is heavily favored in pure CO₂ conditions through the dissociation into oxygen and carbon monoxide. Due to the low partial pressure of oxygen produced from this reaction some oxides cannot thermodynamically form. Carbide formation was shown to be thermodynamically allowed in pure CO₂ conditions if the oxide is treated as a diffusion barrier. A second mechanism for carbon deposition was theorized to be caused by saturation of CO which causes precipitation of carbon during temperature transients. Each of these effects were exaggerated when impurities such as oxygen or carbon monoxide are added to the CO₂ stream.

Experimental work was completed on a wide variety of commercial alloys (T92, T122, 347, 316L, 310S, 709, 800H, Inconel 718, Inconel 740H, Haynes 625, Haynes 230, Haynes 282, HR120, AFA alloys, Powder Metallurgy alloys, and SiC) as well as a few model alloys (Ni, Cr, Ni-20Cr). Mass change data showed that ferritic alloys such as T92 can not withstand the corrosion rates at and exceeding 450°C, austenitic alloys such as 316L and 347 can not withstand temperatures above 550°C, and the Ni-Cr superalloys were able to handle the corrosive environments up to 750°C in RG and IG CO₂. The structure of the oxides were found to be iron and chromium rich for ferritic and low Cr austenitics, while a thin protective chromium rich oxide was formed on the surface of nickel base superalloys. Significant data was collected on 625, 230, 740H, and 282, each of which exhibited slightly different corrosion effects and has been explained. Major conclusions from this work include:

- Altering pO_2 changes the stability of different oxides (specifically Ni-NiO). (Chapter 4.1)
- Coupling of pO_2 and a_C throughout the oxide leads to carburizing environments at the M-O interface. (Chapter 4.2)
- Saturation of CO_2 with CO (high environmental a_C) causes carbon deposition during cool-down. (Chapter 4.3)
- Controlling pO_2 and a_C can be used to alter defect concentration leading to the production of a stoichiometric oxide. (Chapter 4.4)
- Ni-20Cr experienced a lower corrosion rate than pure Cr due to the Ni matrix slowing Cr diffusion. (Chapter 5.1)
- Chromium preferentially oxidizes to produce a protective oxide until depletion reaches a certain point in which nickel oxide will form. This leads to decreased adhesion of the scale, and enhanced corrosion. (Chapter 5.1)
- Exposure to RG CO_2 at $750^\circ C/20MPa$ produces the most protective oxide as NiO is less likely form (due to kinetic limitations), and carbon deposition is limited due to the low levels of CO.(Chapter 5 - Chapter 6)
- Analysis of IG gas showed wide range of purity spanning RG levels to beyond limits set by supplier ($>50ppm$). (Chapter 6.1)
- Samples exposed to RG and IG CO_2 showed similar mass change, oxide morphology, and composition. (Chapter 6.1)
- The small differences in mass change are attributed to systematic differences in testing including but not limited to: Ramp-up and cool-down rates, impurities from cleaning, flow rates, and temperature/pressure transients. (Chapter 6.1)

- Both carbon deposition mechanisms are observed in commercial alloy H625, but added Al could reduce the magnitude of inter-facial carburization. (Chapter 5.2)
- Carburization of base material in Ni based alloys was limited to the first 5-10 microns when exposed to s-CO₂ at 750°C/20MPa for 1,000 hours. (Chapter 5.2)
- Haynes 625 exposed to RG CO₂ showed similarities to previous work on oxidation defect control which would indicate the formation of a nearly stoichiometric chromium oxide. (Chapter 5.2)
- The lack of Al and Ti in both Haynes 230 and Haynes 625 reduces internal oxidation depth and magnitude compared to the gamma prime strengthened alloys (could increase carburization). (Chapter 6.2.1, Chapter 6.2.3)
- Haynes 230 exhibited the best corrosion resistance in all s-CO₂ environments due to minor alloying elements and lack of internal oxidation. (Chapter 6)
- Inconel 740H was susceptible to internal oxidation of chromium and aluminum which was enhanced at grain boundaries due to oxidation of titanium carbide precipitates in the as received samples. (Chapter 6.2.2)
- Haynes 282 was susceptible to internal oxidation of chromium and aluminum. (Chapter 6.2.3)
- Haynes 282 exhibited excellent resistance to impurities testing, specifically RG + 1%CO. (Chapter 6.2.3)
- Selective oxidation of aluminum along grain boundaries in Haynes 282 resulted in gamma prime denudization up to 35 microns beneath the oxide. (Chapter 6.2.3)
- s-CO₂ corrosion rates for nickel base alloys are similar to atmospheric steam corrosion rates. (Chapter 6.3)

- s-CO₂ corrosion rates are 1-3 orders of magnitude lower than those determined in supercritical steam environments. (Chapter 6.3)
- A summary of several commercial alloys that have been tested as a result of this work have been summarized in Appendix J.

Chapter 8

Future Work

A significant amount of work has been conducted on s-CO₂ corrosion with added oxygen and CO impurities. While these are the two most realistic impurities expected in CO₂ environments, many other impurities are likely to be present during s-CO₂ Brayton Cycle operation such as water vapor and hydrocarbons. Perhaps the most interesting of the two being water vapor due to the addition of charge carriers such as H⁺ and OH⁻ species which could result in charge transport characteristics of classical corrosion. The mechanisms will therefore be very different than that of high temperature CO₂, and could potentially be a limiting factor in materials compatibility.

An area discussed briefly in this document was the effect of aluminum on the carburization rate in nickel based alloy. It was suggested that the increased potential barrier created in the formation of alumina (in comparison to chromia) causes lower carburization rates. This could be tested further using GDMS, GDOES, SIMS or other carbon detection instrumentation on samples that have been exposed to s-CO₂ environments to determine the magnitude of carburization.

Another important factor to consider in corrosive environments is mitigating the corrosion through environmental control. This entire document has discussed the effects that oxygen and carbon monoxide have on the corrosion rates and mechanisms in CO₂, and it has been shown to be very important to control the gaseous equilibrium of the environment. This can be accomplished using feedback loops which monitor oxygen and carbon monoxide compositions while injecting the opposite impurity in order to react and form CO₂. The exact equilibrium conditions should be proven and studied in order to prove this concept.

Another way to mitigate the corrosion is to apply a coating to materials. Coatings for

corrosion resistance have been utilized for a long time, and are fairly well understood. CO_2 is an interesting environment due to the extremely low $p\text{O}_2$ associated with dissociation. If the coating can be rendered inert, materials that would otherwise be non-compatible due to corrosion in CO_2 could be used at higher temperatures. An example of this is the oxidation of nickel which cannot thermodynamically form (and wasn't) in CO_2 with 1%CO addition. Another material that is rendered inert, which is perhaps more interesting than Ni, is copper. Copper is normally not used in high temperature oxidizing environments due to its very low strength and very quick oxidation kinetics. In CO_2 , copper is rendered inert with around 50ppm CO added. This implies that a copper coating could greatly reduce both oxidation and carburization after being deposited on any material. In order for coatings to be feasible, more work would need to be completed to prove the protectiveness, adherence, and ability to be deposited.

Bibliography

- [1] Jim Diefenderfer, Macroeconomic assumptions Vipin Arora, and Laura E Singer. *International Energy Outlook 2016 Liquid fuels*. Number May. 2016. ISBN 2025866135. doi: DOE/EIA-0484(2014).
- [2] Faith Birol, Laura Cozzi, Tim Gould, Amos Bromhead, and Robert Priddle. World Outlook Energy. *World Energy Outlook 2015*, pages 1–12, 2015. ISSN 0140489X. doi: 10.1787/weo-2014-en.
- [3] Paul Breeze. *Power Generation Technologies*. Newnes, 2nd edition, 2014. ISBN 9780080983363.
- [4] Robert B Jackson, Josep G Canadell, Corinne Le Quéré, Robbie M Andrew, Jan Ivar Korsbakken, Glen P Peters, and Nebojsa Nakicenovic. Reaching peak emissions. *Nature Climate Change*, 338(October):1–4, 2015. ISSN 1758-6798. doi: 10.1038/nclimate2892. URL <http://dx.doi.org/10.1038/nclimate2892>.
- [5] Jeffrey Phillips. Coal Power Generation for the 21st Century: This is Not Your Father's Coal Power Plant, 2012. URL <http://www.slideshare.net/igccengr/21st-century-coal-power-plants>.
- [6] Muslim Dvoyashkin. *Introduction to supercritical fluids*. Handbook of Green Chemistry, 4 edition, 2010.
- [7] Maartje F. Kemmere and Thierry Meyer. *Supercritical Carbon Dioxide*. Wiley-VCH Verlag GmbH & Co. KGaA, Weinheim, FRG, aug 2005. ISBN 9783527606726. doi: 10.1002/3527606726. URL <http://doi.wiley.com/10.1002/3527606726>.

- [8] V Dostal, M.J. Driscoll, and P. Hejzlar. A Supercritical Carbon Dioxide Cycle for Next Generation Nuclear Reactors. *Technical Report MIT-ANP-TR-100*, pages 1–317, 2004. doi: MIT-ANP-TR-100.
- [9] Yamin Liu, Qing Ye, Mei Shen, Jingjin Shi, Jie Chen, Hua Pan, and Yao Shi. *Carbon dioxide capture by functionalized solid amine sorbents with simulated flue gas conditions*, volume 45. 2011. ISBN 8657188273591. doi: 10.1021/es200619j.
- [10] Edward J. Parma, Steven A. Wright, Milton E. Vernon, Darryn D. Fleming, and Gary E. Rochau. Supercritical CO₂ Direct Cycle Gas Fast Reactor (SC-GFR) Concept. In *Supercritical CO₂ Power Cycle Symposium*, pages 91–94, 2011. ISBN 978-0-7918-5473-0. doi: 10.1115/SMR2011-6612.
- [11] BNL. Calder Hall Celebrates 40 Years of Operation, 1996.
- [12] Darryn Fleming, Tom Conboy, Gary Rochau, Thomas Holschuh, and Robert Fuller. Scaling Considerations for a Multi-Megawatt Class Supercritical CO₂ Brayton Cycle and Path Forward for Commercialization. In *ASME Turbo Expo 2012*, pages 1–8, Copenhagen, Denmark, 2012.
- [13] David J. Young. *High Temperature Oxidation and Corrosion of Metals*, volume 1. Elsevier, 2008. ISBN 9780080445878. doi: 10.1016/S1875-9491(08)00023-9.
- [14] J.R. Davis, editor. *ASM Specialty Handbook: Heat-Resistant Materials*. ASM International, 1997. ISBN 978-0-87170-596-9.
- [15] Thermodynamics-Gibbs Free Energy, 2004. URL <http://www.wiley.com/college/pratt/0471393878/student/review/thermodynamics/4{ }gibbs.html>.
- [16] A.T. Fromhold. *Theory of Metal Oxidation*. North Holland Publishing, Company, Amsterdam, 1976. ISBN 0444109579.

- [17] D. Caplan and G. I. Sproule. Effect of oxide grain structure on the high-temperature oxidation of Cr. *Oxidation of Metals*, 9(5):459–472, 1975. ISSN 0030770X. doi: 10.1007/BF00611694.
- [18] D Caplan, R J Hussey, G I Sproule, and M J Graham. Effect of Carbon on Cavity Formation During the High-Temperature Oxidation of Ni. 14(4), 1980.
- [19] G. Garnaud and Robert A. Rapp. Thickness of the oxide layers formed during the oxidation of iron. *Oxidation of Metals*, 11(4):193–198, 1977. ISSN 0030770X. doi: 10.1007/BF00606543.
- [20] J.S. Dunn. The High Temperature Oxidation of Metals. *Proceedings of the Royal Society of London*, 111(757):203–209, 1926.
- [21] Edward McCafferty. *Introduction to Corrosion Science*. Springer New York, New York, NY, 2010. ISBN 978-1-4419-0454-6. doi: 10.1007/978-1-4419-0455-3. URL <http://link.springer.com/10.1007/978-1-4419-0455-3>.
- [22] V R Howes. THE SPALLING OF CHROMIUM OXIDE ON A N Fe-Cr ALLOY. 6 (June):549–551, 1966.
- [23] Michael Schutze and D.R. Holmes. *Protective Oxide Scales and Their Breakdown*. Wiley, 1997. ISBN 978-0-471-95904-5.
- [24] Jun-you Liu, Feng Li, Jie Liu, Yi Zhang, Jin-cheng Jiang, and Dun-xu Zou. Oxidation behavior of the Fe-36Al-0.09C-0.09B-0.04Zr alloy at 1250 degrees C. *International Journal of Minerals Metallurgy and Materials*, 17(4):441–447, 2010. ISSN 1674-4799. doi: 10.1007/s12613-010-0338-0.
- [25] Fen Ren Chien and R. Brown. Cyclic oxidation of Haynes 230 alloy. *Journal of Materials Science*, 27(6):1514–1520, 1992. ISSN 00222461. doi: 10.1007/BF00542912.

- [26] F. Rouillard and T. Furukawa. Corrosion of 9-12Cr ferritic-martensitic steels in high-temperature CO₂. *Corrosion Science*, (JANUARY), 2016. ISSN 0010938X. doi: 10.1016/j.corsci.2016.01.009.
- [27] D.R. Holmes, R.B. Hill, and L.M. Wyatt. Corrosion of steels in CO₂. In *British Nuclear Energy Society*, Reading University, 1974.
- [28] Daniel Herring. What to Do About Metal Dusting. (August):33–35, 2003.
- [29] Jacob Mahaffey, David Adam, Andrew Brittan, Mark Anderson, and Kumar Sridharan. Corrosion of Alloy Haynes 230 in High Temperature Supercritical Carbon Dioxide with Oxygen Impurity Additions. *Oxidation of Metals*, 2016. ISSN 0030-770X. doi: 10.1007/s11085-016-9654-8. URL <http://link.springer.com/10.1007/s11085-016-9654-8>.
- [30] W J Quadackers and H Schuster. Corrosion of High Temperature Alloys in the Primary Circuit Helium of High Temperature Gas Cooled Reactors. -Part I: Theroetical Backround. 150:141–150, 1985.
- [31] J. Ehlers, D.J. Young, E.J. Smaardijk, A.K. Tyagi, H.J. Penkalla, L. Singheiser, and Willem J. Quadackers. Enhanced Oxidation of the 9%Cr Steel P91 in Water Vapour Containing Environments. *Corrosion Science*, (48):3428–3454, 2006.
- [32] Stuart R J Saunders and Neil L McCartney. Current Understanding of Steam Oxidation - Power Plant and Laboratory Experience. In *High-Temperature Oxidation and Corrosion 2005*, volume 522 of *Materials Science Forum*, pages 119–128. Trans Tech Publications, 2006. doi: 10.4028/www.scientific.net/MSF.522-523.119.
- [33] V.G. Kritsky. *Water chemistry and corrosion of nuclear power plant structural materials*. Russian Materials Monograph Series. American Nuclear Society, 1999. ISBN 9780894485657. URL <https://books.google.com/books?id=xOVSAAAAMAAJ>.

- [34] *Process piping : ASME code for pressure piping, B31*. ASME, 1999. ISBN 0-7918-2760-7.
- [35] Chih-Chun Haieh and Weite Wu. Overview of Intermetallic Sigma (σ) Phase Precipitation in Stainless Steels. *ISRN Metallurgy*, page 16, 2012. doi: 10.5402/2012/732471.
- [36] Jacob Jellinek and Mark Anderson. Corrosion Behavior of Alloys in High Temperature Supercritical Carbon Dioxide. In *NACE International*, 2012.
- [37] L. Tan, M. Anderson, D. Taylor, and T. R. Allen. Corrosion of austenitic and ferritic-martensitic steels exposed to supercritical carbon dioxide. *Corrosion Science*, 53(10): 3273–3280, 2011. ISSN 0010938X. doi: 10.1016/j.corsci.2011.06.002.
- [38] G. Cao, V. Firouzdor, K. Sridharan, M. Anderson, and T. R. Allen. Corrosion of austenitic alloys in high temperature supercritical carbon dioxide. *Corrosion Science*, 60:246–255, 2012. ISSN 0010938X. doi: 10.1016/j.corsci.2012.03.029. URL <http://dx.doi.org/10.1016/j.corsci.2012.03.029>.
- [39] V. Firouzdor, K. Sridharan, G. Cao, M. Anderson, and T. R. Allen. Corrosion of a stainless steel and nickel-based alloys in high temperature supercritical carbon dioxide environment. *Corrosion Science*, 69:281–291, 2013. ISSN 0010938X. doi: 10.1016/j.corsci.2012.11.041. URL <http://dx.doi.org/10.1016/j.corsci.2012.11.041>.
- [40] Jacob Mahaffey and Mark Anderson. MATERIALS CORROSION IN HIGH TEMPERATURE SUPERCRITICAL CARBON DIOXIDE. In *The 4th International Symposium - Supercritical CO2 Power Cycles*, pages 1–8, Pittsburgh, Pennsylvania, 2014.
- [41] P A Strakey, O N Dogan, G R Holcomb, and G A Richards. Technology needs for fossil

- fuel supercritical CO₂ power systems. *The 4th International Symposium - Supercritical CO₂ Power Cycles*, 2014. ISSN 1098-6596. doi: 10.1017/CBO9781107415324.004.
- [42] H Saari, R Petrusenko, K Zanganeh, C Parks, and B Maybee. Corrosion testing of high temperature materials in supercritical carbon dioxide. *The 4th International Symposium - Supercritical {CO}₂ Power cycles*, pages 1–13, 2014.
- [43] Robert Moore and Thomas Conboy. Metal Corrosion in a Supercritical Carbon Dioxide - Liquid Sodium Power Cycle. *Sandia Report*, (2012-0184):1–50, 2012.
- [44] Ling Feng He, Paul Roman, Bin Leng, Kumar Sridharan, Mark Anderson, and Todd R. Allen. Corrosion behavior of an alumina forming austenitic steel exposed to supercritical carbon dioxide. *Corrosion Science*, 82:67–76, 2014. ISSN 0010938X. doi: 10.1016/j.corsci.2013.12.023. URL <http://dx.doi.org/10.1016/j.corsci.2013.12.023>.
- [45] Bruce a Pint and James R Keiser. THE EFFECT OF TEMPERATURE ON THE sCO₂ COMPATIBILITY OF CONVENTIONAL STRUCTURAL ALLOYS. In *The 4th International Symposium - Supercritical CO₂ Power Cycles*, pages 1–13, Pittsburgh, Pennsylvania, 2014.
- [46] Jacob T Mahaffey and David Adam. Effect of Oxygen Impurity on Corrosion in Supercritical CO₂ Environments. In *5th international Symposium on Supercritical CO₂ Power Cycles*, San Antonio, Texas, 2016.
- [47] Bin Leng, Paul Roman, and Lingfeng He. Corrosion Behavior of 347 and 316 Stainless Steels in Supercritical Carbon Dioxide of Different Purity. Technical report, University of Wisconsin-Madison, 2013.
- [48] Ho Jung Lee, Gokul Obulan Subramanian, Sung Hwan Kim, and Changheui Jang. Effect of pressure on the corrosion and carburization behavior of chromia-forming heat-

- resistant alloys in high-temperature carbon dioxide environments. *Corrosion Science*, 111:649–658, 2016. ISSN 0010938X. doi: 10.1016/j.corsci.2016.06.004. URL <http://dx.doi.org/10.1016/j.corsci.2016.06.004>.
- [49] Bruce a Pint. The Effect of Temperature and Pressure on Supercritical CO₂ Compatibility of Conventional Structural Alloys. In *Proceeds of the supercritical CO₂ power cycle symposium*, San Antonio, Texas, 2015.
- [50] Gerald H. Meier, Keeyoung Jung, Nan Mu, Nazik M. Yanar, Frederick S. Pettit, J. Pirón Abellán, Tomasz Olszewski, L. Nieto Hierro, Willem J. Quadackers, and Gordon R. Holcomb. Effect of alloy composition and exposure conditions on the selective oxidation behavior of ferritic Fe-Cr and Fe-Cr-X alloys. *Oxidation of Metals*, 74(5-6):319–340, 2010. ISSN 0030770X. doi: 10.1007/s11085-010-9215-5.
- [51] Soraya Bouhieda, Fabien Rouillard, Vincent Barnier, and Krzysztof Wolski. Selective oxidation of chromium by O₂ impurities in CO₂ during initial stages of oxidation. *Oxidation of Metals*, 80(5-6):493–503, 2013. ISSN 0030770X. doi: 10.1007/s11085-013-9392-0.
- [52] J E Antill and J B Warburton. Behaviour of Carbon During the Corrosion of Stainless Steel by Carbon Dioxide. 7(February):645–649, 1967.
- [53] Y Gong, D J Young, P Kontis, Y L Chiu, H Larsson, A Shin, J M Pearson, M P Moody, and R C Reed. On the breakaway oxidation of Fe₉Cr₁Mo steel in high pressure CO₂. *Acta Materialia*, pages 1–14, 2017. ISSN 1359-6454. doi: 10.1016/j.actamat.2017.02.034. URL <http://dx.doi.org/10.1016/j.actamat.2017.02.034>.
- [54] W J Quadackers. Corrosion of High Temperature Alloys in the Primary Circuit Helium of High Temperature Gas Cooled Reactors . Part II : Experimental Results. 347:335–347, 1985.

- [55] Yet-Ming Chiang, Dunbar P. Birnie, and Kingery David. *Physical Ceramics: Principles for Ceramic Science and Engineering*. Wiley, 1996. ISBN 0471598739, 9780471598732.
- [56] L Latu-Romain, Y Parsa, S Mathieu, M Vilasi, M Ollivier, A Galerie, and Y Wouters. Duplex n- and p-Type Chromia Grown on Pure Chromium: A Photoelectrochemical and Microscopic Study. *Oxidation of Metals*, 86(5):1–13, 2016. ISSN 1573-4889. doi: 10.1007/s11085-016-9648-6. URL <http://dx.doi.org/10.1007/s11085-016-9648-6>.
- [57] F.N. Rhines. A metallographic study of internal oxidation in the alpha solid solutions of copper. *Trans. Met. Soc. AIME*, (137):246–286, 1940.
- [58] L. Latu-Romain, Y. Parsa, S. Mathieu, M. Vilasi, A. Galerie, and Y. Wouters. Towards the growth of stoichiometric chromia on pure chromium by the control of temperature and oxygen partial pressure. *Corrosion Science*, (February):0–1, 2017. ISSN 0010938X. doi: 10.1016/j.corsci.2017.07.005. URL <http://dx.doi.org/10.1016/j.corsci.2017.07.005>.
- [59] X Ledoux, S Mathieu, M Vilasi, Y Wouters, and M Wagner. Oxide Growth Characterization During Short-Time Oxidation of a Commercially Available. pages 25–35, 2013. doi: 10.1007/s11085-013-9367-1.
- [60] Chunwen Sun, Rob Hui, Wei Qu, and Sing Yick. Progress in corrosion resistant materials for supercritical water reactors. *Corrosion Science*, 51(11):2508–2523, 2009. ISSN 0010938X. doi: 10.1016/j.corsci.2009.07.007. URL <http://dx.doi.org/10.1016/j.corsci.2009.07.007>.
- [61] Peter Kritzer. Corrosion in high-temperature and supercritical water and aqueous solutions: A review. *Journal of Supercritical Fluids*, 29(1-2):1–29, 2004. ISSN 08968446. doi: 10.1016/S0896-8446(03)00031-7.

- [62] Malgorzata M Lencka and Richard E Riman. Thermodynamic Modeling of Hydrothermal Synthesis of. *Chemistry Materials*, 5(8):61–70, 1993. ISSN 0897-4756. doi: 10.1021/cm00025a014. URL <http://pubs.acs.org/doi/pdf/10.1021/cm00025a014>.
- [63] Mh Lietzke and C Mullins. The thermal decomposition of carbon dioxide. *Journal of Inorganic and Nuclear Chemistry*, 43(8):1769–1771, 1981. ISSN 00221902. doi: 10.1016/0022-1902(81)80381-8. URL <http://www.sciencedirect.com/science/article/pii/0022190281803818>.
- [64] X G Zheng and D J Young. High-Temperature Corrosion of Cr₂O₃-Forming Alloys in CO–CO₂–N₂ Atmospheres. 42, 1994.
- [65] L. Latu-Romain, S. Mathieu, M. Vilasi, G. Renou, S. Coindeau, A. Galerie, and Y. Wouters. The Role of Oxygen Partial Pressure on the Nature of the Oxide Scale on a NiCr Model Alloy. *Oxidation of Metals*, pages 1–13, 2016. ISSN 0030770X. doi: 10.1007/s11085-016-9670-8. URL "<http://dx.doi.org/10.1007/s11085-016-9670-8>".
- [66] Ming-Yih Su and Simkovich George. Point Defect Structure of Chromium (III) Oxide. *Non-Stoichiometric Compounds*, 276:99–113, 1989.
- [67] D.J. Young. *High Temperature Oxidation and Corrosion of Metals*. Corrosion Series. Elsevier Science, 2016. ISBN 9780081001196. URL <https://books.google.com/books?id=TVXBBwAAQBAJ>.
- [68] I. Wolf and H. J. Grabke. A study on the solubility and distribution of carbon in oxides. *Solid State Communications*, 54(1):5–10, 1985. ISSN 00381098. doi: 10.1016/0038-1098(85)91021-X.
- [69] G.R. Smolik, D.a. Petti, and S.T. Schuetz. Oxidation and volatilization of TZM alloy in air. *Journal of Nuclear Materials*, 283-287(January):1458–1462,

2000. ISSN 00223115. doi: 10.1016/S0022-3115(00)00303-2. URL <http://www.sciencedirect.com/science/article/pii/S0022311500003032>
<http://linkinghub.elsevier.com/retrieve/pii/S0022311500003032>.
- [70] Haynes International. HAYNES ® 625 alloy. 2017.
- [71] S Floreen, G E Fuchs, and W J Yang. The Metallurgy of Alloy 625. pages 13–37, 1994.
- [72] K Linga Murty and M D Mathew. Nondestructive monitoring of structural materials using automated ball indentation (ABI) technique. *Nuclear Engineering and Design*, 228(1-3):81–96, 2004. doi: 10.1016/j.nucengdes.2003.06.006.
- [73] Special Metals. Inconel Alloy 740H, 2017. URL <http://www.specialmetals.com/assets/smc/documents/alloys/inconel/inconel-alloy-740-h.pdf>.
- [74] Haynes International. Haynes 282 Alloy, 2017. URL <http://haynesintl.com/docs/default-source/pdfs/new-alloy-brochures/high-temperature-alloys/brochures/282-brochure.pdf?sfvrsn=20>.
- [75] J.P. Shingledecker. EPRI_Ni-Based Alloys for Advanced Ultra supercritical Steam Boilers, 2014.
- [76] Fan Zhang, W Cao, S Chen, C Zhang, and J Zhu. Precipitation Simulation of Ni-base Superalloys Outline of Presentation, 2014. URL https://www.nist.gov/sites/default/files/documents/mml/msed/thermodynamics_{_}kinetics/Precipitation-Simulation_{_}CompuTherm.pdf.
- [77] EPRI. U.S. Department of Energy and Ohio Coal Development Office Advanced Ultra-Supercritical Materials Project for Boilers and Steam Turbines: Summary of Results. Technical report, 2011.

- [78] Gordon R Holcomb. HIGH PRESSURE STEAM OXIDATION OF NI-BASE SUPER-ALLOYS IN ADVANCED ULTRA-SUPERCRITICAL STEAM BOILERS AND TURBINES. Technical report.
- [79] W. E. Ruther, R. R. Schlueter, R. H. Lee, and R. K. Hart. Corrosion Behavior of Steels and Nickel Alloys in Superheated Steam. *Corrosion*, 22:147–155, 1965.
- [80] I. G. Wright, P. F. Tortorelli, and M. Schütze. Oxide Growth and Exfoliation on Alloys Exposed to Steam. Technical report, Report 1013666, EPRI, 2007.
- [81] I. G. Wright and R. B. Dooley. A Review of the Oxidation Behaviour of Structural Alloys in Steam. *International Materials Reviews*, 55(3):129–167, 2010.
- [82] J. Sarver. Private communication from J. Sarver, Babcock & Wilcox, to I. Wright, Oak Ridge National Laboratory, 2009.
- [83] H. E. McCoy and B. McNabb. Corrosion of Several Metals in Supercritical Steam at 538C. Technical report, Report ORNL/TM-5781, Oak Ridge National Laboratory, 1977.
- [84] J. C. Griess, J. M. Devan, and W. A. Maxwell. Effect of a high heat flux on the corrosion of 2.25Cr-1Mo steel in superheated steam. *Materials Performance*, 17(1):9–15, 1978.
- [85] Michael Scott. Eskolaite. URL <http://rruff.info/chem=Cr,0/display=default/R060892>.
- [86] University of Arizona. Hematite. URL <http://rruff.info/chem=Fe,0/display=default/R040024>.
- [87] Merry Widow Mine. Magnetite. URL <http://rruff.info/chem=Fe,0/display=default/R060191>.

- [88] James Shigley. Chromite. URL <http://rruff.info/chem=Fe,0/display=default/R110059>.
- [89] William W. Bunsenite. URL <http://rruff.info/chem=Ni,0/display=default/R080121>.

Appendices

Appendix A

Alloy Compositions

Table A.1: Composition of tested materials.

	740H	H230	617	H282	H625	718	800H	HR120	709*	310S	316L	347	T122	T92	Ni-200	Pure Cr	Ni-20Cr
Si	.17	.31	.04	.15	.25	.09	.29	.60		.63	.29	.77	.10	.10	.07		
S	.00	<.002	<.001		<.002		<.001			.00	<0.001	.02	.00	.00			
P	.00	.01	<.005		.01	<.005				.02	.03	.03	.02	.02			
Mn	.25	.52	.07	.30	.26	.23	.77	.70		1.70	1.56	1.66	.45	.45	.24		
C	.02	.10	.07	.06	.02	.05	.06	.05		.02	.03	.05	.12	.12	.02	.01	
Cr	24.57	22.08	22.04	20.00	21.89	18.10	19.63	25.00	20.00	25.34	17.09	17.67	8.94	8.94		100.00	20.00
Ni	50.04	Bal	Bal	57.00	Bal	53.10	33.17	37.00	25.00	19.42	10.12	9.62	.21	.21	99.00		80.00
Mo	.35	1.23	9.49	8.50	8.59	3.06		1.00		.25	2.01	.38	.50	.50			
Cu	.02	.04				.09	.20			.19	.45	.38			.06		
V	.01												.20	.20			
W	.02	14.17					.50						1.91	1.91			
Nb	1.46				3.51	4.14	.70			<.01	.72	.08	.08				
Co	20.09	.21	12.58	10.00	.28	.30	3.00			.31	.20						
Pb						<.0005											
Fe	.15	1.02	1.13	1.50	5.00	18.50	44.89	Bal	Bal	Bal	Bal	Bal	Bal	Bal	.04		
Al	1.33	.37	1.21	1.50	.22	.53	.46	.10					.02	.02			
Ti	1.33	<.01	.43	2.10	.29	1.05	.53	.20			<.01						
Bi						<.00003											
B	.00	.00	.00	.01		.00		.00					.00	.00			
Ag						<.0002											
N	.00							.20			.05		.05	.47			
La		.01															
Ta	0.004				<.05	<.05					<.01	.21					

Appendix B

Volatility Diagrams

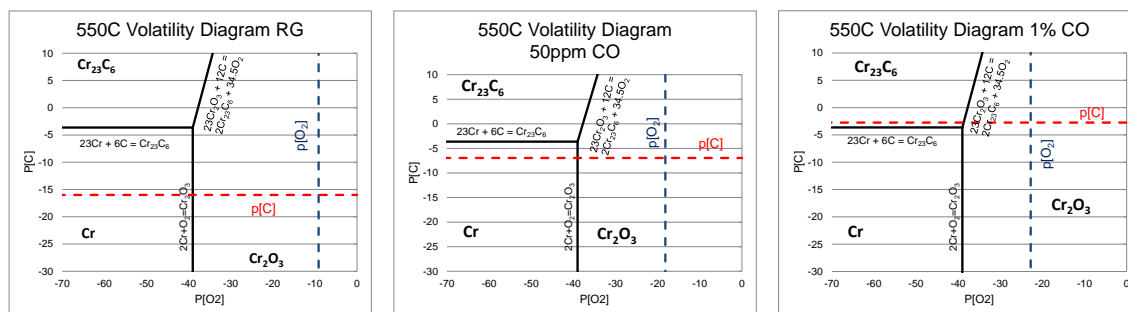


Figure B.1: Volatility diagrams for chromium oxide/carbide formation in research grade (left) 50ppm CO doped CO_2 (middle), and 1% CO doped CO_2 at 550°C.

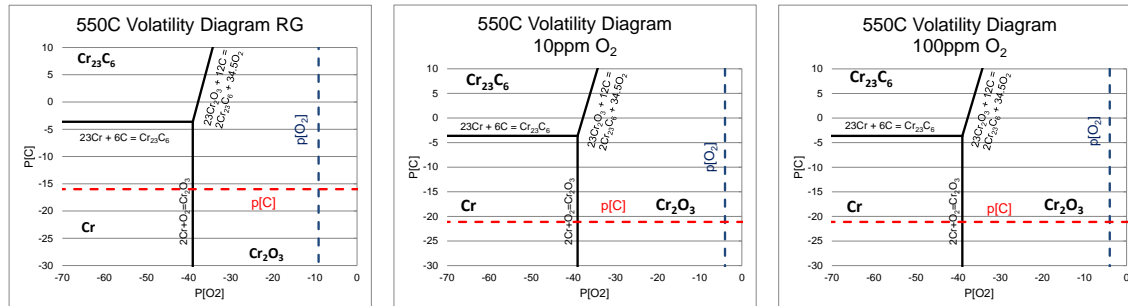


Figure B.2: Volatility diagrams for chromium oxide/carbide formation in research grade (left) 10ppm O_2 doped CO_2 (middle), and 100ppm O_2 doped CO_2 at 550°C.

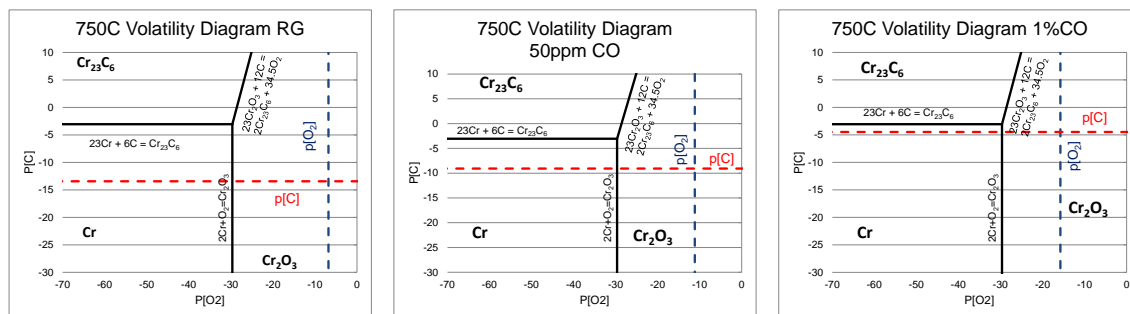


Figure B.3: Volatility diagrams for chromium oxide/carbide formation in research grade (left) 50ppm CO doped CO_2 (middle), and 1% CO doped CO_2 at 750°C .

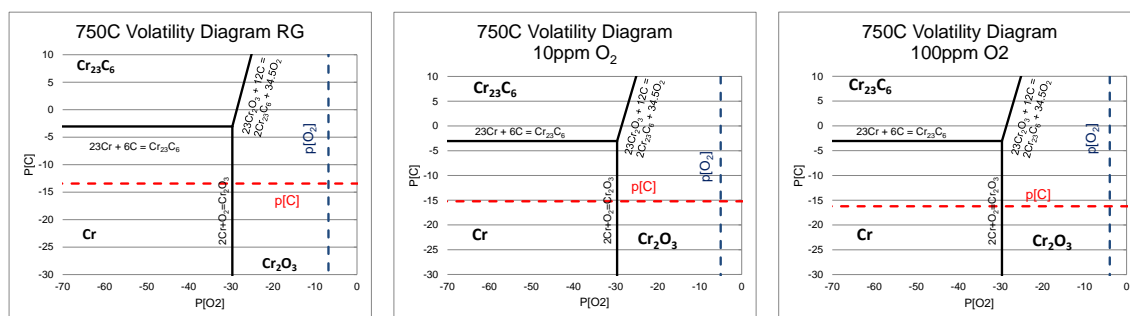


Figure B.4: Volatility diagrams for chromium oxide/carbide formation in research grade (left) 10ppm O_2 doped CO_2 (middle), and 100ppm O_2 doped CO_2 at 750°C .

Appendix C

Time Dependant Mass Change Data in s-CO₂

Environments

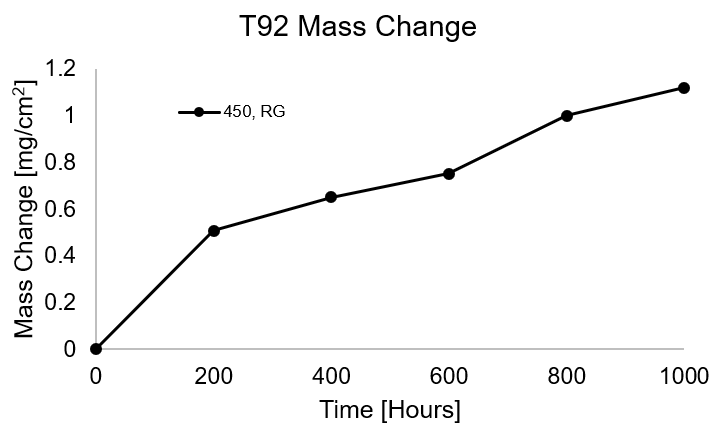


Figure C.1: Mass change results for alloy T92.

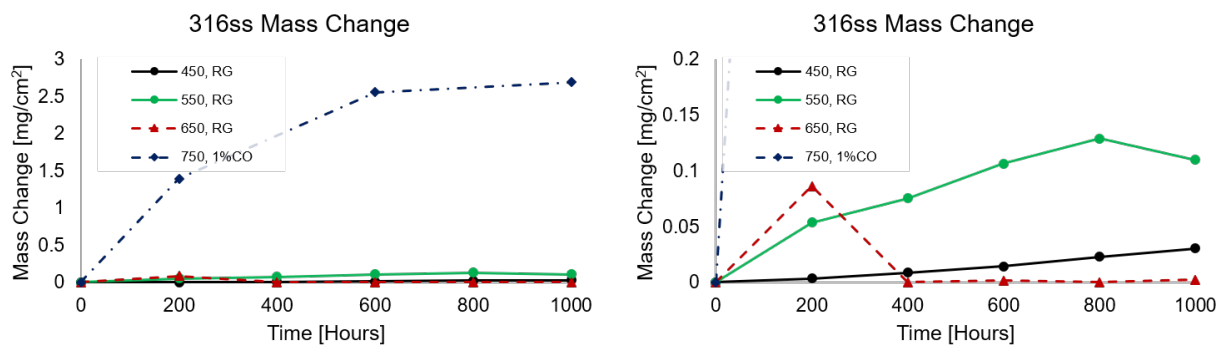


Figure C.2: Mass change results for alloy 316L.

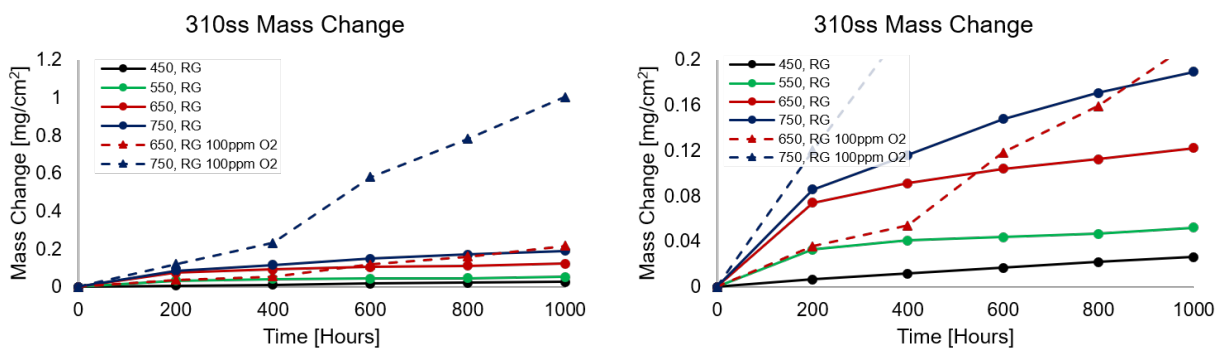


Figure C.3: Mass change results for alloy 310S.

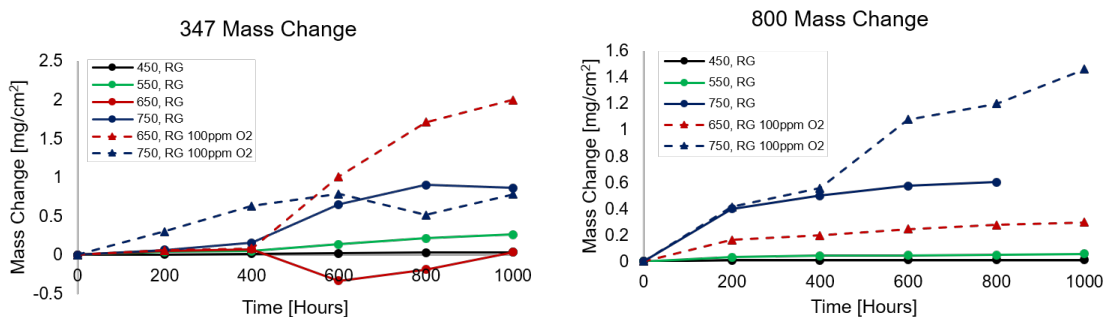


Figure C.4: Mass change results for alloys 346 (left) and 800H (right).

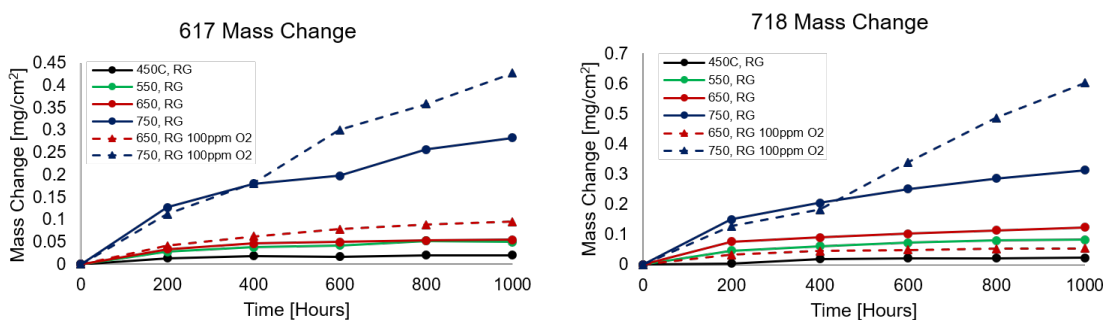


Figure C.5: Mass change results for alloys 617 (left) and 718 (right).

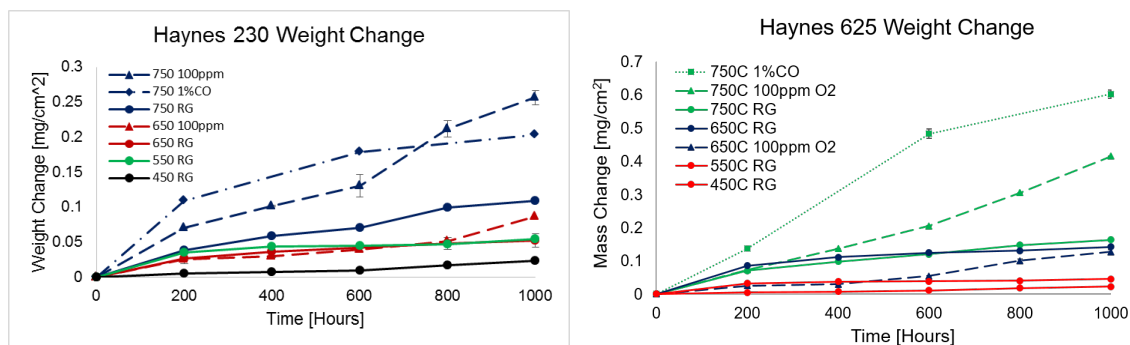


Figure C.6: Mass change results for alloys H230 (left) and H625 (right).

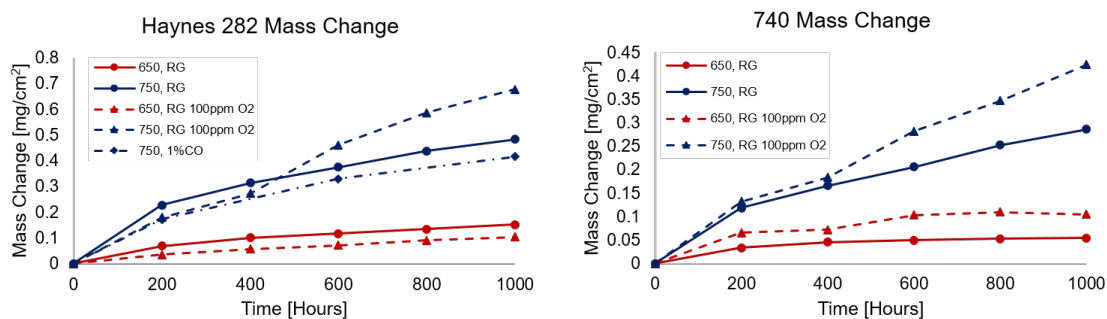


Figure C.7: Mass change results for alloys H282 (left) and 740H (right).

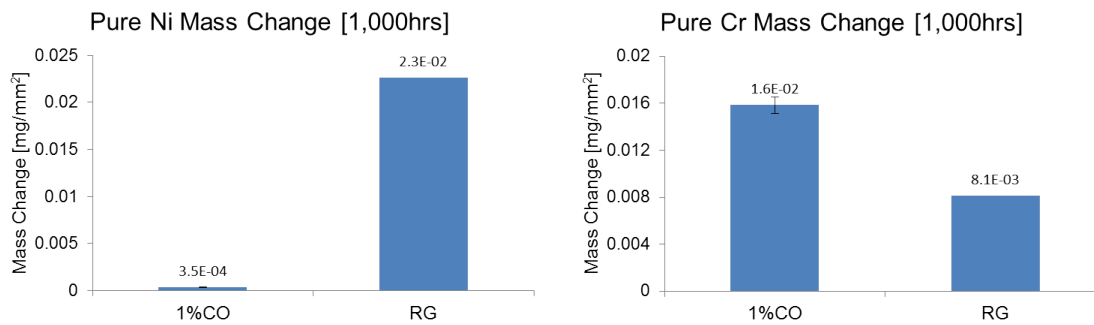


Figure C.8: Mass change results for pure Ni (left) and Cr (right).

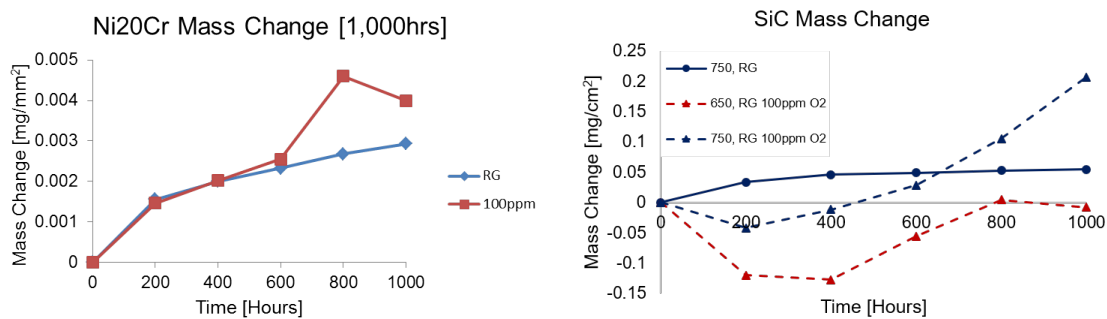


Figure C.9: Mass change results for alloys Ni-20Cr (left) and SiC (right).

Appendix D

Raman Spectral Summary

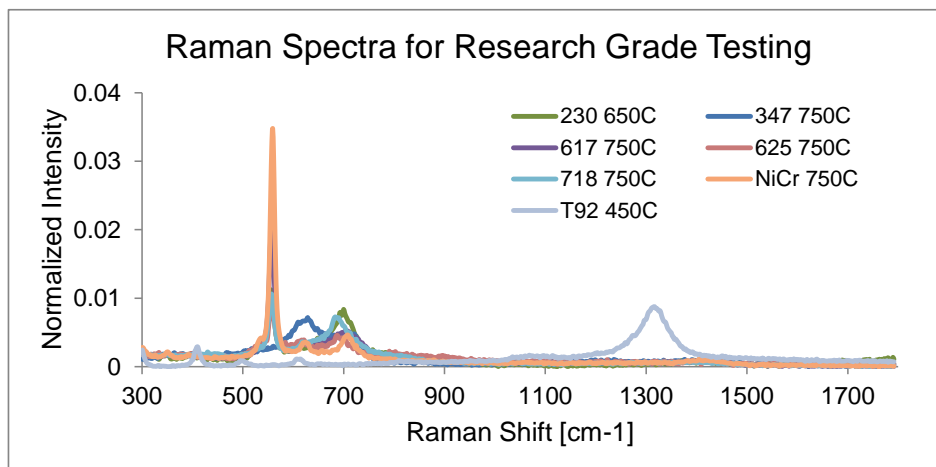


Figure D.1: Raman spectra for samples exposed to research grade CO₂ at maximum temperature testing condition.

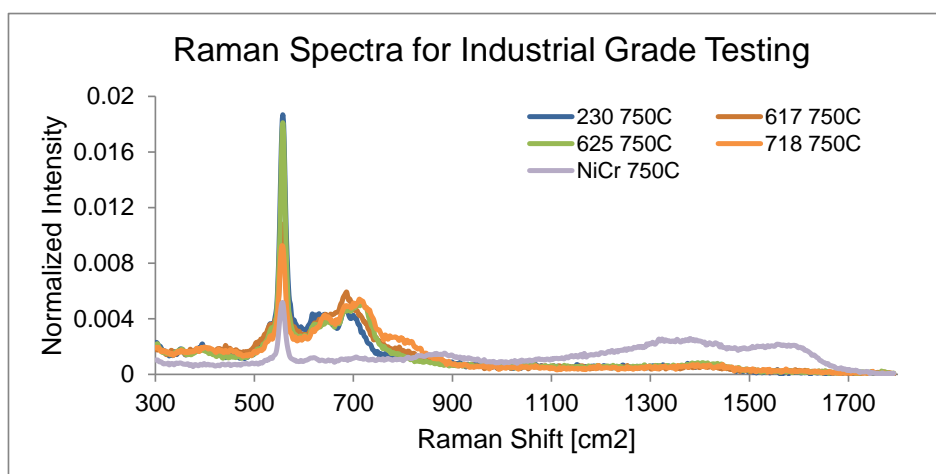


Figure D.2: Raman spectra for samples exposed to industrial grade CO₂ at maximum temperature testing condition.

Appendix E

Raman Standards

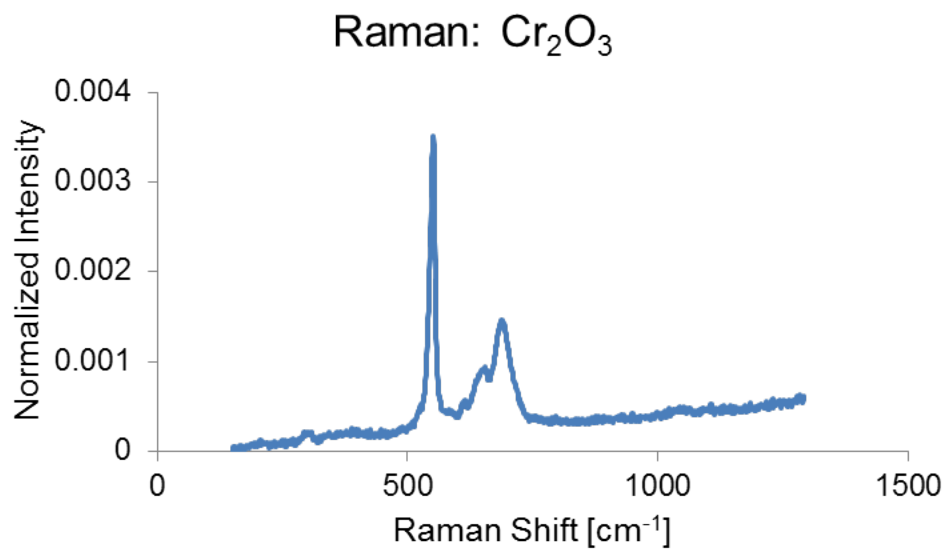


Figure E.1: Raman standard spectrum for Cr_2O_3 [85].

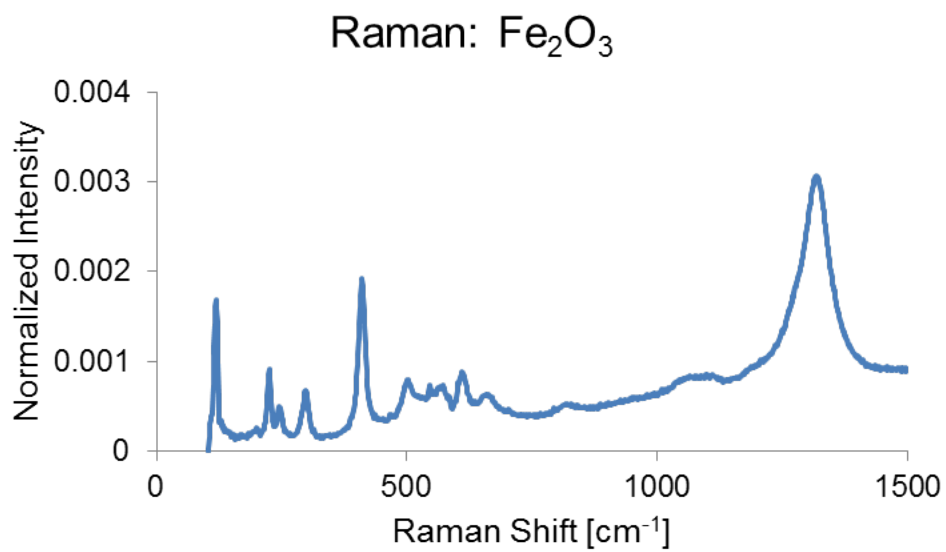


Figure E.2: Raman standard spectrum for Fe_2O_3 [86].

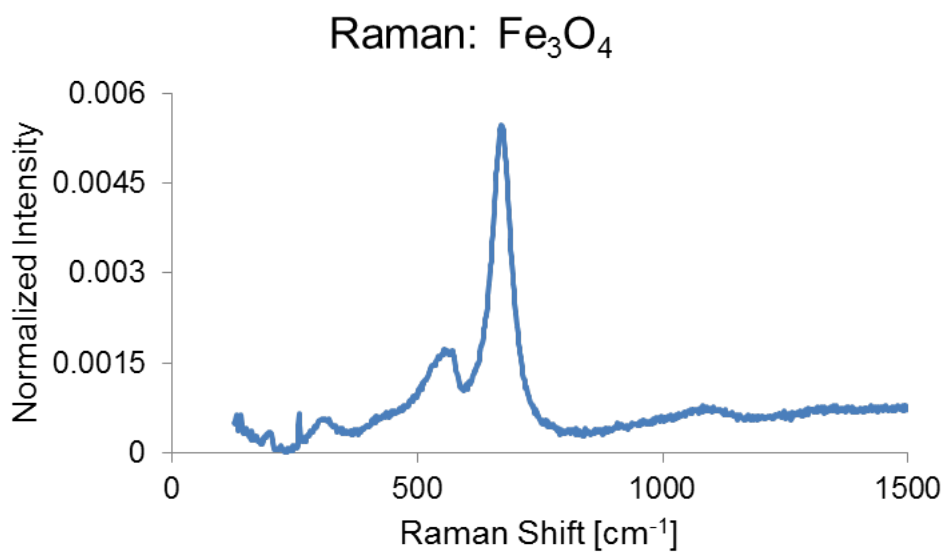


Figure E.3: Raman standard spectrum for Fe_3O_4 [87].

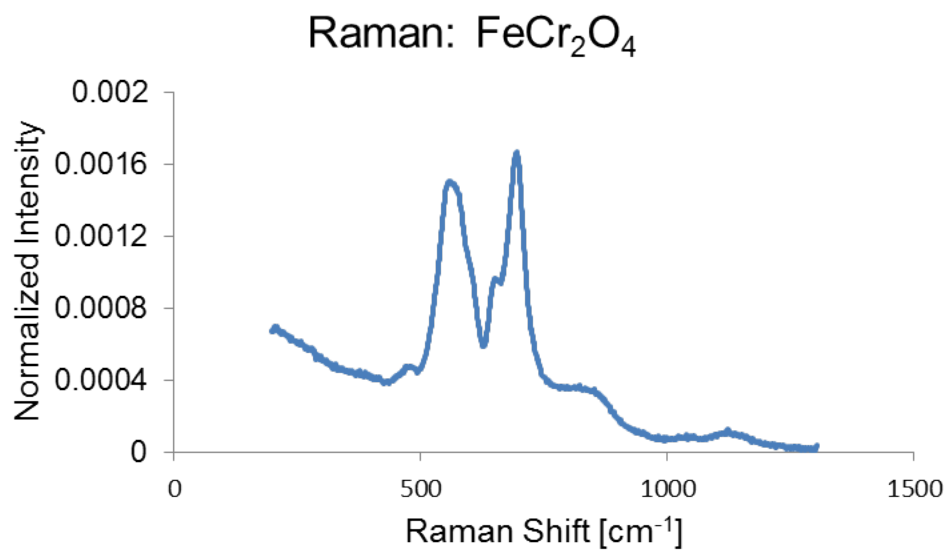


Figure E.4: Raman standard spectrum for FeCr_2O_4 [88].

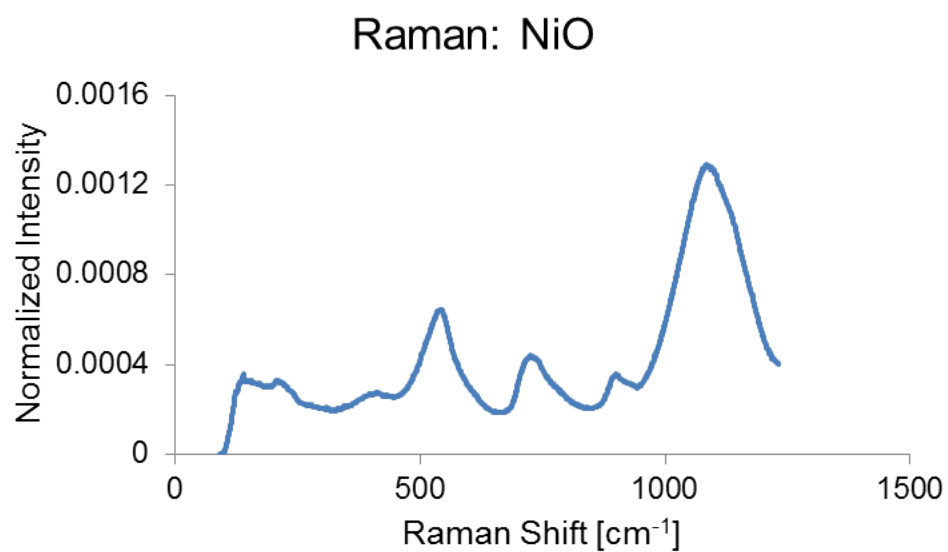


Figure E.5: Raman standard spectrum for NiO [89].

Appendix F

XRD Standards

All standards found using Bruker D8 Discovery DiFFRACEVA software with COD2013 database.

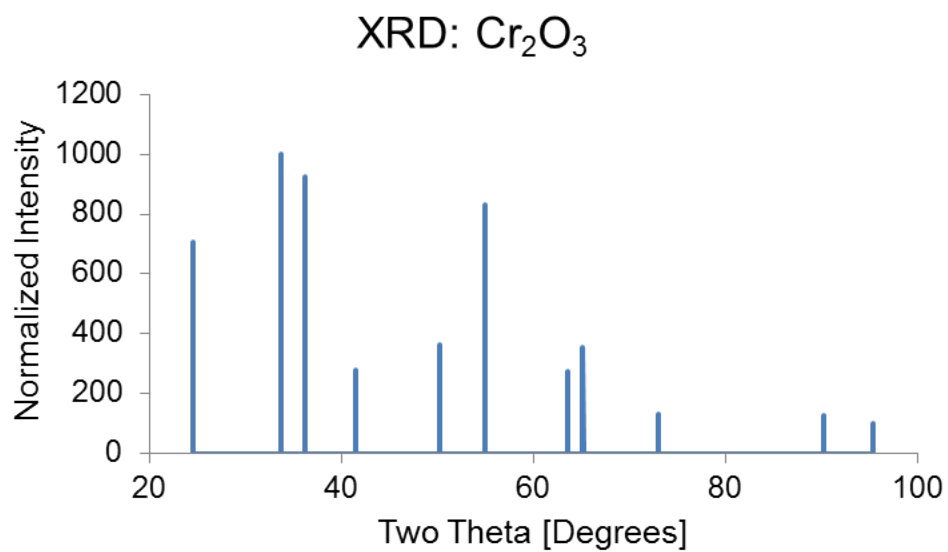


Figure F.1: XRD standard spectrum for Cr_2O_3 .

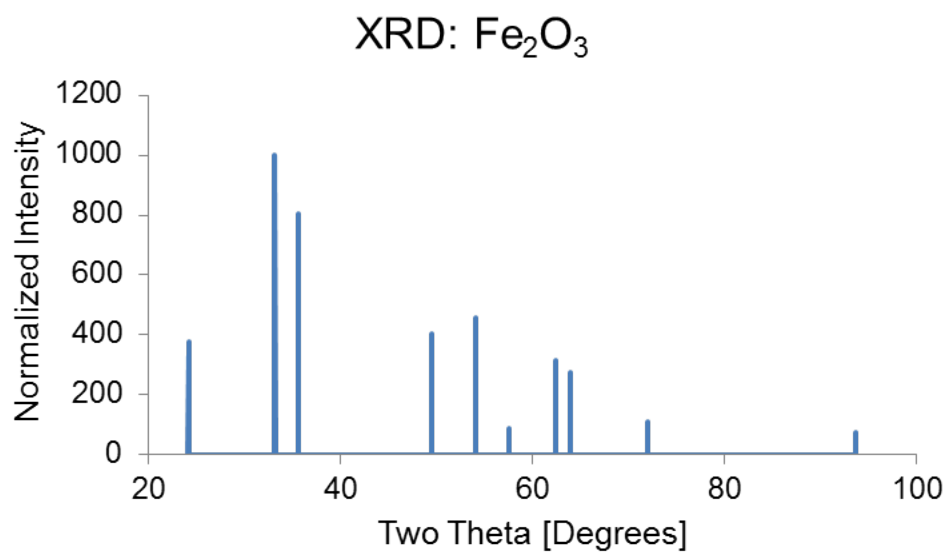


Figure F.2: XRD standard spectrum for Fe₂O₃.

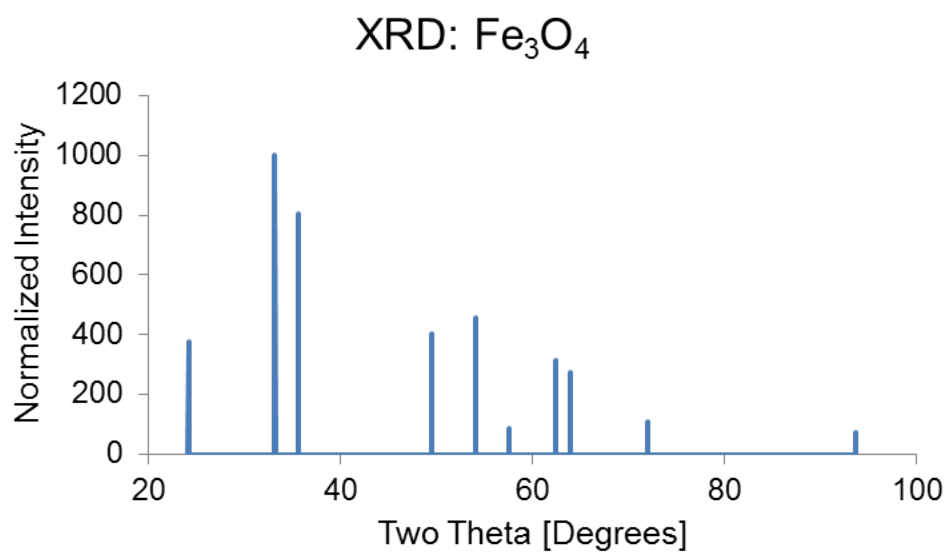


Figure F.3: XRD standard spectrum for Fe₃O₄.

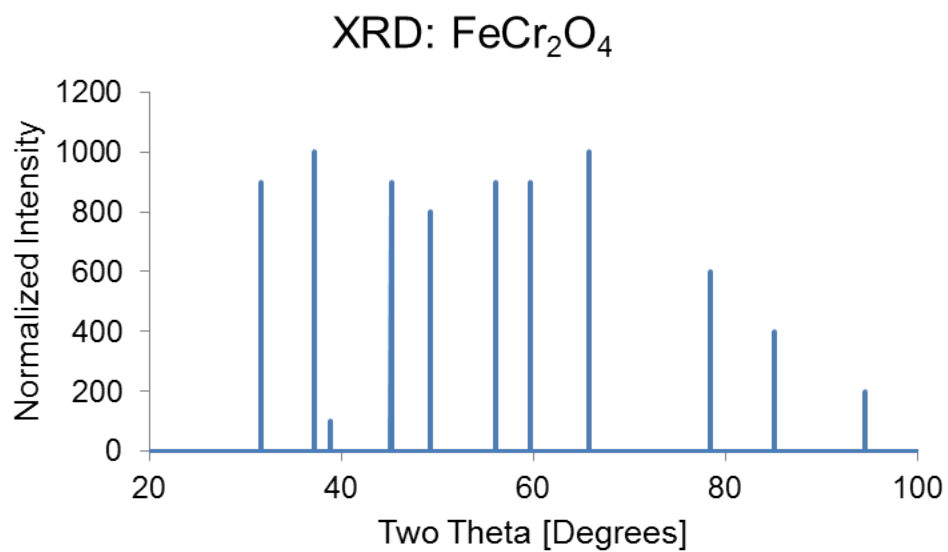


Figure F.4: XRD standard spectrum for FeCr_2O_4 .

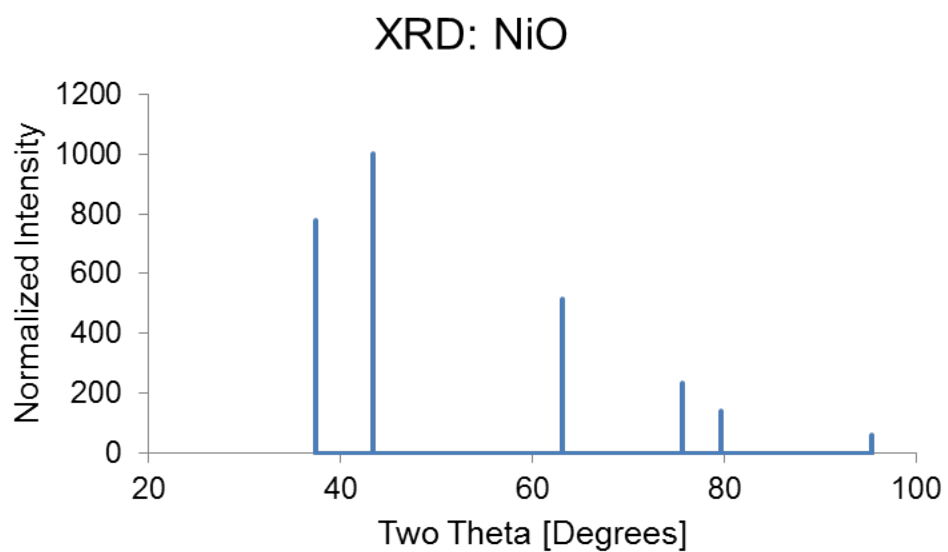


Figure F.5: XRD standard spectrum for NiO.

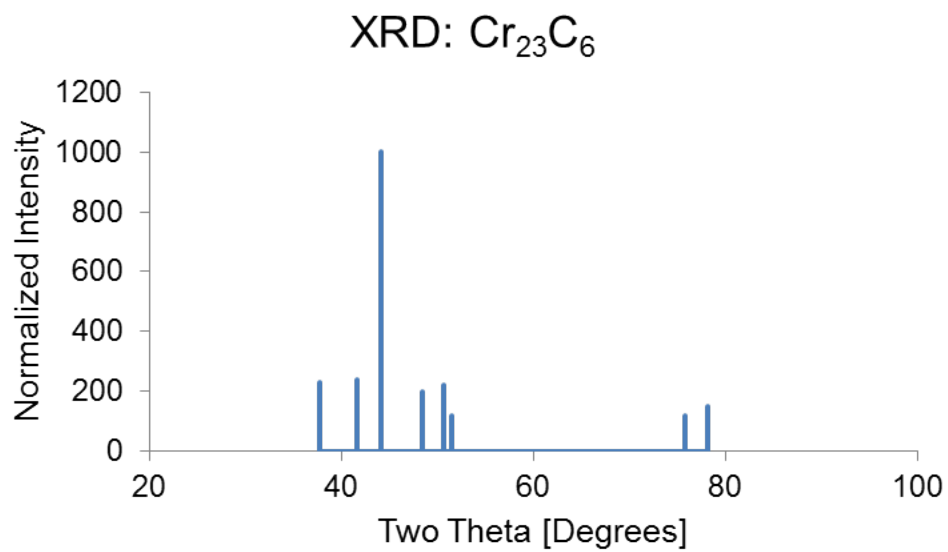


Figure F.6: XRD standard spectrum for Cr_{23}C_6 .

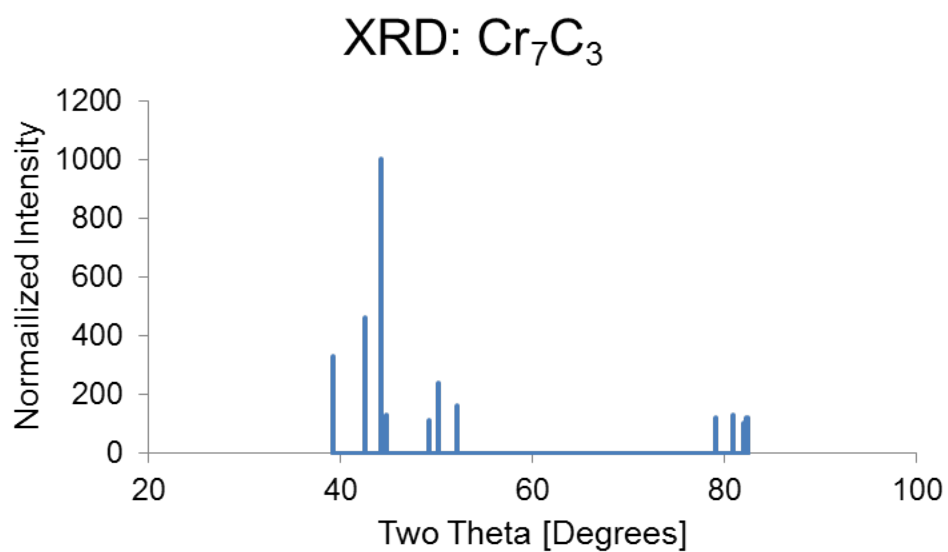


Figure F.7: XRD standard spectrum for Cr_7C_3 .

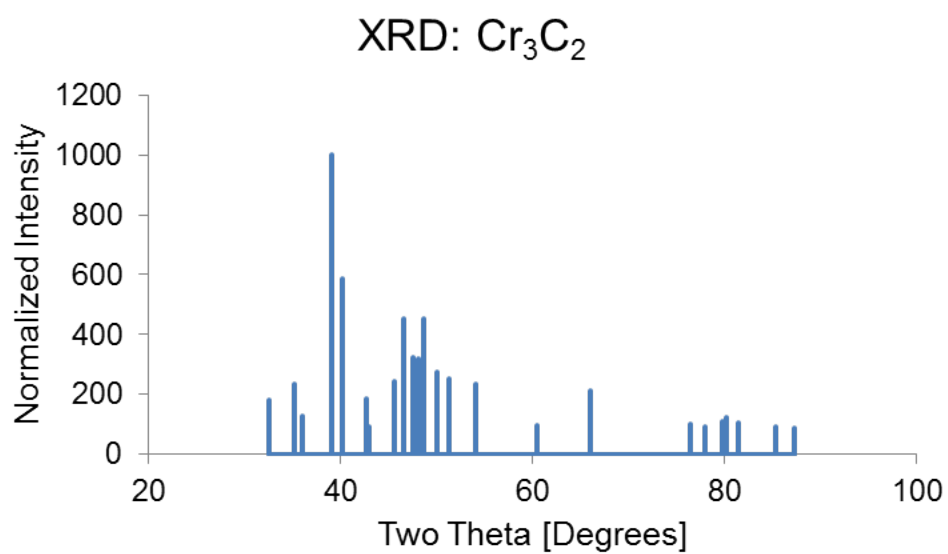


Figure F.8: XRD standard spectrum for Cr_3C_2 .

Appendix G

Round-Robin Mass Change

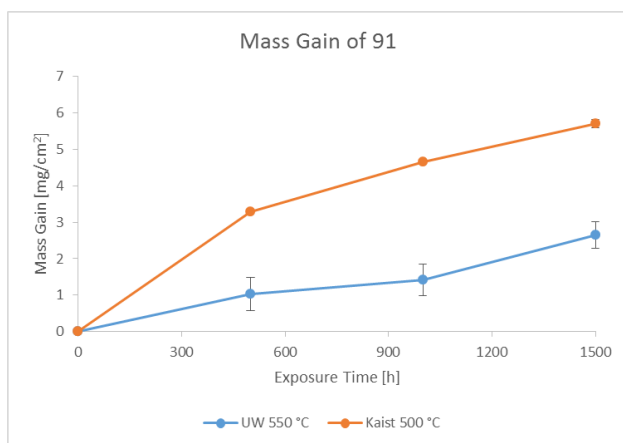


Figure G.1: Round Robin mass change results alloy T91 exposed to s-CO₂ at 550°C, 20MPa for 1500 hours.

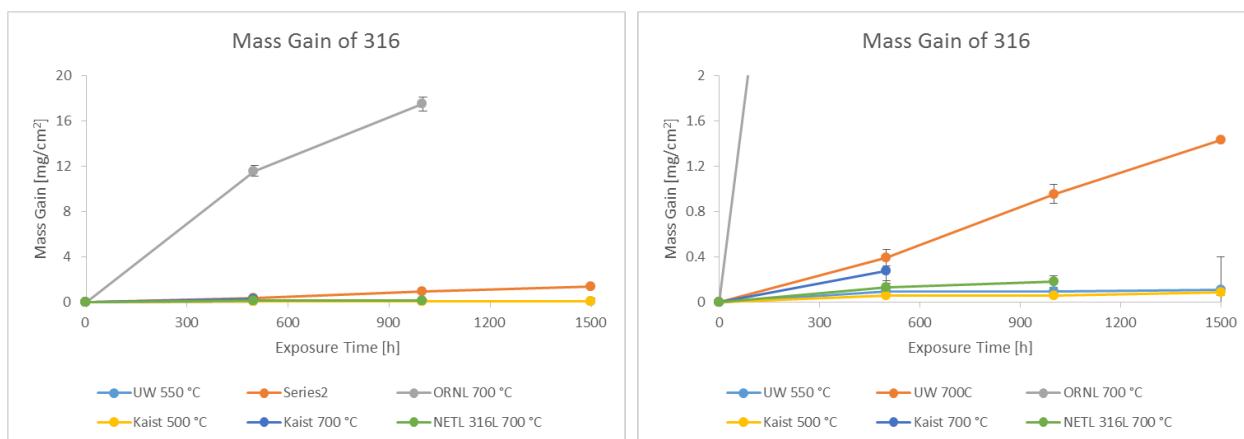


Figure G.2: Round Robin mass change results alloy 316 exposed to s-CO₂ at 550°C, 20MPa for 1500 hours..

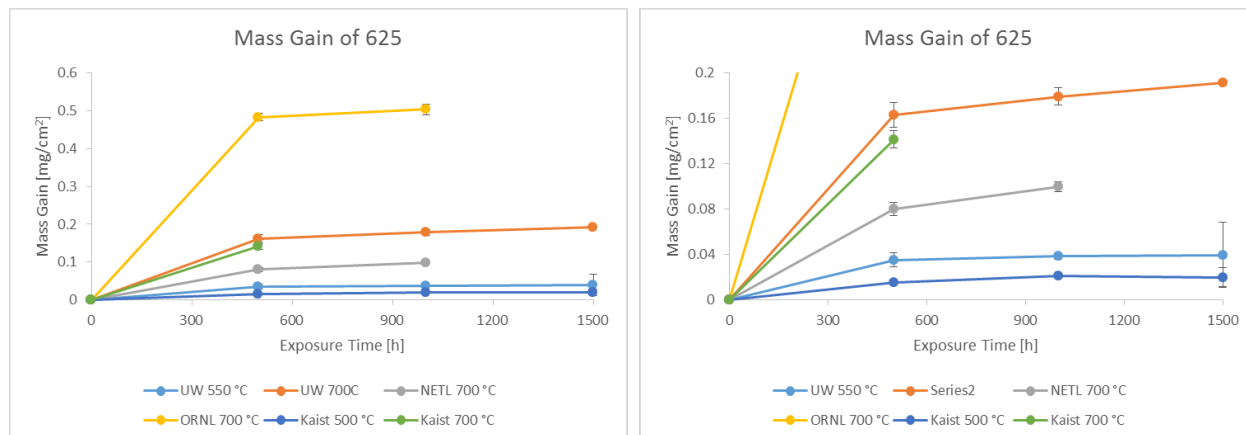


Figure G.3: Round Robin mass change results alloy 625 exposed to s-CO₂ at 550°C, 20MPa for 1500 hours.

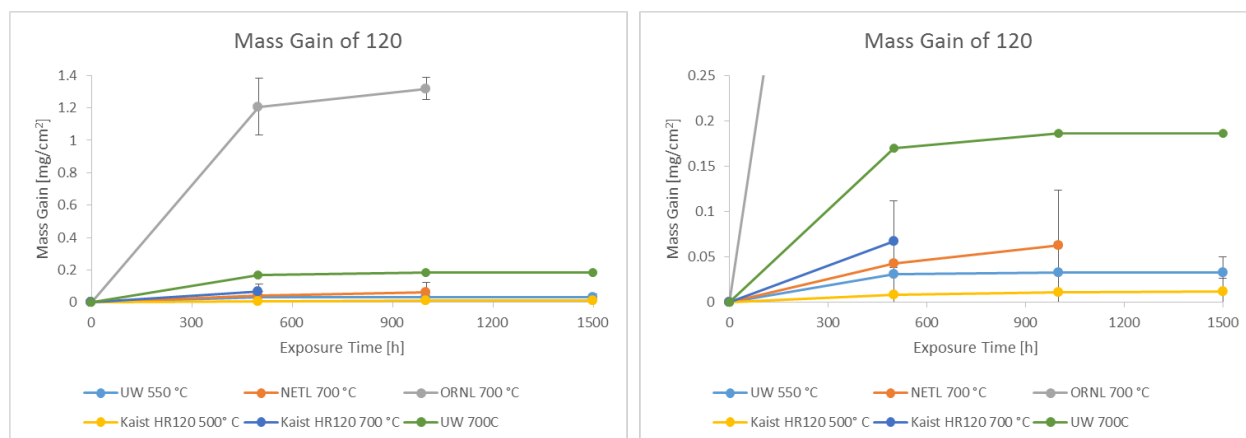


Figure G.4: Round Robin mass change results alloy 120 exposed to s-CO₂ at 550°C, 20MPa for 1500 hours.

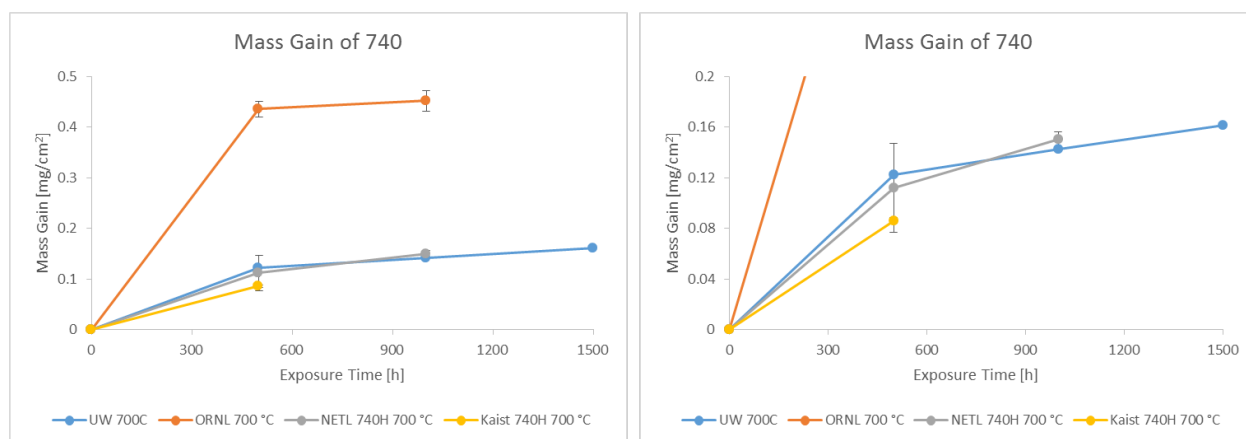


Figure G.5: Round Robin mass change results alloy 740 exposed to s-CO₂ at 550°C, 20MPa for 1500 hours.

Appendix H

Round-Robin Parameters and Transients

Test conditions	7/6/2016 12/23/2016 12/23/16 11.3pm H625	7/6/2016 5/13/2017 5/13/2017 11:02am H625	7/6/2016 7/23/2016 7/23/16 4:48pm H625	7/6/2016 9/6/2016 9/6/2016 9:08am H625	7/6/2016 12/23/2016 12/23/16 11.3pm H625	Test chamber volume Refresh rate, min Ramp up time to temperature (upload data), h (Note A) Hold time to CO2 start, h (Note A) Ramp up time to pressure, h (Note A) Number and distribution of thermocouples in chamber Thermocouple calibration date and temperature range (upload data), (Note A) Mean T, °C T std dev, °C Mean P, std dev, bar P std dev, bar
University of Wisconsin- Madison 1650 Engineering Dr Madison, WI 53706 Jacob Maloney 217482285 jmaloney@wisc.edu	None 1L 0.08%/hr 198min 2.7hr	None 1L 0.08%/hr 198 \$2.50/hr	4791 Samples in/bank of autoclave 2hr** 30* 1 hr, 23 min	4791 Samples in/bank of autoclave 0.08%/hr 198 2.9hr	None 1L 0.11%/hr 170 2.6	Date of samples loaded Date/time of test run started Material of test chamber/sample rack Location of samples and spacing between samples on sample rack Other materials present in chamber during run (other samples, fixtures, thermocouples)
Chromatech/Supercritical 24 Haynes 625 1L -3 mL/min (from bottle) +/- .3C +/- 2.2C +/- 1.2.5psi +/- 3.4psi	None 3 6/20/2016	None 3 6/20/2016	4791 Samples in/bank of autoclave 6/20/2016	4791 Samples in/bank of autoclave 6/20/2016	None 3 6/20/2016	
Haynes 625 1L -3 mL/min (from bottle) +/- .3C +/- 2.2C +/- 1.2.5psi +/- 3.4psi	None 3 6/20/2016	None 3 6/20/2016	4791 Samples in/bank of autoclave 6/20/2016	4791 Samples in/bank of autoclave 6/20/2016	None 3 6/20/2016	

Figure H.1

Appendix I

1,000 Hour Mass/Thickness Measurements [mg/mm²]

Mass Change Measurements:

Figure I.1: 1,000 hour mass change measurements for s-CO₂ environments.

[mg/mm ²]	450C		550C		650C				700C	750C				
	IG	RG	IG (600hrs)	RG	IG (600hrs)	RG	10ppm O ₂	100ppm O ₂	RG	IG (600hrs)	RG	10ppm O ₂	100ppm O ₂	1%CO
T92		1.1E-02		3.3E-02		x**								
T122		1.1E-02		2.9E-03										
347	3.1E-04	3.5E-04	2.0E-04	2.6E-03	3.7E-04	3.5E-04	2.2E-02	2.0E-02			8.6E-03	1.7E-02	7.8E-03	
316L		3.0E-04	3.2E-04	1.1E-03		9.7E-03			9.5E-02					2.7E-02
310S		2.6E-04	1.7E-04	5.2E-04	4.0E-04	1.2E-03	3.8E-03	2.2E-03		2.2E-03	1.9E-03	7.7E-03	1.0E-02	
709						1.1E-03								
800H	3.7E-04	1.2E-04		5.8E-04	1.6E-03	1.3E-03	3.8E-03	3.0E-03		3.0E-03		1.4E-02	1.5E-02	
H718		2.3E-04	2.6E-04	1.0E-03	5.3E-04	1.2E-03	1.2E-03	9.2E-04		2.1E-03	3.1E-03	6.3E-03	6.0E-03	
H625		2.2E-04	1.9E-04	4.6E-04	3.8E-04	1.4E-03	2.1E-03	1.3E-03	1.8E-02	1.3E-03	1.6E-03	2.0E-03	4.2E-03	6.0E-03
H230		2.3E-04	1.8E-04	5.4E-04	3.6E-04	5.2E-04	6.3E-03	8.6E-04		1.1E-03	1.1E-03	2.0E-03	2.6E-03	2.0E-03
617		2.0E-04	1.5E-04	5.0E-04	5.8E-04	2.0E-03	2.5E-03	9.5E-04		1.7E-03	2.8E-03	3.6E-03	4.3E-03	
740H					6.1E-04	8.6E-04		1.0E-03	1.4E-02	1.8E-03	2.9E-03		4.2E-03	
H282					7.6E-04	1.5E-03	2.1E-03	1.0E-03		2.9E-03	4.8E-03	7.0E-03	6.8E-03	4.2E-03
HR120				3.3E-03					1.9E-02					
Pure Fe		8.7E-03												
Fe12Cr		4.4E-03												
Pure Ni														3.5E-04
Pure Cr							2.3E-02							1.6E-02
Ni20Cr							8.3E-03	3.4E-03		1.5E-03	2.9E-03		4.0E-03	
SiC					-8.6E-04		-2.5E-04	-8.1E-05		-6.1E-04	-2.4E-05		2.1E-03	
AFA OC6,7,10	x	x												
PM2000						4.7E-04								
PE16						1.1E-03								
Al-6XN						2.1E-03								

Thickness conversion based on 100% dense chromia growth [$\mu\text{m} = \text{mg}/\text{mm}^2$]:

$$1\mu\text{m} = 1.6E-3 \quad 5\mu\text{m} = 8.2E-3 \quad 10\mu\text{m} = 1.6E-2 \quad 20\mu\text{m} = 3.3E-2$$

Actual Thickness Values:

Figure I.2: 1,000 hour thickness measurements for s-CO₂ environments found using SEM imaging [μm].

	450°C	550°C	650°C		700°C	750°C		
(nodule) {internal}	RG [μm]	RG [μm]	RG [μm]	100ppm O ₂ [μm]	RG [μm]	RG [μm]	100ppm O ₂ [μm]	1%CO [μm]
T91	9.0	39.7						
316L		.5 (6.1)			2.9 (36)			41.0
H625		0.2		0.6	1.3	0.9	1.9 (6.7)	2.2
H230	<.5		<.5	.8 ()		0.5	1.4 (4.4)	0.9
H282						1.6(2.3)	5.5()	3.8
740H					1.0	1.2 {2.6}	2 (10)	
HR120		3.15??			1.3 (3.1)			
Cr						1.9		4.2 [4.2]
Ni						14.0		0.0
Ni20Cr						1.3(2.0)	3.9 (6.5)	

Appendix J

Summary of Commercial Alloy Performance in s-CO₂

Figure J.1: Table of commercial alloy compatibility in s-CO₂.

Alloy	Oxidation Notes	Carburization Notes	Oxide Thickness* [microns/1000hr]	Susceptibility to Impurities Corrosion
T92	Outer Fe rich oxide Inner Fe,Cr rich oxide Spallation observed at 550C	Significant (~180µm @450C)	450C – 6.8 550C – 20.3	NA
T122	Outer Fe rich oxide Inner Fe,Cr rich oxide Spallation observed at 550C	Significant (~120µm @450C)	450C – 6.4 550C – 1.8	NA
347	Outer Fe rich oxide Inner Cr rich oxide Spallation observed at 650/750C	Carburization Found Below Thick Nodules	450C – .2 550C – 1.6 650C – .2 750C – 5.2	Oxygen rich environments accelerate oxidation/spallation
316L	Cr rich oxide Fe rich nodules with inner Fe,Cr oxide Spallation observed at 650/700C	Carburization Found Below Thick Nodules	450C – .2 550C – .7 650C – 5.9 700C – 5.8	NA
310S	Cr rich oxide	NA	450C – .2 550C – .3 650C – .7 750C – 1.1	NA
709	Cr rich oxide	NA	650C – .7	NA
800H	Cr rich oxide	NA	450C – .1 550C – .4 650C – .8	Oxygen rich environments severely increase oxidation
718	Cr rich oxide Nodules of Fe rich oxide at T=750C Ti/Al internal oxidation	NA	450C – .1 550C – .6 650C – .8 750C – 1.9	Oxygen rich environments accelerate oxidation/spallation
H282	Cr rich oxide Ti/Al internal oxidation Some oxide cracking	Assumed to be Less Than 625	650C – .9 750C – 2.9	Poor resistance to oxygen rich environments Excellent resistance to CO rich environments
H625	Cr rich oxide	<5 Microns in RG Environments <10 Microns in CO Mixed Environment	450C – .1 550C – .3 650C – .3 700C – 1.1 750C – 1.7	Oxygen environments enhanced oxidation CO environments enhanced oxidation and caused oxide buckling
617	Cr rich oxide Ti/Al internal oxidation	Assumed to be Less Than 625	450C – .1 550C – .3 650C – 1.2 750C – 1.7	Good resistance to oxygen rich environments NA
740H	Cr rich oxide Cr/Ti rich nodules oxide nodules Ti/Al internal oxidation	Assumed to be Less Than 625	650C – .5 700C – .9 750C – 1.7	Good resistance to oxygen rich environments NA
H230	Cr rich oxide	Assumed to be Similar to 625	450C – .1 550C – .3 650C – .3 750C – .7	Excellent resistance to impurities corrosion
*Oxide thickness is converted from mass to thickness using density of chromium (spallation and nodule formation can alter these measurements slightly) – Estimates are 20 ± 9% accurate based on SEM imaging of 5 different alloys				
This table is based on Research Grade (99.999%) CO ₂ with impurities consisting of 100ppm O ₂ and 1%CO additions				

Appendix K

Certificates for Tested Alloys

Figure K.1: Certificate for Alloy 310S.

NOTICE OF SHIPMENT / PACKING LIST

DATE OF NO SHIPMENT: 11/09/12
 CARRIER: GREEN LINES TRANSP., INC.
 CARRIER CODE: 13920103060000
 CARRIER NAME: 12/28/12
 CARRIER ADDRESS: 1219 LODIVILLE, OH 45405

CERTIFICATE OF TEST

DATE OF TEST: 12/28/12
 TEST NUMBER: 244055

GRADE AND SPECIFICATIONS

"ATI 310S" STAINLESS STEEL SHEET C R COILS ANNEALED 2D FIN 3 EDGE (AMS 5521J) (ASME-SA-240 ED 2010) (UNS S31008) (PDS-10702RL REV SWPC B) (09/26/09 EXCEPTS TO PDS-10702RL) (UNS S31000) (ASTM-A-240-12)

ITEM PCS DIMENSIONS W/G/L

ITEM	PCS	DIMENSIONS W/G/L	HEAT #	COIL #	TEST #	GROSS TARE NET	THRO	TAG #/	CD SKID #
001	1	48 / .048 / 625	839088	12012N359A	1258584	5300	40	5260	5199 209312
			839088	12012N359B	1258584	5360	40	5320	5259 209312
			839088	12012N359C	1258584	4960	40	4920	4860 209314
						15620	120	15500	15318

GAUGE TOL: + 0.00300 - 0.00300

PHYSICALLY VERIFIED BY: *[Signature]*

YIELD TENSILE & ELONG

TYPE HEAT/TEST	YIELD TENSILE	ELONG
HEAT 839088	0.02	1.70
TEST LOCATION	BN	BN

TEST RESULTS

ITEM TEST NO	TEST LOCATION	YIELD TENSILE	ELONG	HARDNESS	BEND	GRAIN SIZE	HARDENABILITY
001	1258584	47000	88500	40	78 HRBW		
		TC	TC	TC	81 HRBW		

* Y.S. BY 0.2% OFFSET METHOD

PAGE 01 - CONTINUED ON PAGE 02

12/28/12 11:06:14

NOTICE OF SHIPMENT/
PACKING LIST

QTY	NO	DATE	DATE	DATE	DATE	DATE	DATE	DATE	DATE
C31002	001	11/09/12	11/09/12	11/09/12	11/09/12	11/09/12	11/09/12	11/09/12	11/09/12
111/09/12	0773550	LOUISVILLE, OH	563671	13020103060000	30-112-252	12/28/12	1219	LOUISVILLE	OH
100386-0	1311	001	001	001	001	001	001	001	001
584	584	584	584	584	584	584	584	584	584



CERTIFICATE OF TEST

GRADE AND SPECIFICATIONS
 "ATI 111/09/12 BUSINESS STEEL SHEET C R COILS ANNEALED 2D FIN 3 EDGE (AMS 5521J) (ASME-SA-240 ED 2010) (DMS S31006) (PDS-10702RL NEW SPC B) (03/26/09 EXCEPTS TO PDS-10702RL) (DMS S31000) (ASTM-A-240-12)

ITEM TEST NO
 001 L258584

TEST LOCATION
 GRADE VERIFICATION WAS CARRIED OUT SPECTROSCOPICALLY

DIN EN 10204:2005 - 3.1 CERTIFICATE DOES NOT INDICATE PED APPROVAL FOR THIS MATERIAL.

THIS DIN EN 10204:2005 - 3.1 CERTIFICATE OF TEST SHALL NOT BE REPRODUCED EXCEPT IN FULL. FEDERAL LAW PROHIBITS THE RECORDING OF FALSE, FICTITIOUS, OR FRAUDULENT STATEMENTS OR ENTRIES ON THE CERTIFICATE. MATERIAL IS NOT MANUFACTURED IN ACCORDANCE WITH THE FOLLOWING TECHNICAL SPECIFICATIONS:
 ATI ALLEGHENY LUDLUM PERFORMS CHEMICAL ANALYSIS BY THE FOLLOWING TECHNIQUES:
 C, S BY COMBUSTION/INFERRED
 N, O, H BY INERT FUSION/THERMAL CONDUCTIVITY
 MN, P, SI, CR, NI, MO, CU, CB, CO, V BY WDXRF
 B BY ORS
 TD AND TT (S=0.10%) BY WDXRF, OTHERWISE BY ORS
 PB, BI, AG BY GPM

THE MATERIAL WAS HEAT-TREATED AT APPROPRIATE TEMPERATURES TO MEET DESIGNATED PROPERTIES OF THE REFERENCED SPECIFICATION.
 PAGE 02 - CONTINUED ON PAGE 03
 12/28/12 11:06:14

ATI Allegheny is a registered trademark of ATI Allegheny Steel Corporation. All other trademarks are the property of their respective owners. This document is the property of ATI Allegheny Steel Corporation and is not to be distributed, copied, or reproduced in any form without the written permission of ATI Allegheny Steel Corporation. © 2012 ATI Allegheny Steel Corporation. All rights reserved.

**NOTICE OF SHIPMENT
PACKING LIST**

CURT CODE NO 3/LINE	CURT CODE	ACCEPTING BILL	SHIPMENT NO	PRODUCT CODE	BILL OF MATERIALS	DATE SHIPPED
C31002	11/09/128773550	LOUISVILLE, OH	563671	1302010306000	30-12-252	12/28/12
FORM PERMITTED	00386-01311	SHIP TO	1319	LOUISVILLE	OH	244055
FORM NO	584					



CARRIER - GREY LINES TRAMP, INC.
 "ATI 310S" STAINLESS STEEL SHEET C R COLLS ANNEALAD 2D FIN 30201 (AMS-A-211) (ASME-SA-240 ED 2010)
 (DNS S31008) (PDS-10702RL REV SPC B) (03/26/09 EXCEPTS TO PDS-10702RL) (DNS S31000) (ASTM-A-240-12)

TESTING WAS PERFORMED AT THE FOLLOWING LOCATIONS:
 BN = ATI-ALLEGHENY LUDLOW; 100 RIVER ROAD; BRACKENRIDGE, PA 15014
 TC = ATI-ALLEGHENY LUDLOW; 1300 PACIFIC AVENUE; NATRONA HEIGHTS, PA 15065

PAGE 03 - FINAL PAGE
 ISSUED BY ATI ALLEGHENY LUDLOW - 01/02/2013 08:00
 CARRIER METAL - QUALITY ASSURANCE DEPT.
 THE INFORMATION ON THIS LABEL IS THE PROPERTY OF ATI ALLEGHENY LUDLOW. IT IS TO BE USED FOR IDENTIFICATION PURPOSES ONLY. IT IS NOT TO BE REPRODUCED OR TRANSMITTED IN ANY FORM OR BY ANY MEANS, ELECTRONIC OR MECHANICAL, INCLUDING PHOTOCOPYING, RECORDING, OR BY ANY INFORMATION STORAGE AND RETRIEVAL SYSTEM. ANY UNAUTHORIZED REPRODUCTION OR TRANSMISSION IS STRICTLY PROHIBITED. THE USER AGREES TO HOLD ATI ALLEGHENY LUDLOW HARMLESS FROM ANY AND ALL DAMAGES, INCLUDING ATTORNEY'S FEES, THAT MAY BE INCURRED BY ANY PARTY AS A RESULT OF THE USER'S USE OF THIS LABEL.

Figure K.2: Certificate for Alloy 316L.



ANALYSIS REPORT

University Of Wisconsin-Madison
1500 Engineering Drive Rm #809
Madsion, WI 53706

U111

Date: 07/09/13

PO#: Q13-0374-2

Attn: Mr. Paul Roman

Sample Identification: 316L- FLAT 0.5"X0.5"X0.0625

Laboratory File # G3-28217

Silicon: .29	Vanadium: _____	Aluminum: _____	Silver: _____
Sulfur: <.001	Tungsten: _____	Zinc: _____	Mercury: _____
Phosphorus: .032	Columbium: <.01	Magnesium: _____	Tantalum <.01
Manganese: 1.56	Cobalt: .31	Titanium: <.01	Nitrogen .050
Carbon: .03	Selenium: _____	Arsenic: _____	_____
Chromium: 17.09	Antimony: _____	Bismuth: _____	_____
Nickel: 10.12	Tin: _____	Cadmium: _____	_____
Molybdenum: 2.01	Lead: _____	Zirconium: _____	_____
Copper: .45	Iron: Base	Boron: _____	_____

Analysis in weight percent unless noted

Original Dimension, In.: _____	Bend Diameter: _____
Original Area, Sq. In.: _____	Bend Test Angle: _____
Yield, PSI: _____	Character of Fracture: _____
Yield Method: _____	Approved: _____ Rejected: _____
Tensile, PSI: _____	Charpy, Ft. lbs.: _____
Elongation, %: _____	Charpy Specimen Size: _____
Gauge Length, In.: _____	Lateral Exp., Mills: _____
Red. in Area, %: _____	Shear Fracture, %: _____
Character of Fracture: _____	Test Temperature: _____
Hardness, Actual Reading: _____	Character of Fracture: _____
Converted Value: _____	

Results reported apply only to the sample submitted.

The above tests were performed with the application of one or more of the following specifications: ASTM A48, A126, A370, A395, E8, E10, F18, E23, E354, E403, E415, E478, E536, E1019, E1024, E1086, E1409, E1447, E1473, 10CFR21, LECD GDS 400A App. & E-2 SM 5-17, ISO 148 Parts 1 & 2, EN 10002 Part 1, EN 10204 Sec. 3.1C, and Anderson Laboratories' Quality Manual Revision K dated 10/12/09.

This report shall not be reproduced except in full, without the written approval of Anderson Laboratories, Inc.

Michael Porfilio
Michael Porfilio, Director of Operations

Figure K.3: Certificate for Alloy 347H.

Crucible Specialty Metals **Certificate of Test**

PO BOX 977
SYRACUSE, NY 13201-0977

METALMEN SALES, INC.
P.O. BOX 54
NEW YORK, NY 10044

SHIP TO

OUR ORDER NO.
P5-16002-8-01

DATE
12/16/08

SHIPPED FROM
SYRACUSE

CUSTOMER ORDER NO. 45262-2/S42170 CUSTOMER REQ NO. DISTRICT B PARSONS

DESCRIPTION OF MATERIAL

CRU 347/347H HRAP (C .04/.08) S#42170 SIZE 3 X .500
 QQS-763F COND A AMS-QQS-763B ASTM-A484-06B ASTM-A479-06A ASME-SA479-07ED
 ASTM-A276-08A ASTM-A193-08B GR B8C CL1 ASTM-A320-07A GR B8C CL A AMS-5646M
 (EX FIN)
 DPARS 252.225.7014 ALT 1 AND 225.7002-3 (B) (1) COMPLIANT

HEAT NO. CHEMICAL ANALYSIS

A19926	C	MN	P	S	SI	NI	CR	MO	CO	CU	CB	TA
	.051	1.66	.027	.024	.77	9.62	17.67	.38	.20	.38	.72	.021

QUANTITY HEAT NO. MECHANICAL PROPERTIES

1014 #	A19926	TENSILE PSI	YLD.2&PSI	%ELONG4D	RED/AREA%	HARDNESS
1	BDL	89,500	35,680	55.9	74.6	BHN 143/ 151

MACRO TEST OK
 MICRO TEST OK
 GRAIN SIZE # 7
 INTERGRANULAR CORROSION TEST OK PER ASTM A262, PRACTICE E.

MATERIAL WAS ANNEALED BY HEATING TO 1950 DEG. F. FOR A SUFFICIENT TIME TO DISSOLVE RESIDUAL CARBIDES AND QUENCHED IN WATER.

"THE RECORDING OF FALSE, FICTITIOUS OR FRAUDULENT STATEMENTS OR ENTRIES ON THIS DOCUMENT MAY RESULT IN PUNISHMENT OR DISMISSAL."

UNIVERSITY OF WISCONSIN
 1pc) 1/2" x 3" x 10"

MATERIAL FREE FROM MERCURY CONTAMINATION AT TIME OF SHIPMENT, NO WELD REPAIR PERFORMED, AND MATERIAL MELTED IN U.S.A.

THE ABOVE MATERIAL WAS MANUFACTURED AND TESTED ACCORDANCE WITH ABOVE SPECIFICATIONS AND IS IN CONFORMANCE WITH THE SPECIFICATION REQUIREMENTS.
 CRUCIBLE MATERIALS CORPORATION ACTING BY AND THROUGH ITS SPECIALTY METALS DIVISION

CERTIFIED BY *[Signature]*
 JOHN M. PIRMAN - MANAGER OF QUALITY ASSURANCE

Page 1 of 1

Figure K.4: Certificate for Alloy H625.

CERTIFICATION OF TESTS • RAPPORT DES SAIS CERTIFIÉ • VERKLEENIS																
Invoice No.	Date Issued	Customer Reference	Report No.	Page of Pages												
35890901-0	03/07/02	JOETECH	20020315019	1 of 4												
No. By Request 35890901-0		Customer Reference JOETECH	Report No. 20020315019	Page of Pages 1 of 4												
Test # • Item • Part/Description HAYNES INTL (TRANSFER R AND D) INVTRY TRANSFER R AND D 1020 W PARK AVE KOKOMO IN 469029013 USA																
Test # • Item • Part/Description HAYNES INTL (TRANSFER R AND D) INVTRY TRANSFER R AND D 1020 W PARK AVE KOKOMO IN 469029013 USA																
Specifications • Specifications • Specifications AMS 5699 Rev F																
Quantity Ordered Quantity Received 1 PC																
Quantity Shipped Quantity Expended 1 PC																
FILE COPY 2 Haynes International 1020 West Park Avenue PO Box 9013 Kokomo, Indiana, 46902 HAYNES International																
Product Description • Description Produit • Shorter Description 0.058/0.065 X 9 X 20 HAYNES(R) 625 ALLOY SHEET HAYNES(R) 625 ALLOY SHEET NADCAP CERTIFICATE NUMBER 0089 S400D.S1000D																
Heat Number 2650 J 6980																
Al	B	C	GH/IN	Co	Cr	Cu	Fe	Ma	Mo	NI	P	S	Si	Ti	V	W
0.22		0.020	0.28	21.89	5.00	0.26	8.59	BAL	0.006	<0.002	0.25	0.29				
2650 J 6980	3.510	<0.050														
Certified By • Certifié Par • Bescheinigt Durch • Pego Certin Certification Supervisor/Technician Peggy S. Griffin																

THE INFORMATION CONTAINED HEREIN IS THE PROPERTY OF HAYNES INTERNATIONAL, INC. AND IS NOT TO BE REPRODUCED OR TRANSMITTED IN ANY FORM OR BY ANY MEANS, ELECTRONIC OR MECHANICAL, INCLUDING PHOTOCOPYING, RECORDING, OR BY ANY INFORMATION STORAGE AND RETRIEVAL SYSTEM, WITHOUT THE WRITTEN PERMISSION OF HAYNES INTERNATIONAL, INC. HAYNES INTERNATIONAL, INC. IS NOT RESPONSIBLE FOR THE CONTENTS OF ANY CERTIFICATE OR REPORT PREPARED BY AN ANALYST OR OTHER PERSON WHOSE NAME APPEARS ON THIS CERTIFICATE OR REPORT. HAYNES INTERNATIONAL, INC. IS NOT RESPONSIBLE FOR THE CONTENTS OF ANY CERTIFICATE OR REPORT PREPARED BY AN ANALYST OR OTHER PERSON WHOSE NAME APPEARS ON THIS CERTIFICATE OR REPORT. HAYNES INTERNATIONAL, INC. IS NOT RESPONSIBLE FOR THE CONTENTS OF ANY CERTIFICATE OR REPORT PREPARED BY AN ANALYST OR OTHER PERSON WHOSE NAME APPEARS ON THIS CERTIFICATE OR REPORT.

CERTIFICATION OF TESTS • RAPPORT DE RESULTATS CERTIFIÉ • WERKSZELIGNIS

Anzahl No. of Pieces Brennung Nr. 358503001-0	Zeitpunkt Date of Test Beendigung 03/07/02	Kunde Customer Name Kundenbestellung JOE/TECH	Report No. Prüfung Nr. Zertifikat Nr. 2002031019	Seite Page of Pages Anzahl der Seiten 2 Of 4
---	--	---	--	--

Satz **To • Clavier • Seriennummer**:
 HAYNES INTL (TRANSFER R AND D)
 INVTRY TRANSFER R AND D
 1020 W PARK AVE
 KOKOMO
 IN 469029013 USA

Ship To • Destination • Beschreibung:
 HAYNES INTL (TRANSFER R AND D)
 INVTRY TRANSFER R AND D
 1020 W PARK AVE
 KOKOMO
 IN 469029013 USA

Product Description • Description Produit • Material Beschreibung:
 0,058/0,065 x 9 x 20
 HAYNES(R) 625 ALLOY SHEET
 HAYNES(R) 625 ALLOY SHEET
 NADCAP CERTIFICATE NUMBER 0089
 S400D,S1000D

Specifications • Spécifications • Specifications
 AMS 5599 Rev F

Tabelle 1 Test of Hardness Temperature: 20-150 °F, 7-60°C 1 Temp. Ambiance •	Tabelle 2 Test of Elongation Temperature: 20-150 °F, 7-60°C 1 Also Temp.	Stroke Support Temperature • Essai à Charge De Support à Diverses Temp.	
		% Elongation	% Elongation
Umwelt Zugfestigkeit	Umwelt Zugfestigkeit	Zeitpunkt	Zeitpunkt
Temp. 20 ± 2 °F / 7 ± 1 °C	Temp. 20 ± 2 °F / 7 ± 1 °C	Temp. 20 ± 2 °F / 7 ± 1 °C	Temp. 20 ± 2 °F / 7 ± 1 °C
133000 PSI	70000 PSI 49 %	(1) AS	

Tabelle 3 Test of Tensile Strength Temperature: 20-150 °F, 7-60°C 1 Temp. Ambiance •			Tabelle 4 Test of Elongation Temperature: 20-150 °F, 7-60°C 1 Also Temp.		
Umwelt Zugfestigkeit	Umwelt Zugfestigkeit	Umwelt Zugfestigkeit	Umwelt Zugfestigkeit	Umwelt Zugfestigkeit	Umwelt Zugfestigkeit
Temp. 20 ± 2 °F / 7 ± 1 °C	Temp. 20 ± 2 °F / 7 ± 1 °C	Temp. 20 ± 2 °F / 7 ± 1 °C	Temp. 20 ± 2 °F / 7 ± 1 °C	Temp. 20 ± 2 °F / 7 ± 1 °C	Temp. 20 ± 2 °F / 7 ± 1 °C

Certified By • Certifé Par • Bescheinigt Durch: **Peggy Griffin**
 Certification Supervisor/Technician

Peggy Griffin

THE DATA CONTAINED HEREIN WERE OBTAINED FROM LABORATORY TESTS CONDUCTED AT THE REQUEST OF THE CLIENT AND ARE INTENDED TO BE RELIABLE. WE DISCLAIM ANY LIABILITY FROM USE OF THIS DATA. WE MAKE NO WARRANTY OF ANY KIND. THE USER SHALL BE RESPONSIBLE FOR THE PROPER USE OF THE DATA. THE USER SHALL BE RESPONSIBLE FOR THE PROPER USE OF THE DATA. THE USER SHALL BE RESPONSIBLE FOR THE PROPER USE OF THE DATA. THE USER SHALL BE RESPONSIBLE FOR THE PROPER USE OF THE DATA.

FILE COPY 2

HAYNES International
 Hayes International
 1020 West Park Avenue
 Kokomo, IN 46902

CERTIFICATION OF TESTS • RAPPORT DES SAIS CERTIFIÉ • WIRKSZELECNIS			Product Name	Date Entered	Customer Reference	Report No.	Page of Pages
Product No. 338305001-0	Date Entered 03/07/02	Customer Reference JOB/TECH	Report No. 20020133019	Page of Pages 3 of 4	HAYNES International Haynes International 1020 West Park Avenue PO Box 5013 Kokomo, IN 46902 U.S.A.		
HAYNES INTL (TRANSFER R AND D) INVTRY TRANSFER R AND D 1020 W PARK AVE KOKOMO IN 469029013 USA				Ship to • Destinace • Destinace			
AMS 3599 Rev F				Quantity Ordered 1 PC	Quantity Shipped 1 PC	Product Description • Description Produit • Produkciwny Opis	
				0.058/0.065 x 9 x 20			
				HAYNES(R) 625 ALLOY SHEET			
				HAYNES(R) 625 ALLOY SHEET			
				NADCAP CERTIFICATE NUMBER 0089			
				S400D.S1000D			

Material Designation Cetnik	Material Designation Cetnik	Material Designation Cetnik	Material Designation Cetnik	Material Designation Cetnik	Material Designation Cetnik	Material Designation Cetnik	Material Designation Cetnik	Material Designation Cetnik	Material Designation Cetnik	Material Designation Cetnik	Material Designation Cetnik	Material Designation Cetnik	Material Designation Cetnik	Material Designation Cetnik	Material Designation Cetnik	Material Designation Cetnik
96 HRB	6.5	0.0001 In														
Certified By: • Certifé Par • Bescheinigt Durch: Pragy Gillin Certification Supervisor/Technician <i>Pragy Gillin</i>																
03/15/02 (1) 3433481101																

THE DATA CONTAINED HEREIN IS THE PROPERTY OF HAYNES INTERNATIONAL INC. IT IS TO BE USED ONLY FOR THE PURPOSES INTENDED. IT IS NOT TO BE USED FOR ANY OTHER PURPOSES. HAYNES INTERNATIONAL INC. IS NOT RESPONSIBLE FOR THE USE OF THIS INFORMATION IN ANY MANNER OTHER THAN THAT INTENDED. HAYNES INTERNATIONAL INC. IS NOT RESPONSIBLE FOR THE USE OF THIS INFORMATION IN ANY MANNER OTHER THAN THAT INTENDED. HAYNES INTERNATIONAL INC. IS NOT RESPONSIBLE FOR THE USE OF THIS INFORMATION IN ANY MANNER OTHER THAN THAT INTENDED. HAYNES INTERNATIONAL INC. IS NOT RESPONSIBLE FOR THE USE OF THIS INFORMATION IN ANY MANNER OTHER THAN THAT INTENDED.

CERTIFICATION OF TESTS • RAPPORT PISSAS CERTIFIÉ • WEKSTELIGNIS				
Invoice No No De Facture 33830500-0	Date Examined Date Commande 03/07/02	Customer Reference Référence Client JOE/TECH	Report No Numéro de Rapport 20020315019	Page of Pages Nombre de Pages 4 Of 4
Send To • Client / Destinataire HAYNES INTL (TRANSFER R AND D) INVTRY TRANSFER R AND D 1020 W PARK AVE KOKOMO IN 469029013 USA		Ship To • Manufacture / Destinataire HAYNES INTL (TRANSFER R AND D) INVTRY TRANSFER R AND D 1020 W PARK AVE KOKOMO IN 469029013 USA		
Specifications • Spécifications / Spécifications AMS 5999 Rev F		Quantity Ordered Quantité Commandée 1 PC	Quantity Shipped Quantité Expédiée 1 PC	Product Description • Description Produit • Niveau de Matériau HAYNES International 0.038/0.065 X 9 X 20 HAYNES(R) 625 ALLOY SHEET HAYNES(R) 625 ALLOY SHEET NADCAP CERTIFICATE NUMBER 0089 S400D.S1000D

This material is free of mercury contamination.
 This material has been annealed and cooled in a protective atmosphere.
 Mill Orders Used: 343481101 (1 PC)
 (A) 1750 °F to 1950 °F

Certified By • Certifié Par • Bechtelndig Durich: Peggy Griffin
 Certification Supervisor / Technicien

THE INFORMATION CONTAINED HEREIN IS THE PROPERTY OF HAYNES INTERNATIONAL. IT IS TO BE USED ONLY FOR THE SPECIFIC PURPOSES FOR WHICH IT WAS OBTAINED. HAYNES INTERNATIONAL IS NOT RESPONSIBLE FOR THE USE OF THIS INFORMATION FOR ANY OTHER PURPOSES. HAYNES INTERNATIONAL IS NOT RESPONSIBLE FOR THE USE OF THIS INFORMATION FOR ANY OTHER PURPOSES. HAYNES INTERNATIONAL IS NOT RESPONSIBLE FOR THE USE OF THIS INFORMATION FOR ANY OTHER PURPOSES.

FILE COPY 2

Haynes International
 1020 West Park Avenue
 PO Box 9013
 Kokomo, Indiana 46902

Figure K.5: Certificate for Alloy H718.

CERTIFICATION OF TESTS • RAPPORT D'ESSAIS CERTIFIÉ • VEKERSZETÉCNIS																
Star Order No. Rendelési Szám ~1706001-0	Date Entered Beviteli Dátum 08/09/12	Customer Reference Küldeményazonosító RSEKORAVES	Report No. Zajlás Szám 20120827020	Page of Pages Analízis Oldal 1 of 3	HAYNES International Haynes International 1020 W Park Ave Kokomo, Indiana 46902					CUSTOMER COPY Haynes International 1020 W Park Ave Kokomo, Indiana 46902						
Title: Client's Identification HAYNES INTL (TRANSFER R AND D) INVENTORY TRANSFER R AND D 1020 W PARK AVE KOKOMO IN 46901 USA				Title: Manufacturer's Identification HAYNES INTL (TRANSFER R AND D) PARK AVENUE TECHNOLOGY DEPT KOKOMO IN 46901 USA												
Specifications • Specifications • Szabványok AMS 5996 K, ASTM-B-670, 07 UNS# N07718, B50TF4, S22, Cl. A, B50TF4, S22, Cl. 1 PC E: MSRR 7116, 9																
Heat Number Számszám 2180 2 9798	Chemical Analysis • Analízis Quantity: Original Quantity: Certified Reference: 1 PC															
Heat Number Számszám 2180 2 9798	Al	B	C	Co	Cr	Fe	Mn	Mo	Ni	P	S	Si	Ti	V	W	
0.53	0.003	0.047	5.15	0.30	18.10	0.09	18.50	0.23	3.06	53.10	<0.005	<0.002	0.09	1.05		
2180 2 9798	0.05	0.05	Zr	Bi	Se	La	Cu	As	Mg	Y	Al	N	Ca	Al-Ti	Ni-Co	Ni-Mo
5.140	<0.05	<0.0003					<0.0005				<0.0002					
Certified By: • Certifié Par: • Bejelentő: Durch: Amber Dubois Certification Technician 8/27/2012																

THE INFORMATION ON THIS CERTIFICATE IS THE PROPERTY OF HAYNES INTERNATIONAL, INC. AND IS NOT TO BE REPRODUCED OR TRANSMITTED IN ANY FORM OR BY ANY MEANS, ELECTRONIC OR MECHANICAL, INCLUDING PHOTOCOPYING, RECORDING, OR BY ANY INFORMATION STORAGE AND RETRIEVAL SYSTEM, WITHOUT THE WRITTEN PERMISSION OF HAYNES INTERNATIONAL, INC.

CERTIFICATION OF TESTS • RAPPORT D'ESSAIS CERTIFIÉ • WERKSZELJENIS

HAYNES International

CUSTOMER COPY

Haynes International
1020 West Park Avenue
PO Box 9013
Kokomo, Indiana, 46912

Order No: 1790001-0
Material: 133000 PSI
Reference: 2090000 PSI

Date Entered: 08/09/12
Date by Command: 08/09/12
Customer Reference: R. SEAGERAYES

Report No: 20120827010
Page of Pages: 2 OF 3

Page of Pages: 2 OF 3

Tensile Test at Room Temperature • Essai de Traction à Temp. Ambiante • Zugsproben	Tensile Test at Elevated Temperature • Essai de Traction à Haute Temp.		Tensile Test at Elevated Temperature • Essai de Traction à Haute Temp.		Stress Relaxation Temperature • Essai à Charge de Relâchement de Tension		Stress Relaxation Temperature • Essai à Charge de Relâchement de Tension					
	Yield Strength	Ultimate Tensile Strength	Yield Strength	Ultimate Tensile Strength	Yield Strength	Ultimate Tensile Strength	Stress Relaxation	Stress Relaxation				
133000 PSI 2090000 PSI	48 % 20 %	11A) 11B) 11C)	1200 °F 1200 °F	172000 PSI 168500 PSI	156500 PSI 143000 PSI	18 % 21.5 %	11B) 11C)	1200 °F 1200 °F	105000 PSI 105000 PSI	375 HRS 156 HRS	16 % 20 %	11B) 11C)

Acid Etching Date by Command	Grain Size		Grain Size		Grain Size		Grain Size		Grain Size		Grain Size	
	Grain Size	Grain Size	Grain Size	Grain Size	Grain Size	Grain Size	Grain Size	Grain Size	Grain Size	Grain Size	Grain Size	Grain Size
95 HRBW 44 HRC 11D 11C)	7.5	7.5	100	0	7.5	0.0001 IN	1	SP7				

Certified By: *Amber Dubois*
Certification Technician: 82727012 | 13954538101

THE HAYNES CORPORATION MAKES NO WARRANTY, REPRESENTATION OR AGREEMENT, EXPRESS OR IMPLIED, IN CONNECTION WITH THE SALE OF THESE PRODUCTS. THE HAYNES CORPORATION SHALL NOT BE LIABLE FOR ANY DAMAGE, LOSS OR INJURY TO PERSONS OR PROPERTY, OR FOR ANY DEFECTS IN THE PRODUCTS, WHICH ARE THE RESULT OF THE NEGLIGENCE OF THE USER OR OTHER THIRD PARTY. THE HAYNES CORPORATION SHALL NOT BE LIABLE FOR ANY DAMAGE, LOSS OR INJURY TO PERSONS OR PROPERTY, OR FOR ANY DEFECTS IN THE PRODUCTS, WHICH ARE THE RESULT OF THE NEGLIGENCE OF THE USER OR OTHER THIRD PARTY.

Size Order No. Reference Commande 17080150	Date de Commande 08/09/12	Kuesteradresse R. SCHOENAVES	Report No. 2012087010	Page of Page Page de Page 3 of 3
--	------------------------------	---------------------------------	--------------------------	--

HAYNES
International

CUSTOMER COPY
 Haynes International
 1020 West Park Avenue
 PO Box 9013
 Kokomo, Indiana, 46902

CERTIFICATION OF TESTS • RAPPORT D'ESSAIS CERTIFIÉ • VERSUCHSBERICHT

All tests and inspections have been performed and results meet specification requirements. THIS MATERIAL WAS MELTED AND MANUFACTURED IN THE UNITED STATES. When microstructure analysis is performed, the etchant used is H2O2 and HCl. Samples were viewed at 100-500x magnification. Grain size evaluation is performed to the requirements of ASTM E112-96/2004a2 Plate 1. Samples are prepared per ASTM E3.01. The material has been evaluated for alloy depletion.

Microstructure: Acceptable
 Surface microstructural evaluation was performed at 500X magnification.
 Tested at Haynes International, Inc. Kokomo, IN
 Samples tested to B50TF4, C1, F condition and material supplied to C1E condition.
 Microstructure complies with E50TF133 Class C.
 This material has passed the bend test as specified in B50TF4, Class A.
 Samples tested to B50TF4, C1, B condition and material supplied to C1A condition.
 This material was vacuum induction melted followed by electro flux remelt.
 This material meets the requirements of R89000.5ABR.
 Material produced by Manufacturer's Standard Procedure No. 043 Amend. 4H/2
 BEND TEST: Passed
 Material annealed in a continuous high-temperature furnace.
 Mill Order Used: 396358101 (PC)

A) 1750 °F to 1815 °F
 Method of Chemistry Analysis for Heat: 29798 PRIMARY, GFAA (AG,BI,PI),
 Method of Chemistry Analysis for Heat: 29798 BUTT END-02, OLE, ALB (G,PS), LECO (C,S), XARL DIRECT (CA10) (CS,CL,FE), XARL LINEP (CBT,CA,Mo,Mn,Ni,Ti,TR),
 Method of Chemistry Analysis for Heat: 29798 BUTT END-02, OLE, ALB (G,PS), LECO (C,S), XARL DIRECT (CA10) (CS,CL,FE), XARL LINEP (CBT,CA,Mo,Mn,Ni,Ti,TR),
 C) 1750 °F to 1815 °F, 1 Hr., Sep 2, 1325 °F, 8 Hr., Sep 3, 1150 °F, 8 Hr., Total Time: 18 Hr.

Certified By • *Amber Dubois*
 Certification Technician
 8/27/2012

THE INFORMATION ON THIS CERTIFICATE IS VALID ONLY IF THE TESTS WERE PERFORMED IN ACCORDANCE WITH THE TEST METHOD(S) SPECIFIED. THE TEST METHOD(S) SPECIFIED ARE SUBJECT TO CHANGE WITHOUT NOTICE. THE TEST METHOD(S) SPECIFIED ARE SUBJECT TO CHANGE WITHOUT NOTICE. THE TEST METHOD(S) SPECIFIED ARE SUBJECT TO CHANGE WITHOUT NOTICE. THE TEST METHOD(S) SPECIFIED ARE SUBJECT TO CHANGE WITHOUT NOTICE.

Figure K.6: Certificate for Alloy 740H.



SPECIAL METALS CORPORATION

3200 Riverside Drive
Huntington, WV 25705Brian A. Baker
Product and Applications Development
EngineerPh. 304-526-5740
Email: bbaker@specialmetals.com

12/18/2012

Mr. Mark Anderson
737 Engineering Research Bldg
1500 Engineer Dr.
Madison, WI 53706

Enclosed you will find a sample of 0.5" thick, hot-rolled, solution-annealed and aged INCONEL® alloy 740H® plate. The sample provided was manufactured from SMC heat number HT3130JY. The sample has been solution annealed and aged. The chemical composition of heat HT3130JY is shown in Table 1.

The material has been solution annealed at 2075°F and water-quenched, followed by aging at 1472°F (800°C) for 4 hours and air cooling.

Regards,

A handwritten signature in cursive script that reads "Brian A. Baker".

Brian A. Baker

Table 1. Chemical Composition of INCONEL alloy 740H Heat HT3130JY

HEAT	HT3130JY
ALIM_ID	2012E5060
ALLOY	740H
C	0.023
MN	0.245
FE	0.1491
S	0.003
SI	0.17
CU	0.015
NI	50.04
CR	24.57
AL	1.33
TI	1.33
CO	20.09
MO	0.35
NB	1.46
TA	0.004
P	0.0023
B	0.0013
N	0.0038
V	0.012
W	0.022
ZR	0.021

Figure K.7: Certificate for Alloy 800H.

THE RECORDS OF THIS NETWORK OF LABORATORY STATEMENTS
 ON ENTERIES ON THIS DOCUMENT IS THE PROPERTY OF THE ISSUING LABORATORY
 FEDERAL LAW TITLE 18 CHAPTER 47 18 USC 853 AS A FELLOW MEMBER

INCO ALLOYS INTERNATIONAL
 11410 LBS
 CERTIFIED MATERIAL TEST REPORT No. 59210
 01-77912 A/CO9253 01-77912 A/CO9253
 INCOLOY ALLOY 800H/800HT HR PLATE DESQALLED ANN
 5000 92-98 192-208 IN SHR

QUANTITY 1
 HARDNESS 1
 TENSILE 1
 DEC 2

DATE 08/07/95
 INDICATED BY IATI
 INVOICE NUMBER 01-77912 A/CO9253

DATE OF TEST 08/07/95
 TESTED BY IATI
 TESTED AT IATI
 TESTED BY IATI
 TESTED AT IATI
 TESTED BY IATI
 TESTED AT IATI

UNIVERSITY OF WISCONSIN
 1pc 2.80" X 10"

UNSN00810/N00811

HEAT# C
 PROCESS TI
 HEAT# C
 PROCESS TI

MECHANICAL PROPERTIES
 HARDNESS 44.89
 TENSILE 64.8
 YIELD 33.17
 DEC 19.63
 CR 0.46

HEAT/LOT HH9259AG 0.06
 QUANTITY 0.77
 HARDNESS 44.89
 TENSILE 64.8
 YIELD 33.17
 DEC 19.63
 CR 0.46

ROOM TEMP-HRB 11
 GRAIN SIZE-AS SHIPPED 1 PC.
 ROOM TEMP-HRB 13
 GRAIN SIZE-AS SHIPPED 1 PC.
 ROOM TEMP-HRB 14
 GRAIN SIZE-AS SHIPPED 1 PC.

YIELD STRENGTH HAS DETERMINED USING A STRESS STRAIN CURVE

COPIES OF THIS REPORT OR ANALYSIS STATEMENTS
 SENT BY MAIL TO THE CUSTOMER AT THE ADDRESS SPECIFIED ON THE
 FEDERAL LAW, THE IN COMPLIANCE WITH THE PROVISIONS OF THE
 FEDERAL LAW, THE IN COMPLIANCE WITH THE PROVISIONS OF THE

INCO ALLOYS INTERNATIONAL
 INCO ALLOYS INTERNATIONAL, INC.
 1000 WEST VIRGINIA STREET
 PITTSBURGH, PA 15220

CERTIFIED MATERIAL TEST REPORT

NO. 59320

DATE 08/07/95

QUANTITY 1

WEIGHT 1410 LBS

CHANGE ORDER NO. 01-77912 A/C09753

DESCRIPTION INCOLOY ALLOY 800H/800H HR PLATE DESGALD ANN

INSPECTOR IALL

LABORATORY 01-72912 A/C09753

PLATE OR 2

58253

1410 LBS

01-77912 A/C09753

INCOLOY ALLOY 800H/800H HR PLATE DESGALD ANN

5000 92-96 192-288 IN SHR

THIS IS TO CERTIFY THAT THE ABOVE STATED INFORMATION IS THE PROPERTY OF INCO ALLOYS INTERNATIONAL, INC. AND IS NOT TO BE REPRODUCED OR TRANSMITTED IN ANY FORM OR BY ANY MEANS, ELECTRONIC OR MECHANICAL, INCLUDING PHOTOCOPYING, RECORDING, OR BY ANY INFORMATION STORAGE AND RETRIEVAL SYSTEM, WITHOUT THE WRITTEN PERMISSION OF INCO ALLOYS INTERNATIONAL, INC.

QUALITY CERTIFICATION REPRESENTATIVE

(Signature)

VISUAL AND DIMENSIONAL EXAMINATION SATISFACTORY.
 MATERIAL, WHEN SHIPPED, IS FREE FROM CONTAMINATION BY MERCURY, RADIIUM, ASBESTOS SOURCE,
 AND LOW MELTING ELEMENTS.
 AUTHORIZED QUALITY CERTIFICATION REPRESENTATIVES - D. B. WATSON, W. E. BOLEN, R. A. CRAZE, G. B. SIMPSON

Figure K.8: Certificate for Alloy AFA-OC6,7,10.

10/19/10

Please ship the following samples by overnight service *c.

Professor Todd Allen
 915 Engineering Research Building
 1500 Engineering Drive
 Department of Engineering Physics
 University of Wisconsin, Madison
 Madison, WI 53706-1687
 Tel: 608-265-4083

Please charge 327100EF

Thanks,
 Mike Brady
bradyp@ornl.gov
 574 5153

History of Material: These are developmental alumina forming austenitic stainless steels for testing at University of Wisconsin. There are no radiation concerns with this material.

Heat No	001919 OC-6	001920 OC-7	001923 OC-10
C	.114	.112	.114
Mn	1.99	1.92	6.96
Si	.13	.13	.13
P	.022	.020	.010
S	.0009	.0009	.0022
Cr	13.84	13.80	13.85
Ni	25.04	25.08	12.18
Mo	.18	1.98	.15
Cu	.51	.52	3.10
W	.16	.96	.15
V	.05	.05	.05
Ti	.05	.05	.05
Al	3.56	3.59	2.54
Nb	2.51	2.50	1.02
B	.0080	.0085	.0086
N	.0010	.0010	.0017
Zr	-----	.16	-----
Hf	-----	-----	-----
Y	-----	-----	-----
Fe	Bal	Bal	Bal

Figure K.9: Certificate for Alloy T92.



6330 INDUSTRIAL LOOP
 GREENDALE, WI 53129-2434
 (414) 421-7600 1-800-950-6330
 FAX (414) 421-6540

ANALYSIS REPORT

UW-Madison
 1500 Engineering Drive Room 841
 Madison, WI 53706

U113

Date: 03/19/14

PO#: CREDIT CARD

Attn: Mr. Jacob Mahaffey

— Sample Identification: 10G T92 —

Laboratory File # C4-12145

Silicon: .10	Vanadium: .20	Aluminum: .016	Silver: _____
Sulfur: .003	Tungsten: 1.91	Zinc: _____	Mercury: _____
Phosphorus: .016	Columbium: .08	Magnesium: _____	Nitrogen: .047
Manganese: .45	Cobalt: _____	Titanium: _____	_____
Carbon: .12	Selenium: _____	Arsenic: _____	_____
Chromium: 8.94	Antimony: _____	Bismuth: _____	_____
Nickel: .21	Tin: _____	Cadmium: _____	_____
Molybdenum: .50	Lead: _____	Zirconium: _____	_____
Copper: _____	Iron: _____	Boron: .001	_____

Analysis in weight percent unless noted

Original Dimension, In.: _____	Bend Diameter: _____
Original Area, Sq. In.: _____	Bend Test Angle: _____
Yield, PSI: _____	Character of Fracture: _____
Yield Method: _____	Approved: _____ Rejected: _____
Tensile, PSI: _____	Charpy, Ft. lbs.: _____
Elongation, %: _____	Charpy Specimen Size: _____
Gauge Length, In.: _____	Lateral Exp., Mills: _____
Red. in Area, %: _____	Shear Fracture, %: _____
Character of Fracture: _____	Test Temperature: _____
Hardness, Actual Reading: _____	Character of Fracture: _____
Converted Value: _____	


Results reported apply only to the sample submitted.

The above tests were performed with the application of one or more of the following specifications: ASTM A48, A126, A370, A395, E8, E10, E18, E23, E354, E403, E415, E478, E536, K1019, E1024, E1086, E1409, E1447, E1473, 10CPR21, LECD GDS 400A App. 6 E-2 SM 5-17, ISO 148 Parts 1 & 2, EN 10002 Part 1, EN 10204 Sec. 3.1, and Anderson Laboratories' Quality Manual Revision M dated 02/26/14

This report shall not be reproduced except in full, without the written approval of Anderson Laboratories, Inc.

Michael Porfilio
 Michael Porfilio, Director of Operations

Figure K.10: Certificate for Alloy T122.



**ANDERSON
LABORATORIES, INC.**
6330 INDUSTRIAL LOOP
GREENDALE, WI 53129-2434
(414) 421-7600 1-800-950-6330
FAX (414) 421-6540

ANALYSIS REPORT

UW-Madison
1500 Engineering Drive Room 841
Madison, WI 53706

Attn: Mr. Jacob Mahaffey

U113

Date: 03/19/14
PO#: CREDIT CARD

Sample Identification: **10G T122**

Laboratory File # **C4-12144**

Silicon: .27	Vanadium: .21	Aluminum: .011	Silver: _____
Sulfur: .002	Tungsten: 1.90	Zinc: _____	Mercury: _____
Phosphorus: .016	Columbium: .08	Magnesium: _____	Nitrogen: .063
Manganese: .63	Cobalt: _____	Titanium: _____	_____
Carbon: .11	Selenium: _____	Arsenic: _____	_____
Chromium: 10.72	Antimony: _____	Bismuth: _____	_____
Nickel: .41	Tin: _____	Cadmium: _____	_____
Molybdenum: .35	Lead: _____	Zirconium: _____	_____
Copper: 1.01	Iron: _____	Baron: .001	_____


Analysis in weight percent unless noted

Original Dimension, In.: _____	Bend Diameter: _____
Original Area, Sq. In.: _____	Bend Test Angle: _____
Yield, PSI: _____	Character of Fracture: _____
Yield Method: _____	Approved: _____ Rejected: _____
Tensile, PSI: _____	Charpy, Ft. lbs.: _____
Elongation, %: _____	Charpy Specimen Size: _____
Gauge Length, In.: _____	Lateral Exp., Mills: _____
Red. in Area, %: _____	Shear Fracture, %: _____
Character of Fracture: _____	Test Temperature: _____
Hardness, Actual Reading: _____	Character of Fracture: _____
Converted Value: _____	

Results reported apply only to the sample submitted.

The above tests were performed with the application of one or more of the following specifications: ASTM A48, A126, A370, A395, E8, E10, E18, E23, E354, E403, E415, E478, E536, E1019, E1024, E1086, E1409, E1447, E1473, 10CFR21, LECO GDS 400A App. & E-2 SM 5-17, TEO 148 Parts 1 & 2, EN 10002 Part 1, EN 10204 Sec. 3.1, and Anderson Laboratories' Quality Manual Revision M dated 02/24/14

This report shall not be reproduced except in full, without the written approval of Anderson Laboratories, Inc.



Michael Porfilio, Director of Operations

Figure K.11: Certificate for Alloy 617.



ANALYSIS REPORT

UW-Madison
 1500 Engineering Drive Room 841
 Madison, WI 53706

U113

Date: 03/19/14

PO#: CREDIT CARD

Attn: Mr. Jacob Mahaffey

The data reported is certified to meet
 ASTM B168-11
 Alloy N06617

Sample Identification: 10G 617

Laboratory File # C4-12146

Silicon: .04	Vanadium: _____	Aluminum: 1.21	Silver: _____
Sulfur: <.001	Tungsten: _____	Zinc: _____	Mercury: _____
Phosphorus: <.005	Columbium: _____	Magnesium: _____	
Manganese: .07	Cobalt: 12.58	Titanium: .43	
Carbon: .07	Selenium: _____	Arsenic: _____	
Chromium: 22.04	Antimony: _____	Bismuth: _____	
Nickel: Base	Tin: _____	Cadmium: _____	
Molybdenum: 9.49	Lead: _____	Zirconium: _____	
Copper: _____	Iron: 1.13	Boron: .002	

Analysis in weight percent unless noted

Original Dimension, In.: _____	Bend Diameter: _____
Original Area, Sq. In.: _____	Bend Test Angle: _____
Yield, PSI: _____	Character of Fracture: _____
Yield Method: _____	Approved: _____ Rejected: _____
Tensile, PSI: _____	
Elongation, %: _____	Charpy, Ft. lbs.: _____
Gauge Length, In.: _____	Charpy Specimen Size: _____
Red. in Area, %: _____	Lateral Exp., Mile: _____
Character of Fracture: _____	Shear Fracture, %: _____
Hardness, Actual Reading: _____	Test Temperature: _____
Converted Value: _____	Character of Fracture: _____

Results reported apply only to the sample submitted.

The above tests were performed with the application of one or more of the following specifications: ASTM A48, A126, A370, A395, E8, E10, E18, E23, E334, E403, E415, E478, E536, E1019, E1024, E1086, E1409, E1447, E1473, 10CFR21, LSCD GDS 400A App. 4 & R-2 SM 5-17, ISO 148 Parts 1 & 2, EN 10002 Part 1, EN 10204 Sec. 3.1, and Anderson Laboratories' Quality Manual Revision N dated 02/24/14

This report shall not be reproduced except in full, without the written approval of Anderson Laboratories, Inc.

Michael Porfilio
 Michael Porfilio, Director of Operations

Figure K.12: Certificate for Alloy Fe-12Cr.



P.O. BOX 2245 BUTLER, PA 16003
(724) 789-0158 • FAX: (724) 789-0189

CERTIFICATE OF ANALYSIS

Bill To

University of Wisconsin - Madison
Accounts Payable
21 North Park, Suite 5301
Madison, WI 53715-1218

Ship To

Novar
UW-Madison I
1500 Engineer
Madison, WI 5
Attn: Mr. Ale

Purchase Order # 258K495 115794
Description Fe/Cr (89/12) Wt.% Alloy Sheet
Dimensions 0.063" x 0.070" x 14" RW x 9' RL
Condition Hot Rolled, Flattened, De-oxid
Heat # 10105481
Quantity 30 Lbs.

CHEMICAL ANALYSIS

ELEMENT	COMPOSITION (WT.%)
Fe	Balance
Cr	11.89

SAI certifies that this alloy was manufactured using material of the following purity:

Iron — Lot #: 10G-128

Element	Composition (Wt.%)	Element	Composition (Wt.%)
C	0.0004	B	0.0002
Si	<0.0005	Co	0.0029
Mn	0.0001	Cu	0.0001
P	0.0003	H	0.0008
S	0.0005	Sn	<0.0001
Cr	0.0002	Pb	0.0001
N	0.0005	O	0.0090
Ni	0.0010		
Zn	0.0005		
As	<0.0001		

Chromium — Lot #: 10082

Element	Composition (Wt.%)	Element	Composition (Wt.%)	Element	Composition (Wt.%)
C	0.013	Bi	<0.001	Sb	<0.002
Si	<0.01	Cu	<0.002	Sn	<0.001
S	0.004	Fe	0.14	Zn	<0.002
P	<0.005	Ga	<0.005	N	0.006
Al	<0.005	Mn	0.003	O	0.035
As	<0.002	Pb	<0.001	H	0.0005

Figure K.13: Certificate for Alloy H230.

CERTIFICATION OF TESTS • RAPPORT DES SAIS CERTIFIÉ • WERKSZELTENS										CUSTOMER COPY																																																																							
Sales Order No Reference Commande Beschreibung Nr 50015900140		Date Entered Date de Commande Beschreibung 07/10/09		Customer Reference Reference Client Kundenbestellnr VERBAL KEITH		Report No. Zeugnis Nr 20090715085		Page of Pages Page de Pages Anzahl der Seiten 1 of 3		<p>HAYNES International</p> <p>HAYNES INTERNATIONAL 1020 West Park Avenue PO Box 9013 Kokomo, Indiana, 46902</p>																																																																							
<p>Sold To • Client • Beschirmer/berf MARKETING MANAGEMENT DOMESTIC IN 000000 USA</p>																				<p>Ship To • Destinataire • Bestimmung HAYNES INTL INC 2000 W DEFFENBAUGH KOKOMO IN 46902 USA</p>																																																													
<p>Specification • Specification • Spezifikation AMS 5878, C</p>										<p>Quantity Ordered Quantité Commandée Bestelldmenge 1 PC</p> <p>Quantity Shipped Quantité Expédiée Liefermenge 1 PC</p>																																																																							
<p>Heat Number Numéro de Cales 8305 8 7828</p>										<p>Product Description • Description Produit • Material Bezeichnung 0.063 (0.061/0.065) x 48 x 72 HAYNES(R) 230(R) ALLOY SHEET - Nadcap CERTIFICATE NUMBER 0089 GE# 19762, S400 10/10/2008, S1000 1/2/2008, EN 10204 3.1, AS9100</p>																																																																							
<p>Chemical Analysis • Analyse Chimique • Chemische Analyse</p> <table border="1"> <thead> <tr> <th>Al</th> <th>B</th> <th>C</th> <th>Cr</th> <th>Fe</th> <th>Mn</th> <th>Mo</th> <th>Ni</th> <th>P</th> <th>S</th> <th>Si</th> <th>Ti</th> <th>V</th> <th>W</th> </tr> </thead> <tbody> <tr> <td>0.37</td> <td>0.002</td> <td>0.100</td> <td>0.21</td> <td>22.08</td> <td>0.04</td> <td>1.02</td> <td>0.52</td> <td>1.23</td> <td>BAL</td> <td>0.005</td> <td><0.002</td> <td>0.31</td> <td><0.01</td> <td>14.17</td> <td>BUTT END '01</td> </tr> <tr> <td></td> <td></td> <td></td> <td></td> <td></td> <td></td> <td></td> <td></td> <td></td> <td></td> <td></td> <td></td> <td></td> <td></td> <td></td> <td>BUTT END '01</td> </tr> <tr> <td></td> <td></td> <td></td> <td></td> <td></td> <td></td> <td></td> <td></td> <td></td> <td></td> <td></td> <td></td> <td></td> <td></td> <td></td> <td>BUTT END '01</td> </tr> </tbody> </table>										Al	B	C	Cr	Fe	Mn	Mo	Ni	P	S	Si	Ti	V	W	0.37	0.002	0.100	0.21	22.08	0.04	1.02	0.52	1.23	BAL	0.005	<0.002	0.31	<0.01	14.17	BUTT END '01																BUTT END '01																BUTT END '01	<p>Quantity Shipped Quantité Expédiée Liefermenge 1 PC</p>									
Al	B	C	Cr	Fe	Mn	Mo	Ni	P	S	Si	Ti	V	W																																																																				
0.37	0.002	0.100	0.21	22.08	0.04	1.02	0.52	1.23	BAL	0.005	<0.002	0.31	<0.01	14.17	BUTT END '01																																																																		
															BUTT END '01																																																																		
															BUTT END '01																																																																		
<p>Certified By • Certifié Par • Bescheinigt Durch: Tammy Shepherd Certification Technician</p> <p><i>T Shepherd</i></p>										<p>7/15/2009</p>																																																																							

CUSTOMER COPY

HAYNES
INTERNATIONAL

Haynes International
1020 West Park Avenue
PO Box 9013
Kokomo, Indiana, 46902

Customer Order No. 59015600140	Date Entered 07/11/09	Customer Reference VERBAL KEITH	Report No. 209071585	Page of Pages 2 of 3
Order Number 59015600140	Order Date 07/11/09	Manufacturer VERBAL KEITH	Report Date 209071585	Material or Specs ASME B72.1

Trade Test at Room Temperature • Load By Tension A Temp. Ambient • Zugsversuch				Trade Test at Elevated Temperature • Load By Tension A 150 F Temp.				Stress Relaxation Temperature • Load A Change By Report Zusatzversuch										
Yield	Tensile	Elong.	Red.	Yield	Tensile	Elong.	Red.	Time	Force	Force	Time	Force	Force	Time	Force	Force	Time	Force
MPa	MPa	%	%	MPa	MPa	%	%	hrs	MPa	MPa	hrs	MPa	MPa	hrs	MPa	MPa	hrs	MPa
120000 PSI	65000 PSI	47 %	DAI						1700 hr	10000 PSI	110 HRS	15 %	DAI					

Material Description Order Part No.	Trade Test Order Part No.	General Data				RCA	Tensile	Customer Data		Customer Part	Order Part No.	Change Impact Test				Comp Report			
		Order Part No.	Material	Spec	Temp			Temp	Temp			Temp	Temp	Temp	Temp	Temp	Temp	Temp	Temp
95 HRBW	1AN	43			40000 IN														

T. Shepherd

Certified By • Certified For • Inspecting Durch: **Tranny Shepherd**
Certification Technician

7/15/2009 [J] 34551-99201

INTERNATIONAL HAYNES METALS COMPANY IS AN EQUAL OPPORTUNITY EMPLOYER. MINORITY AND FEMALE EMPLOYMENT IS ENCOURAGED. ALL RIGHTS RESERVED. HAYNES METALS COMPANY IS NOT RESPONSIBLE FOR THE ACTIONS OF ITS CUSTOMERS OR SUPPLIERS. HAYNES METALS COMPANY IS NOT RESPONSIBLE FOR THE ACTIONS OF ITS CUSTOMERS OR SUPPLIERS. HAYNES METALS COMPANY IS NOT RESPONSIBLE FOR THE ACTIONS OF ITS CUSTOMERS OR SUPPLIERS. HAYNES METALS COMPANY IS NOT RESPONSIBLE FOR THE ACTIONS OF ITS CUSTOMERS OR SUPPLIERS.

CERTIFICATE OF TESTS • RAPPORT D'ESSAIS CERTIFIÉ • WEINSTEIGENIS			
Substrate No. Reference No.	Date Issued Revised	Customer Reference Manufacturer	Report No. Zaprosy No.
560159001-0	07/10/09	VERBAL KEITH	20990715085
			Page of Pages Number of Pages
			1 OF 3

HAYNES
International

CUSTOMER COPY
Haynes International
1020 West Park Avenue
PO Box 9013
Kokomo, Indiana 46903

All tests and inspections have been performed and results meet specification requirements.
THIS MATERIAL IS FREE FROM MERCURY, CADMIUM, RADIUM, AND ALPHA SOURCE CONTAMINATION.
This material conforms to all technical requirements of AMS 578.
MIL-D-13811 Class 32519201 (I PC)
MIL-D-13811 Class 32519201 (I PC)
Method of Chemistry Analysis for Lead 8728 BILT END #1: OE (ALBA)PS8 LECO(CS) XRD LIMIT (CFC)C&M&M&N(TW)
At 2150 °F to 2275 °F

Certified By • **Cristie Par • Beckwith/Dave; Tammy Shepard** 7152009
Certification Technician

T. Shepard

© 2009 Haynes International, Inc. All rights reserved. This document is the property of Haynes International, Inc. and is not to be distributed, copied, or reproduced in any form without the written permission of Haynes International, Inc. The information contained herein is confidential and proprietary to Haynes International, Inc. and is not to be disclosed to any third party without the written permission of Haynes International, Inc. The information contained herein is for informational purposes only and does not constitute an offer of insurance or any other financial product. The information contained herein is not to be used as a basis for any investment decision. The information contained herein is not to be used as a basis for any investment decision. The information contained herein is not to be used as a basis for any investment decision.

Figure K.14: Certificate for pure Fe.

Certificate Of Analysis

Metal Men

Material: Iron

Size: Thickness: 0.062 Inch Width: 5.5 Inch Length: 10.5 Inch

Qty/Unit: 1 Piece(s)

Lot Number: FE29639381

Temper: Annealed

Material(s)	Percentage			
Iron	99.6			
--- Element ---	PPM	Percentage	Included	Method
C Carbon	250	0.025		
Cr Chromium	300	0.03	✓	
Cu Copper	400	0.04	✓	
Mn Manganese	1800	0.18	✓	
Ni Nickel	500	0.05	✓	
P Phosphorus	120	0.012	✓	
S Sulfur	250	0.025	✓	
Si Silicon	500	0.05	✓	

Notes: Typical values

This material cannot be rejected based on test results of another analytical laboratory alone. Test results may deviate from these values due to variations in each laboratory's testing methods. Any differences will be evaluated.

By: Thomas H. Goodloe
 Thomas H. Goodloe, Vice President

UNIVERSITY OF WISCONSIN
 P.O. V202-PAUL
 1pc) 5 1/2" x 10 1/2"

* I = Ion Interference C = Instrument Contamination S = Source Contamination
 Lot Number: FE29639381

Iron

Page 1 of 1

Figure K.15: Certificate for pure Ni.

9359-1

HUNTINGTON ALLOYS
A Special Metals Company
HUNTINGTON, WEST VIRGINIA 25701

NOTE: THE RECORDS OF THESE ACTIVITIES OR PRODUCTS
AS A PROPERTY OF THE COMPANY ARE NOT TO BE
OTHER DIRECTLY NOT ASSIGNABLE TO THE COMPANY

METALMEN SALES, INC. P.O. BOX 54 NEW YORK, NY 10044		CERTIFIED MATERIAL TEST REPORT		No. 61131
IN ORDER NO.	DATE	MANUFACTURER	HA/PMC	PLANT OR
30001725 1	05/30/78			1 2
QUANTITY				
3150 LBS				
ORDER NO.	ORDER NO.			
4500198555				
DESCRIPTION				
NICKEL 300 CR SHEET 1/4" THK CR 1/4"				
0.010 IN 49.0000 IN COIL				

*****THIS REPORT RELATES ONLY TO THE ITEM(S) TESTED AND MAY NOT BE REPRODUCED EXCEPT IN FULL.*****

UNSM:MO2200

SPECIFICATIONS: MAT 328 REV PLASTM B 162-94(2005)
 ASME B8-15 1087 EDITION NO ADDENDA
 QUALITY SYSTEM CERTIFICATION: ISO 9001:2000 (ABS-Q2 CERT. 30125)
 EN 10 204/DIN 5083 (TYPE 3.1)

HEAT#	C	HW	FE	S	CHEMICAL ANALYSIS (WT. %)	CU	NI
#1308AG	0.02	0.24	0.04	<0.001	0.07	0.05	99.52

MELT METHOD: A1M - ELECTROSLAG REHEATED

MECHANICAL PROPERTIES

HEAT/LOT	QUANTITY	HARDNESS	GRAIN YIELD TENSILE	SELG.	W/M	DEC
#1308AG C85A 1 PC			2"	X	F	
MOON TEMP-HRB	-AS SHIPPED	37.8	0192	0393	43.8	

YIELD STRENGTH WAS DETERMINED USING A STRESS STRAIN CURVE

COUNTRY OF ORIGIN: MELTED AND MANUFACTURED IN THE USA

VISUAL AND DIMENSIONAL EXAMINATION SATISFACTORY.

MATERIAL, WHEN SHIPPED, IS FREE FROM CONTAMINATION BY MERCURY, SADIUM, ALPHA SODIUM, & LOW MELTING ELEMENT

"CHEMICAL ANALYSIS AS REQUIRED FOR CARBON, SILICON, NITROGEN OR OXYGEN IS PERFORMED BY CONSUMPTION TECHNIQUES.

ALL OTHER REPORTED ELEMENTS ARE ANALYZED BY X-RAY AND/OR EMISSION SPECTROSCOPY."

"QUALITY SYSTEM MEETS REQUIREMENTS OF DIRECTIVE 91/271/EE (PRESSURE EQUIPMENT DIRECTIVE).

AND CHAPTER 4.3 PER ABS GROUP LTD CERTIFICATE 008(EXPIRES AUGUST 2003) AND

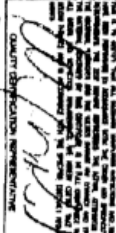
TUV CERTIFICATE 20674926 (EXPIRES MAY 2003)."

University of Wisconsin
P.O. VIAL PAUL
1pc) 10" x 10"

NOTE: THE RECEIPT OF THIS REPORT IS PRESUMED TO BE A RECEIPT FOR THE MATERIALS LISTED THEREON UNLESS THE BUYER SPECIFICALLY ADVISES THE SELLER TO THE CONTRARY. THIS REPORT IS NOT ASSIGNABLE TO OTHER DIRECT BUYERS.

HUNTINGTON ALLOYS
A Special Metals Company
HUNTINGTON, WEST VIRGINIA 25701

INSTALLER SALES, INC.
P.O. BOX 54
NEW YORK, NY 10044

CERTIFIED MATERIAL TEST REPORT		No.	62131
IN ORDER NUMBER	DATE	PAGE	OF
30001235 1	05/30/08	2	2
QUANTITY	INSPECTED BY	QUALITY CONTROL REPRESENTATIVE	
31.90 LBS	H.A./SNC		
CHANGE ORDER NO.	MARK ORDER NO.		
4500195555			
NICEET 200 CR SHEET IN COIL CR ANN			
.0520 IN 49.0000 IN COIL COIL			

AUTORIZED QUALITY CERTIFICATION REPRESENTATIVES:
W.C. BOLLEN, P.D. CUSTER, M.A. MORRISON, P. WUBB

4359-2

Figure K.16: Certificate for Alloy GR22.

TEST CERTIFICATE

SHIP TO: ARCELORMITTAL PLATE LLC
 METALMEN SALES, INC.
 P.O. BOX 84
 NEW YORK, NY 10044

PAGE NO: 01 OF 02
 FILE NO: 0284-01-05
 MILL ORDER NO: 14249-001
 MELT NO: C6886
 SLAB NO: 398A
 DATE: 05/20/13

SEND TO: UNIVERSITY OF WISCONSIN
 P.O. VABL- PAUL 01-C

1pc) 10" x 10"

PLATE DIMENSIONS / DESCRIPTION

TOTAL QTY	GAUGE	WIDTH	LENGTH	DESCRIPTION	PIECE WEIGHT
1	.5"	96"	480"	RECTANGLE	6534#

CUSTOMER INFORMATION
 CUSTOMER PO: 94436-NY
 PART NO. 4

SPECIFICATION(S)
 THIS MATERIAL HAS BEEN MANUFACTURED AND TESTED IN ACCORDANCE WITH PURCHASE ORDER REQUIREMENTS AND SPECIFICATION(S).
 ASTM A387 YR 10 GR 22 CL 2
 ASME SA387 ED 10 11A ADDENDA GRADE 22 CLASS 2
 THE MANAGEMENT SYSTEMS FOR MANUFACTURE OF THIS PRODUCT ARE CERTIFIED TO ISO 9001:2008 (CERTIFICATE NO. 30130) AND ISO 14001 (CERTIFICATE NO. 009496).

CHEMICAL COMPOSITION

MELT: C6886	C	MN	P	S	CU	SI	NI	CR	MO
	.14	.52	.008	.007	.10	.21	.08	2.31	.96

MELT: C6886	V	TI	B	AL	CB	SB	AS	SN
	.004	.002	.0001	.026	.001	.0010	.0020	.005

MANUFACTURE
 ELECTRIC FURNACE QUALITY - FINE GRAIN PRACTICE

HEAT TREAT CONDITION

MATL OR TEST	HEAT TREAT DESCRIPTION	NOM TEMP	HOLD MINS	COOL MTHD
PL/TEST	NORMALIZE	1660F	40	AIR COOL
PL/TEST	TEMPER	1320F	39	AIR COOL

WE HEREBY CERTIFY THE ABOVE INFORMATION IS CORRECT:

ARCELORMITTAL PLATE LLC
 QUALITY ASSURANCE LABORATORY
 139 MODENA ROAD
 COATESVILLE, PA 19320

Elinore Zaplitny
 SUPERVISOR - TEST REPORTING
 ELINORE ZAPLITNY

TEST CERTIFICATE

PAGE NO: 02 OF 02
 FILE NO: 0284-01-05
 MILL ORDER NO: 14249-001
 MELT NO: C6886
 SLAB NO: 39BA
 DATE: 05/20/13

TENSILE PROPERTIES

SLAB NO.	LOC	DIR	YIELD STRENGTH PSI X 100	TENSILE STRENGTH PSI X 100	ELONGATION GAGE LGTH	%	RA.
39BA	BOT.	TRANS.	754	908	2.00"	26.0	57.0

GENERAL INFORMATION

ALL STEEL HAS BEEN MELTED AND MANUFACTURED IN THE U.S.A.
 TEST CERTS. ARE PREPARED IN ACCORD. WITH PROCEDURES
 OUTLINED IN EN 10204:2004 TYPE 3.1.
 ACID SOLUBLE ALUMINUM
 FOR MORE INFORMATION AND PROCESSING GUIDELINES, REFER TO
 WWW.ARCELORMITTAL.COM/PLATEINFORMATION
 B/L #22544 SOU 114245

WE HEREBY CERTIFY THE ABOVE
 INFORMATION IS CORRECT:

ARCELORMITTAL PLATE LLC
 QUALITY ASSURANCE LABORATORY
 139 MODENA ROAD
 COATESVILLE, PA 19320

Elinore Zaplitny
 SUPERVISOR - TEST REPORTING
 ELINORE ZAPLITNY

Figure K.17: Certificate for pure Cr.

Certificate Of Analysis

Metal Men

Material: Chrome
 Size: Thickness: 0.5 Inch Width: 1.5 Inch Length: 8 Inch
 Qty/Unit: 1 Piece(s)
 Lot Number: CR39762511

*UNIVERSITY OF WISCONSIN
 P.O. VEBER PAUL
 1pc) 1 1/2" x 8"*

Materials(s)	Percentage	PPM	Percentage Included	Method
Chromium	99.97			
Ag Silver		0.18	0.000018 ✓	GDMS
Al Aluminum		1.3	0.0013 ✓	GDMS
As Arsenic		0.79	0.000079 ✓	GDMS
Au Gold		0.05	0.000005 ✓	GDMS
B Boron		0.05	0.000005 ✓	GDMS
Ba Barium		1.6	0.00016 ✓	GDMS
Be Beryllium		0.005	0.0000005 ✓	GDMS
Bi Bismuth		0.01	0.000001 ✓	GDMS
Br Bromine		0.01	0.000001 ✓	GDMS
C Carbon		5.3	0.0053	LECO
Ca Calcium		3.2	0.00032 ✓	GDMS
Cd Cadmium		0.1	0.00001 ✓	GDMS
Ce Cerium		0.008	0.0000008 ✓	GDMS
Cl Chlorine		11	0.0011 ✓	GDMS
Co Cobalt		2	0.0002 ✓	GDMS
Cs Cesium		0.01	0.000001 ✓	GDMS
Cu Copper		2.4	0.00024 ✓	GDMS
Dy Dysprosium		0.005	0.0000005 ✓	GDMS

* I = Ion Interference C = Instrument Contamination S = Source Contamination

Lot Number: CR39762511

Chrome

Page 1 of 3

Appendix L

Certificates of Conformance

Figure L.1: Certificate of conformance for example Omega pressure transducer.

**OMEGA ENGINEERING INC.
CERTIFICATE OF CALIBRATION**

Model Number: PX409-5.0KG5V	Capacity: 5000.00 PSIG
Serial Number: 445460	Excitation: 24.00 Vdc
Date: 6/6/2014	Technician: GRS
Job: R9822	

Pressure Connection: 1/4-18 NPT Male

Electrical Connection: **WIRING CODE**
Integral Cable 4-Cond
BLACK = - EXCITATION
WHITE = + OUTPUT
GREEN = N/C
RED = + EXCITATION

CALIBRATION WORKSHEET		NOTES
Pressure PSIG	OUTPUT Vdc	
0.00	- 0.001	
2500.00	2.499	
5000.00	5.002	
2500.00	2.501	
0.00	0.000	

NIST Traceable Number(s): C-2505, C-1316

Omega Eng. Inc., certifies that the above instrumentation has been calibrated and tested to meet or to exceed the published specifications. This calibration was performed using instrumentation and standards that are traceable to the National Institute of Standards and Technology. This document also ensures that all testing performed complies with MIL-STD 45662-A, ISO 10012-1, and ANSI/NCSS Z540-1-1994 requirements. After Final Calibration our products are stored in an environmentally controlled stock room and are considered in bonded storage. Depending on environmental conditions and severity of use, factory calibration is recommended every one to three years after the initial service installation date.

Bruce Lott
Accepted and Certified By

6/6/2014
Date

Omega Engineering Inc., One Omega Drive, Stamford, CT 06907
http://www.omega.com email: info@omega.com phone (800) 826-6342

GAGE & ABSOLUTE PRESSURE TRANSDUCER																					
PX409, 409C, 419, 429 & 459 0 TO 5 VDC																					
CERTIFICATE OF CONFORMANCE DOCUMENT A012570																					
MODEL NUMBER INTERPRETATION																					
PX	PRODUCT SERIES			ELECTRICAL CONNECTOR			RANGE CODE			GAGE	ABSOLUTE	0 to 5 VDC OUTPUT	PRESSURE RANGE (PSI)	SUPPLY VOLTAGE (VDC)	OUTPUT (VDC)	COMPENSATION TEMPERATURE (°C)	ZERO BIFT ±1/SPAN	SPAN BIFT ±1/SPAN	OVER PRESSURE (TIMES)	CONTAINMENT GAGE UNITS (PSI)	CONTAINMENT ABS UNITS (PSI)
	X1	X2	X3	X4	X5	X6	X7	X8													
CABLE	4	0	9	1	0	W	G	N/A	5V	10 ² H2O	10 TO 30	0 TO 5	-17 TO 85	1.00	1.00	10	1000	NA	1000	NA	
DIN	4	1	9	0	0	1	G	N/A	5V	1	10 TO 30	0 TO 5	-17 TO 85	1.00	1.00	6	1000	NA	1000	NA	
BENDIX	4	2	9	2	...	S	G	N/A	5V	2.5	10 TO 30	0 TO 5	-17 TO 85	1.00	1.00	4	1000	NA	1000	NA	
CONDUIT	4	0	9C	0	0	S	G	A	5V	5	10 TO 30	0 TO 5	-17 TO 85	1.00	1.00	4	1000	6000	6000	6000	
M12	4	5	9	0	1	S	G	A	5V	15	10 TO 30	0 TO 5	-29 TO 85	0.50	0.50	4	3000	6000	6000	6000	
				0	3	0	G	A	5V	30	10 TO 30	0 TO 5	-29 TO 85	0.50	0.50	4	3000	6000	6000	6000	
				0	5	0	G	A	5V	50	10 TO 30	0 TO 5	-29 TO 85	0.50	0.50	4	3000	6000	6000	6000	
				1	0	0	G	A	5V	100	10 TO 30	0 TO 5	-29 TO 85	0.50	0.50	4	3000	6000	6000	6000	
				1	5	0	G	A	5V	150	10 TO 30	0 TO 5	-29 TO 85	0.50	0.50	4	3000	6000	6000	6000	
				2	5	0	G	A	5V	250	10 TO 30	0 TO 5	-29 TO 85	0.50	0.50	4	3000	6000	6000	6000	
				5	0	0	G	A	5V	500	10 TO 30	0 TO 5	-29 TO 85	0.50	0.50	4	3000	6000	6000	6000	
				7	5	0	G	A	5V	750	10 TO 30	0 TO 5	-29 TO 85	0.50	0.50	4	3000	6000	6000	6000	
				1	0	K	G	A	5V	1000	10 TO 30	0 TO 5	-29 TO 85	0.50	0.50	4	3000	6000	6000	6000	
				1	5	K	G	A	5V	1500	10 TO 30	0 TO 5	-29 TO 85	0.50	0.50	7250 PSI	10000	10000	10000	10000	
				2	5	K	G	A	5V	2500	10 TO 30	0 TO 5	-29 TO 85	0.50	0.50	7250 PSI	10000	10000	10000	10000	
				3	5	K	G	A	5V	3500	10 TO 30	0 TO 5	-29 TO 85	0.50	0.50	7250 PSI	10000	10000	10000	10000	
				5	0	K	G	A	5V	5000	10 TO 30	0 TO 5	-29 TO 85	0.50	0.50	7250 PSI	10000	10000	10000	10000	

SERIES TYPE	RANGE TYPE AND OUTPUT	ACCURACY IDENTIFIER	ACCURACY STATEMENT
PX 409, 409C, 419, 459	X4, X5, X6, X7, X8	NO IDENTIFIER	0.06% BSL INC NON LINEARITY, HYST AND NON REPEAT
		EH	0.05% BSL INC NON LINEARITY, HYST AND NON REPEAT
		XL	0.03% BSL INC NON LINEARITY

GENERAL SPECIFICATION	
INPUT	VDC SEE TABLE
OUTPUT	0 TO 5 VDC SEE TABLE
OVER PRESSURE	SEE TABLE
CONTAINMENT	SEE TABLE
ACCURACY	SEE TABLE
SETTING ACCURACY ZERO	± 5% FS TYP 1% MAX (± 1% TYP ± 2% MAX FOR 2.5 PSI AND BELOW)
SETTING ACCURACY SPAN	± 5% FS TYP 1% MAX (± 1% TYP ± 2% MAX FOR 2.5 PSI AND BELOW)
	CALIBRATION IN VERTICAL DIRECTION WITH FITTING DOWN
LONG TERM STABILITY	± 0.1% FS TYPICAL (1 YEAR)
DURABILITY	1 MILLION TYPICAL
MEDIA COMPATIBILITY	ALL WETTED MATERIALS 316 (L) STAINLESS STEEL
EMC COMPATIBILITY (CE)	EC DIRECTIVE 2004/108/EC (CONSOLIDATED 89/338); STANDARD IEC 61326:2005 FOR INDUSTRIAL LOCATIONS
ROHS	YES

0 TO 5 VDC EXTERNAL WIRING CODES			
	CABLE PX409 & PX409C	MINI DIN PX419 & M12 PX459	TWIST LOCK PX429
EXCITATION (+)	RED	PIN 1	PIN A
EXCITATION (-)	BLACK	PIN 2	PIN B
OUTPUT (+)	WHITE	PIN 3	PIN C
NC *	GREEN	PIN 4	PIN D
NC *			PIN E
NC *			PIN F

M12 PX459

KEY

PIN 1

PIN 2

PIN 3

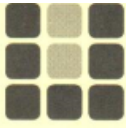
PIN 4

FACTORY PIN. DO NOT CONNECT TO PIN

Figure L.2: Certificate of conformance for Sartorius high precision scale.

CALIBRATION SERVICE RECORD

Traceability includes no less than: An unbroken chain of comparison, realization of SI units, measurement uncertainty, documentation, competence, periodic recalibration, and measurement assurance. United Scale documents the traceability of measurements to the SI units through the National Institute of Standards and Technology (NIST) or the National Research Council of Canada (NRC), or other recognized national measurement institutes (NMI's) or international standard bodies, or to measurable conditions created in our laboratory, or accepted fundamental and/or natural physical constants, ratio type of calibration, or by comparison to consensus standards.



**UNITED
SCALE
& ENGINEERING
CORPORATION**
A TRANSCAT Company

16725 W. Victor Road
New Berlin, Wisconsin 53151-4132
262-785-1733 • 800-236-1733
FAX 262-785-9754

1322 Russett Court
Green Bay, Wisconsin 54313-8999
920-434-2737 • 800-236-2737
FAX 920-434-9605

4123 Terminal Drive, Suite 230
McFarland, Wisconsin 53558-8701
608-838-8058 • 800-747-4474
FAX 608-838-9098

Page 1 of 1

MODEL NO. <u>CPA26P</u>		SERIAL NO. <u>23105705</u>	DEVICE ISO CODE: <u>—</u>
CAL DATE: <u>6-14-16</u>	MANUFACTURER: <u>SARTORIUS</u>	TOLERANCE: <u>1/10000000</u>	CAL LOCATION: <input checked="" type="checkbox"/> Customer <input type="checkbox"/> Other
NEXT DUE: <u>6-17</u>	CAPACITY X RESOLUTION: <u>21X,00001 g</u>	CUSTOMER: <u>UN ENR</u>	
FREQ: <u>1 yr</u>	CALIBRATION REASON: <input type="checkbox"/> Scheduled <input checked="" type="checkbox"/> Demand <input type="checkbox"/> Other	CERT/ISO NBR: <u>DK6C2</u>	
LOCATION: <u>Room 914</u>		DESCRIPTION: <u>BALANCE</u>	

Parameter Tested	Actual as Found	Deviation	Final Reading
<u>1.00500 G</u>	<u>1.005004</u>	<u>+1.000004</u>	<u>1.005004</u>
<u>1.0000 G</u>	<u>1.00008</u>	<u>+1.000008</u>	<u>1.00008</u>
<u>1.00000 G</u>	<u>1.000014</u>	<u>+1.000014</u>	<u>1.000014</u>
<u>10.00000 G</u>	<u>10.00000</u>	<u>10.00000</u>	<u>10.00000</u>
<u>20.00000 G</u>	<u>20.00004</u>	<u>20.00004</u>	<u>20.00004</u>

Shift Test

CORNER	LOAD	ERROR	FINAL READING
1	<u>10</u>	<u>0</u>	<u>10.00000</u>
2	<u>10</u>	<u>+0.00001</u>	<u>10.00001</u>
3	<u>10</u>	<u>0</u>	<u>10.00000</u>
4	<u>10</u>	<u>0</u>	<u>10.00000</u>

1	2
4	3

Were actual values within tolerance? Yes No

Was device adjusted? Yes No

Were final values within tolerance? Yes No

LABEL USED: Calibration / Tested Limited Calibration DO NOT USE - Out of Calibration Leveled: Yes No

United Scale's Operations Procedure P1511 is followed for device calibration. TEST WEIGHT STANDARDS USED (Test weights calibrated per NIST HANDBOOK 105-1):

USM MWS

UNCERTAINTY MEASUREMENT: 1.000013 g

COMMENTS: TESTED

TESTED BY: (Technician): SJM Date: 6-14-16

This calibration is accredited and meets the requirements of ISO/IEC 17025 as verified by ANSI-ASQ National Accreditation Board / ACLASS. Refer to certificate and scope to accreditation AC-1148. This certificate may not be reproduced except in full, without the written approval of Transcat, Inc.

F0172R0 May 2, 2014

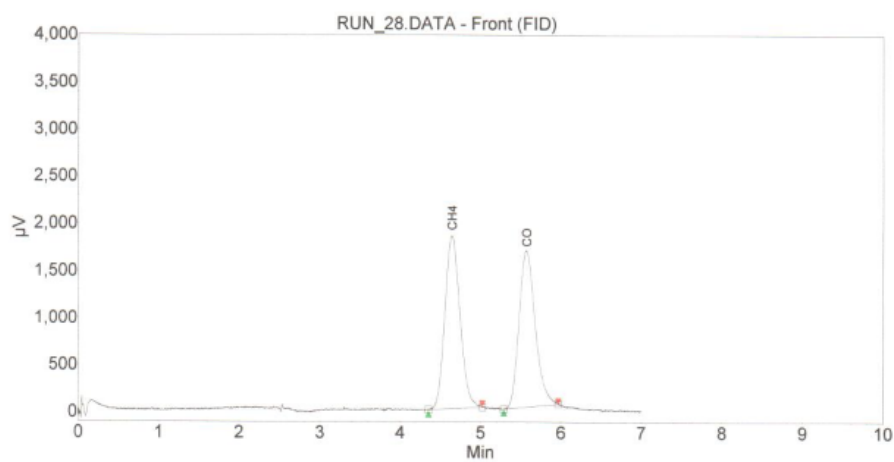
 UNITED SCALE A ENGINEERING CORPORATION A TROBAGT Company		CUSTOMER COPY		SERVICE ORDER REPORT ISO/IEC 17025 ACCREDITED		• SALES • SERVICE • RENTALS • WEBSITE: www.unitedscale.com • E-MAIL: sales@unitedscale.com			
<input type="checkbox"/> 16725 W. Victor Rd., New Berlin, WI 53151-4132 262-785-1733 • 800-236-1733 • FAX 262-785-9754		<input type="checkbox"/> 1322 Russett Ct., Green Bay, WI 54313-8999 920-434-2737 • 800-236-2737 • FAX 920-434-9605		<input type="checkbox"/> 4123 Terminal Dr., Suite 230, McFarland, WI 53558-8701 608-838-8058 • 800-747-4474 • FAX 608-838-9098					
SHIP TO: UNIVERSITY OF WISCONSIN NUCLEAR ENG./ENG. PHYSICS NEEP 1500 ENGINEERING DRIVE MADISON WI 53706				SOLD TO: UNIVERSITY OF WISCONSIN 1500 ENGINEERING DRIVE MADISON WI 53706					
SPECIAL INSTRUCTIONS:						ORDER DATE: 6/09/16			
CONTACT: JACOB MAHAFFEY			PER:		PHONE: 217-493-2385		CERT/ISO NBR: 01 DK6CZ 00		
SERVICE CALL		INSPECTION NUMBER:		P.O. NUMBER: ANDERSON - CC		CUSTOMER ACCOUNT NUMBER: 0000572468			
						SERVICE REQUIRED BY: 6/13/16			
QTY.	SCALE IDENTIFICATION						SERVICE PERFORMED		USED VOL
	SERVICE CALL ON PORTARIUS CAPACIT SCALE						PROBLEM: TEST & CALIBRATE		
1	SERVICE Labor & Travel Time Hours						TESTED @ BAWANRE		
STANDARDS USED:									
THIS SERVICE AS DESCRIBED HAS BEEN PERFORMED									
CUSTOMER SIGNATURE				QTY.		PARTS REPLACED:		INV. SITE	PRICE
DATE PERFORMED									
TECHNICIAN				REG. TIME		TRAVEL TIME			
ARRIVAL TIME	DEPART TIME	TECH#	DATE	HOURS ON JOB	T.T.	TOTAL	TRUCK NO.	TOTAL LBR/TT	@
2:00		45	6/14/16				45		
								OVERTIME	@
								MILEAGE	@
								MISC.	
								OTHER	
								SUB TOTAL	
								TAX	rate
TEST REPORTS TO BE ISSUED: YES <input type="checkbox"/> NO <input type="checkbox"/>				TYPE/NO		WAS JOB COMPLETED? YES <input type="checkbox"/> NO <input type="checkbox"/>		TOTAL	
<small>07990 May 7, 2014</small> I WOULD LIKE INFORMATION ON A SERVICE CONTRACT <input type="checkbox"/>									

Figure L.3: Certificate of conformance for Varian 450 Gas Chromatograph.

Chromatogram : RUN_28_channel1

System : Univ of Wisconsin
Method : UW Madison
User : Administrator

Acquired : 8/21/2015 5:01:21 PM
Processed : 8/24/2015 8:02:42 AM
Printed : 8/24/2015 8:03:06 AM



Peak results :

Index	Name	Time [Min]	Quantity [% Area]	Height [μV]	Area [μV Min]	Area % [%]
1	CH4	4.64	50.81	1833.5	399.9	50.806
2	CO	5.57	49.19	1661.6	387.2	49.194
Total			100.00	3495.1	787.1	100.000

Figure L.4: Certificate of conformance for SSI Supercritical-24 pump.

1. Serial Number: A 200 58559

2. Part Number: S10SNXP1

3. Model: **Supercritical**

4. Customer: Ches-Tec

5. Sales Order Number: M283230

6. Fluid Path: **SS & Peek**

8. Voltage: **115V / 230V SMT**

48. Pump Head Setting Check: **(S12)**

61. a. Frequency/External enable Input Test Passed: **(Yes)**
b. Pump Run Input Test Passed: **(Yes)**
c. Pump Stop Input Test Passed: **(Yes)**
d. Output Relay Test Passed: **(Yes)**
e. Voltage Input Test Passed: **(Yes)**
f. Frequency Input Test Passed: **(Yes)**

510. Temp Tests:

Static Head Temp w/ Pellets: -2.1 deg C
Pumping Head Temp @ 5.500psi: -3.1 deg C
Flowrate @ 5.500 w/backpressure coil: 1.85 mL/min

999. Assembly / Test Acceptance: JW Date: 12-29-16

1000. QC / QA Release: [Signature] Date: 12-29-16

Figure L.5: Manual for calibration of Alpha-Omega Series 3000 Trace Oxygen Analyzer.

ALPHA OMEGA INSTRUMENTS CORP.
SERIES 3000 TRACE OXYGEN ANALYZER

Instruction Manual

Section 6.0
CALIBRATION PROCEDURES

6.1 Initial & Routine Calibration Checks

All Series 3000 Oxygen Trace Oxygen Analyzers are fully calibrated at the factory prior to shipment. However, with the potential hazards associated with shipping instrumentation, it is advisable that the analyzer be given a system calibration check at the time of startup. Alpha Omega Instruments trace oxygen sensors features high accuracy and excellent long term stability characteristics. As a result, routine maintenance is kept to a minimum. As is the case with all gas analyzers, it is advisable to periodically check the overall system calibration. The frequency of these checks is often determined by in-house calibration protocols. If none exists, Alpha Omega Instruments Corp. recommends that a calibration check be made on an average of once every 2-3 months.

6.1.2 Calibration Gas

The oxygen sensor used in the Series 3000 Trace Oxygen Analyzer has a linear output. As a result, it can be calibrated using a single calibration gas as long as the test is performed accurately. The calibration gas should contain a defined concentration of oxygen with a balance of nitrogen (N₂). The actual concentration of oxygen should be chosen based on the range(s) of the instrument. For single range analyzers, choose a calibration gas that is somewhere between 30%-70% of the analyzer's range. For instance, if the analyzer has a range of 0-1,000 ppm, it is advised that the calibration gas should have an oxygen concentration between 300-700 ppm/balance N₂. For three range analyzers, use the same rule of thumb choosing the range most often used as the basis for selecting the calibration gas. As an example, if the analyzer has three ranges consisting of 0-10/100/1,000 ppm and the 0-100 ppm is the most often used range, the calibration gas selected should have an oxygen concentration between 30-70 ppm/balance N₂. Most major gas manufacturers can readily supply calibration gases.

6.1.3 Procedure for Checking Calibration

1. Select a cylinder of calibration gas as described in Section 6.1.2.
2. When selecting a pressure regulator to use with the cylinder gas, it is advisable to use a two-stage regulator with the second stage capable of delivering a gas sample at a pressure of under 1.0 psig. Also, be sure to choose a regulator with a metal diaphragm, preferably stainless steel.
3. In addition to the selection of the pressure regulator, care must be given to choose the correct sample tubing materials. For trace oxygen measuring applications, stainless steel tubing should be used. An alternate choice is copper.



DO NOT USE RUBBER OR PLASTIC TUBING. AIR CONTAINS 209,000 PPM OF OXYGEN. A MINUTE LEAK OF AIR INTO THE EITHER THE CALIBRATION GAS OR SAMPLE GAS LINE CAN CAUSE SIZABLE ERRORS IN READINGS. LEAKAGE CAN BE THROUGH CRACKS IN THE TUBING OR BY DIFFUSION THROUGH THE TUBING.

4. If not already equipped with one, install a flowmeter on the discharge side of the sensor. Being on the downside of the sensor, the materials of construction are of no significance to the readings obtained so acrylic flowmeters are permissible.

SECTION 1.5
Specifications**PERFORMANCE****Measurement Ranges** (parts per million)

Single-range	Three-range
0-10,000	0-100/1,000/10,000
0- 5,000	0- 50/500/5,000
0-1,000	0-10/100/1,000
0-100	0- 5/50/500
0- 50	0-1/10/100

Accuracy¹:	±1% of full scale (±5% FS 0-1ppm range)
Linearity:	±1%
Response Time:	90% of full scale response in less than 10 seconds (typical). The response time for ranges of 0-50 PPM or less depend to a great extent on the design of the sample delivery system including the materials used.
Sensor Type:	Long-life Ambient Temperature Electrochemical Sensor(Optional CO ₂ Resistant Sensor Available).
Temperature Compensation:	Standard
Operating Temperature	(both sensor and electronics): 40° to 104° F (5° to 40° C) <40° F (5° C) use heated sensor enclosure >104° F (40°) cooling of sample gas/sensor required
Warranty:	2 years electronics, 1 year sensor
ELECTRICAL	
Display:	0.4" (10.2 mm) high, 4-1/2 digit LCD
Resolution of Display:	0.1 ppm for ranges <100 ppm 1.0 ppm for ranges >100 ppm
Input Power:	115/230 VAC, 50-60Hz or 18-32 VDC. Optional battery backup available.
Outputs:	4-20 mADC and 0-2 VDC standard as is a TTL output for range identification. RS-232C or RS-485 serial communication optional.
Oxygen Alarm Relays:	Three (3) SPDT Form C contacts rated 10 A @ 30 VDC/115/230 VAC. User selectable for fail-safe or non fail-safe.
Instrument Status Alarm:	Rated identically to the O ₂ relays

**ALPHA OMEGA INSTRUMENTS CORP.
SERIES 3000 TRACE OXYGEN ANALYZER**

Instruction Manual

Audible Alarm:	Internal buzzer with audible cancel
SAMPLE GAS CHARACTERISTICS	
Flow Rate:	1.0 to 2.0 SCFH (0.5 to 1.0 liter/min)
Sample Gas Temperature:	40° to 104° F (5° to 40° C)
Sample Gas Pressure:	0.1 to 1.5 psig (0.007 kg/cm ² to 0.1 kg/cm ²)
Entrained Solids:	<3 mg/ft ³ : no in-line filter required >3 mg/ft ³ : in-line filter is required
Hydrocarbon Mist:	<0.7 mg/ft ³ : no in-line filter required >0.7 mg/ft ³ : in-line filter is required
CONSTRUCTION²	
Electronics Control Unit	(Bench-top without optional equipment): Polycarbonate with a hinged clear front cover, rated NEMA 4X (IP 66)
Control Unit Dimensions:	9.45 in. (240.5 mm) height 6.50 in. (165.1 mm) width 6.20 inches (157.5 mm) Note: All dimensions are without optional equipment
Gas Connections:	1/4" stainless steel compression fittings.
Sensor Mounting:	Local or optional remote mounting
Weight:	11lbs (4.98 kg) (Standard Bench-top Configuration)

¹ Stated at constant temperature and constant pressure.

² Other mechanical configurations available-consult the factory.

³ Alpha Omega Instruments reserves the right to change or modify its product specifications without notice.

Figure L.6: Calibration for Platinum Resistance Temperature Detector.

Fluke Corporation 799 E Utah Valley Drive American Fork, Utah 84003-9775		Fluke Calibration, American Fork Primary Temperature Lab Report of Calibration		 <small>For the Scope of Accreditation Under NVLAP Lab Code 200348-0</small>	
Model: 5624	Description: Platinum Resistance Thermometer	Customer: UW MADISON MADISON, WI, 53706, US			
Serial No.: 0349	Manufacturer: Fluke Calibration				
As Found Condition: Recalibration	As Left Condition: Calibrated	Calibration Model: 1713-6	Calibration Instruction: AFC414 Revision 1		

The above referenced Platinum Resistance Thermometer (PRT) was calibrated by a combination of fixed point and comparison methods over the temperature range(s) specified. The calibration methods used are based on recent publications pertaining to the ITS-90 as it applies to secondary PRT calibrations.


For temperatures above 0°C, this calibration was performed at the appropriate fixed points required for the ITS-90 temperature range identified in the "Calibration Model" location above. For temperatures below 0°C (if applicable), the calibration was performed by comparison against a calibrated SPRT. When the temperature range warrants and additional temperature points are available, measurements at supplementary temperatures are included to improve the quality of the calibration result. The calibration measurements were performed using a digital DC readout and DC reference resistors at one level of excitation current. The value of current used is shown in the calibration data section of this report.

During the course of calibration, the PRT resistance at the triple point of water (RTPW) is measured several times to provide the required calibration data and to verify the stability of the PRT. Additionally, the PRT is annealed after the first RTPW measurement to precondition it for calibration. The initial RTPW measurement shows the "As Found" condition of the PRT and the subsequent RTPW measurements (after annealing) indicate the stability of the PRT during calibration. The procedure places a limit on the amount of change permitted in the RTPW during calibration. Instruments that exceed this value will be given larger uncertainties commensurate with the observed performance and the "As Left" condition will be denoted as "Limited". The "As Found" RTPW, the dRTPW during calibration, the dRTPW limit, and the final RTPW are shown in the calibration data section of this report.

The following reference standards and measurement equipment were used in this calibration.

Instrument	Model	Serial No.	Recall Date
Precision Digital Thermometer	1590	A13130	05/10/2016

Environmental Conditions:
 Temperature: 22.39°C
 Humidity: 38.9% RH
 Calibration Date: 08/11/2015
 Calibration Due: Not Defined
 PO Number: CCS MARK ANDERSON
 Report Number: B5803043
 Page: 1 of 8

Performed by: 
 Matt Newman

Approved by: 
 Mike Coleman
 Corporate Metrologist

This report shall not be reproduced except in full without written approval of Fluke Calibration, American Fork.